Proceedings of the

1st International Conference on Structural Engineering Research (iCSER2017)

20 - 22 November 2017

Sydney, Australia

ISBN: 978-0-6480147-6-8

Zhong Tao, Fidelis R. Mashiri, Md Kamrul Hassan, Eds.

Proceedings of the 1st International Conference on Structural Engineering Research, 20-22 November 2017, Sydney, Australia

Published by Science, Technology and Management Crest Australia (STAMCA)
in association with
Global Circle for Scientific, Technological and Management Research, Sydney, Australia

Editors:

Zhong Tao
Centre for Infrastructure Engineering,
School of Computing, Engineering and Mathematics
Western Sydney University, Australia

Fidelis Rutendo Mashiri
School of Computing, Engineering and Mathematics
Western Sydney University, Australia

Md Kamrul Hassan
Centre for Infrastructure Engineering,
School of Computing, Engineering and Mathematics
Western Sydney University, Australia

Date published: 19 Nov 2017

Publisher:
Science, Technology and Management Crest
12 Boyer Pl, Minto, New South Wales 2565, Sydney, Australia

Paper Peer Review Process:
All full length papers included in the Proceedings of the 1st International Conference on Structural Engineering Research, 20-22 November 2017 have been independently peer reviewed. The submitted abstracts were reviewed by the Technical Committee, and if the abstract was accepted, the author was invited to submit full papers. The full papers were then reviewed by two or more Reviewers as listed in the reviewer list (Page-viii), and the review comments were sent to the authors to address the comments in updating the papers. The revised papers submitted by the authors were then checked by the Editors, and accepted once the papers satisfied the requirements of the 1st International Conference on Structural Engineering Research.

Welcome by Conference Chairs

The International Conference on Structural Engineering Research aims to provide an international platform for effective exchange of ideas, reaffirming the existing collegial contacts, provide opportunities for establishing new ones as well as provide a forum for academics and researchers to present and share the results and findings of their latest research and practice on a wide range of topics relevant to structural engineering.

As the General Co-Chairs of the 1st International Conference on Structural Engineering Research, 20-22 November 2017, Sydney (iCSER2017), we would like to thank the Plenary Speakers, Keynote Speakers, Invited Speakers, Authors, Sponsors, Secretaries, IT Team Members, Conference Advisory Committee Members, Organising Committee Members, Technical Committee Members, Reviewers and Volunteers for making this conference successful.

Professor Zhong Tao and Associate Professor Fidelis Rutendo Mashiri
General Co-Chairs
1st International Conference on Structural Engineering Research (iCSER2017)

Plenary Speaker

****

Professor Brian Uy, Professor of Structural Engineering, Head of School of Civil Engineering, The University of Sydney, Australia.

Title of Presentation: "Australasian Structural Engineering Research in Steel and Composite Structures and its Influence on International Design Codes".

Biography: Brian Uy commenced as Professor of Structural Engineering and Head of the School of Civil Engineering at the University of Sydney in November 2016. He was previously Professor of Structural Engineering and Director of the Centre for Infrastructure Engineering and Safety (CIES) in the School of Civil and Environmental Engineering at The University of New South Wales from 2013-2016 and was awarded a Scientia Professorship from 2017-2022. Brian also holds an Adjunct Professor role within the School of Engineering and Information Technology at UNSW, Canberra (Australian Defence Force Academy (ADFA)).

Plenary Speaker

****

Professor Xiao-Ling Zhao, Chair of Civil Engineering (Structures Engineering), Department of Civil Engineering, Monash University, Australia.

Title of Presentation: Research into Hybrid Construction Utilising FRP and Seawater Sea Sand and Concrete.

Biography: Prof. X.L. Zhao received several prestigious fellowships, such as Alexander von Humboldt Fellowship, Japan Society for Promotion of Science Invitation Fellow, National "1000-Talent" Chair Professorship, China, Chang Jiang Professorship, China, Distinguished Visiting Fellowship Award, The Royal Academy of Engineering, UK, and Visiting Professorship Award, Swiss National Science Foundation. Prof. X.L. Zhao is a Fellow of American Society of Civil Engineers, Engineers Australia, and International Institute for FRP in Construction. He served as a member on the ERA (Excellence in Research for Australia) Research Evaluation Committee for Engineering and Environmental Sciences Cluster in 2015. He was the Head of Department of Civil Engineering at Monash University from 2008 to 2011.

1st International Conference on Structural Engineering Research, 20-22 November 2017, Sydney, Australia

CONFERENCE COMMITTEE

EXECUTIVE COMMITTEE

Professor Zhong Tao and Associate Professor Fidelis Rutendo Mashiri (General Co-Chairs)
Western Sydney University, Australia

Dr Md Kamrul Hassan (Conference Secretary), Western Sydney University, Australia

Dr Md Hasan Hafizur Rahman (Treasurer), Director, Science, Technology and Management Crest Australia (STAMCA), New South Wales, Australia

Dr Rezaul Bashar (IT Team Leader), Director, Science Technology and Management Crest Australia (STAMCA), New South Wales, Australia

TECHNICAL COMMITTEE

TECHNICAL COMMITTEE CHAIRS

Professor Zhong Tao and Associate Professor Fidelis Rutendo Mashiri
Western Sydney University, Australia

TECHNICAL COMMITTEE MEMBERS

Prof Dennis Lam, University of Bradford, UK
Prof Richard Liew, National University of Singapore, Singapore
Prof Takeshi Mori, Hosei University, Japan
Prof Lewei Tong, Tongji University, China
Prof Xiao-Ling Zhao, Monash University, Australia
Prof Scott Smith, Southern Cross University, Australia
Prof Morgan Dundu, University of Johannesburg, South Africa
Prof Muhammad Fauzi Mohd Zain, Universiti Kebangsaan Malaysia, Malaysia
Associate Professor Maslina Jamil, Universiti Kebangsaan Malaysia, Malaysia
Associate Professor Jiting Qu, Dalian University of Technology, China
Associate Professor Neaz Sheikh, University of Wollongong, Australia
Dr Anna Paradowska, ANSTO, Australia
Dr Hui Jiao, University of Tasmania, Australia
Dr Wei Li, Tsinghua University, China
Dr Faesal Alatshan, College of Engineering Technology, Huon, Libya
Dr Abdelmajeed Altlomate, College of Engineering Technology, Huon, Libya

LOCAL ORGANISING COMMITTEE MEMBERS

Professor Zhong Tao (Chair), Western Sydney University, Australia
Professor Bijan Samali, Western Sydney University, Australia
Professor Kenny Kwok, Western Sydney University, Australia
Professor Hamid Ronagh, Western Sydney University, Australia
Professor Yang Xiang, Western Sydney University, Australia
Associate Professor Fidelis Mashiri (Co-Chair), Western Sydney University, Australia
Associate Professor Baolin Wang, Western Sydney University, Australia
Associate Professor Haiping Zhu, Western Sydney University, Australia
Associate Professor Xinqun Zhu, Western Sydney University, Australia
Dr Md Kamrul Hassan (Secretary), Western Sydney University, Australia
Dr Chunwei Zhang, Western Sydney University, Australia
Dr Yaping He, Western Sydney University, Australia
Dr Olivia Mirza, Western Sydney University, Australia
Dr Kejun Dong, Western Sydney University, Australia
Dr Won Hee Kang, Western Sydney University, Australia
Dr Ee Loon Tan, Western Sydney University, Australia
Dr Pezhman Sharafi, Western Sydney University, Australia

REVIEWER LIST

Professor Zhong Tao, Western Sydney University, Australia
Associate Professor Fidelis Mashiri, Western Sydney University, Australia
Associate Professor Xinqun Zhu, Western Sydney University, Australia
Associate Professor Baolin Wang, Western Sydney University, Australia
Associate Professor Haiping Zhu, Western Sydney University, Australia
Associate Professor Muhammad Hadi, University of Wollongong, Australia
Associate Professor Neaz Sheikh, University of Wollongong, Australia
Dr Md Kamrul Hassan, Western Sydney University, Australia
Dr Chao Hou, The Sydney University
Dr Ee Loon Tan, Western Sydney University, Australia
Dr Farhad Aslani, The University of Western Australia
Dr Mohamed Ghannam, Mansoura University, Egypt
Dr Mohammad Yousuf, Western Sydney University, Australia
Dr Pezhman Sharafi, Western Sydney University, Australia
Dr Qinghua Zeng, Western Sydney University, Australia
Dr Tai Thai, La Trobe University, Australia
Dr Tao Yu, University of Wollongong, Australia
Dr Vipulkumar Ishvarbhai Patel, La Trobe University, Australia
Dr Wei Li, Tsinghua University, China
Dr Won Hee Kang, Western Sydney University, Australia
Dr Zhu Pan, Western Sydney University, Australia

Table of Contents

Concrete Materials and Concrete Structures

Composite Structures and Composite Materials

Structural Rehabilitation, Retrofitting and Strengthening

Earthquake, Wind and Fire Engineering

Theories and Methods of Structural Analysis

Proc. 1st International Conference on Structural Engineering Research (iCSER 2017)
20-22 Nov 2017, Sydney, Australia
ISBN: 978-0-6480147-6-8

Australasian Structural Engineering Research in Steel and Composite Structures and its influence on International Design Codes

Brian Uy[1]

[1]Professor of Structural Engineering, Head of School of Civil Engineering, University of Sydney
Corresponding author's E-mail: brian.uy@sydney.edu.au

Extended Abstract

This paper will address the Australasian advances in steel-concrete composite bridge and building structures. The paper will firstly provide an overview for the behaviour and design of bridge structures past, present and future. This will then be followed by an overview of the behaviour and design of building structures, past present and future. Over the last decade there have been significant developments on the development of a draft bridge standard for steel-concrete composite structures, namely AS/NZS 5100 Part 6 and salient elements of recent advances will be highlighted in this paper. In parallel with work being carried out on the development of a draft bridge standard has been work on the development over the last five years on a draft building standard for steel-concrete composite structures, namely AS/NZS 2327. Once again, salient features of this standard will be provided in this paper. The paper will highlight how Australasian Structural Research has influenced international design codes, namely Eurocodes and AISC specifications. The paper will conclude with discussions on ongoing and further research that is required in the area of steel-concrete composite structures to deal with the ongoing demands of modern bridge and building structures, (Figure 1).

Figure 1. Concrete filled steel column, 200 George Street, Sydney

References

American Institute for Steel Construction (2016) Specification for structural steel buildings, USA.

British Standards Institution (2004) Eurocode 4, ENV 1994-1-1 2004. Design of composite steel and concrete structures, Part 1.1, General Rules and Rules for Buildings.

Standards Australia/Standards New Zealand (2017), AS/NZS 5100.6: 2017, Bridge Design, Part 6: Steel and composite construction, Sydney/Wellington, Australia/New Zealand, 2017.

Standards Australia/Standards New Zealand (2017), Composite Structures, AS/NZS 2327-2017, Sydney, Australia.

Proc. 1st International Conference on Structural Engineering Research (iCSER 2017)
20-22 Nov 2017, Sydney, Australia
ISBN: 978-0-6480147-6-8

Research into Hybrid Construction Utilising FRP and Seawater Sea Sand Concrete

Xiao-Ling Zhao[1]
[1]Professor, Department of Civil Engineering, Monash University, Clayton, VIC 3800, Australia
Corresponding author's E-mail: ZXL@monash.edu

Extended Abstract

Australia's population is projected to double within 50 years (ABS 2013). In Australia, about 80% of the population lives along the coast (E-Alert 2009). This will increase the huge demand for resources (e.g. fresh water) and infrastructure (e.g. bridges, highways, buildings, dams) especially along the coast. These are also among the major challenges worldwide because the global population is expected to increase from 6.9 billion in 2010 to 9.6 billion by 2050 (Kochhar 2014). The concrete industry uses about 2.5 billion tons of fresh water annually, for mixing, curing and cleaning (JCI 2014). By 2050, according to the United Nations, more than half of the world's population will be unable to get enough drinking water. The rapid pace of construction has caused large-scale sand-dredging and subsequent sand scarcity. Such over use and dredging can have devastating socio-environmental implications, such as depletion of fish stocks and erosion, landslides and flooding (The Economist 2014). The corrosion of steel reinforcement bars and external steel tubes is a challenge to the long-term performance of steel-concrete composite construction. The hybrid construction utilising seawater sea sand concrete (SWSSC) and fibre reinforced polymer (FRP) could be an attractive solution to address the above challenge (Teng et al. 2011, Teng 2014, Teng et al. 2016), which has attracted much research attention.

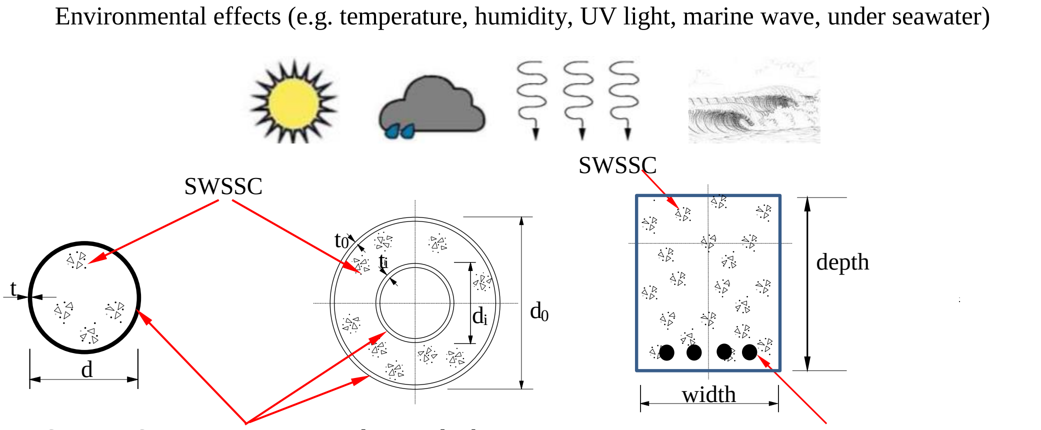

(a) External confinement of SWSSC *(b) Internal reinforcement of SWSSC*

Figure 1. Schematic view of hybrid construction utilising SWSSC and FRP and/or stainless steel

Xiao et al. (2017) recently presented a critical review of existing studies on the effects of using sea sand and/or seawater as raw materials on the performance of concrete. An EU-US project titled SEACON (Bertola et al. 2016, Khatibmasjedi et al. 2016) was also introduced in Xiao et al. (2017), where GFRP reinforcement and SWSSC were used to construct a bridge deck. The research on SWSSC-FRP hybrid construction is still limited (e.g. Zha et al. 2010, Xu et al. 2015, Peng et al. 2014, Li et al. 2016a, 2016b, 2017, Dong et al. 2016, 2017, Wang et al. 2017a, 2017b). This paper gives a summary of current research at Monash University on hybrid construction using FRP and seawater sea sand concrete (SWSSC), as illustrated in Figure 1. This forms part of a research program sponsored by the Australian Research Council in collaboration with The Hong Kong Polytechnic University, Southeast University and Harbin Institute of Technology, China.

(1) Properties of SWSSC: Alkali activated slag concrete with seawater and sea sand was used in this research. Material properties measured include modulus of elasticity, compressive strength, bending strength at ambient temperature as well as elevated temperature. The main conclusions from Li et al. (2017) include:

(a) The mass loss is mainly contributed by the loss of free water, physical- and chemical-bonded water. The seawater and sea sand do not affect the mass loss behaviour obviously.
(b) The seawater, sea sand and coarse aggregate with larger size have a slightly (less than 10%) detrimental effect on residual strength. The samples become more deformable after heating and the residual Young's moduli drop more rapidly than residual strength when temperature is increased.
(c) The mechanical properties degradation of slag paste are mainly caused by cracks induced by temperature gradient and pore pressure and phase changes at high temperature, among which the cracks dominate the degradation. On the other hand, the main mechanism of the mechanical properties degradation of concrete, regardless using slag or cement, seawater or fresh water, river sand or sea sand, is the thermal expansion incompatibility between the contraction of paste matrix and expansion of aggregates. The influence of seawater and sea sand on the thermal properties is not obvious.

(2) Long-term behavior of fiber reinforced polymer (FRP): Filament-wound FRP tubes were adopted with three types of fibres (glass, carbon and basalt). Exposure temperatures include 25, 40, 60˚C with exposure time varies from 1 month to 12 months. Some preliminary results were reported in Guo et al. (2017) for CFRP tubes after pre-exposure to different solutions simulating seawater sea sand concrete and conventional concrete at 60 °C for 3 months. They are summarised here.

(a) Interface debonding and matrix degradation were found in each of the simulated concrete solutions. However, continuous cracks were found along fiber/matrix interface exclusively in the case of normal concrete solutions (i.e. SWSSNC, NC) that could provide easy paths for solution to penetrate.
(b) The highest weight gain (approx. 0.7%) was found in the case of normal concrete (NC) solution, followed by seawater sea sand normal concrete (SWSSNC), distilled water (DW), high performance concrete (HPC) and seawater sea sand high performance concrete (SWSSHPC) solutions. The observed lesser weight gain in SWSSC solutions (i.e. SWSSNC, SWSSHPC) than conventional concrete solutions (i.e. NC, HPC) can be attributed to osmotic effect.

(3) SWSSC-filled FRP and stainless steel (SS) stub columns: Stub columns, including hollow sections and SWSSC fully filled tubes or double-skin tubes, were tested under axial compression. The effects of some key parameters (e.g., tube diameter-to-thickness ratio, cross-section types, outer tube types, and inner tube types) on the confinement effects were discussed. Some typical load versus axial strain curves are shown in Figure 2 for SWSSC-filled double skin tubes. The main conclusions from Li et al. (2016a, 2016b) can be summarised as:

(a) The strength and ductility of SWSSC-filled tubes are significantly enhanced in comparison with hollow section tubes and plain concrete.
(b) The confinement effect provided by SS tubes is lower than that by BFRP/CFRP/GFRP tubes, but the confinement can be maintained for larger axial strain for SS tubes. The strength enhancement and ductility of SWSSC-filled CFRP tubes are higher than those of BFRP tubes

mainly due to its higher hoop strength. The confinement provided by BFRP and GFRP tubes is quite similar.

(c) As the diameter-to-thickness ratio of tubes increases, the level of confinement reduces for all the four types of tubes (SS, GFRP, BFRP and CFRP). When compared with fully filled tubes, the confinement provided by the double skin tubes start to decrease at large deformation due to the buckling of inner FRP tubes. The influence of inner tube on confinement is not significant unless they are slender FRP tubes after an axial strain of 0.03.

(d) Research is being conducted on the theoretical analysis of SWSSC-filled FRP tubes and the durability of SWSSC-filled FRP tubes.

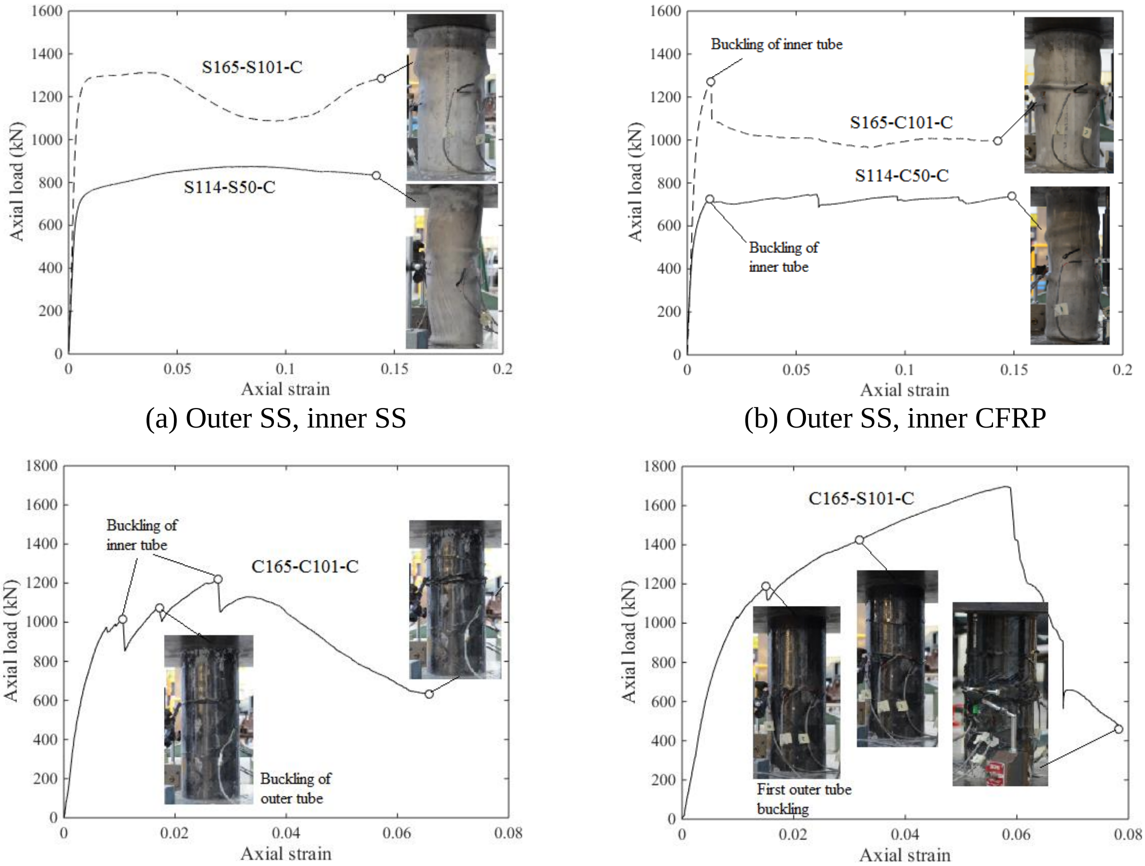

(a) Outer SS, inner SS (b) Outer SS, inner CFRP

(c) Outer CFRP, inner CFRP (d) Outer CFRP, inner SS

Figure 2. Axial load versus axial strain curves for SWSSC-filled double-skin tubes (Li et al. 2016a, 2016b)

(4) Durability of FRP bars in SWSSC environment: Accelerated corrosion tests were conducted on FRP bars using two types of SWSSC solutions at different pH and temperatures, and for different durations. The long-term behaviour of BFRP and GFRP bars under the service construction condition was predicted. The main conclusions from Wang et al. (2017a, 2017b) include:

(a) Nearly no change was found in Young’s Modulus for GFRP and BFRP bars after exposure in SWSSC solutions.

(b) The degradations of GFRP and BFRP bars in SWSSC solution at high temperature both mainly include etching of fibre, hydrolysis of resin, and interface debonding.

(c) The water uptake and desorption results showed that the degradation of epoxy-based BFRP, GFRP and CFRP bars in SWSSC solutions is mainly from the hydrolysis of resin, which was also evidenced by the FTIR results.
(d) Arrhenius relationship theory was found to be conservative in predicting the long-term performance of BFRP and GFRP bars.
(e) A more accurate degradation model should be developed for FRP bars in SWSSC by considering the real temperature and humility ranges and pre-loading stress.

This paper gave a summary of current research at Monash University on hybrid construction using FRP and seawater sea sand concrete (SWSSC). It covered properties of SWSSC, long-term behavior of fiber reinforced polymer (FRP), SWSSC-filled FRP and stainless steel stub columns and durability of FRP bars in SWSSC environment.

The author thanks his collaborators (Professor Raman Singh and Dr. Saad Al-Saadi at Monash University, Professor Jin-Guang Teng at the Hong Kong Polytechnic University, Professor Gang Wu at Southeast University and Professor GuiJun Xian at the Harbin Institute of Technology) and postgraduate students (Yinglei Li, Faye Guo, Zike Wang and ZiQing Dong). The author acknowledges the financial support provided by the Australian Research Council (ARC) through an ARC Discovery Grant (DP160100739). The author also thanks Mr. Damian Carr of Bayside City Council for his permission to obtain seawater and sea sand from Brighton Beach in Melbourne.

References

ABS (2013). Population projections, Australia, 2012 (base) to 2101, Australian Bureau of Statistics, 26 November 2013.

Bertola F, Canonico F, Bianchi M, Nanni A (2016). The SEACON project, International Cement Review, June, 63–66.

Dong Z, Wu G, Xu Y (2016). Experimental study on the bond durability between steel-FRP composite bars (SFCBs) and sea sand concrete in ocean environment, Construction and Building Materials, 115, 277-284.

Dong ZQ, Wu G, Zhao XL, Wang ZK (2017). A refined prediction method for the long-term performance of BFRP bars serviced in field environments, Construction and Building Materials, 155, 1072-1080.

E-Alert (2009). Coastal buildings and infrastructure, Accessed via https://www.maddocks.com.au/reading-room/coastal-buildings-and-infrastructure-e-alert-november-2009/ on 5 January 2015.

Guo F, Al-Saadi S, Singh RK, Zhao XL (2017). Durability of carbon fiber reinforced polymer (CFRP) with combined use of seawater sea sand concrete (SWSSC), The Sixth Asia-Pacific Conference on FRP in Structures (APFIS 2017), Singapore, 19-21 July 2017.

JCI (2014). Technical committee on the use of seawater in concrete, Accessed via http://www.jci-net.or.jp/ on 24 Dec. 2014.

Khatibmasjedi F, Caso FD, Nanni, A (2016). SEACON: Redefining sustainable concrete, in: Proceedings of the 4th International Conference on Sustainable Construction Materials and Technologies (SCMT4), LV. USA, 7 to 11 August 2016.

Kochhar R (2014). 10 projections for the global population in 2050, Pew Research Report, 3 February 2014, Accessed via http://www.pewresearch.org/author/rkochhar/ on 2 January 2015.

Li YL, Zhao XL, Raman Singh RK, Al-Saadi S (2016a). Experimental study on seawater and sea sand concrete filled GFRP and stainless steel tubular stub columns, Thin-Walled Structures, 106, 390-406.

Li YL, Zhao XL, Raman Singh RK, Al-Saadi S (2016b). Tests on seawater and sea sand concrete-filled CFRP, BFRP and stainless steel tubular stub columns, Thin-Walled Structures, 108, 163-184.

Li YL, Zhao XL, Raman Singh RK, Al-Saadi S (2017). Thermal and mechanical properties of alkali-activated slag paste, mortar and concrete utilising seawater and sea sand, Construction and Building Materials, accepted for publication on 25 October 2017.

Peng P, Wang J, Zhang X, Ye LP (2014). Development and innovation on combining FRP and sea sand concrete for structures, Fiber Reinforced Plastics/Composites, 12, 13–18 (in Chinese).

Teng JG (2014). Performance enhancement of structures through the use of fibre reinforced polymer (FRP) composites, in: Proceedings of the 23rd Australian Conference on Mechanics of Structures and Materials (ACMSM23), Lismore, Australia (Abstract), 2014.

Teng JG, Yu T, Dai JG, Chen GM (2011). FRP composites in new construction: current status and opportunities, in: Proceedings of the 7th National Conference on FRP Composition. in Infrastructure (Supplementary Issue of Industrial Construction) (Abstract) Hangzhou, China, 2011.

Teng JG, Yu T, Dai JG, Chen GM (2016). Proceedings of International Workshop on Seawater Sea-sand Concrete (SSC) Structures Reinforced with FRP Composites Hong Kong, China, 13 December 2016.

The Economist (2014). Singapore's sand shortage - The hourglass effect, Accessed via http://www.economist.com/ on 24 Dec. 2014.

Wang ZK, Zhao XL, Xian GJ, Wu G, Singh Raman RK, Al-Saadi S, Haque A (2017a). Long-term durability of basalt- and glass- fibre reinforced polymer (BFRP/GFRP) bars in seawater and sea sand concrete environment, Construction and Building Materials, 139, 467-489.

Wang ZK, Zhao XL, Xian GJ, Singh Raman RK, Al-Saadi S (2017b). Durability study on interlaminar shear behaviour of basalt-, glass- and carbon-fibre reinforced polymer (B/G/CFRP) bars in sea water sea sand concrete environment, Construction and Building Materials, 156, 985-1004.

Xiao JZ, Qiang CB, Nanni A, Zhang KJ (2017). Use of sea sand and seawater in concrete construction: Current status and future opportunities, Construction and Building Materials, 155, 1101–1111.

Xu YQ, Wu G, Wu ZS (2015). Experimental research on steel fiber composite bars (SFCB) reinforced marine sand concrete beams, in: Proceedings of the 9th National Symposium on the Application of FRP in Construction Engineering, Chongqing, China (in Chinese).

Zha XX, Cang YQ, Wang XL, Zhong ST (2010). Investigation of steel-FRP-sea sand concrete stubs under axial compressive loading, Building Structures, 40 (supplement) (in Chinese).

ISBN: 978-0-6480147-6-8

Influence of Longitudinal FRP Straps on the Behaviour of Circularised and FRP Wrapped Square Hollow RC Concrete Specimens

Mohammed T. Jameel[1], M. Neaz Sheikh[2] and Muhammad N.S. Hadi[3]

[1] School of Civil, Mining and Environmental Engineering, University of Wollongong, Australia
Email: mtjj932@uow.edu.au
[2] School of Civil, Mining and Environmental Engineering, University of Wollongong, Australia
E-mail: msheikh@uow.edu.au
[3] School of Civil, Mining and Environmental Engineering, University of Wollongong, Australia, (corresponding author)
E-mail: mhadi@uow.edu.au

Abstract

This paper investigates the influence of longitudinal CFRP straps on the behaviour of circularised and FRP wrapped square hollow reinforced concrete (RC) columns. Twelve square hollow RC specimens were prepared and tested under concentric axial loads, eccentric axial loads and four-point bending. The specimens were divided into three groups of four specimens. The specimens in the first group were the non-strengthened square hollow RC specimens. The specimens in the second group were circularised by adding concrete segments to the sides of the square hollow RC specimens. Then the circularised specimens were wrapped with two layers of CFRP. The specimens in the third group were strengthened by attaching one longitudinal CFRP strap on each side of the square hollow RC specimens. Then the specimens were circularised with concrete segments and wrapped with two layers of CFRP. The test results showed that circularisation of the square hollow RC specimens enhanced the performance of the specimens in terms of ultimate axial load and ductility. The influence of the longitudinal CFRP straps was insignificant in increasing the ultimate axial load and ductility of concentrically loaded specimens. The presence of the longitudinal CFRP straps enhanced the axial load at yield of concentrically loaded specimens. The presence of the longitudinal CFRP straps enhanced the ultimate axial load and ductility of eccentrically loaded specimens. The contribution of the longitudinal CFRP straps to the ultimate axial load and ductility of the circularised square hollow RC specimens increased with the increase in load eccentricity. Also, the longitudinal CFRP straps increased the bending moment capacity of the circularised and CFRP wrapped square hollow RC specimens.

Keywords: Column, circularisation, CFRP, eccentricity.

1. INTRODUCTION

The Fibre Reinforced Polymer (FRP) materials have been used widely in strengthening concrete members in the last few decades. Strengthening concrete columns by wrapping with FRP increased the strength and ductility of the wrapped solid and hollow RC columns (Kusumawardaningsih and Hadi 2010). The increase in strength and ductility of the FRP wrapped columns is due to the confinement caused by FRP. The confinement brings the concrete in solid column into a triaxial state of stresses while FRP confinement brings the concrete in hollow columns into biaxial state of stresses.

The loading eccentricity and column cross-section can influence the efficiency of FRP confinement. The efficiency of FRP confinement decreases with the increase in the load eccentricity (Li and Hadi

2003). The presence of longitudinal FRP straps can reduce the effect of eccentricity and can increase the load and deformation capacities of eccentrically loaded hollow RC columns (Hadi and Le 2014). The FRP effectiveness of confinement is less for square columns than for circular columns. Changing a square cross section into circular cross section and then wrapping with FRP is an effective strengthening method for square solid and hollow concrete columns. (Hadi et al. 2012a; Jameel et al. 2017; Hadi et al. 2017). Hadi et al. (2017) showed that circularisation increased the strength, ductility and bending moment of the FRP wrapped square hollow RC specimens under different loading eccentricities. This paper investigates the influence of longitudinal CFRP straps on the behaviour of circularised and CFRP wrapped square hollow RC specimens under different loading eccentricities.

2. EXPERIMENTAL PROGRAM

Details of the experimental program of testing circularised and CFRP wrapped hollow RC specimens have been reported in Hadi et al. (2017). In this study, three groups are selected to investigate the influence of longitudinal CFRP straps on the behaviour of circularised and FRP wrapped hollow RC specimens under different loading conditions. For clarity, the experimental program is briefly reported herein.

The experimental program comprises twelve square hollow RC specimens of three groups. The specimens were constructed with square cross-section of 150 mm side dimension, square hole of 50 mm side dimension and 800 mm height. Four N12 deformed steel bars were used as longitudinal reinforcement and R6 plain steel bars were used as stirrups placed at 60 mm from centre to centre. The clear covers of concrete were 17 mm on each side and 20 mm on the top and bottom ends of the specimens. The specimens in the first group (Group R) were the non-strengthened hollow RC specimens. The specimens in the second group (Group CC) were the square hollow RC specimens circularised and wrapped with two layers of CFRP. The specimens in the third group (Group LCC) were the square hollow RC specimens strengthened with one longitudinal CFRP strap on each side then circularised and wrapped with two layers of CFRP. The first specimen from each group was tested as a column under concentric axial load. The second and third specimens were tested as columns under 25 mm and 50 mm eccentric axial loads, respectively. The fourth specimen was tested as a beam under four-point bending. Table 1 shows the test matrix of the tested specimens.

Table 1. Test matrix

Specimen	Cross-section (mm)	Gross area (mm^2)	Description of specimen	Eccentricity (mm)
N-0 **N-25** **N-50** **N-F**	150x150	19547	No strengthening	0 25 50 Four-point bending
CC-0 **CC-25** **CC-50** **CC-F**	Φ 212	32360	Circularised with four concrete segments and wrapped with two CFRP layers	0 25 50 Four-point bending
LCC-0 **LCC-25** **LCC-50** **LCC-F**	Φ 212	32360	Strengthened with one longitudinal CFRP straps on each side of square specimens then Circularised and wrapped with two CFRP layers	0 25 50 Four-point bending

The average compressive strength of concrete was 40 MPa and 47 MPa at 28 days and during the testing, respectively, determined according to AS1012.9 (1999). The mechanical properties of CFRP was 1102 N/mm maximum tensile strength per unit width and 0.016 mm/mm corresponding tensile strain determined according to ASTMD7565 (2010). The tensile yield strength was 478 MPa and 570

MPa, respectively, for the N12 and R6 steel bars determined according to AS 1391 (2007). The wet-layup method was used to wrap the specimens with CFRP by using an adhesive mixture of hardener and epoxy resin with ratio of 1:5. The top and bottom 100 mm of column specimens were wrapped with an extra two CFRP layers to prevent the premature failure at these regions. The beam specimens were wrapped with two CFRP layers at the shear span to reduce the shear failure. The Linear Variable Differential Transducers (LVDTs) were used to determine the vertical displacement of the tested specimens. The lateral deflection of the eccentrically tested specimens and the midspan deflection of the beam specimens were determined by using the laser triangulation. The specimens were subjected to displacement control loading of 0.3 mm/min. Figure 1 shows the details of specimens in Group LCC.

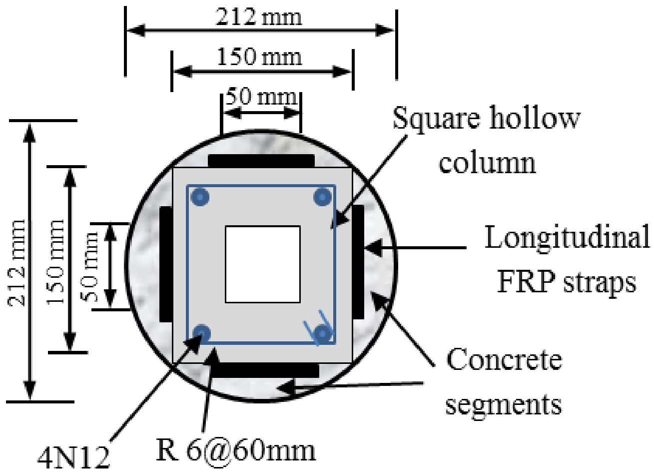

Figure 1. Design details of specimens in Group LCC

3. RESULTS AND DISCUSSIONS

3.1. Failure Mode

The failure of the reference specimens was sudden, brittle and initiated with spalling of concrete cover and buckling of longitudinal steel. The failure of the circularised column specimens was generally explosive and initiated by the rupture of CFRP at the midheight. It was observed that specimens in Group LCC experienced longer time up to failure than the specimens in Group CC.

3.2. Load-deformation Behaviour

Table 2 and Table 3 summarise the experimental results of the specimens tested as column specimens and beam specimens, respectively. Figures 2-5 show, respectively, the load-deformation behaviours of the specimens tested under concentric axial load, 25 mm eccentric axial load, 50 mm eccentric axial load, and four-point bending. Figure 6 shows a comparison of the normalised ultimate axial load and ductility between the tested specimens.

The normalised ultimate load and normalised ductility of specimens were calculated by dividing, respectively, the ultimate load and ductility of specimens by the ultimate load and ductility of the corresponding reference specimens. The ductility of the specimens was calculated by dividing the axial deformation corresponding to 85% of the post ultimate axial load by the deformation at the yield of the specimen.

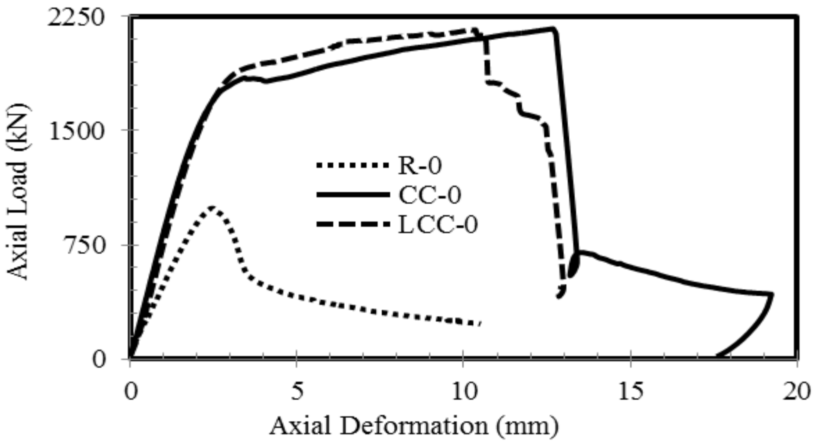

Figure 2. Axial load-axial deformation behaviour of concentrically loaded column specimens.

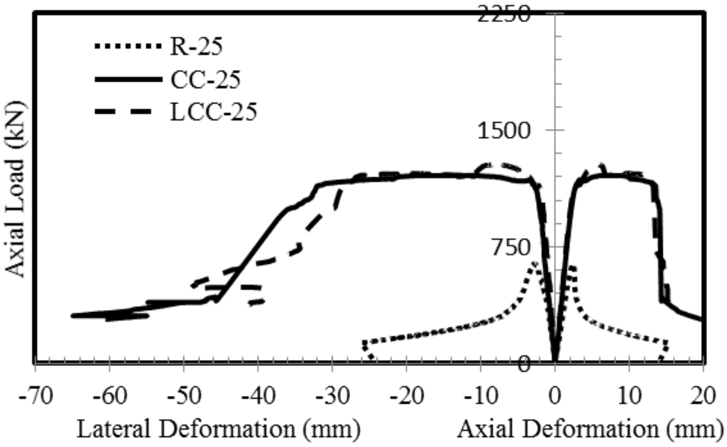

Figure 3. Axial load-deformation behaviour of eccentrically loaded column specimens (e = 25 mm)

The axial load-axial deformation behaviour of Specimen CC-0 showed two peak axial loads. After the first peak axial load of 1848 kN, the load dropped slightly to 1826 kN due to the presence of the hole that resulted in lower confinement gain compared to the degradation of concrete, then the load decreased to 2169 kN. While Specimen LCC-0 showed bi-linear axial load-axial deformation behaviour. Specimens CC-0 and LCC-0 showed similar increase in the ultimate axial load of 119% compared to that of Specimen R-0. Therefore, the contribution of the longitudinal CFRP straps to the ultimate axial load was negligible for the concentrically loaded specimens. Specimen LCC-0 achieved higher axial load at yield of 1508 MPa than that of Specimen CCC-0 of 1403 MPa.

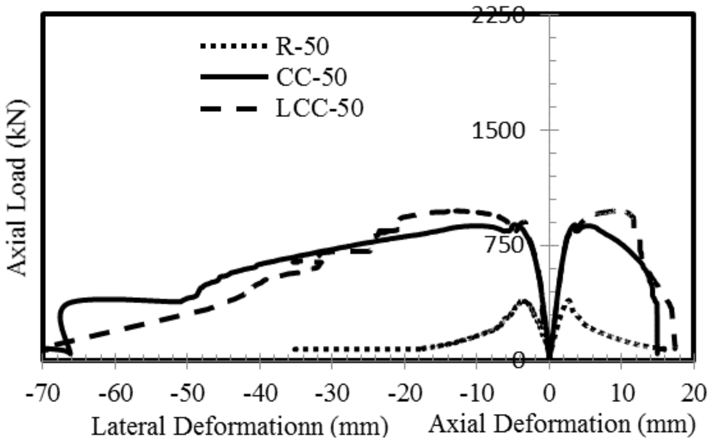

Figure 4. Axial load-deformation behaviour of eccentrically loaded column specimens (e = 50 mm)

The increase in the ultimate axial load was 99% and 88% for Specimens LCC-25 and CC-25, respectively, compared to that of Specimen R-25. The increase in the ultimate axial load was 148% and 125% for Specimens LCC-50 and CC-50, respectively, compared to that of Specimen R-50. The axial load-axial deformation behaviour of Specimen LCC-50 showed two peak axial loads due to the presence of the longitudinal CFRP straps. After the first peak load of 902 kN, the axial load of Specimen LCC-25 dropped to 846 kN then the axial load increased up to the ultimate axial load of 975 kN due to the activation of the longitudinal CFRP straps with the increased applied eccentric loading. The increase in the ultimate axial load was 89% and 143% for Specimens LCC-F and CC-F, respectively, compared to that of Specimen R-F. The load-deflection behaviour of Specimen LCC-F showed three peaks due to the subsequent rupture of the longitudinal CFRP straps in the bottom and the sides of the specimens.

Table 2. Experimental results of the column specimens

Specimen	Axial load at yield (kN)	Axial deformation at yield (mm)	Ultimate axial load (kN)	Axial deformation at ultimate axial load (mm)	Lateral deflection at ultimate axial load (mm)	Ductility	Moment at ultimate load (kN-m)
R-0	800	2.2	989	2.5	-	1.4	-
CC--0	1403	2.3	2169	12.7	-	5.9	-
LCC-0	1508	2.5	2162	10.5	-	4.4	-
R-25	582	2.2	642	2.4	2.3	1.2	17.5
CC--25	985	2.5	1209	6.2	9.0	5.6	41
LCC-25	1011	2.3	1279	5.7	8.6	5.8	43
R-50	315	2.1	393	2.7	4.0	1.5	21.3
CC--50	680	2.4	885	3.5	5.0	4.2	48.5
LCC-50	726	2.5	975	9.7	12.5	4.9	61

Specimen CC-0 achieved the highest ductility of 5.9 followed by Specimen LCC-0 of 4.4. Specimen LCC-25 achieved higher ductility of 5.8 than that of 5.6 for Specimen CC-25. Specimen LCC-50 achieved higher ductility of 4.9 than that of 4.2 for Specimen CC-50. Specimen LCC-F achieved higher ductility of 9.4 than that of 8.4 for Specimen CC-F.

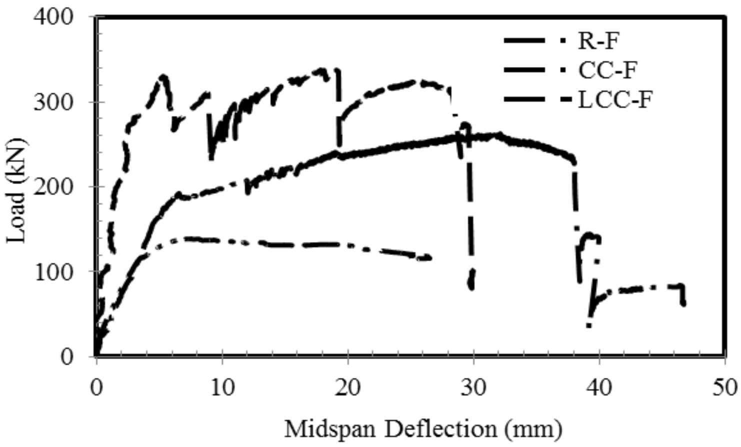

Figure 5. Load-midspan deflection behaviour of beam specimens

3.3. Position of the Longitudinal CFRP Straps

The test results showed that the longitudinal CFRP straps enhanced the performance of the circularised and CFRP wrapped hollow RC specimens subjected to eccentric axial loads and four-point bending. Also, there was no significant contribution of the longitudinal CFRP straps to the concentrically loaded specimens. Based on the above results, the longitudinal CFRP strap on the compression side was negligible. The longitudinal CFRP straps on the tension side contributed directly to the tensile resistance of the column specimens subjected to eccentric axial loads and four-point bending which increased the ultimate load of the specimens. After the rupture of the CFRP straps on the tension side, the CFRP straps on the left and right sides of the square hollow specimens in Group LCC contributed to the ultimate load of the specimens and ruptured as single fibres one after one towards the compression side with the increase in the applied eccentric load. The subsequence ruptures of the CFRP straps increased the ductility of the specimens and were more active for specimens with higher eccentricity. Therefore, it is believed that the longitudinal CFRP straps on the tension side of specimens were more effective in increasing the strength than increasing the ductility, while the longitudinal CFRP straps on the left and right sides of the specimens were more effective in increasing the ductility than increasing the strength of the tested specimens. Therefore, strengthening the circularised hollow RC specimens with longitudinal CFRP straps on the sides of the specimens is significant in increasing the ductility of eccentrically loaded column specimens.

Table 3. Results of specimens tested under four-point bending

Specimen	Yield load (kN)	Midspan deflection at yield (mm)	Ultimate load (kN)	Midspan deflection at ultimate load (mm)	Ductility	Moment at ultimate load (kN-m)
R-F	116	4.2	139	7.6	6.2	16
CC-F	158	4.5	263	32	8.4	30.5
LCC-F	270	3.0	338	19	9.4	40

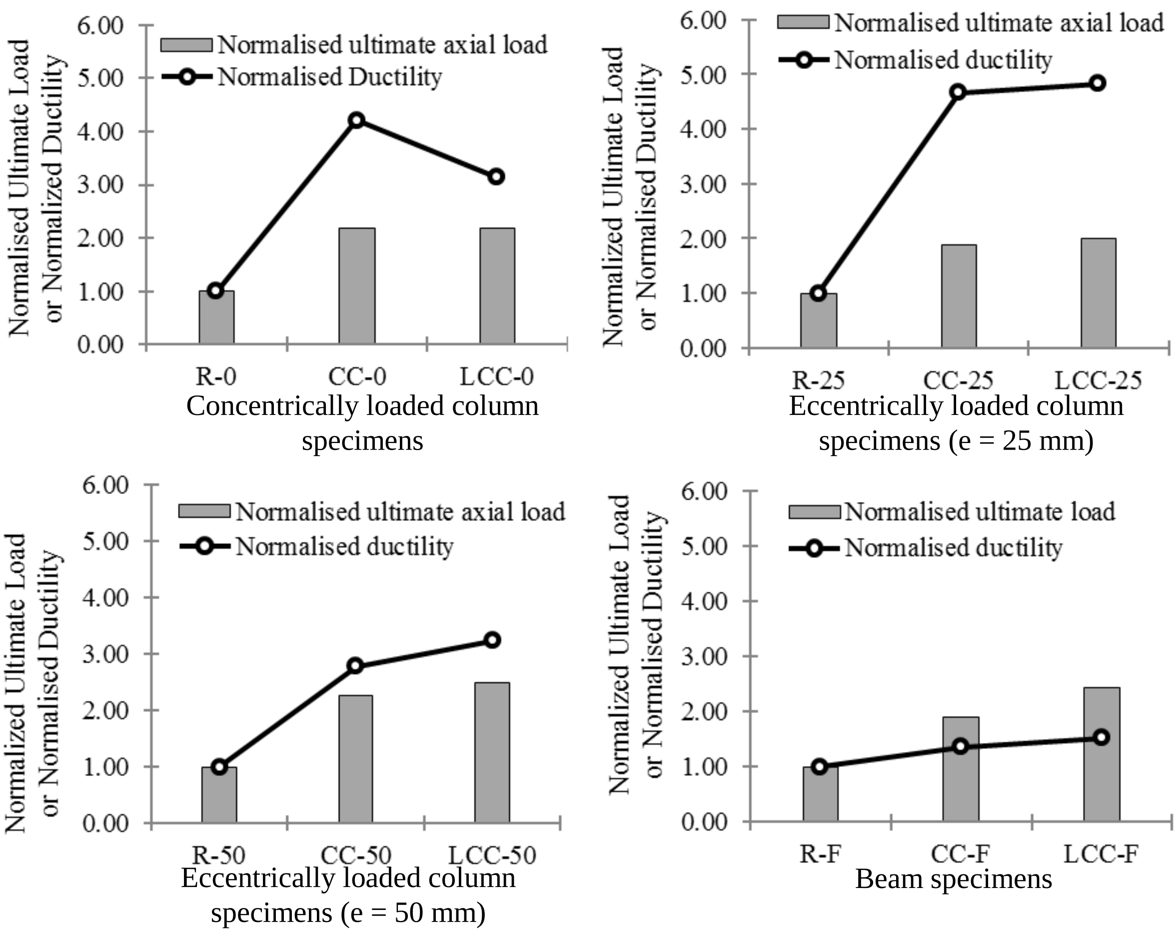

Figure 6. Comparison between specimens (normalised ductility and normalised ultimate load)

Figure 6 shows that the gain in ductility was higher than that of ultimate axial load for the circularised and CFRP wrapped column specimens relative to the reference column specimens. While the gain in ultimate load was higher than the gain in ductility for the circularised and CFRP wrapped beam specimens relative to the reference beam specimens. Also, the gain in ultimate axial load and ductility was higher for Specimens LCC-25 and LCC-50 than that of Specimens CC-25 and CC-50, respectively due to the increase in the effectiveness of the longitudinal CFRP straps with the increased load eccentricity.

3.4. Influence of Load Eccentricity

Figure 7 shows the axial load-axial deformation curves in relation to the eccentricity of the axial load of the tested specimens. The load and deformation capacities of column specimens decreased with the increase in the load eccentricity. The reduction in ultimate axial load of Specimens R-25 and R-50 relative to Specimen R-0 was respectively, 35% and 60%. The reduction in ultimate axial load of Specimen CC-25 and CC-50 relative to Specimen CC-0 was respectively, 44% and 59%. It can be seen that the influence of eccentricity is higher for the circularised and CFRP wrapped group compared to the reference group. This might be because the higher eccentricity increased the concrete area in tension zone and reduced the area of concrete in compression zone, hence, reducing the confined concrete area. The reduction in ultimate axial load of Specimens LCC-25 and LCC-50 relative to Specimen LCC-0 was respectively, 40% and 55%. It is clear that the longitudinal CFRP straps minimized the reduction in the ultimate axial load especially with the high load eccentricity.

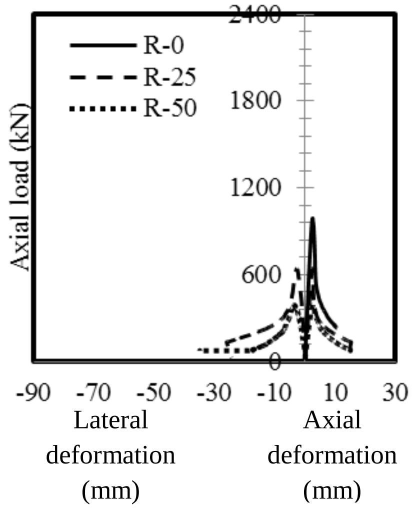

(a) Group R

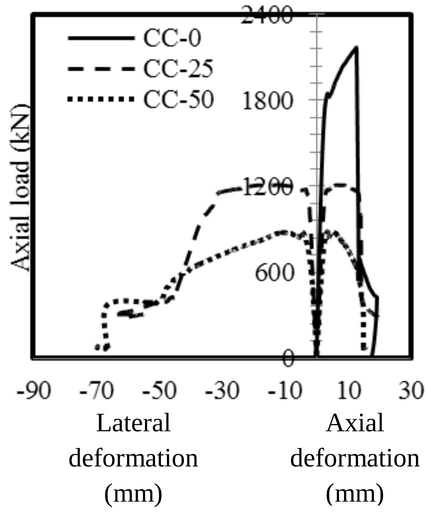

(b) Group CC

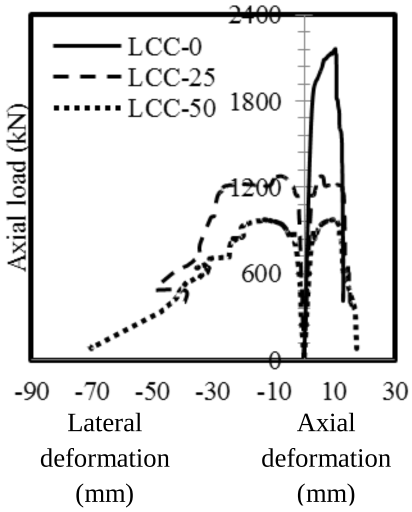

(c) Group LCC

Figure 7. Axial load-deformation behaviour of column specimens with different load eccentricities

3.5. Axial Load-Bending Moment Interactions

Figure 8 shows the axial load-bending moment interactions of the tested specimens. The bending moment (M_u) corresponding to the ultimate axial load of the specimens tested as column specimens was calculated as:

$$M_u = P_u (e + \delta) \tag{1}$$

where *e and* δ are the initial eccentricity and the lateral deformation at the ultimate axial load (P_u).

The bending moment corresponding to the ultimate load of the specimens tested as beam specimens was calculated as:

$$M_u = 0.5 P_u a \tag{2}$$

where a = 233 mm, is length between the support and the nearest loading point of the beam specimens.

The axial load bending moment interactions comprises four points nominated as A, B, C and D for each group (Figure 5). The first point (A) represents the concentrically loaded column specimens. The second point (B) and the third point (C) represent, respectively, the 25 mm and 50 mm eccentrically loaded column specimens. The fourth point (D) represents the specimens tested under four-point bending. At Point A, the circularised and CFRP wrapped specimens achieved higher ultimate load compared to the reference specimens. At Point B, Specimen LCC-25 achieved slightly higher ultimate axial load and corresponding bending moment than that of Specimen CC-25. At Point C, Specimen LCC-50 achieved 10% higher ultimate axial load and 25% higher corresponding bending moment than that of Specimen CC-50. The increase in the ultimate axial load and the corresponding bending moment of specimens in Group LCC compared to specimens in Group CC was higher at Point C than that at Point B due to the presence of the longitudinal CFRP straps that increased the capacity of column specimens at ultimate load and lateral deformations.

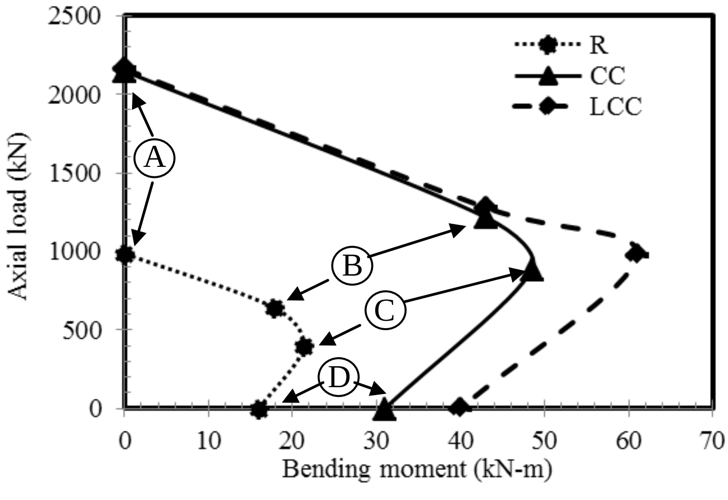

Figure 8. Experimental axial load-bending moment interactions for the tested specimens.

4. CONCLUSIONS

Circularisation and FRP wrapping proved to be an effective method in strengthening hollow RC column specimens subjected to different loading conditions. Strengthening square hollow RC column specimens with longitudinal CFRP straps increased the load capacity, ductility and bending moment capacity of the circularised and FRP wrapped square hollow RC specimens. The presence of longitudinal CFRP straps was insignificant for the concentrically loaded specimens. The effectiveness of the longitudinal CFRP straps increases with the increase in the eccentricity of the applied load. The presence of the longitudinal CFRP straps on the tension side of the eccentrically loaded column specimens and beam specimens was more significant in increasing the strength of the specimen than the ductility. The presence of the longitudinal CFRP straps on the left and right sides of the specimens was more significant in increasing the ductility of column specimens than the ultimate load.

5. ACKNOWLEDGMENTS

The first author acknowledges the Iraqi Government and the University of Wollongong, Australia for the support of his Ph.D. scholarship.

6. REFERENCES

AS (Australian Standard). (1999). "Determination of the compressive strength of concrete specimens." AS 1012.9-1999, Sydney, Australia.

AS (Australian Standard). (2007). “Metallic materials-Tensile testing at ambient temperature." AS 1391-2007, Sydney, Australia.

ASTM (American Society for Testing and Materials). (2010). “Standard test methods for determining tensile properties of fiber reinforced polymer matrix composites used for strengthening civil structures.” ASTM D7565:2010, West Conshohocken, PA 19428-2959, USA.

Hadi, M. N. S. and Le, T. D. (2014). "Behaviour of hollow core square reinforced concrete columns wrapped with CFRP with different fibre orientations."Construction and Building Materials, 50, 62-73.

Hadi, M. N. S., Jameel, M. T. and Sheikh, M. N. (2017). "Behavior of Circularized Hollow RC Columns under Different Loading Conditions." Journal of Composites for Construction, 21, 04017025.

Hadi, M. N. S., Pham, T. M., and Lei, X. (2013). “New method of strengthening reinforced concrete square columns by circularizing and wrapping with fiber-reinforced polymer or steel straps.” Journal of Composites for Construction, 10.1061/(ASCE)CC.1943-5614.0000335, 229–238.

Jameel, M. T., Sheikh, M. N. and Hadi, M. N. S. (2017). "Behaviour of circularized and FRP wrapped hollow concrete specimens under axial compressive load.”Composite Structures, 171, 538-548.

Kusumawardaningsih, Y. and Hadi, M. N. S. (2010). "Comparative behaviour of hollow columns confined with FRP composites."Composite Structures, 93(1), 198-205.

Li, J. and Hadi, M. N. S. (2003). "Behaviour of externally confined high-strength concrete columns under eccentric loading."Composite Structures, 62(2), 145-153.

Proc. 1st International Conference on Structural Engineering Research (iCSER 2017)
20-22 Nov 2017, Sydney, Australia
ISBN: 978-0-6480147-6-8

Fatigue Behaviour of Steel Reinforced Concrete Beams

Lewei Tong[1], Sun Xiao[2], Bo Liu[2] and Xiao-Ling Zhao[3]

[1]Professor, State key Laboratory for Disaster Reduction in Civil Engineering, Tongji University, Shanghai, China
[2]Ph.D student, College of Civil Engineering, Tongji University, Shanghai, China
[3]Professor, Department of Civil Engineering, Monash University, Clayton, Australia
Corresponding author's E-mail: tonglw@tongji.edu.cn

Extended Abstract

Steel reinforced concrete (SRC) structures have been widely applied in civil engineering. High speed railway is quickly developed all over China in recent years. SRC beams are often used in bridges as well as in floors of buildings for high speed railway stations. Fatigue design is essential for a structure subjected to high-cycle fatigue loading. The fatigue behaviour of steel beams, reinforced concrete beams and steel-concrete composite beams has been investigated quite well and relevant fatigue design specifications have come into use (Eurocode 2, 2005; Eurocode 3, 2005). However, fatigue of SRC beams is a new research topic. Tong *et al* (2012; 2013) carried out fatigue tests on SRC beams and their connections in order to meet needs of fatigue design of the engineering project for Shanghai Hongqiao Railway Station. A fundamental study on fatigue behaviour of SRC beams are reported in this paper. Both the experimental and numerical simulation results are presented.

The fatigue test setup is shown in Fig.1. A total of twenty test specimens were organized, including eighteen SRC beams and two pure steel beams. All SRC beams were divided into five groups in such a way that the effects of different parameters could be revealed. The key parameters dealt with the steel ratio of longitudinal reinforcements, the steel ratio of H-steel beams and the situation with or without stud shear connectors.

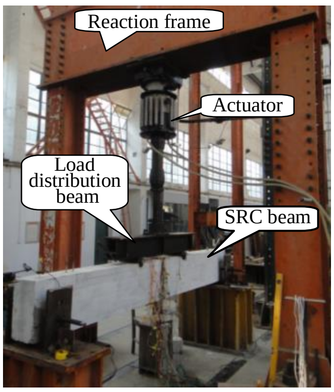

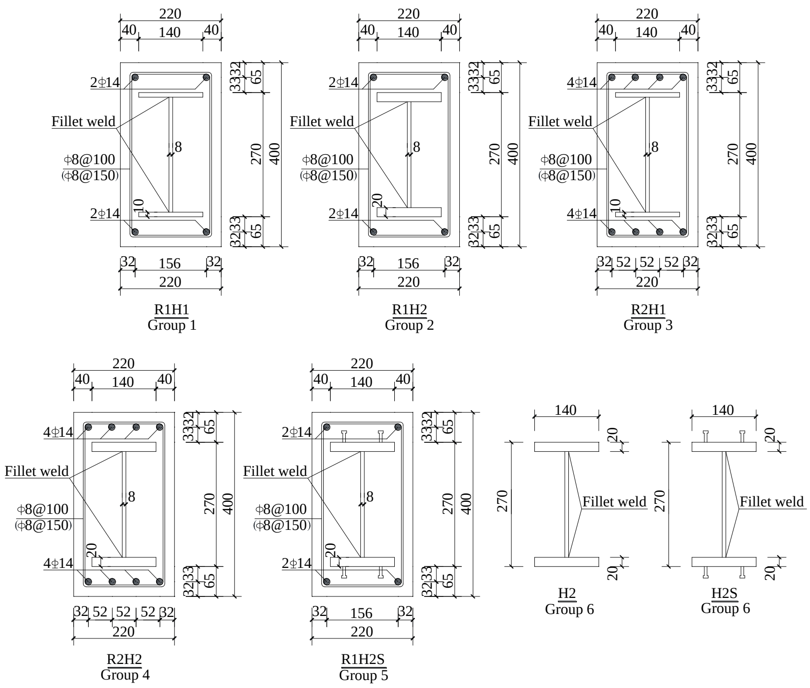

Cross section of SRC beams and H-steel beams (unit: mm)

Figure 1. Fatigue test setup

Fatigue test results are described. Key issues are discussed on failure modes (Fig.2), failure sequences, crack initiation, crack propagation and stiffness of SRC beam. A comparison of fatigue behaviour between H-steel component inside SRC beams and pure H-steel beam has been made. The key parameters influencing the fatigue strength of SRC beams are identified. The regression analysis of S-N curves is conducted for fatigue assessment of welded H-steel components and reinforcement components inside SRC beams, respectively. ABAQUS software was utilized to perform numerical simulation which considers the crack propagation in the H-steel using fracture mechanics theory and the damage evolution of the reinforcement and concrete. The predicted fatigue life of SRC beams was in good agreement with experimental data.

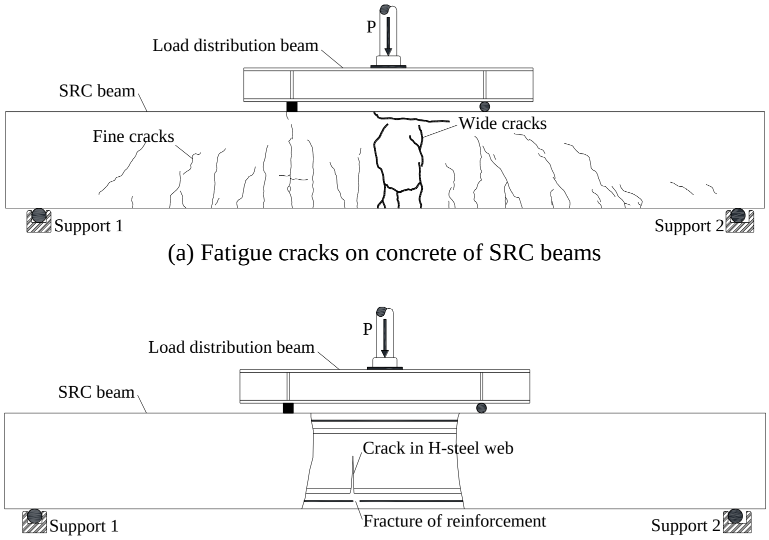

(a) Fatigue cracks on concrete of SRC beams

(b) Fatigue fracture of reinforcement and H-steel inside SRC beam after removal of concrete

Figure 2. Schematic of typical fatigue failure of SRC beams

The following conclusions can be drawn: (1) For the H-steel with stud shear connectors, cracking started from the weld toe of connection between a stud shear connector and the bottom flange in tension. For the H-steel without stud shear connectors, cracking started from the weld toe of connection between the bottom flange and web in tension. The fatigue strength of SRC beams with stud shear connectors was much lower than for those without stud shear connectors. (2) The H-steel section inside SRC beams had significantly higher fatigue strength (or fatigue life) than the pure H-steel when H-steel in both cases was subjected to the same value of stress range in the tensile flange. (3) Increasing the steel ratio of the H-steel components or the steel ratio of reinforcement components could more or less benefited the increase of fatigue strength of SRC beams. (4) For fatigue design of SRC composite beams, S-N curves are recommended respectively for fatigue assessment of welded H-steel components without stud shear connectors on the flange, and for reinforcement components.

REFERENCES

Eurocode 2 (2005). Design of concrete structures - Part 2: Concrete bridges - Design and detailing rules, EN 1992-2, European Committee for Standardization, Brussels.

Eurocode 3 (2005). Design of steel structures -Part 1-9: Fatigue, EN 1993-1-9, European Committee for Standardization, Brussels.

Tong LW, Xian QJ, Zhou LY, Chen YY and Zhang YF (2012). Experimental investigation on fatigue behaviour of steel reinforced concrete composite beam-to-girder joints, International Journal of Steel Structures, 12(4), pp. 461-472.

Tong LW, Xian QJ, Zhou LY and Chen YY (2013). Fatigue test of steel reinforced concrete girders in high-speed railway station, Proceedings of 7th International Structural Engineering and Construction Conference, Honolulu, Hawaii, June 18-23.

Proc. 1st International Conference on Structural Engineering Research (iCSER 2017)
20-22 Nov 2017, Sydney, Australia
ISBN: 978-0-6480147-6-8

Structural Topology Optimization Considering Buckling Constraints

Haitao Ma and Xingjun Gao

Professor of Civil Engineering, Engineering Research and Test Center, Guangzhou University, Guangzhou 510405, China.

Corresponding author's E-mail: htma@gzhu.edu.cn

Abstract

Structural strength, stiffness, and stability are three of the most important factors which should be considered for assessing structural designs. Therefore, in order to achieve safe and practical designs, structural stability must be taken into account during a structural optimization procedure. Buckling optimization has drawn more research attention in recent years.

Some issues in the topology optimization of continuum structures considering structural stability are investigated. The optimization problem of compliance minimization under constraints on material volume and buckling load factors is considered. The Solid Isotropic Material with Penalization (SIMP) material model is used for topology optimization and a hybrid stress element is employed in structural analysis.

An adaptive continuation method is proposed, in which the penalty parameter in the SIMP model is automatically adjusted during the optimization procedure according developed rules. Using these rules, buckling constraints would be properly considered throughout the optimization to guide optimized designs to move in more appropriate directions.

Numerical examples will be presented to demonstrate the effectiveness of the proposed method and future applications of the method discussed.

ISBN: 978-0-6480147-6-8

Recent Research Progresses on CFDST Structures

Wei Li

Associate Professor, Department of Civil Engineering, Tsinghua University, Beijing, 100084, China
Corresponding author's E-mail: iliwei@tsinghua.edu.cn

Extended Abstract

Concrete-filled double skin steel tubular (CFDST) member consists of inner and outer steel tubes with concrete in-filled in the sandwiched cavity. It inherits advantages of the common concrete-filled steel tube, such as high resistance, high stiffness and good constructability. It also has some other characteristics, such as lighter self-weight and better fire performance. It is found that the inner tube can provide a sufficient support to the sandwiched concrete, and the steel-concrete-steel interfaces can work together effectively under various loading conditions. The concrete-filled double skin steel tubes may provide a better design option when designing members of large cross-sectional profile. Therefore they have been used in some engineering projects in China.

This presentation introduces some research progresses on the CFDST structures, including the tensile behavior of the member, the life-cycle performance of the member and the fatigue behavior of T-joint.

For the tensile strength of CFDST member, both numerical and experimental investigations were conducted. The numerical model was established and calibrated against the test results for the CFDST member under axial and eccentric tension. The comparison showed the proposed FE model was capable to capture the structural behavior of the tensile loading experiments. Parametric studies were then conducted to investigate the influence of some key parameters, such as the material strength, the nominal steel ratio and the hollow ratio on the tensile behavior of composite members. The composite action on the composite member, the effect of loading paths and the tension-bending interaction diaphragm were also discussed. It is found that the tensile strength of the member depends on the composite action between steel tubes and sandwich concrete, and the tension-bending interaction diaphragm could be represented by a simple linear relationship. Finally, design equation to predict the tensile strength of CFDST member was proposed, and the comparison results showed that the proposed formula has a good accuracy.

For the life-cycle performance of the member, multiple factors were identified and the influences were evaluated for the CFDST stub columns. During the construction stage, the inner and outer tubes were subjected to constructional loads. While during the service stage of CFDST member, the whole composite column is subjected to service loads, occasional loads as well as environmental actions (e.g. chloride corrosion). The finite element analysis (FEA) model was developed to predict the structural behaviour with considerations of these factors. The experimental work was also conducted for CFDST columns subjected to corresponding loading protocols, and test results were used to calibrate numerical models. Discussions were made on the differences of specimens with and without considerations of these factors. Both experimental and numerical results showed that the deformation and the ultimate strength were affected by the preload, long-term sustained load, corrosion and their combinations. The effect of corrosion was significant and leads to a large reduction of column strength, and the influences of the preload and long-term sustained load could be tentatively estimated by multiplying different coefficients together.

For the fatigue behavior of T-joint, the preliminary experimental investigations were conducted on the fatigue behavior of composite T-joint consists of circular concrete-filled double-skin steel tubular

(CFDST) chord and circular hollow section (CHS) brace. The test parameters in the direct fatigue tests included the load range, the chord to brace diameter ratio and the hollow ratio of the cross section, while those in the stress concentration tests included the loading type, the chord to brace diameter ratio and the hollow ratio of the cross section. The brace was subjected to axial tension or compression during the test. The development of cracks and the degradation of joint stiffness were monitored during the fatigue loading. Stress concentration factors (SCFs) and strain concentration factors (SNCFs) were obtained from the test. Generally, SCFs increase with the increase of the parameters of cross-sectional hollow ratio and radius to thickness ratio of chord tube. It was found that the SCFs near the saddle point of the chord were higher than other positions, and steel cracks usually initiated between the saddle and the crown points, and the sandwiched concrete constrained the deformation around the connection zone.

REFERENCES

Li W, Han LH, Chan TM (2014). Numerical investigation on the performance of concrete-filled double-skin steel tubular members under tension. Thin-walled Structures, 79(6): 108-118.

Li W, Han LH, Chan TM (2014). Tensile behaviour of concrete-filled double-skin steel tubular members. Journal of Constructional Steel Research, 99(8): 35-46.

Li W, Han LH, Zhao XL (2015). Behavior of CFDST stub columns under preload, sustained load and chloride corrosion. Journal of Constructional Steel Research, 107(4): 12-23.

Li W, Wang D, Han LH, Zhao XL (2017). Fatigue behavior of CFDST chord to CHS brace T-joints. Tubular Structures XVI (ISTS 16). Melbourne, Australia, Dec. 4-6, 2017.

Proc. 1st International Conference on Structural Engineering Research (iCSER 2017)
20-22 Nov 2017, Sydney, Australia
ISBN: 978-0-6480147-6-8

FRP-strengthened RC Structures: Research, Design and Knowledge Gaps

Scott T. Smith

Foundation Professor of Engineering, Southern Cross University, Australia
E-mail: scott.smith@scu.edu.au

Extended Abstract

Fibre-reinforced polymer (FRP) composite materials can be applied to existing reinforced concrete (RC) structures for a variety of reasons ranging from strengthening and retrofitting to rehabilitation and repair. Experimental and numerical investigations over the last two decades and more have demonstrated the effectiveness of the FRP intervention. By far and large the most commonly investigated scenarios include the flexural and shear strengthening of flexural members such as beams, as well as the confinement of compression members such as columns. As a result of such research advances and understanding, design guidelines have been steadily appearing throughout the world since the middle to late 1990s. Leading design guidelines are now available in their second or third versions (e.g. ACI 440.2R-17, Concrete Society 2012) and some countries are at the stage of developing and publishing standards.

(a) Beam flexural and shear strengthening (Conventional)

(b) Column confinement (Conventional)

(c) Column confinement (Non-conventional)

(d) Wall edge strengthening (Non-conventional)

Figure 1. Conventional and non-conventional applications of FRP strengthening (KL Structures 2017)

The practical applications of FRP strengthening measures have been gaining in popularity over the last two decades too. Figures 1a and 1b show popular applications of flexural and shear strengthening, as well as column confinement. Existing design guides can generally cater for such strengthening scenarios quite well. There are, however, a lot of scenarios that are not explicitly addressed by design guidelines. Figures 1c and 1d provide some examples. In the design of such cases, engineers need to apply guidelines with sufficient interpretation and adaption, and also use their good engineering judgement. In addition, mock-up tests in cases need to be resorted to.

While design guidelines are not meant to be overly prescriptive, they are limited by our current state-of-the-art knowledge. As a result, a greater practical uptake of FRP strengthening measures is inhibited. In some cases industry has pushed ahead and companies have developed their own in-house design guidelines. In a lot of other cases though companies without sufficient resources will not entertain FRP strengthening solutions.

This presentation will provide an overview of design guideline development to date in selected regions of the world, followed by the identification of key knowledge gaps. The identification of such gaps will help inform impactful future research projects and design guideline development. A case study will also be presented that will discuss the synergistic effects of industry demand as well as research interests regarding the design guideline development for anchorage devices. Such devices can be applied to increase the efficiency of externally bonded FRP systems. The author is of the opinion that prescriptive design measures for anchorage devices will provide a tremendous benefit to the industry. The design of anchors will enable the application of FRP to more exotic structure configurations and hence unlock the true potential of the strengthening technology.

REFERENCES

ACI 440.2R-17 (2017). Guide for the Design and Construction of Externally bonded FRP Systems for Strengthening Concrete Structures, American Concrete Institute (ACI), Farmington Hills, MI, USA.

Concrete Society (2012). TR55 Design guidance for strengthening concrete structures using fibre composite materials, 3rd Edition, Concrete Society, UK.

KL Structures (2017). Photographs provided courtesy of KL Structures, USA.
http://www.klstructures.com/

Proc. 1st International Conference on Structural Engineering Research (iCSER 2017)
20-22 Nov 2017, Sydney, Australia
ISBN: 978-0-6480147-6-8

Influence of Analysis Approach on the Design of High-Rise Buildings with Transfer Plate

A. Osman[1] and M. Abdel Azim[2]

[1]Professor, Structural Eng. Dept., Cairo University, Egypt
[2]Structural Engineer, DAR Al-Handasah, Egypt
Corresponding author's E-mail: Mohamed.AbdelAzim@dargroup.com

Abstract

This study examines the consequences of the different analysis approaches traditionally followed by designers in consulting offices during the design process of high-rise buildings utilizing thick transfer slabs between their tower and podium floors. Emphasis is placed on the importance of accounting for the interaction between the transfer plate slabs and the building structural elements during the analysis process. The effect of the transfer slab span to thickness ratio on the structural behaviour of such buildings is investigated. It was concluded that interaction between the transfer slabs and building vertical structural elements can significantly affect the straining actions calculated within these elements and consequently this effect should be accounted for during analysing these structures. Also, it was shown that the transfer slab should be accurately modelled during developing the building structural numerical model to simulate the real structural behaviour for such type of building.

Keywords*: *High-rise buildings, transfer plate, finite elements, two-stage analysis.

1. INTRODUCTION

Currently, high-rise buildings are commonly constructed for various uses and occupancy demands. Lower floors (podiums) are conventionally used as parking zones, shopping malls, assembly halls or open spaces for different functional requirements, while higher floors (towers) accommodate apartments, offices or hotel rooms. Such diversity in architectural functional demands forces the vertical structural elements, such as columns, walls and cores, within podium floors not to be vertically aligned with those belonging to the tower floors. In turn this leads to the need for utilizing structural transfer system to transmit the heavy loads from tower vertical structural elements to podium vertical structural elements. One of these transfer systems that are recently becoming common and sometimes even inevitable in modern building developments is the transfer plate slab system. This system involves the use of 2 to 3m thick reinforced concrete solid slab located about 20 to 30m above ground level at the interface level between tower and podium. Although, the system gained popularity due to its ability to satisfy easily the architectural layouts and provide column- free open space areas at podium floors, from structural prospective, it poses a great challenge to structural designers. This is attributed to the fact that transfer slab thickness is not only dictated by the magnitude of applied loads over it (strength design), but also by its contribution to building overall behavior (stiffness effects).

Current design practice followed by most consulting offices for analyzing this type of structure is usually limited to one of two codified approaches. In the first, the so called two-stage analysis technique is adopted (ASCE, 2010). In this approach, the tower is analyzed separately assuming it is fixed at the transfer slab level which is presumed to be infinitely rigid. Then, the obtained reactions are reversed in directions and applied to the below podium structure. In the second approach, the structure is globally simulated numerically using finite element technique and the transfer slab is modelled using either thick shell elements, as in most cases, or solid elements, as in lesser cases (Zhang, 2004).

This raised an important questions regarding understanding the consequences of following each approach on the design of vertical structural elements within the building and its global behavior.

Therefore, in this study real buildings utilizing transfer slabs were developed and analyzed using the previously described different design approaches. The consequence as a result of following these analysis approaches on the design the structural elements were evaluated. The evaluation included; (1) Examining the variation in the straining actions developed within the vertical structural elements; (2) The resulting story drift and lateral displacement for the buildings; and (3) The structural stiffness and natural periods. In addition, the study examined the effect of transfer slab depth-thickness ratio and stiffness on the design behavior of such structures types.

2. STUDIED BUILDINGS

For this study, three real structures designated as A, B and C were developed and analyzed under the action of both gravity and lateral loads. Both two stage and global modelling techniques were utilized for analyzing these structures to assess the effect of different analysis approaches on the design outcomes for these structures. With the global modelling approach, the transfer slabs were modelled once using thick shell elements and in another case was modeled using solid element. Various design aspects for the transfer slab such as depth-thickness ratio and stiffness were varied in order to examine their effects on the behavior and design of these structures.

The buildings were accurately modelled to simulate to great extant its real structural behavior. For analysis purpose SAP2000 program (integrated software for structural analysis and design) was used to model the structures with transfer slab simulated as solid element, while ETABS (integrated analysis design and drafting of building system) program was used to model structures with transfer slabs simulated using thick shell elements.

In all these models, the tower and podium beams and columns were simulated using beam-column elements, while walls and floor slabs were simulated using shell elements. The transfer slab was modelled using thick shell elements or solid elements. The applied gravity loads to all the examined buildings consisted of both dead and live loads. The dead loads included the structure self-weight, flooring, partitions, and electro-mechanical installation loads. The live loads were in accordance to UBC code (1997). No reduction to live loads was considered in these analyses. Also, for all buildings, seismic loads are calculated using UBC (1997).

3. ANALYSIS RESULTS

Figure 1 shows the global finite element model for building A. As shown it consisted of 24 stories forming the tower top supported over 10 stories representing the podium with total height of 130.50m.The concrete transfer slab were located at the interface between podium and tower floors at elevation 46m from the ground level and its thickness was 2m thick. The building resists the lateral loads by several shear walls and cores. All floor slabs were flat slabs having thickness 0.30m.

For all tower typical floors which were designated as residential floors, the gravity loads were assumed to be equal to the self-weight of the structural elements determined from calculating their weights based on density of construction material and element dimensions, 0.55 t/m^2 as superimposed dead loads and 0.20 t/m^2 as live loads. For the transfer floor level, superimposed dead load and live loads were taken to be 0.65 t/m^2 and 0.50 t/m^2, respectively. For all podium floors which were designated as commercial floors, in addition to structural elements self-weight, 0.65 t/m^2 superimposed dead loads and 0.5t/m^2 as live loads were considered. For lateral loads acting on the building, the equivalent seismic forces were calculated based on UBC(1997) and the seismic parameters utilized were based on assuming that the soil type is SB (Rock), the seismic zone factor (Z) was 0.075 and seismic coefficient (C_a) was 0.08. The reduction coefficient (R) which is representing the inherent over-strength and ductility capacity of the lateral force-resisting systems was taken as 5.50, the seismic coefficient (C_v) was taken 0.08 and the numerical coefficient (C_t) was taken as 0.02. For mass source, dead load factor was assumed to be 1.0.

For analyzing the structure, three different approaches were adopted. In the first approach, two stage analysis technique was used, since the building satisfied the approach requirements, were the lateral stiffness of the podium were equal to 21.3 times and 29.2 times the stiffness of the tower in both x- and y-directions, respectively, and the period of the entire structure was equal 0.91 times the period of the tower. In this approach the tower floors were modelled separately using the widely used commercial code SAP2000 (integrated software for structural analysis and design) assuming fixed bases and the outcome reactions of this first stage analysis were reversed and applied to podium floors which were modelled separately in the second stage. In the second and third approaches the structure was globally modelled once using the commercial code ETABS (integrated analysis design and drafting of building system) with the transfer slab simulated using thick shell and another using the commercial code SAP2000 (integrated software for structural analysis and design) with the transfer slab modelled using solid element. The columns and beams in both cases were modelled using the available beam-column elements, while the cores and shear walls were modelled using shell elements.

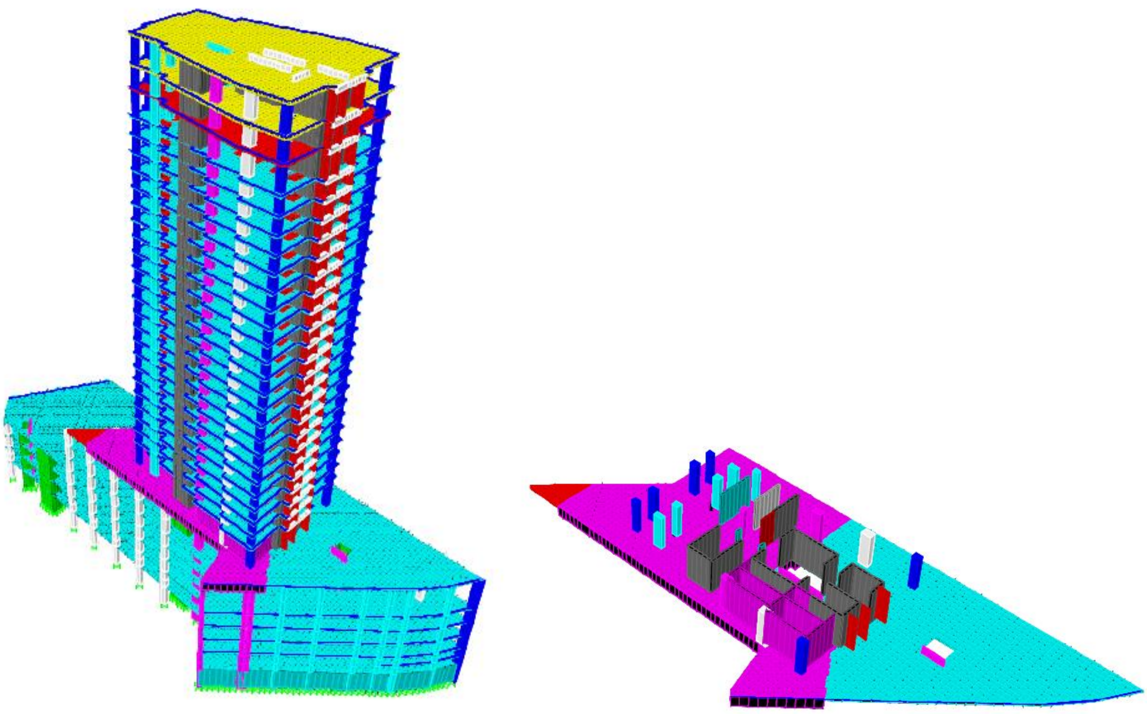

Figure 1: 3D view for the finite element model for building A with close up to transfer slab

The straining actions (axial forces, bending moments in both directions) were determined and compared for the three cases. Figures 2, 3, 4 and 5 show the axial forces, bending moments around the two principal axes and shear forces, respectively for some of the tower columns located directly above the transfer slab. As can be noted, the columns axial forces were slightly affected regardless of the followed analysis approach. On the contrary different trends for the moments and shear forces were observed. Separated model (two-stage-analysis) gave the lowest moment and shear force results while the global model utilizing shell elements for the transfer slab gave the highest moment and shear force values. This can be understood by examining the deformation of the transfer slab in the three approaches along the same section. As can be noted from Figure 6, the deformation and rotation of the transfer slab at same node in global model using shell element for transfer slab was the highest compared to those of other models. Such high slab rotations induced high rotations for tower column at connection with the transfer slab producing these observed high moments. On the other hand for separated model the deformation and rotation were nil, since the tower column bases were assumed fixed. This drastically reduced the resulting bending moments on these columns, since the transfer slab deformations and rotations were not accounted for. Analysis showed that this effect is dying with height. In other words after about six floors, the moments within the columns became the same regardless the followed analysis approach, which indicate that it is a local effect confined to few floors above the transfer slabs. For the columns below the transfer slab similar behavior was noted. Regarding the building overall lateral displacement, Figure 7 shows the building lateral displacement values in X-direction plotted along the building height. The figure indicated that the analysis approach followed affected the obtained displacement values. For instance, when solid element utilized for modelling transfer slab the drift was less than when the transfer slab was modelled using shell elements. In addition, eigenvalue analyses showed that natural periods for building analyzed with transfer slab modelled using shell element were longer than this analyzed with transfer slab modelled using solid element.

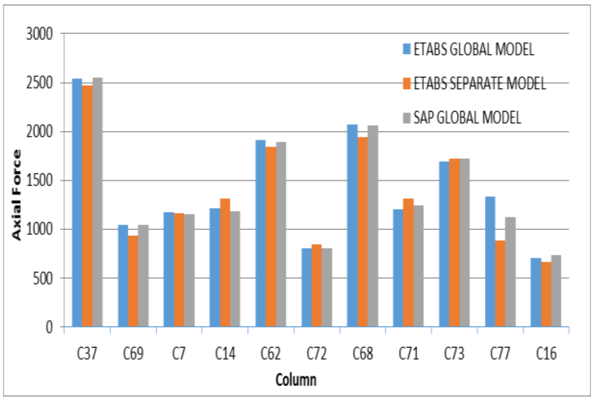

Figure 2. Axial force for tower columns above transfer levels

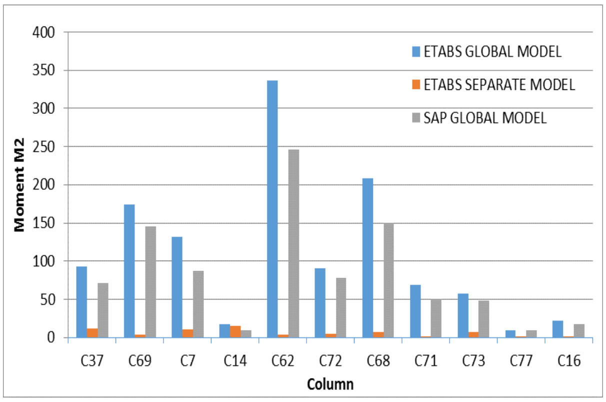

Figure 3. Moments in x-direction for columns above transfer levels

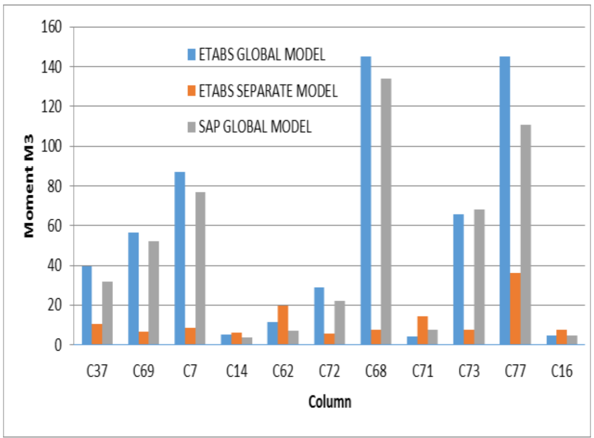

Figure 4: Moments in Y-direction for columns above transfer levels

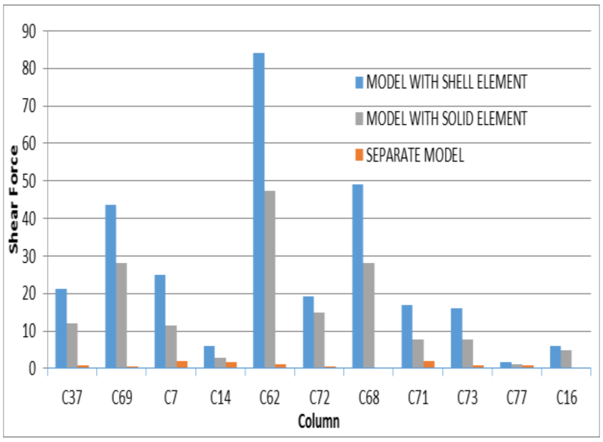

Figure 5: Shear forces for columns above transfer levels

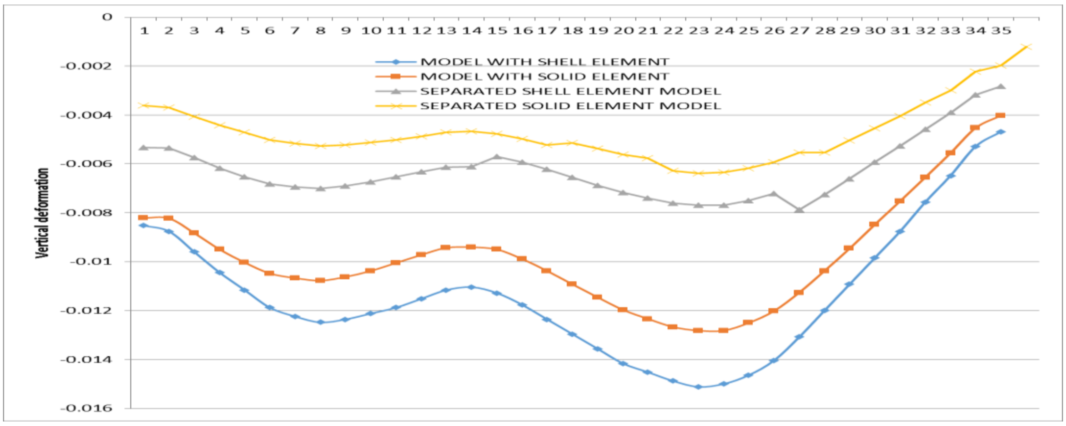

Figure 6. Vertical deformation of points in a horizontal section at the transfer level

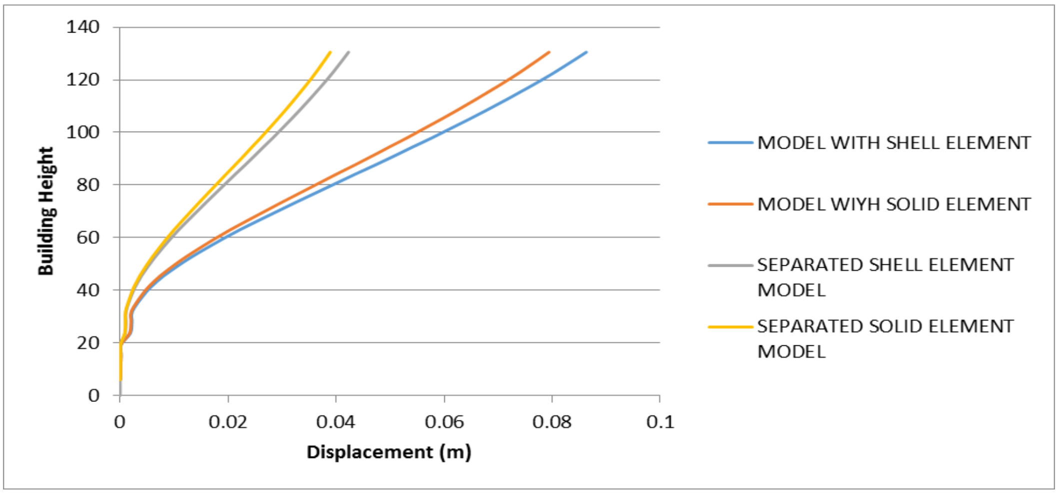

Figure 7. Story displacement in X-direction due to lateral load

To examine the effect of transfer slab span to it thickness ratio on the behavior, a modified building was produced from model A by removing many of the tower floors to allow for adopting less transfer slab thickness. This situation can exist in reality if the tower is not high-rise one, and still the design requesting podium utilized for different architectural purposes other than that of tower. For such purpose the tower was assumed to be only 6 floors high and the transfer slab was taken as 60 cm thick. Consequently the aspect ratio for the transfer slab span to depth ratio was about 16.66. In this case the structure was modelled globally once utilizing transfer slab modelled using thick shell elements and in other case the transfer slab was modelled using solid elements. Figures 8 and 9 show the moments and shears in columns above transfer slab for both analyses. As can be noted the obtained results are approximately the same. This proves that in case the aspect ratio of the transfer slab (span to depth ratio) is ranging between 14 and 18, which will be the case for low and intermediate high-rise towers, using solid elements or thick shell will yield the same results. However, for less aspect ratio the transfer slab should be modelled using solid elements to capture the real deformation and rotation behavior of the transfer slab, since shell element developed based on plate bending theory cannot simulate behaviour of thick slabs.

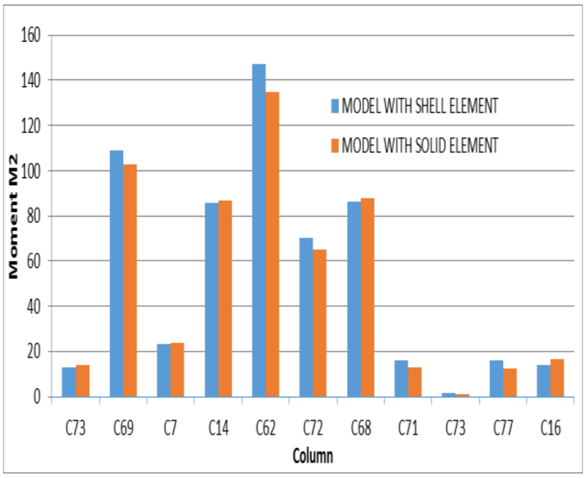

Figure 8. Moment of columns above transfer level

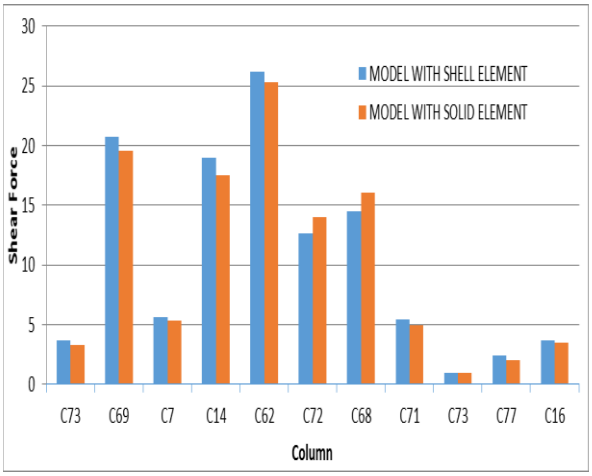

Figure 9. Shear forces of columns above transfer levels

Similarly, the above indicated analyses were performed for buildings B and C shown on Figures 10 and 11, respectively. Building B is 291 m high (21 podium storey and 44 typical storey) and having a transfer slab 4.5 m thick located at elevation 112.8 m from ground level, while building C is 230.15 m high (18 podium storey and 34 typical storey) and having a transfer slab 3 m thick located at elevation 84.5 m from ground level. Results from these analyses supported the previously achieved conclusions (Abdel Azim 2016). It is worth to mention here that the lateral loading system for building B consisted mainly from shear walls and cores, while that of Building C, similar to building A, consisted of cores and columns.

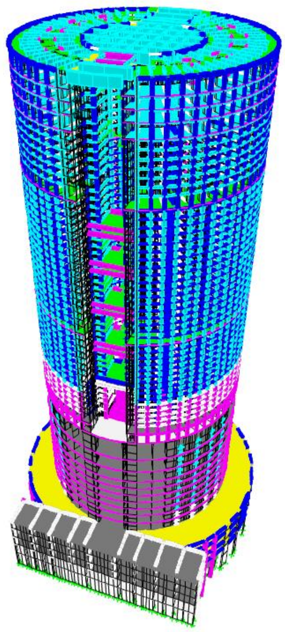

Figure 10. 3D view for building B

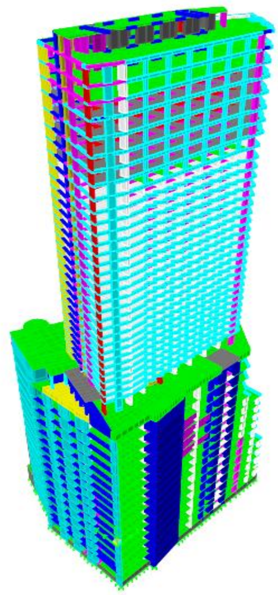

Figure 11. 3D view for building C

4. CONCLUSION

In conclusion, the two stage analysis technique should not be used in analyzing high-rise buildings with transfer slab in spite of it is allowed by codes, since it neglects the interaction between the transfer floor and the vertical structural elements of the building resulting in estimating the straining actions acting on these elements and building lateral deformation incorrectly. In addition, it was showed that in global modelling to such buildings type, the transfer slab should be modelled accurately with elements capable of capturing its real structural behavior in order to achieve accurate results. In this regard for transfer slabs having span to thickness ratio less than 1:15 ,the use of solid elements, although considered tedious and time consuming task, may be the solution for this problem. Shell elements developed based on plate bending theory, in spite of their simplicity, should not be utilized for modelling the transfer slab except if the span to depth ratio of the transfer slab exceeded 1:14.

5. REFERENCES

Abdel Azim M (2016). Structure behaviour of buildings with transfer plate system. M.Sc, Structural Engineering Department, Cairo University, Egypt.

ASCE (2010). Minimum design loads for buildings and other structures -7-2010. American Society of Civil Engineers, U.S.A.

UBC (1997).Uniform Building Code. International Conference of Building Officials, California, U.S.A.

Zhang H (2004). Finite element modelling of transfer plates in tall buildings. Ph.D. thesis, Civil and Structural Engineering, Hong Kong University.

Proc. 1st International Conference on Structural Engineering Research (iCSER 2017)
20-22 Nov 2017, Sydney, Australia
ISBN: 978-0-6480147-6-8

Test-aided Calibrations for Design of Steel Fibre Reinforced Recycled Aggregate Concrete Beams

Rakul Bharatwaj Ramesh[1], Won-Hee Kang[2], Olivia Mirza[3], Dane Wigg[4], Sepani Senaratne[3], and Vivian Tam[5]

[1]PhD student, Centre for Infrastructure Engineering, Western Sydney University, Penrith, NSW 2751, Australia
[2]Lecturer, Centre for Infrastructure Engineering, Western Sydney University, Penrith, NSW 2751, Australia
[3]Senior Lecturer, School of Computing Engineering and Mathematics, Western Sydney University, Penrith, NSW 2751, Australia
[4]Masters student, Centre for Infrastructure Engineering, Western Sydney University, Penrith, NSW 2751, Australia
[5]Associate Professor, School of Computing Engineering and Mathematics, Western Sydney University, Penrith, NSW 2751, Australia
Corresponding author's E-mail: W.Kang@westernsydney.edu.au

Abstract

This research proposes to combine recycled aggregate concrete (RAC) with steel fibres (SF), to provide an environment-friendly, sustainable, and structurally sound alternative to natural aggregate concrete (NAC). When steel fibre reinforced recycled aggregate concrete (SFRRAC) is used in construction, the existing design equations and associated safety factors need to be revised; the existing design provisions are applicable only to NAC and cannot be applied to SFRRAC directly. In this research, safety factors of design equations for beams provided in the current Australian, American, and European design codes are calibrated based on the first-order reliability method (FORM) when used for the structural design of SFRRAC beams. This is carried out based on a proposed prediction model for the flexural capacity of SFRRAC, which considers the contribution of SF unlike the conventional prediction model for RC beams. The uncertainty of the prediction model is estimated based on nine experimental results of secondary SFRRAC beams tested for flexural failure under three-point bending. These beams are fabricated with varying contents of recycled aggregate and steel fibre ratios. Furthermore, the reliability index ratios of the different SFRRAC mixes considered are estimated.

Keywords: Reliability analysis, Concrete structures, Recycled aggregates, Steel fibres, Safety factor calibration.

1. INTRODUCTION

Using recycled aggregate (RA) in concrete decreases the environmental impact of concrete production and provides an effective alternative for meeting the demands of the construction industry. However, recycled aggregate concrete (RAC) has inferior mechanical properties compared to natural aggregate concrete (NAC) (Kang et al 2017). Although replacement of NA with RA by up to 25% does not significantly change the mechanical properties of concrete, higher replacement proportions affect its performance (Etxeberria et al 2007). On the other hand, steel fibre (SF) increases the performance of concrete under different load actions. The degree of improvement in mechanical properties by adding SF is greater in RAC than in NAC (Erdem et al 2011). To exploit the advantages of both RA and SF, they are combined to produce a new material, namely steel fibre reinforced recycled aggregate concrete (SFRRAC). Previous studies have focussed on the use of RAC and SFRC individually and not on their combination, SFRRAC at the member level.

The flexural test of SFRRAC beams recently conducted by Mirza et al (2017), in which nine SFRRAC beams were tested with different combinations of RA and SF contents, is a preliminary part of this research. This study was carried out to apply their experimental observations to real structural design. This study aims to evaluate the relation between the safety factor and the target reliability level for SFRRAC beams, based on a newly developed material strength prediction model. The reliability analysis method is extensively based on the calibration method discussed in Eurocode (2002) and ISO 2394 (1998). The reliability index ratios of all the beams tested by Mirza et al. were evaluated.

2. TEST RESULTS

The following were the moment capacities of the beams tested by Mirza et al. (2017).

Table 1. Moment capacities

Beam no. (RA%-SF%)	**1** (0-0)	**2** (30-0)	**3** (100-0)	**4** (0-0.3)	**5** (30-0.3)	**6** (100-0.3)	**7** (0-0.6)	**8** (30-0.6)	**9** (100-0.6)
Mom. Capacity (kN-m)	375	385	378	413	420	406	476	413	420

3. MODEL FOR PREDICTING THE CAPACITY OF SFRRAC BEAMS

In this section, a prediction model is proposed for theoretically calculating the flexural resistance of SFRRAC beams by considering the effect of SF and it is used for the reliability analysis in the next section. Fig. 1a shows the stress strain diagram of a NAC beam having a rectangular cross section (Bandyopadhyay 2008) without SF. According to the Linear Bending Theory of reinforced concrete beams, the concrete part below the neutral axis in a rectangular cross section (the unshaded region in Fig. 1a) is disregarded in strength and moment capacity calculations (Bandyopadhyay 2008). In Fig. 1a, the compressive force in concrete (C_c) and the compressive force in the compression reinforcement (C_s) are balanced by the tensile force in the tension reinforcement (T_s).

In SFRRAC, the added SF improves the tensile behaviour of SFRRAC as shown by the horizontally striped region below the neutral axis in Fig. 1b. Although the tensile strength of RAC is negligible, SF increases its load and moment carrying capacities improving the tensile strength of SFRRAC. An additional tensile force representing the tensile strength of SFRRAC (T_{SFRRAC}) acts as shown in Fig. 1b. In this study, an equation that represents this tensile strength of SFRRAC under flexure is proposed. The equation form proposed by Song and Hwang (2008) is adopted. A regression analysis on the tensile strength data of SFRRAC obtained by Vaishali and Rao (2012) and Bhikshma and Manipal (2012) was used to obtain the following equation.

$$f_{ct,sp} = 0.54\sqrt{f_c'} + 3.0451\,V_f - 1.5177\,V_f^2 \quad (1)$$

where $f_{ct,sp}$ is the split tensile strength of concrete, f_c' is the compressive strength of concrete, and V_f is the volume of SF in concrete. The axial tensile strength of a concrete matrix (f_{ct}) in a beam is related to its experimentally measured split tensile strength ($f_{ct,sp}$) as follows (AS 3600, 2009):

$$f_{ct} = 0.9 \times f_{ct,sp} \quad (2)$$

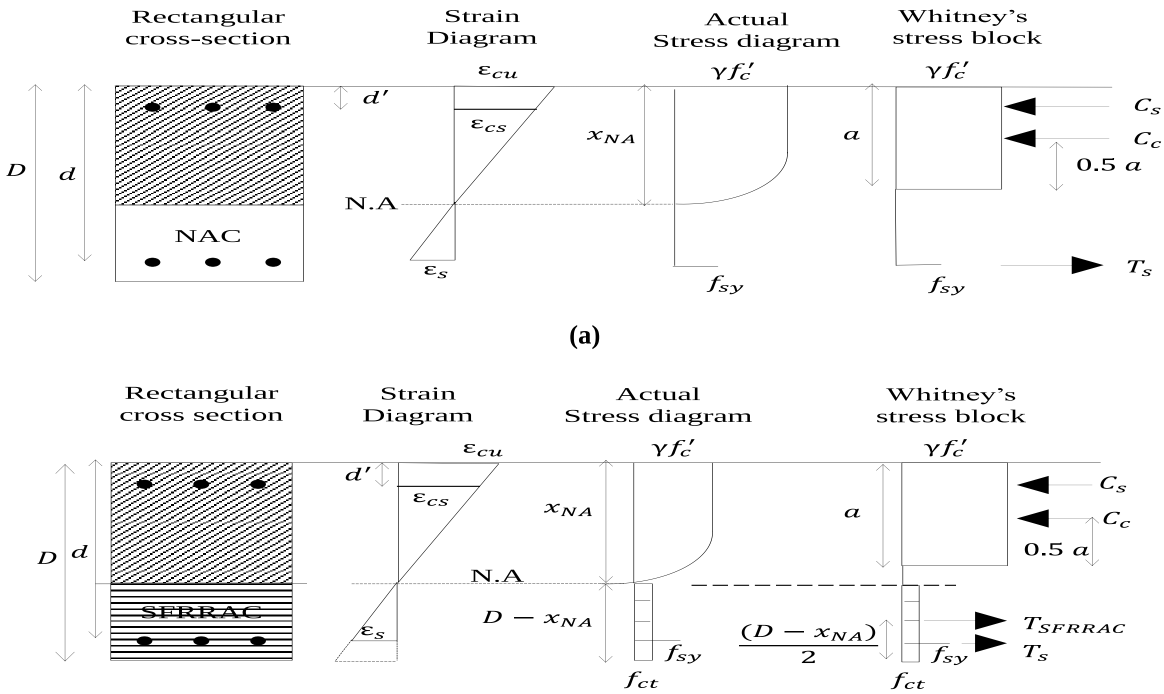

(a)

(b)

Figure 1. Stress and strain diagrams of doubly reinforced (a) NAC and (b) SFRRAC beams with rectangular cross sections

4. RELIABILITY ANALYSIS

To calibrate the safety factors for the flexural capacity prediction of SFRRAC, the reliability analysis method provided in Annex D of Eurocode (2002) and ISO 2394 (1998) is extensively used in this study. The numerical value of the target reliability index (*β*) adopted in this study when considering resistance separately is 3.04. The safety factor for each beam (ϕ_i) is calculated using the following equation:

$$\phi_i = r_{di}/r_{ki} \tag{3}$$

where r_{di} and r_{ki} are obtained from the calculation procedure provided in the following sub sections.

4.1. Calculation of design capacity (r_d)

The design moment capacity of the i[th] SFRRAC beam out of the nine beams tested by Mirza et al. (2017) (r_{di}) can be theoretically estimated using the prediction model provided in the previous section, which considers the flexural tensile strength of SFRRAC using Equation 2.

$$r_{di} = \bar{b} \times r_{ti} \times \exp(-k_i \times Q_i - 0.5 \times Q_i^2) \tag{4}$$

where r_{ti} is the theoretically estimated moment carrying capacity of the i[th] beam; $\bar{b}$ is the bias correction factor estimated using the following equation, and k_i and Q_i are coefficients estimated using Equations 7 and 8, respectively as stated below.

$$\bar{b} = (\textstyle\sum_i^n r_{ei} \times r_{ti})/\sum_i^n r_{ti}^2 \tag{5}$$

where r_{ei} and r_{ti} are the experimental and theoretical moment carrying capacities of the i[th] beam obtained experimentally, respectively. The prediction error in the model for i[th] value is calculated as:

$$\delta_i = r_{ei}/(\bar{b}r_{ti}) \tag{6}$$

The modelling error of the theoretical prediction model proposed in Section 2 is denoted by V_δ^2, and is found to be 0.0029. To account for the error due to finite number of data, design fractile factor k_d is applied.

$$k_i = (k_d \times V_\delta^2 + \beta \times V_{rti}^2)/V_{ri}^2 \tag{7}$$

where k_d is obtained from Table D2 in Annex D of Eurocode (2002), β = 3.04 is the target reliability index, V_{rti}^2 represents the total parametric uncertainty in the ith beam, and V_{ri}^2 represents the combined modelling and parametric uncertainty in the ith beam. Q_i in Equation 4 is estimated as follows:

$$Q_i = \sqrt{\ln(1 + V_{ri}^2)} \tag{8}$$

4.2. Calculation of characteristic capacity (r_k)

The characteristic design moment capacity value r_{ki} is used when the nominal design moment capacity value r_{ni} for each beam is not available. r_{ki} is calculated by plugging in the characteristic values of material strengths obtained from Equations 9 and 10, in the equations for calculating ultimate moment capacity. The characteristic values of the compressive strength of NAC (f_{cki}) and the yield strength of the steel reinforcement bars in the ith beam (f_{syki}), respectively, at 5% significance are given by the following equations:

$$f_{cki} = f_{c_i} \times \exp(-1.64 \times \sigma_{lnf_{c_i}} - 0.5 \times \sigma_{lnf_{c_i}}^2) \tag{9}$$

where, f_{c_i} is the nominal value of the compressive strength of concrete for the ith beam, and $\sigma_{lnf_{c_i'}}$ = 0.15 is the c.o.v of the compressive strength of concrete obtained from Johnson and Huang (1994), similar to the calculations in Eurocode (2002).

$$f_{syki} = f_{syi} \exp(-1.64 \times \sigma_{lnf_{syi}} - 0.5 \times \sigma_{lnf_{syi}}^2) \tag{10}$$

where f_{syi} is the nominal value of the yield strength of the steel reinforcement bars for the ith beam, $\sigma_{lnf_{syi}}$ = 0.07 is the c.o.v of yield strength of steel reinforcement bars (JCSS, 2001).

5. RESULTS AND DISCUSSION

5.1. Safety factors and reliability indices for a NAC beam

The safety factors for flexural action (ϕ) for Beam 1 (NAC) corresponding to the reliability index β = 3.04 are 0.8878, 0.8874 and 0.8824 when AS 3600 (2009), ACI 318-11 (2011), and Eurocode 2 (2004) are used, respectively. The safety factors are estimated using Equation 3, in which the design and characteristic moment carrying capacities (r_{di}, r_{ki}) of Beam 1 (NAC) are found using the flexural moment capacity calculations provided in Eurocode 2 (2004), AS 3600 (2009), and ACI 318-11 (2011). The values of these safety factors are approximately 0.885 for all the three international standards. For this calculation, the design fractile factor (k_d) was obtained from Table D2 in Annex D of Eurocode (2002). The adopted value corresponds to the number of test data available (*n* = 9). If further data are collected, the design fractile factor will decrease, and accordingly, the safety factor of NAC will increase. The current safety factor values used in the national standards are 0.8 (capacity factor) in AS 3600 (2009) and 0.9 (strength reduction factor) in ACI 318-11 (2011). The equivalent safety factor for flexural moment capacity derived from the material partial safety factors used in Eurocode 2 (2004) is 0.86. For NAC, the reliability indices that correspond to these safety factors are inversely calculated as shown in Fig. 2. From Fig. 2, it can be seen that the reliability indices are 4.57, 2.83 and 3.42 for the current safety factor values used in AS 3600 (2009), ACI 318-11 (2011) and Eurocode 2 (2004), respectively. These target reliability indices are greater than or around the target reliability index value of 3.04 according to Eurocode (2002) and ISO 2394 (1998).

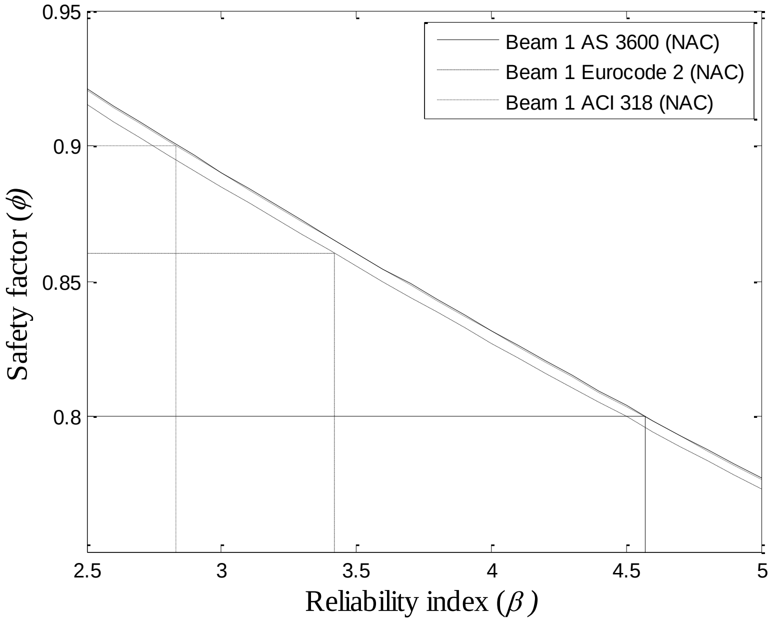

Figure 2. Target reliability indices for NAC corresponding to the existing safety factors in AS 3600 (2009), ACI 318-11 (2011) and Eurocode 2 (2004)

5.2. Reliability index ratios

Table 2 lists the reliability indices of the nine beams normalised by that of Beam 1 (NAC beam). The meaning of these normalised reliability indices is that if the value is close to 1, the SFRRAC beam is equivalent to a normal NAC beam.

Table 2. Reliability index ratio for the SFRRAC mixes with respect to the NAC mix

RA (%) -SF (%)	0-0	30-0	100-0	0-0.3	30-0.3	100-0.3	0-0.6	30-0.6	100-0.6
	1	0.981	0.975	1.593	1.569	1.561	2.029	2.027	2.020
	1	0.967	0.957	1.846	1.807	1.793	2.475	2.471	2.457
	1	0.970	0.960	1.732	1.696	1.683	2.275	2.272	2.262

6. CONCLUSION

This paper proposed a reliability analysis framework for the structural design of SFRRAC beams that includes the contribution of SF to the tensile strength of the beams., based on the method discussed in Eurocode (2002) and ISO 2394 (1998). The reliability indices decreased as the RA content increased, when the safety factor was fixed. The safety factors for NAC corresponding to the values of the reliability indices currently used in the design standards (Eurocode 2 (2004), AS 3600 (2009), and ACI 318-11 (2011)) were around 0.885.

REFERENCES

ACI (American Concrete Institute) (2011). ACI 318-11, Building Code Requirements for Structural Concrete and Commentary.

Bandyopadhyay JN (2008). Design of concrete structures, Prentice Hall of India Learning Pty. Ltd.

Bhikshma V, Manipal K (2012). Study on mechanical properties of recycled aggregate concrete containing steel fibers, Asian Journal of Civil Engineering (Building and Housing), 13, 155–164.

BSI (2002). BS EN 1992:2002, Eurocode Basis of structural design.

BSI (2004). BS EN 1992-1-1:2004 Eurocode 2, Design of concrete structures, Part 1-1: General rules and rules for buildings.

Erdem S, Dawson AR, Thom NH (2011). Microstructure-linked strength properties and impact response of conventional and recycled concrete reinforced with steel and synthetic macro fibres, Construction and Building Materials 25, 4025–4036.

Etxeberria M, Vázquez E, Marí A, Barra M (2007). Influence of amount of recycled coarse aggregates and production process on properties of recycled aggregate concrete, Cement and Concrete Research 37, 735–742.

International Organization for Standardization (1998). ISO 2394-1998, General principles on reliability for structures.

JCSS (Joint Committee on Structural Safety) (2001). JCSS Probabilistic model code Part 3: Material Properties.

Johnson RP, Huang D (1994). Calibration of safety factors $\gamma_M$for composite steel and concrete beams in bending, In: Proceedings of the Institution of Civil Engineers – Structures and Buildings, 104, 193–203.

Mirza O, Wigg D, Kang W-H, Ramesh RB, Senaratne S, Tam VWY (2017). Flexural behaviour of reinforced concrete beams with recycled aggregates and steel fibres. KSCE Journal of Civil Engineering, Submitted for review.

Song PS, Hwang S (2004). Mechanical properties of high-strength steel fiber-reinforced concrete, Construction and Building Materials, 18, 669–673.

Standards Australia (2009). AS 3600-2009, Australian Standard Concrete structures.

Kang, WH, Ramesh RB, Mirza O, Senaratne S, Tam V, Wigg D (2017). Reliability Based Design of RC Beams With Recycled Aggregate and Steel Fibres, Structures, 11, 135-145.

Vaishali GG, Rao HS (2012). Strength and permeability characteristics of fiber reinforced high performance concrete with recycled aggregates, Asian Journal of Civil Engineering, 13, 55–77.

Proc. 1st International Conference on Structural Engineering Research (iCSER 2017)
20-22 Nov 2017, Sydney, Australia
ISBN: 978-0-6480147-6-8

Performance Evaluation of Square High Strength Concrete (HSC) Columns Reinforced with Steel Equal Angle (SEA) Sections under Axial Compression

Ayoob A. Ibrahim[1], M. Neaz Sheikh[2] and Muhammad N.S. Hadi[3]

[1]Ph.D. Candidate, School of Civil, Mining and Environmental Engineering, University of Wollongong, Australia,
[2]Associate Professor, School of Civil, Mining and Environmental Engineering, University of Wollongong, Australia
[3]Associate Professor, School of Civil, Mining and Environmental Engineering, University of Wollongong, Australia
Corresponding author's Email: aaii884@uowmail.edu.au

Abstract

This paper reports the results of an experimental investigation on the behaviour of square High Strength Concrete (HSC) columns reinforced longitudinally with either steel bars or Steel Equal Angle (SEA) sections under concentric axial compression. The use of SEA sections as longitudinal reinforcement may enhance the load carrying capacity and ductility of concrete columns. These enhancements are because for a given cross-sectional area, a SEA section has a higher second moment of area and radius gyration than a steel bar. Also, the SEA sections provide a greater confinement area for the concrete core of columns. A total of 6 column specimens with a square cross section of 210 mm and 600 mm height were tested under concentric axial compression. The specimens were divided into two groups and each group contains three specimens. The specimens in the first group (Group 1) were reinforced longitudinally with four N12 (12 mm diameter) deformed steel bars and served as reference specimens. The remaining four specimens in the second group (Group 2) were reinforced longitudinally with four A30 (29.1 mm x 29.1 mm x 2.25 mm) SEA sections. The lateral reinforcement spacing in each group of specimens varied between 50 mm and 200 mm. The influence of the type of longitudinal reinforcement (steel bars and SEA sections) and the spacing of the lateral reinforcement on the performance of the column specimens were investigated and discussed. The results of this investigation showed that for specimens reinforced with SEA sections, the ductility significantly enhanced compared to corresponding specimens reinforced with steel bars. The test results also indicated that as the lateral reinforcement increased from 50 mm to 200 mm, specimens reinforced with SEA sections showed better enhancement in ductility and strength than the specimens reinforced with steel bars.

Keywords: Columns, Steel equal angle sections, High strength concrete, Axial compression, Ductility.

1. INTRODUCTION

The use of high-strength concrete (HSC) in buildings has increased over the last decades. However, HSC reinforced concrete (RC) columns exhibit a lower ductility than normal strength concrete (NSC) (Razvi and Saatcioglu 1999). Therefore, many studies attempted to investigate the ductility and the strength of HSC columns (Bhowmick et al. 2006). Most of these studies indicated that more lateral reinforcement is required in HSC columns than in NSC columns to achieve a similar ductility. Also, it was reported that HSC columns under concentric compression experience premature concrete cover spalling, which can lead to decreasing the column strength due to reducing its cross-section (Cusson and Paultre 1994; Samani et al. 2015).

The lateral reinforcement may be in the form of helices or ties. The mechanism of confinement by lateral reinforcement can be demonstrated by reviewing the behaviour of reinforced concrete (RC) columns under axial compressive load. When the columns are subjected to an axial compressive load, these columns will be shortened axially and expanded laterally. As the applied load increases and reach the maximum strength of columns, the concrete cover cracks and spalls due to the stress concentration produced at the interface between the lateral reinforcement and the surrounding concrete (Bresler and Gilbert 1961), then the longitudinal reinforcement buckles outwards. The use of sufficient lateral reinforcement to confine concrete under axial compressive load can restrain the lateral expansion of the concrete. When the reinforced concrete (RC) column is axially loaded, the concrete core starts to expand outwards. At this stage, the lateral reinforcement tends to prevent the lateral expansion of the concrete core. This process can generate a reactive confining pressure against the concrete core of the column. When the concrete core is confined by lateral square ties, the concrete expands laterally and bears against the lateral ties. This study summarizes the results of an experimental program investigating the behaviour SEA reinforced square HSC columns under pure concentric axial compression. The main parameters investigated included the type of longitudinal reinforcement and the spacing of lateral ties.

2. EXPERIMENTAL WORK

2.1 Design of Specimens

In this study, a total of six square reinforced high strength concrete (HSC) column specimens were cast and tested under concentric axial load. In this study, concrete compressive strength greater than 50 MPa is referred to as high-strength concrete (HSC). All specimens had 210 mm square cross-section and 600 mm height. Table 1 presents the reinforcement details of the tested specimens. Specimens N12-S50, B-S100 and N12-S200 served as reference specimens and reinforced longitudinally with four N12 (12 mm diameter) deformed steel bars. Specimens SEA-S50, SEA-S100, and SEA-S200 were reinforced longitudinally with four A30 (29.1 mm x 29.1 mm x 2.25 mm) steel equal angle (SEA) sections. All specimens were reinforced laterally with R10 (10 mm diameter) plain steel bars with a spacing that varied between 50 mm and 200 mm at centres (centre-to-centre). Also, the spacing of lateral reinforcement was decreased to 40 mm at the top and bottom ends of specimens to prevent failure during testing. The column specimens are labelled by the type of longitudinal reinforcement and the lateral tie spacing. For instance, Specimen N12-S200 is reinforced longitudinally with four N12 steel bars and laterally with square ties at 200 mm spacing centre-to-centre.

Table 1. Test matrix.

Group	Specimen	Longitudinal Reinforcement			Lateral Reinforcement	
		Type	ρ[a] %	f_y[b] (MPa)	Diameter (mm)	Spacing (mm)
1	N12-S50	N12 steel bars	1.03	556	10	50
	N12-S100		1.03	556	10	100
	N12-S200		1.03	556	10	200
2	SEA-S50	A30 SEA sections	1.11	374	10	50
	SEA-S100		1.11	374	10	100
	SEA-S200		1.11	374	10	200

[a] ρ is the volumetric ratio of longitudinal reinforcement.
[b] f_y is yield tensile strength of the longitudinal reinforcement.

2.2 Preliminary Tests

Preliminary testing involved testing concrete cylinder samples, steel bars, and steel equal angle (SEA) sections. The concrete cylinder samples were 100 mm in diameter and 200 mm in height. The concrete compressive strength was 68.5 MPa. Three pieces of each bar diameter N12 and R10 were tested to determine the mechanical properties of the reinforcing steel bars according to Australian Standard AS 1391 (2007), and the results were 556 MPa and 323 MPa, respectively. Also, three coupon pieces of each SEA A30 sections were tested to determine the average yield strength of the reinforcing SEA section according to AS 1391(2007), and the result was 374 MPa.

2.3 Test Procedure

The column specimens were tested under displacement controlled pure axial compression at a displacement rate of 0.3 mm/min. Two Linear Variable Displacement Transformers (LVDTs) were mounted at 180-degrees around the tested column specimen to monitor axial deformation. Two of LVDTs were mounted on the lower steel plate of the 5000 kN Denison testing machine (Figure 1). The top and bottom end of each specimen were wrapped with a double layer of Carbon Fiber Reinforced Polymer (CFRP) sheets to avoid premature failure of the specimens ends under pure axial loads. The width of CFRP sheet was 90 mm.

Figure 1 Test setup of specimen

3. EXPERIMENTAL RESULTS AND DISCUSSION

3.1 General Behaviour

Figure 2 presents the failure modes of the tested specimens after failure. The SEA and steel bar reinforced concrete (RC) column specimens had a similar behaviour up to their maximum axial load. During testing, vertical hairline cracks started to appear before reaching their maximum axial loads. It can also be seen that the failure of the SEA and the steel bar RC specimens were characterised by spalling of the concrete cover, followed by outward buckling of the longitudinal reinforcement (steel bars and SEA sections). The ductility of the tested specimens was calculated as the ratio of the areas under the axial load-axial deformation curves (Hadi et al. 2016). The ductility (μ) of the tested specimens was measured using Equation (1).

$$\mu = \frac{A_2}{A_1} \quad (1)$$

where A_1 and A_2 are the areas under the axial load-deformation curve up to the yield deformation and to the ultimate deformation, respectively. The ultimate deformation was computed at 85% of maximum axial load in the descending part of the axial load-axial deformation curves.

N12-S50 N12-S100 N12-S200 SEA-S50 SEA-S100 SEA-S200

Figure 2 Failure modes of the tested specimens

3.2 Influence of Longitudinal Reinforcement Type

The type of longitudinal reinforcement was one of the main parameters investigated in this study. The effect of longitudinal reinforcement type (N12 steel bars and SEA sections) was examined by comparing experimental results of four pairs each of N12 steel bar specimens and A30 SEA specimens (Figure 3). The compared specimens of each pair had the same spacing of lateral tie, but a different type of longitudinal reinforcement (N12 steel bars or A30 SEA sections). From Table 2, it can be observed that Specimen N12-S50 exhibited about 11.6% higher maximum axial load compared to Specimen SEA-S50. Specimens N12-S100 and SEA-S100 had similar ductilities. However, the increase in the maximum axial load was 2.9% for Specimens SEA-S200 relative to the maximum axial loads of Specimens N12-S200. Also, the increase in the ductility of Specimens SEA-S50, SEA-S100 and SEA-S200 was 44.4%, 12.5% and 6.7%, respectively, relative to the ductilities of Specimens N12-S50, N12-S100 and N12-S200. This indicates that the use of A30 SEA sections instead of the steel bars led to increasing the strength and ductility of the HSC specimens.

Table 2. Test results of the tested specimens.

Specimen	**Maximum axial load P_{max}, kN**	**Deformation at P_{max}, mm**	**Ductility**
N12-S50	2929	2.3	1.8
N12-S100	2626	2.1	1.6
N12-S200	2399	1.8	1.5
SEA-S50	2625	2.2	2.6
SEA-S100	2619	2.3	1.8
SEA-S200	2469	1.9	1.6

[a]The ductility was not calculated as the specimen failed prematurely.

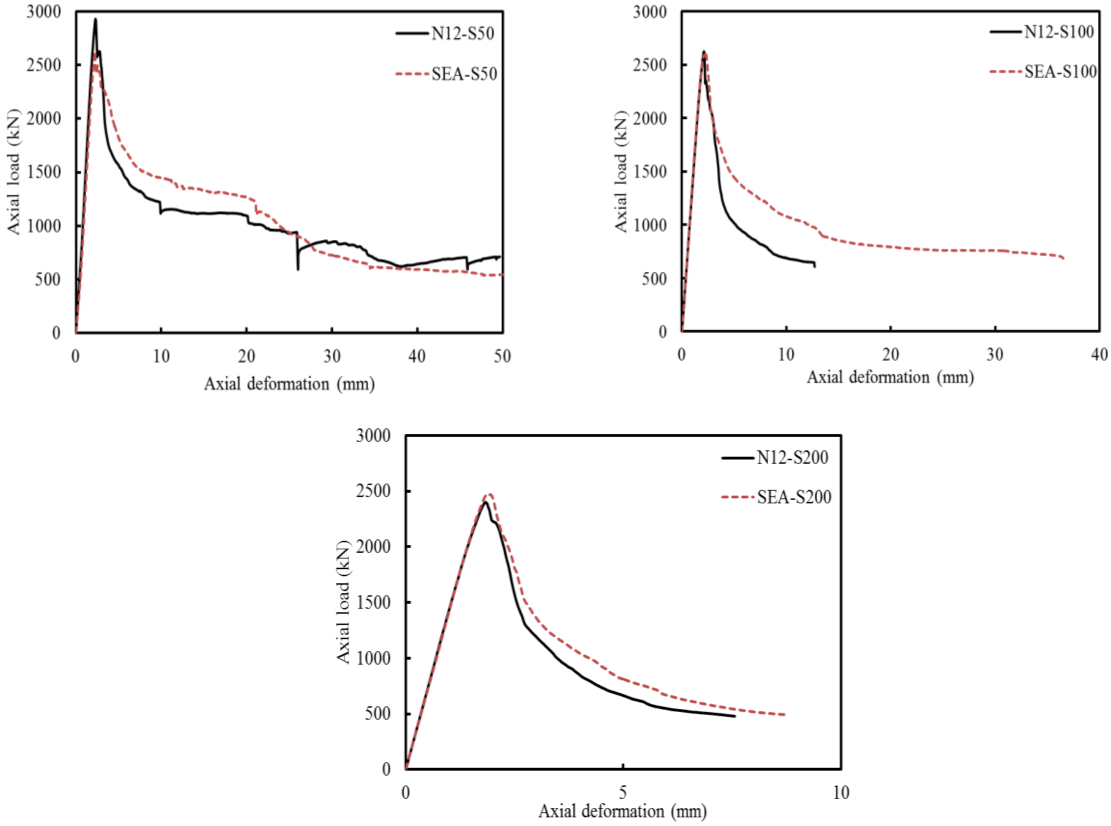

Figure 3 Influence of the longitudinal reinforcements (steel bars and SEA sections)

3.3 Influence of Lateral Tie Spacing

The spacing of lateral ties was the most significant and one of the main variables investigated extensively in this study. The lateral confining pressure in the concrete core is significantly affected by an increase in the spacing of the lateral tie. Also, the spacing of lateral ties is one of the most important variables that impact on the distribution of the laterally confining pressure on the concrete core as well as controlling of the stability of the longitudinal reinforcement. Figure 4 presents comparisons of N12 steel bar specimens and A30 SEA specimens with different lateral tie spacing, which ranged from 50 mm to 400 mm. From this figure, it can be observed that as the spacing of lateral ties increased, the post-peak behaviour of the specimens became steeper. Also, from Table 2, it was found that the decrease in the maximum axial load was 11.5% and 22.1% for Specimens N12-S100 and N12-S200 respectively, relative to the maximum axial load of Specimen N12-S50. Also, the decrease in the ductility was 12.5% and 20.0% for Specimens N12-S100 and N12-S200 respectively, compared to the ductility of Specimen N12-S50. This is because as the spacing of lateral ties increases, the effective confinement of concrete core decreases.

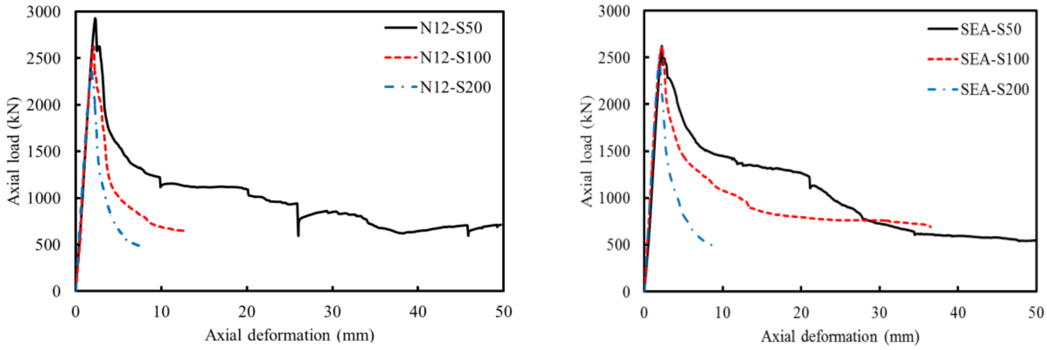

Figure 4 Influence of lateral tie spacing of the tested specimens

It was also observed that the decrease in the maximum axial load was only 0.2% and 6.3% for Specimens SEA-S100 and SEA-S200, respectively, relative to the maximum axial load of Specimen SEA-S50. Also, the decrease in the ductility was 44.4% and 62.5% for Specimens SEA-S100 and SEA-S200, respectively, compared to the ductility of Specimen SEA-S50.

4. CONCLUSIONS

In this study, an experimental program was carried out on eight square HSC columns under axial compression. The main objective of this study was to investigate the behaviour and efficiency of specimens reinforced longitudinally with steel equal angle (SEA) sections. The effect of longitudinal reinforcements and spacing of lateral ties were investigated. From the test results, it can be concluded that the improvements in the strength and ductility of the specimens reinforced longitudinally with SEA sections are because the SEA sections increase the effectively confined concrete core. Also, the use of SEA sections as longitudinal reinforcement led to increasing the buckling resistance of the specimens, in particular for specimens with high lateral tie spacing.

ACKNOWLEDGMENTS

The authors would like to thank the University of Wollongong, Australia and technical officers at the High Bay laboratory. Also, the first author would like to acknowledge the Iraqi Government for the support of his full PhD scholarship.

REFERENCES

AS (Australian Standard). (2007). "Metallic materials tensile testing at ambient temperature." AS 1391-2007, Sydney, Australia.

Bhowmick, R., Sharma, U., Bhargava, P. (2006). Numerical simulation of confined concrete columns and a parametric study, Asian Journal Of Civil Engineering (Building And Housing), 7, 269-286.

Bresler, B., Gilbert, P. (1961). Tie requirements for reinforced concrete columns, ACI Journal, Proceedings, 58, 555-570.

Cusson, D., Paultre, P. (1994). High-strength concrete columns confined by rectangular ties, Journal of Structural Engineering, 120, 783-804.

Hadi, M. N. S., Khan, Q. S., Sheikh, M. N. (2016). Axial and flexural behavior of unreinforced and FRP bar reinforced circular concrete filled FRP tube columns, Construction and Building Materials, 122, 43-53.

Razvi, S., Saatcioglu, M. (1999). Confinement model for high-strength concrete, Journal of Structural Engineering, 125, 281-289.

Samani, A. K., Attard, M. M., Foster, S. J. (2015). Ductility in concentrically loaded reinforced concrete columns, Australian Journal of Structural Engineering, 16, 237-250.

ISBN: 978-0-6480147-6-8

Axial Load and Bending Moment Behaviour of Square High Strength Concrete (HSC) Columns Reinforced with Steel Equal Angle (SEA) Sections

Ayoob A. Ibrahim[1], M. Neaz Sheikh[2] and Muhammad N.S. Hadi[3]

[1]Ph.D. Candidate, School of Civil, Mining and Environmental Engineering, University of Wollongong, Australia,
[2]Associate Professor, School of Civil, Mining and Environmental Engineering, University of Wollongong, Australia
[3]Associate Professor, School of Civil, Mining and Environmental Engineering, University of Wollongong, Australia
Corresponding author's Email: aaii884@uowmail.edu.au

Abstract

This paper presents the behaviour of square high-strength concrete (HSC) specimens reinforced longitudinally with steel equal angle (SEA) sections under different loading conditions. For the same cross-sectional area, a SEA section has a higher second moment of area than a steel bar, which results in a greater bending stiffness of the concrete member reinforced with SEA sections. Also, the area of confined concrete is greater in concrete members reinforced with SEA sections compared to members reinforced with steel bars, which results in higher strength and ductility. A total of 8 specimens of 210 mm square cross-section and 800 mm height were constructed and tested. The specimens were divided into two groups with four specimens in each group. Group R-S50 specimens serve as the reference group and were reinforced longitudinally with four N12 (12 mm diameter) deformed steel bars. Group A30-S50 specimens were reinforced longitudinally with four A30 (29.1 mm x 29.1 mm x 2.25 mm) SEA sections. All specimens were reinforced laterally with R10 (10 mm diameter) plain steel bars and spaced at 50 mm centres. The main variables considered in the study included the type of longitudinal reinforcement and the magnitude of load eccentricity. It was obtained from the experimental results that specimens reinforced longitudinally with SEA sections showed greater ductility compared to specimens reinforced longitudinally with steel bars under different loading conditions.

Keywords: High strength concrete, Columns, Ductility, Steel equal angle sections, Eccentric axial load.

1. INTRODUCTION

The use of high strength concrete (HSC) in the construction of concrete structures has been increased over the last few decades. The main problem associated with the use of HSC in the construction of columns is the lower ductility of the HSC column than the ductility of the Normal Strength Concrete (NSC) column for the same amount of confinement reinforcement (Ho et al. 2010). This is because the ductility of concrete decreases with the increase in the compressive strength.

Columns are structural members subjected to a combined axial compression and bending moment, rather than pure axial compression as flexural effects may be created by construction errors and lateral forces (Hadi et al. 2016). A number of researchers have studied the behaviour of the HSC columns under axial compression. However, a few research studies were carried out on the behaviour of the high strength concrete (HSC) columns under eccentric axial loads. The most important factor is the value of initial eccentricity of the axial load that affects the performance of the columns. The effectiveness of lateral confinement on the ductility decreases when the initial eccentricity is less than 30% of the lateral dimension of the cross-section of the RC column (Lloyd and Rangan 1995). Furthermore, as the initial eccentricity of axial load decreases, the spalling of the concrete cover increases (Lee and Son 2000). Also, the value of initial eccentricity affects the strength of columns. In this study, a new method is proposed to reinforce HSC columns with steel equal angle (SEA) sections as longitudinal reinforcement. For a given cross-sectional area, the use of longitudinal SEA sections as main reinforcement results in improving the effectively confined core of the columns and also the minimum second moment of area of SEA section is greater than steel bar, thus leading to the increase of the ductility and the delay buckling of longitudinal reinforcement. Parameters investigated included the type of longitudinal reinforcement and the magnitude of load eccentricity of SEA specimens.

2. EXPERIMENTAL PROGRAM

2.1 Test Specimens

A total of 8 specimens of 210 mm square cross-section and 800 mm height were constructed and tested under different loading conditions. The specimens were divided into two groups with four specimens in each group, as shown in Table 1. Group R-S50 specimens were reinforced longitudinally with four N12 deformed steel bars of 12 mm diameter. Group A30-S50 specimens were reinforced longitudinally with four A30 steel equal angle (SEA) sections. For lateral reinforcement, R10 plain steel bars (10 mm diameter) were used to fabricate lateral square ties for all specimens with spacings of 50 mm centre-to-centre.

From each group, the first specimen was tested under monotonic increased concentric axial load and labelled as C. The second specimen was tested under 25 mm eccentric axial load and labelled as E25. The third specimen was tested under 50 mm eccentric axial load and labelled as E50. The fourth specimen was tested under four-point bending and labelled as F. All specimens were reinforced laterally with constant tie spacing of 50 mm and labelled as S50.

Table 1. Test matrix.

Group	Specimen	Longitudinal Reinforcement			Lateral Reinforcement		Eccentricity
		Type	ρ^a %	fy^b (MPa)	Diameter (mm)	Spacing (mm)	
R-S50	R-S50-C	N12 steel bars	1.03	556	10	50	0
	R-S50-E25		1.03	556	10	50	25 mm
	R-S50-E50		1.03	556	10	50	50 mm
	R-S50-F		1.03	556	10	50	Flexural
A30-S50	A30-S50-C	A30 SEA sections	1.11	374	10	50	0
	A30-S50-E25		1.11	374	10	50	25 mm
	A30-S50-E50		1.11	374	10	50	50 mm
	A30-S50-F		1.11	374	10	50	Flexural

$^a\rho$ is the volumetric ratio of longitudinal reinforcement.
$^b fy$ is yield tensile strength of the longitudinal reinforcement.

2.2 Material Properties

All column specimens were cast vertically from the same batch of ready mix high strength concrete (HSC) with an average 28 day compressive strength of 68.5 MPa. Two different types of longitudinal reinforcement were used to reinforce the reinforced concrete (RC) column specimens. Three pieces of each steel bar diameter (N12 and R10) were tested to determine the mechanical properties of the reinforcing steel bars according to AS 1391 (2007), and the results were 556 MPa and 323 MPa, respectively. Also, three coupon pieces of A30 SEA sections were tested to determine the tensile strength of the reinforcing SEA section according to Australian Standard AS 1391 (2007), and the result was 374 MPa.

2.3 Preparing of Specimens

The formwork used for constructing the column specimens was fabricated from 17 mm thick plywood. The longitudinal N12 steel bars and A30 SEA sections were cut to 760 mm to have 20 mm clear cover at the top and bottom of the steel cage. The square ties were fabricated from mild R10 bars in the lab with 21 mm clear side covers to the face of the formwork. These ties were made with 90-degree hooks around one of the longitudinal reinforcement and extended to a minimum overlap of 80 mm at both free ends. Afterwards, each tie was welded at three points on the hook corner to ensure that the ties would provide adequate confinement. Then, the steel cages were prepared by assembling longitudinal and lateral reinforcement. Wooden timbers were used vertically and transversely to fix the formwork before pouring the concrete and then the steel cages were inserted into the wooden formwork. The concrete was poured into the formwork and vibrated using an internal vibrator to compact and to expel the air bubbles. After 24 hours, the specimens were cured by covering with wet hessian and kept in the lab at an ambient temperature for four weeks before testing.

2.4 Test set up and instrumentation

A total of 8 specimens were cast and tested at the laboratories of the School of Civil, Mining, and Environmental Engineering at the University of Wollongong, Australia. The Denison 5000 kN compression testing machine was used to test the specimens. After removing the formwork, the top and bottom of each specimen were wrapped by two layers of CFRC sheet with a width of 100 mm to prevent premature failure during testing. The eccentric axial load was applied to the specimen by an eccentric loading head system manufactured at the University of Wollongong, Australia . The axial deformation of the specimens was measured by using two Linear Variable Differential Transducers (LVDTs) placed vertically in the testing machine in the diagonal opposite direction (Figure 1). For eccentric load tests, as well as to the two LVDTs a laser triangulation was used to capture the lateral deformation of the tested specimens. For flexural loading, the load was applied to the beam specimen using two rigs; one under the specimen and the other above the specimen (Figure 1 (b)). A laser triangulation was attached in the mid-span on the tension side of the beam specimen to monitor the mid-span deflection. All specimens were tested under displacement control with a loading of 0.3 mm/min. Figure 1 shows a typical testing setup for the tested specimens.

(a) (b)

Figure 1. Test setup: (a) Axial compression and (b) Four-point bending

3. EXPERIMENTAL RESULTS AND DISCUSSION

Table 1 summarises test results of the tested column specimens under different eccentric axial loads. To evaluate the performance of the column and beam specimens, ductility capacity is conducted for all specimens. The ductility capacity in this study was calculated as the ratio of the deformation at 80% of the applied axial load in the descending branch of the load-deformation curves to the deformation at yield axial load. The yield load was taken as the load at the end of the limit of the elastic behaviour

(Pessiki and Pieroni 1997). The failure of Specimens R-S50-C and A30-S50-C was characterised by sudden loss of the concrete cover, followed by the dilation in the lateral direction and outward buckling of the longitudinal reinforcement (Figure 2). The failure of Specimens R-S50-E25, R-S50-E50, A30-S50-E25 and A30-S50-E50 was characterised by the forming of lateral cracks in the tension zone, and then spalling of the concrete cover and outward buckling of the longitudinal reinforcement in the compression zone (Figure 2). The failure of specimens R-S50-F and A30-S50-F was due to the rupture of longitudinal reinforcement (Figure 2)

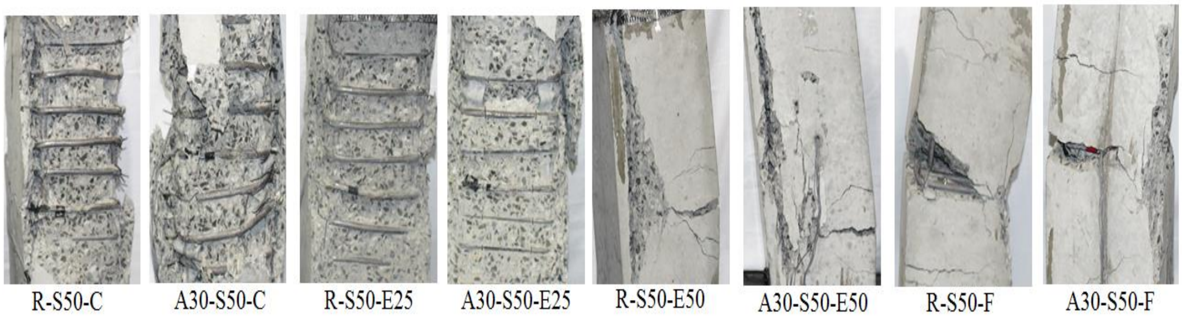

Figure 2 Failure modes of the tested specimens

The load versus deformation curves of the tested specimens under different loading conditions are presented in Figure 3. The axial load versus axial deformation of the column specimens tested under axial compression (Figure 3 (a)). Specimen R-S50-C achieved only 6.6% higher maximum axial load compared to Specimen A30-S50-C because the yield tensile strength of the steel bars was 49% higher than the yield tensile strength of A30 SEA sections. However, the ductility of Specimen A30-S50-C was increased by 21.4% compared with Specimen R-S50-C. This indicates that the use of SEA sections as longitudinal reinforcement into HSC columns results in a significant increase in the effective confined concrete core, thus leading to increase the ductility of the columns. The axial load versus axial and lateral deformations of the specimens that were tested under 25 mm and 50 mm eccentric axial loads are shown in Figure 3 (b) and (c), respectively. The maximum axial load of Specimen R-S50-E25 showed only 8.8% higher than that of Specimen A30-S50-E25. However, Specimen A30-S50-E25 exhibited 16.7% increase in the ductility compared to Specimen R-S50-E25. For the column specimens that were tested under 50 mm eccentricities, Specimen R-S50-E50 was only 6.3% higher maximum axial load compared to Specimen A30-S50-E50. Specimens R-S50-E50 and A30-S50-E50 had about similar ductilities.

Table 2 shows test results of the tested beam specimens under four-point bending. The load versus midspan deflection curves for the specimens testing under four-point bending are shown in Figure 3 (d). It can be noted that the maximum load and ductility of Specimen R-S50-F was 6.6% and 45.2% lower than the maximum load and ductility of Specimen A30-S50-F, respectively. This was because the bending stiffness of SEA sections was much higher than the bending stiffness of steel bar with a similar cross sectional area.

Table 1 Summarise test results of specimens testing under different eccentricity

Specimen	Maximum Axial Load (kN) P_{max}	Deformation at P_{max} (mm)		Ductility
		Axial	Lateral	
R-S50-C	2716	2.8	-	1.4
R-S50-E25	1967	2.7	1.2	1.7
R-S50-E50	1340	2.7	1.9	1.2
A30-S50-C	2548	2.6	-	1.4
A30-S50-E25	1808	2.9	2.2	1.1
A30-S50-E50	1260	2.5	1.1	1.1

Table 2 Summarise test results of specimens testing under four-point bending

Specimen	Maximum load P_{max} (kN)	Midspan deflection at P_{max} (mm)	Ductility
R-S50-F	244	9.5	3.1
A30-S50-F	260	9.5	4.5

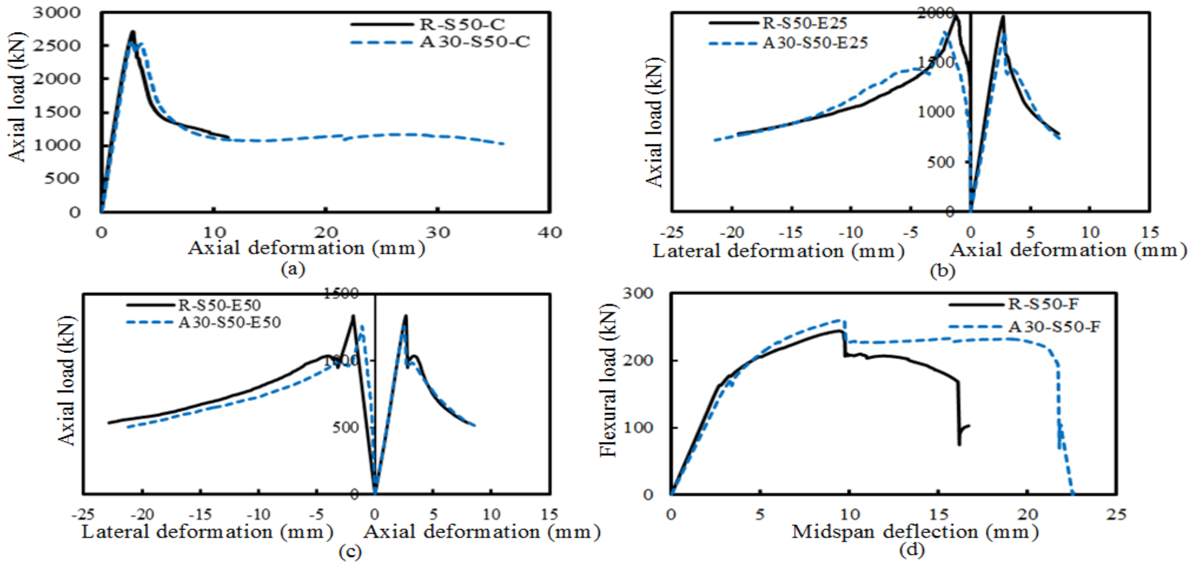

Figure 3 Test results of specimens under (a) concentric axial load (b) 25 mm eccentric axial load (c) 50 mm eccentric axial load and (d) four-point bending

4. AXIAL LOAD-BENDING MOMENT (*P-M*) INTERACTIONS

The experimental axial load-bending moment (*P-M*) interactions were constructed using pure concentric axial load, combined axial load and bending moment and pure bending moment. The bending moment capacity of the specimens under eccentric axial load was calculated using Equation 1:

$$M=P(e+\Delta) \tag{1}$$

where P is the maximum axial load, e is the axial load eccentricity, and Δ is the lateral deformation at the maximum axial load. The pure bending moment capacity at the mid-height of the specimens tested under four-point bending was calculated using Equation 2:

$$M=FL/6 \tag{2}$$

where F is the maximum load under four-point loading and L is the clear span of the tested specimen. The experimental axial load-bending moment (*P-M*) interactions of Groups R-S50 and A30-S50 specimens are shown in Figure 3. It can be seen that SEA reinforced A30-S50 specimens showed slightly lower maximum axial load than the steel bar reinforced R-S50 specimens. This is because steel bars had 49% higher yield tensile strength than A30 SEA sections. However, it can be observed that specimen reinforced with SEA sections exhibited higher bending moments than specimens reinforced with steel bars. This is because the bending stiffness of a SEA section is much higher than the bending stiffness of steel bar with the similar cross-sectional area.

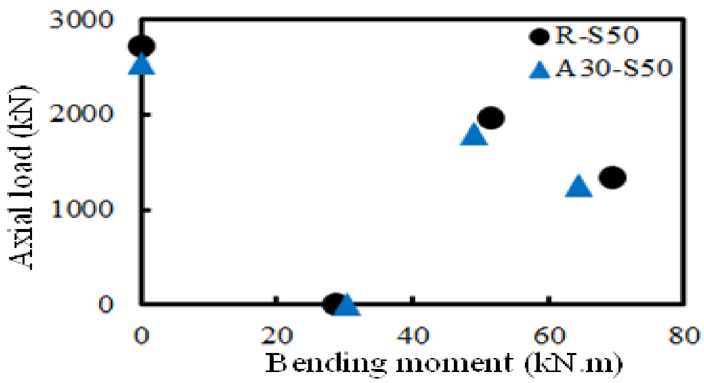

Figure 3 Experimental axial load-bending moment interaction diagram of specimens

5. CONCLUSIONS

The behaviour of 8 square HSC specimens reinforced longitudinally with either steel bars or SEA sections was experimentally investigated. Six specimens were tested as columns under concentric, 25 mm eccentric and 50 mm eccentric axial loads, the remaining two specimens were tested as beams under four-point bending. The test results presented that the maximum axial load of SEA RC column specimens were slightly lower than steel bar RC column specimens because the yield strength of SEA sections was 49% lower than the yield strength of steel bars. However, the improvement in the ductility capacities of the SEA RC specimens was higher than steel bar RC column specimens.

ACKNOWLEDGMENTS

The authors would like to thank the University of Wollongong, Australia and technical officers at the High Bay laboratory. Also, the first author would like to acknowledge the Iraqi Government for the support of his full PhD scholarship.

REFERENCES

AS (Australian Standard). (2007). "Metallic materials tensile testing at ambient temperature." AS 1391-2007, Sydney, Australia.

Hadi, M. N. S., Khan, Q. S., Sheikh, M. N. (2016). Axial and flexural behavior of unreinforced and FRP bar reinforced circular concrete filled FRP tube columns, Construction and Building Materials, 122, , 43-53.

Ho, J., Lam, J., Kwan, A. (2010). Effectiveness of adding confinement for ductility improvement of high-strength concrete columns, Engineering Structures, 32, 714-725.

Lee, J. H., Son, H. S. (2000). Failure and strength of high-strength concrete columns subjected to eccentric loads, Structural Journal, 97, 75-85.

Lloyd, N. A., Rangan, B. V. (1995). 'High strength concrete columns under eccentric compression', School of Civil Engineering, Curtin University of Technology.

Pessiki, S., Pieroni, A. (1997). Axial load behavior of large-scale spirally-reinforced high-strength concrete columns, ACI Structural Journal., 94, 304-313.

Proc. 1st International Conference on Structural Engineering Research (iCSER 2017)
20-22 Nov 2017, Sydney, Australia
ISBN: 978-0-6480147-6-8

Mix Design of Recycled Aggregate Concrete Using Packing Density Method

Qingtao Huang[1], Lang Lin[1], Ee Loon Tan[1] and Balbir Singh[1]

[1]School of Computing, Engineering and Mathematics,
Western Sydney University, Sydney, Australia
Corresponding author's E-mail: e.tan@westernsydney.edu.au

Abstract

Packing density method is new kind of mix design method, generally used for design normal, high-strength and self-compacting concrete. This method considers the volume and density variation between different types and sizes of aggregate. The adoption of packing density method optimises the particle packing density of concrete by selecting the right amount of various aggregates to fill up the voids between large and small aggregates, which allows a more dense and stiff structure. This paper is devoted to the studies of material and mechanical properties of recycled aggregate concrete using packing density method. This paper considers mix of two different aggregate sizes of 10 and 20mm, 0, 30, 50, 70 and 100% recycled aggregate replacement ratios, and water-cement ratio of 0.35, 0.45 and 0.55. In total of fifteen concrete mix designs are considered. The paper presents the material properties of aggregates which were obtained from the material testing. The mix design method and results of mechanical testing will be discussed. The results show that the packing densities of natural and recycled aggregates are different, and should not be treated in the same way. By using packing density mix design method, recycled aggregated concrete strengths fluctuation can be resolved, and the concretes can have similar strengths consistency, regardless the recycled concrete aggregate replacement ratios. This method minimise the influence of recycled concrete aggregates obtain from various sources with variable quality.

Keywords: Recycled Aggregate Concrete, Packing Density Method, Concrete Mix Design, Recycled Concrete Aggregate.

1. INTRODUCTION

In Australia, about 17 million tonnes of construction waste is landfilled each year, the amount of solid waste has increased over the last few years, hence the landfill space quickly becomes limited (Kotrayothar 2012; Poon, Shui & Lam 2004). Recycling and reuse of concrete waste is necessary from the viewpoints of environmental preservation and effective utilisation of resource, it helps to limit the environmental impact by reducing landfilling and limiting the exploitation of natural resources. Many researchers have tried to promote the use of recycled concrete aggregate (RCA) in conventional concrete, to reduce the use of NA (Rahal 2007; Tam 2005; Xiao, JianZhuang, Li & Poon 2012). However, many studies have shown that concrete mixed with RCA usually have mechanical strength variations compared to those conventional concrete made with NA (Rahal 2007; Singh 2014; Xiao, JianZhuang, Li & Poon 2012). This is mainly due to the method used to obtain the RCA, usually produced through mechanical crushing of old concretes that are obtained from demolished structures (Wagih et al. 2013). The crushing process often involves several stages to achieve desirable shapes and sizes (RILEM 1992). It can result in non-homogeneous and round-shaped property, which hinders their wide use (de Juan & Gutiérrez 2009).

In addition, recycled concrete aggregates have higher water absorption capacity due to the presence of old motor attached to the surface (Huang 2015; Sidorova et al. 2014). The water absorption capacity affects both fresh and hardened properties of recycled aggregate concrete (RAC). In order to obtain the similar workability as conventional concrete, additional quantity of water is required. It would often cause increase of water-cement ratio (*w/c*) and affect the strength of the RAC (Huang et al. 2016;

Wardeh, Ghorbel & Gomart 2015). Moreover, several studies have shown that the porosity of RAC is modified and increased with the RCA replacement ratio, as a result, high porosity can leads to reduce of mechanical strengths (Gomez-Soberon and Kou et al., cited in Wardeh, Ghorbel & Gomart 2015). In addition, the mechanical properties of RAC also depends on other parameters, such as quality of concrete from which RCAs are obtained (Xiao, Jz, Li & Zhang 2005).

In general, the higher the parking density of aggregates, the smaller the voids need to be filled by the cement paste. It also reduces the amount of excess concrete paste, because cement paste has to fill up the voids between aggregates. In other words, minimum voids and maximum density concrete can be generated, with less cement and water required (Raj, Patil & Bhattacharjee 2014). Moisture content and material properties of RCAs are also considered in the mix design, so the amount of water and aggregates can be predict (Wardeh, Ghorbel & Gomart 2015). This paper is devoted to the studies of material and mechanical properties of recycled aggregate concrete using packing density method.

2. MATERIALS

Cement Australia® Builders Cement (Type GB) was used in the mix. It is a fly ash blended Portland cement in conformity with the requirements of AS 3972 for general purpose and blended cements. The specific gravity of Builders Cement is 3.11, and its compressive strength after 28 days is 46 MPa. The fine aggregate sand is air dried and passed through a 3.55 mm sieve. And two natural and recycled concrete coarse aggregates of size 10 and 20 mm were used. Natural aggregates were from Penrith Sand and Soil, and RCAs were from a retreatment of demolition materials. Bulk density, specific gravity and absorption tests were carried out according to ASTM C127 for coarse aggregate and ASTM C128 for fine aggregate, the test results are shown in Table 1. The high range water reducing admixture, a liquid based superplasticizer, was used to increase the workability of concrete.

Table 1. Bulk density, specific gravity and absorption of aggregates

Materials	**Bulk density** (g/cm^3)	**Bulk specific gravity**	**Absorption** (%)
1.Fine Sand	1.552	2.683	0.2
2.NA 10 mm	1.518	2.829	1.48
3.NA 20 mm	1.555	2.875	0.91
4.RCA 10 mm	1.310	2.337	4.73
5.RCA 20 mm	1.256	2.276	5.16

3. PACKING DENSITY MIX METHOD

The packing density of aggregate mixture is defined as the solid volume in a unit total volume. The aim of obtaining packing density is to predict the amount of aggregates used in the mixture, and to minimise porosity and reduce amount of cement used in the concrete (Raj, Patil & Bhattacharjee 2014; Wardeh, Ghorbel & Gomart 2015). The values of bulk density of aggregates mixture were first determined by backfill of natural and/or recycled concrete coarse aggregates and fine aggregate sand, with different proportions into an empty mould, using Equation 1 (Raj, Patil & Bhattacharjee 2014). The coarse aggregates 20 mm (CA20) and 10 mm (CA10) were mixed in 60:40 by mass. The coarse aggregate (CA) and fine aggregate sand (FA) were mixed in 64:36 by mass. The ratio of aggregates mixture of CA20, CA10 and FA are 38.4:25.6:36 by mass. The mixture proportions was from IS-10262 (2009) Concrete Mix Proportioning-Guidelines, for Mix Design M-40 Grade concrete. A total of five aggregates mixtures of 0 (NA), 30, 50 70 and 100% are tested, and the test results are shown in Table 2.

$$Mixture\ bulk\ density\ (Maximum) = \frac{Mass\ of\ aggregates\ mixture}{Volume\ of\ mould} \tag{1}$$

Table 2. Maximum aggregates mixture bulk density

RCA replacement	**Mixture of aggregates**	**Weight fraction** (Aggregates mixture ratio)	**Mixture bulk density** (g/cm^3)
0% RCA	NA20:NA10:FA	38.4: 25.6: 36	2.169
30% RCA	NA20:RCA20:NA10:RCA10:FA	26.88: 11.52: 17.92: 7.68: 36	2.123
50% RCA	NA20:RCA20:NA10:RCA10:FA	19.2: 19.2: 12.8: 12.8: 36	2.065
70% RCA	NA20:RCA20:NA10:RCA10:FA	11.52: 26.88: 7.68: 17.92: 36	2.015
100% RCA	RCA20:RCA10:FA	38.4: 25.6: 36	1.973

The packing density of individual aggregate in the mixture is determined from its maximum bulk density and individual aggregate bulk specific gravity, using Equation 2 (Raj, Patil & Bhattacharjee 2014). The voids content of aggregates mixture is determined from its total packing density, using Equation 3. Assume the excess paste content for concrete is 30%, based on the results from Raj, Patil and Bhattacharjee (2014) IS1199-1959 flow table tests. The paste content for concrete and volume of aggregates are determined using Equation 4 and 5. The solid volume of aggregate is determined from individual aggregate weight fraction and bulk specific gravity in the mixture, using Equation 6. The weight of aggregate in the mixture is determined using Equation 7 (Raj, Patil & Bhattacharjee 2014), and all results are shown in Table 3.

$$Packing\ density = \frac{Maximum\ mixture\ bulk\ density \times weight\ fraction}{Individual\ bulk\ specific\ gravity\ of\ aggregate} \times \frac{1}{100} \quad (2)$$

$$Voids\ content = 1 - total\ packing\ density\ of\ the\ mixture \quad (3)$$

$$Paste\ content = Voids\ content \times (1 + \frac{excess\ paste\ content\ \%}{100}) \quad (4)$$

$$Volume\ of\ aggregates = 1 - paste\ content \quad (5)$$

$$Solid\ volume\ of\ aggregate = \frac{Indvidual\ aggregate\ weight\ fraction}{Individual\ bulk\ specific\ gravity\ of\ aggregate} \quad (6)$$

$$Weight\ of\ aggregate = \frac{Volume\ of\ aggregates}{Total\ solid\ volume\ of\ aggregates} \times \text{weight fraction} \times \frac{1000}{100} \quad (7)$$

Three water-cement ratios 0.35, 0.45 and 0.55 were considered in the mix design. The total paste of concrete is determined by the specific gravity of cement and water-cement ratio (w/c), using Equation 8. The total paste for 0.35, 0.45 and 0.55 w/c is 0.6715c, 0.7715c and 0.8715c. The cement content of the concrete is determined by paste content and total paste, using Equation 9, and then calculated the water content of the concrete, using Equation 10 (Raj, Patil & Bhattacharjee 2014). All results are shown in Table 4.

$$Total\ paste = C + W = (\frac{1}{Specific\ gravity\ of\ cement} + \frac{w/c}{1}) \times c \quad (8)$$

$$Cement\ content = \frac{Paste\ content}{Total\ paste} \times 1000 \quad (9)$$

$$Water\ content = paste\ content \times w/c \quad (10)$$

Table 3. Packing density and weight of aggregates

RCA replacement	**Materials**	**Packing density**	**Voids content**	**Paste content**	**Volume of aggregates** ($\mathbf{cm^3}$)	**Solid volume of aggregate** ($\mathbf{cm^3}$)	**Weight of aggregate** (kg/$\mathbf{m^3}$)
0% RCA	Fine Sand	0.2910	-	-	-	0.1342	713.62
	NA 10 mm	0.1963	-	-	-	0.0905	507.46
	NA 20 mm	0.2897	-	-	-	0.1336	761.19
	RCA 10 mm	-	-	-	-	-	-
	RCA 20 mm	-	-	-	-	-	-
	Total	0.7770	0.2230	0.2899	0.7101	0.3582	1982.28
30% RAC	Fine Sand	0.2848	-	-	-	0.1342	704.96
	NA 10 mm	0.1344	-	-	-	0.0633	350.91
	NA 20 mm	0.1984	-	-	-	0.0935	526.37
	RCA 10 mm	0.0698	-	-	-	0.0329	150.39
	RCA 20 mm	0.1074	-	-	-	0.0506	225.59
	Total	0.7949	0.2051	0.2667	0.7333	0.3745	1958.22
50% RAC	Fine Sand	0.2770	-	-	-	0.1342	686.05
	NA 10 mm	0.0934	-	-	-	0.0452	243.93
	NA 20 mm	0.1379	-	-	-	0.0668	365.89
	RCA 10 mm	0.1131	-	-	-	0.0548	243.93
	RCA 20 mm	0.1742	-	-	-	0.0844	365.89
	Total	0.7956	0.2044	0.2657	0.7343	0.3853	1905.68
70% RAC	Fine Sand	0.2704	-	-	-	0.1342	670.64
	NA 10 mm	0.0547	-	-	-	0.0271	143.07
	NA 20 mm	0.0808	-	-	-	0.0401	214.61
	RCA 10 mm	0.1545	-	-	-	0.0767	333.83
	RCA 20 mm	0.2380	-	-	-	0.1181	500.75
	Total	0.7985	0.2015	0.2620	0.7380	0.3962	1862.90
100% RAC	Fine Sand	0.2648	-	-	-	0.1342	661.62
	NA 10 mm	-	-	-	-	-	-
	NA 20 mm	-	-	-	-	-	-
	RCA 10 mm	0.2162	-	-	-	0.1095	470.48
	RCA 20 mm	0.3329	-	-	-	0.1687	705.73
	Total	0.8138	0.1862	0.2420	0.7580	0.4124	1837.83

Table 4. Cement and water contents

RCA replacement	**Cement content** (kg/m^3)			**Water content** (kg/m^3)		
	0.35 w/c	**0.45 w/c**	**0.55 w/c**	**0.35 w/c**	**0.45 w/c**	**0.55 w/c**
0% RCA	431.69	375.74	332.63	151.09	169.08	182.95
30% RCA	397.08	345.61	305.96	138.98	155.53	168.28
50% RCA	395.66	344.37	304.86	138.48	154.97	167.67
70% RCA	390.15	339.58	300.62	136.55	152.81	165.34
100% RCA	360.36	313.66	277.67	126.13	141.15	152.72

4. MIX METHOD AND CONCRETE PROPORTIONS

All 20 and 10 mm natural and recycled concrete aggregates was soaked in water for 12 hours, then air dried till the saturated-surface-dry (SSD), to reduce the effect of water absorption and increase the workability of RCAs without change the water-cement ratio in concrete. Fine sand was air dried and passed through 3.35 mm sieve. Pre-wetted drum concrete mixer was used to mix the concretes, the sand and aggregates were dry-mixed for 5 minutes before the cement and water was added. The liquid-based superplasticizer was first dissolved in water, and then the solution was proportionally split into two parts that were added into the mixture at different time. The concrete was poured into three 100 x 100 x 400 mm prisms and twelve 100 x 200 mm cylinders steel moulds. The concrete specimens were demolded a day after pouring and were cured in a room temperature. A total of fifteen concretes were produced, includes five different RCA replacement ratios of 0, 30, 50, 70 and 100, with three different water-cement ratios of 0.35, 0.45 and 0.55. The mix proportions are shown in Table 5.

Table 5. Mix proportions in 1 m^3

0.35 w/c (kg/m^3)	**Mix 1** 0% RCA	**Mix 2** 30% RCA	**Mix 3** 50% RCA	**Mix 4** 70% RCA	**Mix 5** 100% RCA
Type GB Cement	431.69	397.08	395.66	390.15	360.36
Water	151.09	138.98	138.48	136.55	126.13
Fine Sand	713.62	704.96	686.05	670.64	661.62
NA 10mm	507.46	350.91	243.93	143.07	-
NA 20mm	761.19	526.37	365.89	214.61	-
RCA 10mm	-	150.39	243.93	333.83	470.48
RCA 20mm	-	225.59	365.89	500.75	705.73
Superplasticizer	2.75	2.75	2.75	2.75	2.75
0.45 w/c (kg/m^3)	**Mix 6** 0% RCA	**Mix 7** 30% RCA	**Mix 8** 50% RCA	**Mix 9** 70% RCA	**Mix 10** 100% RCA
Type GB Cement	375.74	345.61	344.37	339.58	313.66
Water	169.08	155.53	154.97	152.81	141.15
Fine Sand	713.62	704.96	686.05	670.64	661.62
NA 10mm	507.46	350.91	243.93	143.07	-
NA 20mm	761.19	526.37	365.89	214.61	-
RCA 10mm	-	150.39	243.93	333.83	470.48
RCA 20mm	-	225.59	365.89	500.75	705.73
Superplasticizer	2.75	2.75	2.75	2.75	2.75
0.55 w/c (kg/m^3)	**Mix 11** 0% RCA	**Mix 12** 30% RCA	**Mix 13** 50% RCA	**Mix 14** 70% RCA	**Mix 15** 100% RCA
Type GB Cement	332.63	305.96	304.86	300.62	277.67
Water	182.95	168.28	167.67	165.34	152.72
Fine Sand	713.62	704.96	686.05	670.64	661.62
NA 10mm	507.46	350.91	243.93	143.07	-
NA 20mm	761.19	526.37	365.89	214.61	-
RCA 10mm	-	150.39	243.93	333.83	470.48
RCA 20mm	-	225.59	365.89	500.75	705.73
Superplasticizer	2.75	2.75	2.75	2.75	2.75

5. RESULTS AND DISCUSSION

Table 6 shows the compressive strength (f_c') of fifteen concretes. The concrete cylinders were tested after 28 days, and the testing procedure was according to AS 1012.14. The compressive strength of recycled aggregate concrete with same water-cement ratio the test results show the strength fluctuation between different RCA replacement ratios are small. The small fluctuations are due to the reduction in cement concentration of the cement paste and porosity variations between aggregates (Wardeh, Ghorbel & Gomart 2015). Overall, 50% RCA recycled aggregate concretes has higher compressive strength.

Table 6. Compressive strength (f'_c) of recycled aggregate concretes

No. of mix	w/c	RCA%	Reading 1 (MPa)	Reading 2 (MPa)	Reading 4 (MPa)	Average (MPa)
Mix 1	0.35	0	40.20	46.72	45.63	44.18
Mix 2		20	37.55	34.21	38.25	36.67
Mix 3		50	51.27	46.62	51.65	49.85
Mix 4		70	45.26	43.32	43.14	43.91
Mix 5		100	35.52	39.33	40.35	38.40
Mix 6	0.45	0	37.87	35.01	29.71	34.19
Mix 7		20	32.74	28.78	30.81	30.77
Mix 8		50	35.65	33.22	35.54	34.80
Mix 9		70	30.51	28.93	30.81	30.08
Mix 10		100	29.39	26.15	27.34	27.62
Mix 11	0.55	0	18.69	19.33	19.21	19.08
Mix 12		20	14.97	16.94	19.42	17.11
Mix 13		50	20.11	21.57	22.95	21.55
Mix 14		70	14.23	19.10	16.86	16.73
Mix 15		100	14.01	13.64	13.96	13.87

The flexural tensile strength ($f'_{ct.f}$) of fifteen recycled aggregates are show in Table 7. The concrete prisms were tested after 28 days, and the testing procedure was according to AS 1012.11. It is possible to conclude that the tensile strength variations of recycled aggregate concrete with different RCA replacement ratios are very small, so the tensile strength fluctuations are insignificant.

Table 7. Flexural tensile strength ($f'_{ct.f}$) of recycled aggregate concretes

No. of mix	w/c	RCA%	Reading 1 (MPa)	Reading 2 (MPa)	Reading 4 (MPa)	Average (MPa)
Mix 1	0.35	0	4.38	4.26	4.09	4.24
Mix 2		20	4.78	3.52	4.06	4.12
Mix 3		50	4.06	4.45	5.16	4.56
Mix 4		70	3.79	5.04	4.31	4.38
Mix 5		100	4.24	4.38	5.06	4.56
Mix 6	0.45	0	3	3.61	3.99	3.53
Mix 7		20	-	4.03	3.69	3.86
Mix 8		50	4.7	4.04	3.57	4.10
Mix 9		70	3.74	3.43	3.81	3.66
Mix 10		100	3.23	3.62	-	3.43
Mix 11	0.55	0	2.88	2.9	2.77	2.85
Mix 12		20	2.57	2.79	3.04	2.80
Mix 13		50	3.01	-	2.84	2.93
Mix 14		70	2.47	2.79	2.47	2.58
Mix 15		100	2.51	2.8	2.56	2.62

6. CONCLUSION

In this paper, the packing density method was used to design the recycled aggregate concretes. A total of fifteen concretes with five RCA replacement ratios of 0, 30, 50 70 and 100% and three water-cement ratios of 0.35, 0.45 and 0.55 were produced, it considered 10 and 20 mm of two size natural and recycled concrete aggregates. From the material test results, found that the natural and recycled concrete aggregates have different density, volume and absorption, hence it should not be considered the same. Unlike the absolute volume method, it considered the individual aggregate as well as the overall mixture density and volume changes. Moisture content and water absorption of aggregates are also being considered in the design. From the mechanical testing results, adoption of packing density method can solve the recycled aggregate concrete strengths fluctuation and minimise the influence of recycled concrete aggregates obtain from various sources with variable quality. Irrespective the RCA replacement ratio, the building can maintain the consistency of the strength of the entire structure.

7. ACKNOWLEDGMENTS

This project is funded by the Western Sydney University Researcher Development Funding in 2015. The authors would like to thank Mr Robert Marshall and all the technical staff of the Structures Laboratory at the Western Sydney University for their assistance with the experimental works.

8. REFERENCES

de Juan, MS & Gutiérrez, PA (2009), 'Study on the influence of attached mortar content on the properties of recycled concrete aggregate', *Construction and Building Materials*, vol. 23, no. 2, pp. 872-7.

Huang, Q (2015), 'Characterisation of Recycled Aggregate Concrete', Bachelor of Engineering (Hons) thesis, Western Sydney University.

Huang, Q, Murphy, T, Tan, EL & Wuhrer, R (2016), 'Characterisation of Recycled Aggregate Concrete Through X-Ray Mapping', *Microscopy and Microanalysis*, vol. 22, no. S3, pp. 124-5.

IS-10262 (2009), *Mix Design M-40 Grade*, Bureau of Indian Standards, viewed 02 Dec 2015 <http://www.engineeringcivil.com/mix-design-m-40-grade.html>.

Kotrayothar, D (2012), 'Recycled aggregate concrete for structural applications', Doctor of Philosophy thesis, University of Western Sydney.

Poon, CS, Shui, ZH & Lam, L (2004), 'Effect of microstructure of ITZ on compressive strength of concrete prepared with recycled aggregates', *Construction and Building Materials*, vol. 18, no. 6, p. 461.

Rahal, K (2007), 'Mechanical properties of concrete with recycled coarse aggregate', *Build. Environ.*, vol. 42, no. 1, pp. 407-15.

Raj, N, Patil, S & Bhattacharjee, B (2014), 'Concrete Mix Design By Packing Density Method', *IOSR Journal of Mechanical and Civil Engineering*, vol. 11, no. 2, pp. 34-46.

RILEM (1992), *Recycling of demolished concrete and masonry : report of Technical Committee 37-DRC, Demolition and Reuse of Concrete*, London, New York : E & FN Spon, London, New York.

Sidorova, A, Vazquez-Ramonich, E, Barra-Bizinotto, M, Roa-Rovira, JJ & Jimenez-Pique, E (2014), 'Study of the recycled aggregates nature's influence on the aggregate-cement paste interface and ITZ.(interfacial transition zone)', *Construction and Building Materials*, vol. 68, p. 677.

Singh, B (2014), 'Integration of sustainable recyled concrete aggregates in steel-concrete composite construction', Bachelor of Engineering (Hons) thesis, University of Western Sydney.

Tam, VWY (2005), 'Recycled aggregate from concrete waste for higher grades of concrete construction', Doctor of Philosophy thesis, City University of Hong Kong.

Wagih, AM, El-Karmoty, HZ, Ebid, M & Okba, SH (2013), 'Recycled construction and demolition concrete waste as aggregate for structural concrete', *HBRC Journal*, vol. 9, no. 3, pp. 193-200.

Wardeh, G, Ghorbel, E & Gomart, H (2015), 'Mix Design and Properties of Recycled Aggregate Concretes: Applicability of Eurocode 2', *International Journal of Concrete Structures and Materials*, vol. 9, no. 1, pp. 1-20.

Xiao, J, Li, J & Zhang, C (2005), 'Mechanical properties of recycled aggregate concrete under uniaxial loading', *Cem. Concr. Res.*, vol. 35, no. 6, pp. 1187-94.

Xiao, J, Li, W & Poon, C (2012), 'Recent studies on mechanical properties of recycled aggregate concrete in China—A review', *Science China Technological Sciences*, vol. 55, no. 6, pp. 1463-80.

Proc. 1st International Conference on Structural Engineering Research (iCSER 2017)
20-22 Nov 2017, Sydney, Australia
ISBN: 978-0-6480147-6-8

Addressing the Durability Issues of Construction Materials using Microstructural Analysis

Shamila Salek[1,2], Laurel George[1], Richard Wuhrer[1], Bijan Samali[2]
[1] Advanced Materials Characterisation Facility (AMCF), Western Sydney University, Sydney, Australia
[2] Centre for Infrastructure Engineering (CIE), Western Sydney University, Sydney, Australia

Corresponding author's E-mail: S.salek@westernsydney.edu.au

Abstract

Different materials and structures are designed for a certain service life. However, integrity and durability of materials particularly, newly-developed or waste materials used in construction to make them environmentally friendly, can affect the performance of structures and the design life. This integrity could be in the materials from the beginning like porous recycled aggregates that may cause pops out in concrete. It also could happen during the service life due to different reasons such as exposure to aggressive environments or fire. Loss of integrity of the anode metal used in cathodic protection of concrete structures is an example of the later mentioned issue. Detecting the mechanism of defect of construction materials used, not only assists to improve the development of better future construction materials, but also assists with the repair of the defects. Microstructural analysis of samples is an effective method to assess the integrity of materials. It is used to determine practical solutions for the repair and remediation. This paper reveals the importance of use of microstructural analysis to evaluate materials used in structures through explanation of examples of the application of scanning electron microscopy (SEM), energy dispersive spectroscopy (EDS), X-ray diffraction (XRD) analysis methods and X-ray mapping (XRM) utilised in diagnosis of the construction materials in service.

***Keywords*:** Microstructural analysis, construction materials integrity, new building materials

1. INTRODUCTION

Characterisation is an essential aspect of materials research that involves the determination of point-to-point variation in composition, structure and microstructure of materials. Understanding the distribution of elements and phases in structures is critical to optimising the performance of all materials (Wuhrer, Moran et al. 2006). Apart from its applications in areas of the science, art, biology, medicine, forensic etc, there are many applications and possibilities for the use of microstructural analysis in the area of engineering materials. In this paper the most common types of instruments used in the microstructural study of building materials, including scanning electron microscopy (SEM), Energy dispersive spectroscopy (EDS), X-ray diffraction (XRD) and X-ray mapping (XRM), are introduced in addition to some examples of their applications in understanding the behaviour of building materials.

2. TECHNIQUES AND EXAMPLES

2.1. Scanning electron microscope with energy dispersive spectroscopy (SEM-EDS)

Scanning electron microscope (SEM) equipped with energy dispersive spectroscopy (EDS) is one of the most useful instruments utilised to study the microstructural analysis of construction materials.

Two signals are measured in the SEM providing different information about the sample, namely, secondary electrons (SE) and back-scattered electrons (BSE). Secondary electron (SE) images provide information about the topography of samples, whereas back-scattered electron (BSE) images contain compositional information that is differentiated by their atomic numbers.

Choice of the detector type for SEM imaging depends on the purpose of the analysis. For example, if the chemical impurity and material defect is of interest in a problem, BSE could be more informative, whereas in case of studying the morphological integrity and investigation of microcracks, SE is of more value. On some occasions, the combination of the two is useful.

Energy dispersive spectrometry (EDS), more commonly known as microanalysis, is also an established technique for the analysis of the chemical composition of materials in a SEM. The EDS detector is mounted in the side of the SEM (Figure 1b), and collects characteristic X-rays emitted during interactions with the SEM electron beam and the sample. This signal is given as a spectrum from which the chemical composition of the sample can be determined and quantified.

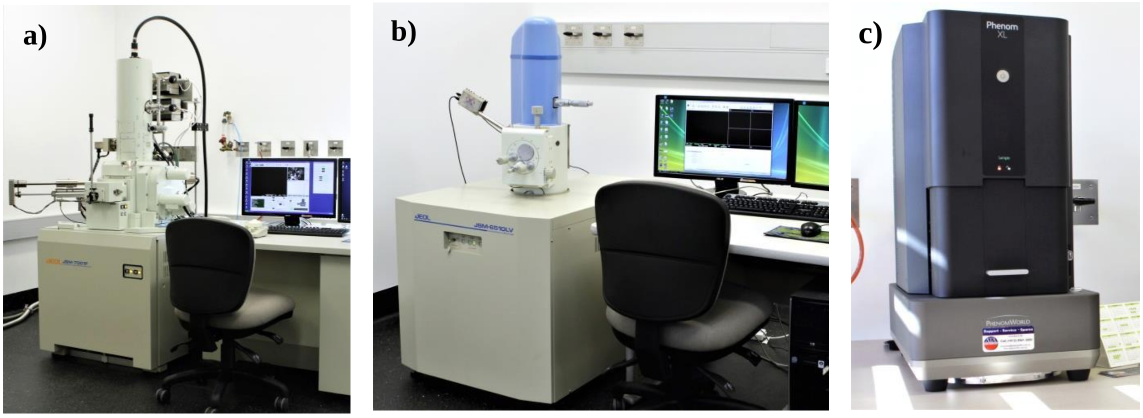

Figure 1. SEM and EDS, a) a JEOL 7001F (high vacuum SEM instrument equipped with Bruker Microanalysis EDS), b) JEOL JSM 6510 equipped with Moran-Amptek Microanalysis-EDS and c) a Phenom XL benchtop SEM/EDS

2.2. Detecting the defects and durability issues in building materials in service

Materials used in construction may have defects or impurity from the beginning or they can be affected by the environments they are exposed to. It may cause an undesirable appearance, not meeting the serviceability requirements and could even cause structural failure. Figure 2 shows some examples of the defects and durability issues in construction materials.

Figures 3(a-c) show a concrete deck that has gone through durability issues. The concrete cover has been degraded and there was no cover left for the reinforcing bars in some areas. Even the reinforcing

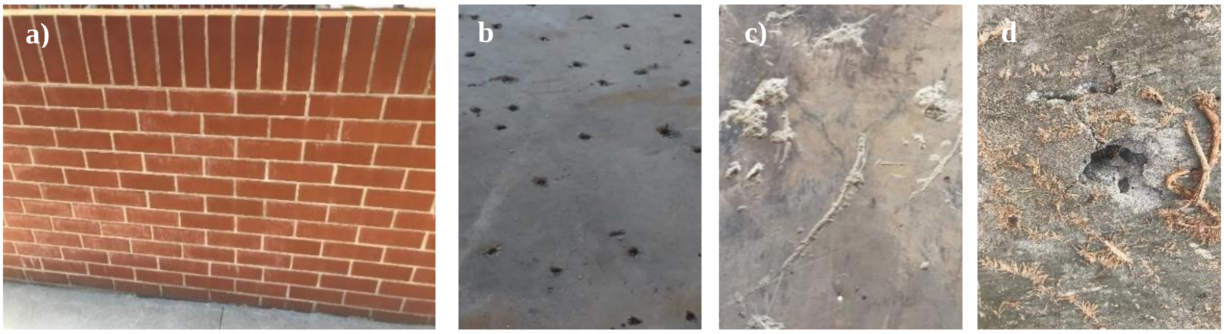

Figure 2. a) Efflorescence defect on brick walls, (b,c) defects in concrete floor and d) reinforced concrete degradation underneath a slab

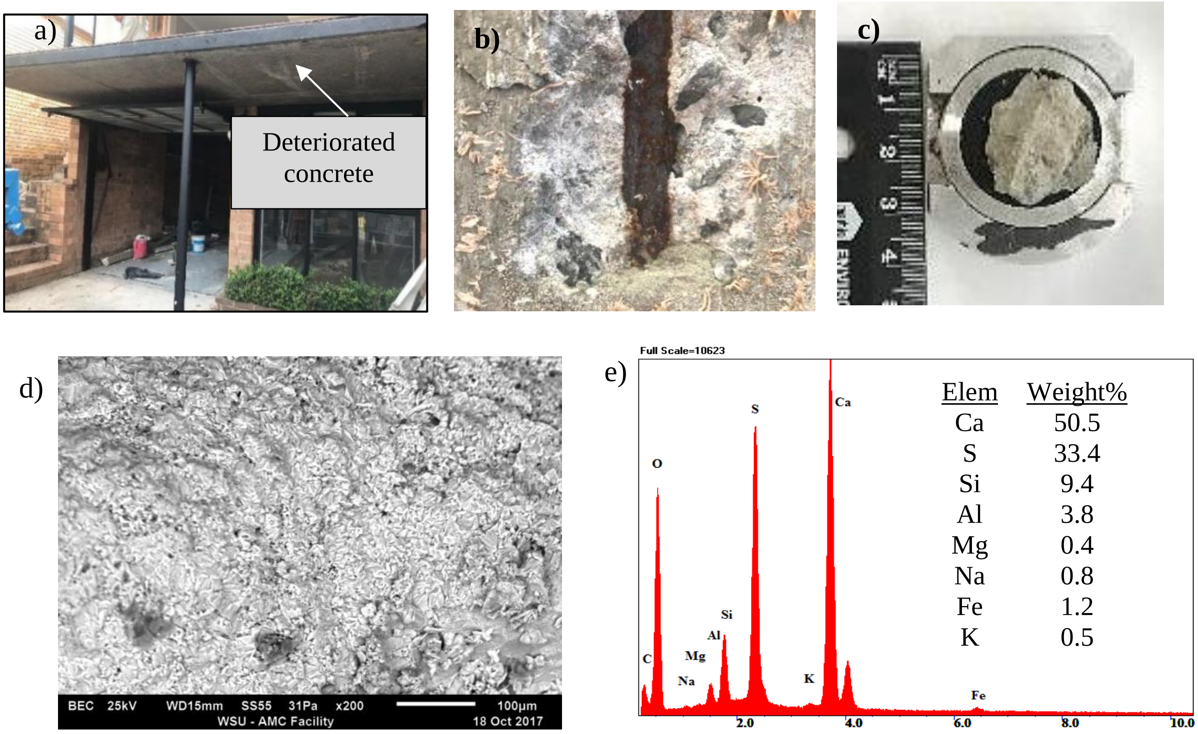

Figure 3. a) Defect under the balcony's reinforced concrete slab, b) corrosion of reinforcing bar and c) mounted sample for SEM/EDS analysis, d) SEM and e) EDS analysis of the deteriorated area of the concrete balcony slab

Bars covered by concrete, had no strength in the structure. To find the reason for this issue, samples were taken from the concrete adjacent to the reinforcing bars. They were examined by SEM and EDS. Figure 3c shows a sample mounted on a SEM stub to investigate the issue.

The results of SEM and EDS analysis are shown in Figure 3d and 3e. As shown, high amounts of sulphur (33.4%, whereas we do not expect more than 2% sulphur in Portland cement) has caused the degradation of concrete cover. Exposure of reinforcement to the air and lack of the protective alkaline layer (concrete) for the reinforcement, led to corrosion of reinforcing bars. This sulphur can come from different sources that is out of the scope of this paper.

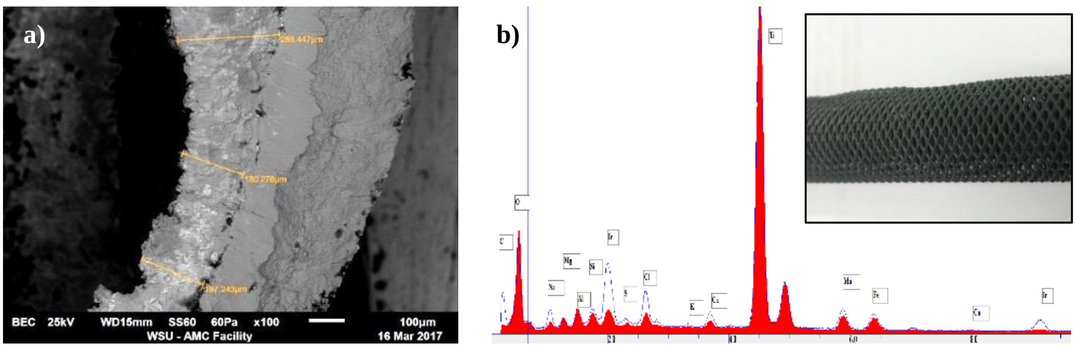

Figure 4. Investigation of a used anode in a cathodic protection system a) SEM image of its thickness and b) EDS analysis of intact and degraded section

Figure 4 shows SEM and EDS analysis of an anode used in cathodic protection of reinforced concrete structures. As shown the integrity of the anode was examined through measuring the thickness of cross section of the sample as well as EDS analysis of different areas (Figure 4b). EDS analysis showed different amounts of Iridium at degraded areas compared to intact areas. Although by optical observation the anode looked sound, from the analysis it was concluded that they needed to be replaced.

2.3. X-ray diffraction (XRD) and its application in building materials study

X-ray diffraction (XRD) is a powerful technique for characterizing crystalline materials that can provide information on crystallinity, phases, preferred crystal orientation, and other structural parameters. X-ray diffraction peaks are produced by constructive interference of a monochromatic beam of x-rays scattered at specific angles from each set of lattice planes in a sample and finally, the phases are identified by searching the standard data base. Figure 5 shows a Bruker XRD instrument and different types of sample preparation for XRD analysis.

Figure 5. a) X-ray diffraction (XRD) instrument and b) sample preparation for the XRD

Depending on the material type, different methods of sample preparation can be used for the XRD analysis. This analysis is very helpful in detecting the new phases resulting from the chemical reactions of corrosive agents to building materials such as concrete.

For example, it is known that Portlandite (Ca $(OH)_2$) in the cement reacts with the sulphur environments such as sewage systems, and forms calcium sulphate (gypsum). XRD reveals phases present in a material, as shown in Figure 6, allowing for the mechanism and sources of deterioration to be identified. In Figure 6, a conventional concrete has been tested before and after exposure to 13% sulphuric acid solution for 4 weeks. Gypsum peaks were observed in the XRD spectra after acid exposure.

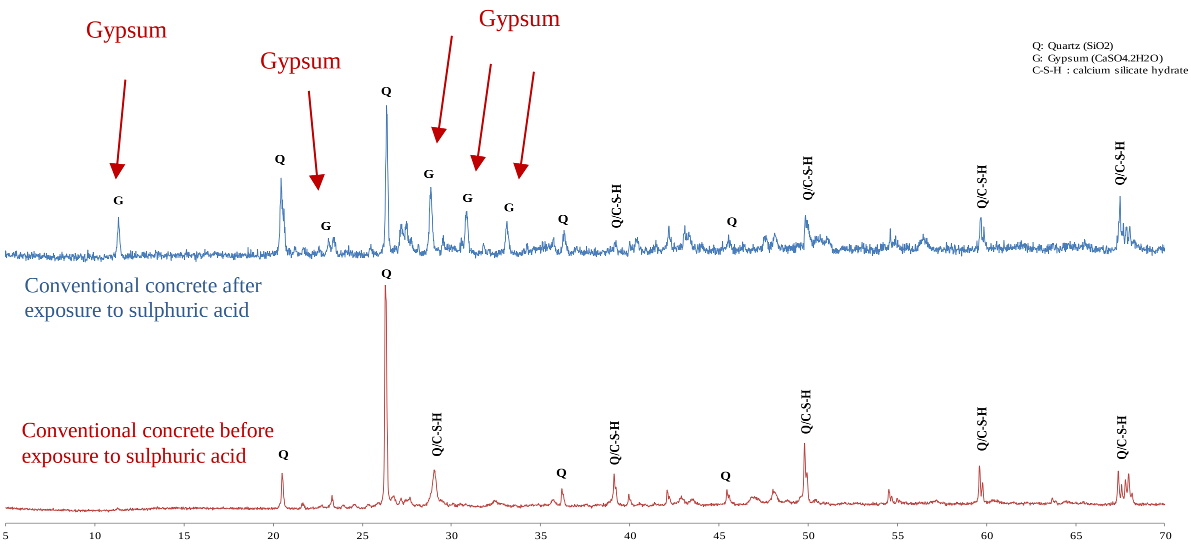

Figure 6. Formation of gypsum in conventional concrete after 4 weeks of exposure to 13% sulphuric acid (Salek, 2016)

Microstructural techniques are also used in the development of new construction material, and can help to predict their performance in real applications (e.g. when subjected to fire). Use of recycled aggregate in concrete, geopolymer or alkali activated concrete and use of wastes like glass and rubber in concrete are few examples of these new materials to move toward more sustainable building materials.

Figure 7 shows the development of phases in a semi geopolymer concrete over time. The sample was mixed and initially analysed by XRD. A new XRD analysis was then performed every hour. Some examples of these analysis are shown in Figure 7 at selected times as an example. As can be seen, phases change over time, some of which are desirable in geopolymer concrete such as muscovite, hematite, kaolinite and zeolite ((Ke, Bernal et al. 2015, Hajimohammadi and van Deventer 2017).

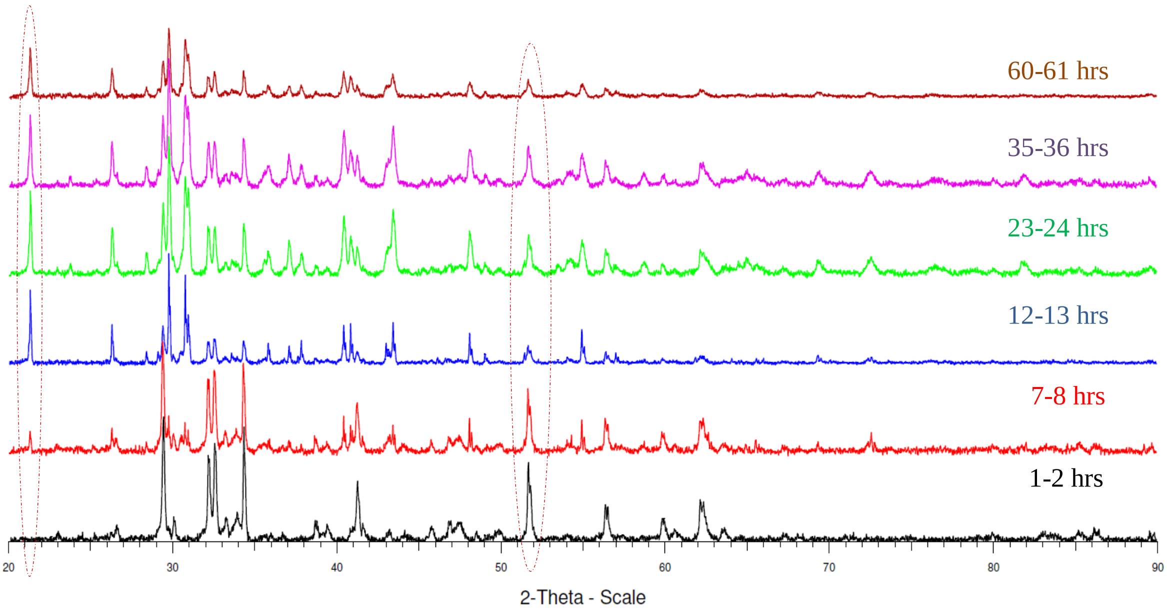

Figure 7. XRD analysis in identification of phases in semi geopolymer concrete starting from the hydration till 3 days every hour.

2.4. X-ray mapping and building materials investigation

X-ray mapping (XRM) is used for identifying the location of individual elements and mapping the spatial distribution of specific elements and phases within a sample (Wuhrer, Moran et al. 2006). Pseudo colouring is a method for determining elemental associations. In this technique, three elemental maps are assigned the colours red, green, and blue (Moran and Wuhrer (2010), (Wuhrer and Moran 2015)). XRM and detecting the distribution of elements in a sample reveals important facts regarding different samples.

Figure 8a shows the super probe used for this purpose and Figure 8b shows a sample prepared for the XRM. Figure 8c shows an example of pseudo colour image of interface of a concrete sample after exposure to sulphuric acid as an example. In this image where is red is rich with sulphur, where is blue has higher silica and the area which is yellow (between red and green based on the scale bar below the image) is a phase containing both calcium and sulphur (Salek 2016).

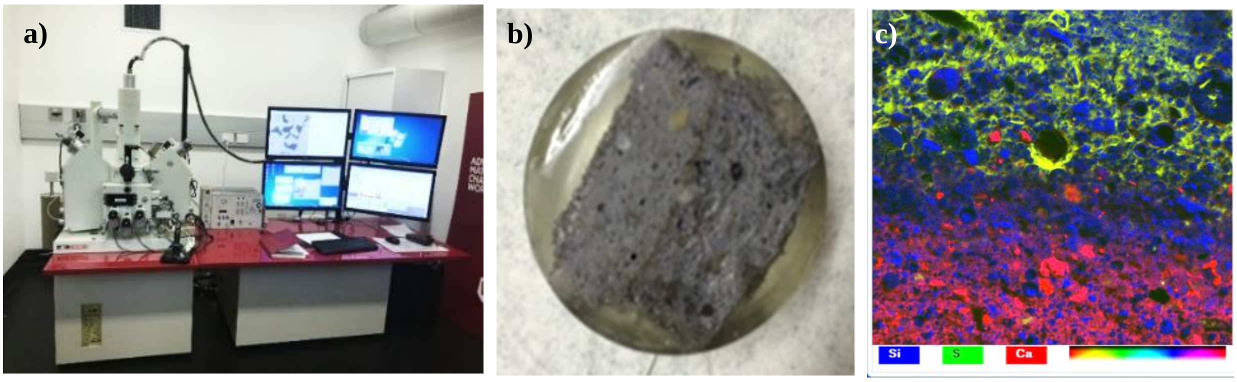

Figure 8. a) A JEOL JXA-8600 super probe used for X-ray mapping, b) a prepared sample for XRM analysis and c) Pseudo colour image from a concrete sample exposed to sulphuric acid.

3. CONCLUSION

Microstructural analysis has an extensive application in the identification of reasons for durability issues or defects in building construction materials. It is also beneficial in the development of new construction materials by investigation of their microstructure and prediction of their behaviour when subjected to different conditions, such as fire or exposure to harsh environments.

SEM equipped with the EDS and XRD analysis are the most commonly used methods for microanalsyis. The combined use of these techniques provides a powerful, complimentary assessment of construction materials.

4. ACKNOWLEDGMENTS

The authors would like to acknowledge the support of Advanced Materials Characterisation Facility (AMCF) and the Centre for Infrastructure Engineering at Western Sydney University (CIE). We would also like to thank Ms. Mahya Askarian and Mr. Michael van Koeverden for use of their data and photos in this paper.

5. REFERENCES

Hajimohammadi, A. and J. S. J. van Deventer (2017). "Characterisation of One-Part Geopolymer Binders Made from Fly Ash." Waste and Biomass Valorization 8(1): 225-233.

Ke, X., S. A. Bernal, N. Ye, J. L. Provis and J. Yang (2015). "One-Part Geopolymers Based on Thermally Treated Red Mud/NaOH Blends." Journal of the American Ceramic Society 98(1): 5-11.

Moran, K. and R. Wuhrer (2010). "Post processing of X-ray mpas-Theortical BSE mapping,Totals mapping and ratio mapping." Microsc.Microanal 16(suppl 2): 940-941.

Salek, S. (2016). Mechanical, structural and microstructural investigations of a novel concrete for special structural applications. PhD, Western Sydney University.

Wuhrer, R. and K. Moran (2015) "Low voltage imaging and X-ray microanalysis in the SEM: challenges and opportunities." EMAS 2015 workshop 109.

Wuhrer, R., K. Moran and L. Moran (2006). "Charactrisation of materials through X-ray mapping." Materials forum 30: 63-70.

Proc. 1st International Conference on Structural Engineering Research (iCSER 2017)
20-22 Nov 2017, Sydney, Australia
ISBN: 978-0-6480147-6-8

Structural Performance of Novel Concrete in Beam-Column Joints

Shamila Salek[1,2], Bijan Samali[1], Richard Wuhrer[2], Georgius Adam[3]

[1] Centre for Infrastructure Engineering (CIE), Western Sydney University, Sydney, Australia
[2] Advanced Materials Charactrisation Facility (AMCF), Western Sydney University, Sydney, Australia
[3] Parchem for Construction Co/Dulux group, Sydney, Australia

Corresponding author's E-mail: s.salek@westernsydney.edu.au

Abstract

Beam-column joints are critical regions in reinforced concrete structures which require proper design approach to lead to ductile behaviour instead of a brittle one and increase resilience and energy absorption capacity of structures particularly during earthquakes. For this purpose, the amount of steel reinforcement in this region has usually high density, particularly the number of stirrups as transverse reinforcement are increased to provide the desired ductility required by different design codes. However, the use of large amounts of reinforcement is associated with difficulties regarding concrete pouring and vibration of fresh concrete. The lack of full concrete penetration into the joint region causes porosity and formation of voids and honey comb in concrete at this critical region. To address this problem extensive studies have been conducted to evaluate and improve structural performance of beam-column connections. This paper is part of an ongoing research in this area through experimental testing of a novel concrete in beam-column joint specimens and a conventional concrete for comparison. To evaluate the behaviour of these beam-column joints, failure mode, crack at the failure, load-deflection behaviour and ultimate load capacity of the subassemblies were investigated according to the data obtained from the experiments. The novel concrete tested in this research showed better performance in terms of failure mode, crack propagation and ultimate load capacity.

Keywords: Beam-column joints, Novel concrete, Crack pattern, Ultimate load capacity

1. INTRODUCTION

Beam–column connection, as a major structural sub-assemblage in reinforced concrete (RC) moment-resisting frame structures, plays a very crucial role during severe loading events such as earthquakes. Furthermore, the well-known design philosophy of strong-column weak-beam only works properly if this component of RC structures performs as intended without brittle failure (Eslamihassanabadi (2013)). To evaluate the performance of beam–column connections during earthquakes, most previous researchers have used cyclic loading tests, focusing on energy dissipation capacity of different types of joints (Durrani and Wight 1985, Joshi, Murty et al. 2005, Nie, Bai et al. 2008), Corinaldesi, Letelier et al. (2011), (Letelier and Moriconi 2014, Ruiz-Pinilla, Pallares et al. 2014, Metelli, Messali et al. 2015). Joshi, Murty et al. (2005) investigated four full-scale beam–column joints under cyclic loading in order to identify a suitable technique for connecting precast beam and column components. Durrani and Wight (1985) reported the results of an experimental investigation on the performance of a beam–column joint under earthquake-type loading. Nie, Bai et al. (2008) tested six beam–column joints for proposing a new connection system for concrete filled steel tube composite column and RC beams.

There are numerous studies available on retrofitting the beam-column joints by use of different methods such as FRP composites (Geng, Chajes et al. 1998, El-Amoury and Ghobarah 2002, Mukherjee and Joshi 2005), Eslamihassanabadi (2013), which emphasized the importance of appropriate performance of this structural component. This paper investigates the use of a type of new concrete in these RC joints and compares it to conventional concrete under same cyclic loading and test set up.

2. EXPERIMENTAL WORK

2.1. Materials

Two types of reinforced concrete (RC) beam-column joins were tested. First series were made of conventional concrete (CC) and the second series were made of a new concrete (ARC). CC was supplied by Concrite Pty Ltd, NSW Australia. It had 28-day compressive strength of 40 MPa and comprised 350 kg/m^3 cement, 150 kg/m^3 fly ash, 960 kg/m^3 coarse and 661 kg/m^3 fine aggregates and 2.3 litre/m^3 water reducing admixtures (Pozz 80 from BASF the Chemical Company). The cement and fly ash used in CC were shrinkage limited Portland cement and low calcium fly ash (type F). The coarse aggregates had maximum size of 10 mm and were sourced from Dunmore Quarry, NSW, Australia and fine aggregates included 600 kg/m^3 of Nepean river sand and 150 kg/m^3 of Kurnell sand. The slump of the concrete was 140 mm and it had the density and air content of 2,360 kg/m^3 and 1.0 % respectively.

The newly developed concrete (ARC), was prepared in the laboratory. It consisted of a durable binder under commercial name of Renderoc-G (Salek, Samali et al. (2015)) from Parchem, Australia, and the same coarse aggregate and same admixtures as used in CC. Its 28-day compressive strength was 31 MPa, the ratio of course to fine aggregate was 0.5, and water to binder ratio was 0.4. It had a slump of 140 mm and density and air content of 2,150 kg/m^3 and 0.8 % respectively.

2.2. Test procedure

The geometry and reinforcement arrangement in the specimens and schematic test set up are presented in Figure 1a and 1b, respectively. The specimens were tested in a 2D testing rig as shown in Figure 1a,1b and 1c. The top and bottom supports of the column were hinged using pins.

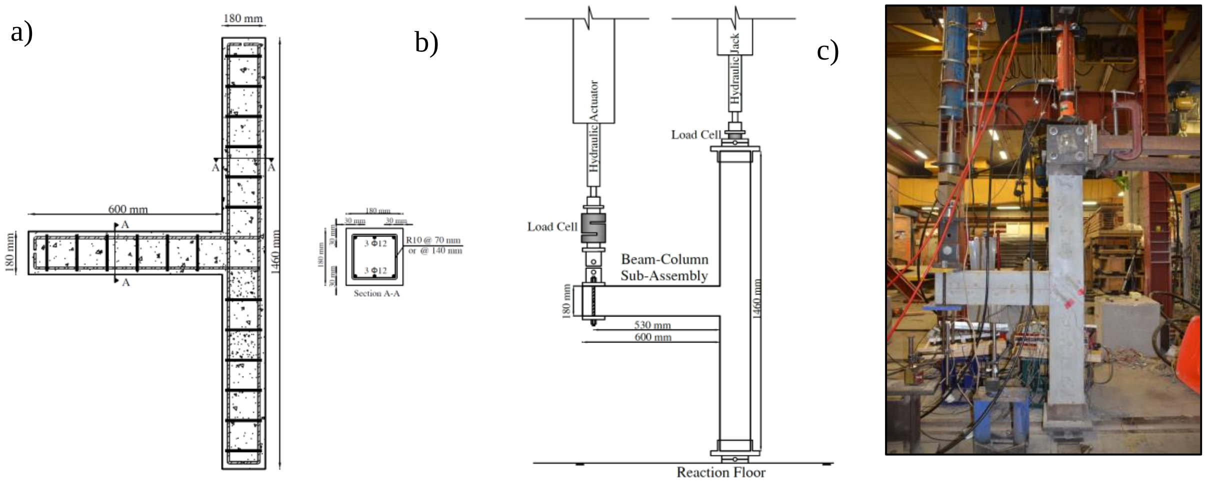

Figure 1. a) Specimens details and reinforcement for beam-column joints used in the experiments b) Schematic test set-up for beam-column joints and c) Actual test set-up for beam-column joints

The load at the tip of the beam, increased with the increments of 0.25kN/s in all cycles till failure (Figure 2). Failure modes, crack patterns at the failure and ultimate load capacity of these subassemblies were evaluated and compared to the CC.

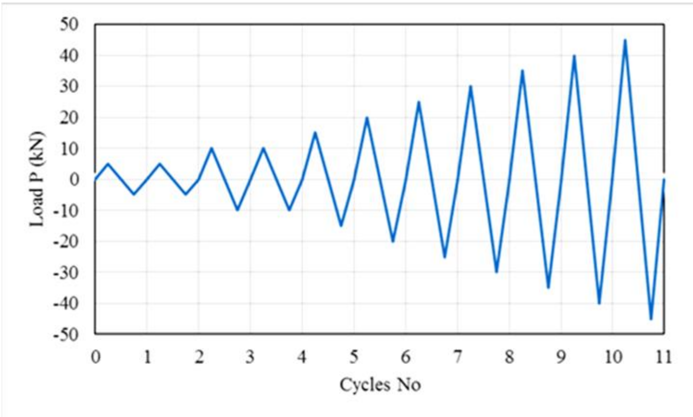

Figure 2. Load pattern in cyclic test of beam-column joints

The first series of specimens were cast with CC and the second and third series were made of ARC. The spacing between the transverse reinforcing bars at the joint in the CC-70mm and ARC-70 mm specimens was 70 mm, and in the third series of specimens, this spacing was 140 mm.

2.3. Results and discussion

2.3.1. Failure mode and cracking

The crack patterns of the three types of specimens at failure are presented in Figure 3. It was observed that at the latest cycle of loading, specimen CC-70 mm was not capable of completing the cycle and the crack widening occurred between beam and column rapidly and the cracks in joint grew dramatically toward the columns and the sample failed by yielding and then, the reinforcing bar in joint section ruptured. Many cracks were observable in joint and column for this specimen.

The specimens ARC-70 mm and ARC-140 mm could complete the last cycle at 40 kN but they could not proceed further to the next cycle. In both samples, the cracks widened in section between beam and column and the cracks in the joint area grew intensely, particularly, the ones in the column. These two specimens also failed by yielding of the reinforcing bars in joint section followed by their rupture.

CC-70 mm ARC-70 mm ARC- 140 mm

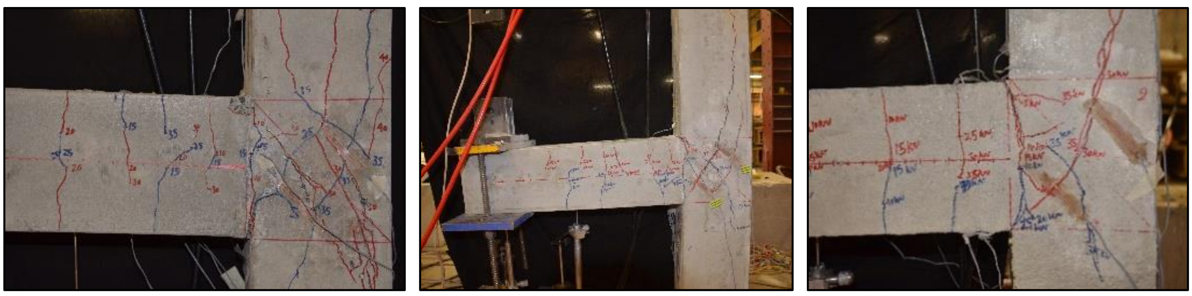

Figure 3. Crack pattern in joint specimens at failure

2.3.2. Load-deflection and ultimate load

Load versus beam tip displacement curves for beam-column subassemblies are shown in Figures 4 to 6. Regardless of the spacing of the transverse bars, ARC specimens showed stiffer behaviour under cyclic load tests as they have closer hysteresis loops in comparison with CC specimens. This is shown in both Figures 4 and 5.

Between the two ARC samples with 70 mm and 140 mm spacing in stirrups, the ARC 70 mm showed stiffer behaviour and had closed hysteresis loops. However, comparing the behaviour of CC-70 mm and ARC-140 mm (Figure 5) reveals that ARC 140 was still stiffer than CC-70 mm. In terms of peak load, specimen ARC-70 mm reached 46.5 kN at the end of 40 kN load cycle while the specimen CC-70 mm could not complete this loop and the ultimate load in this sample was 39.9 kN.

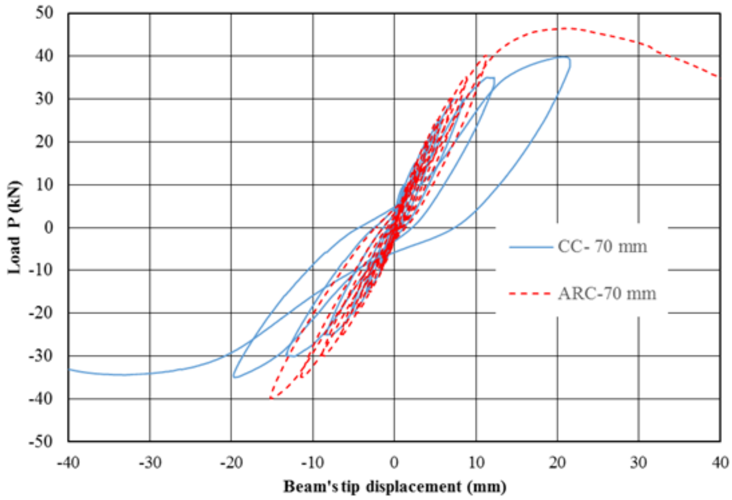

Figure 4. Load versus beam's tip displacement in cyclic load test of beam-column joints for CC versus ARC with 70 mm spacing (CC-70 mm) in the stirrups

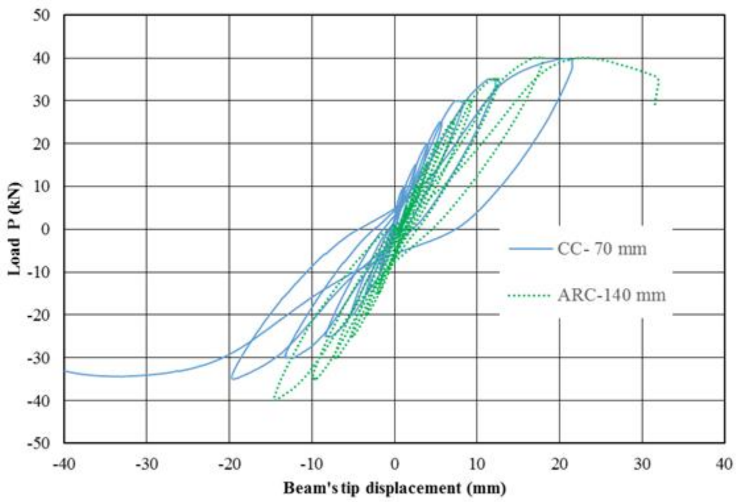

Figure 5. Load versus beam's tip displacement in cyclic load test of beam-column joints for CC-70 mm and ARC with 140 mm spacing between the stirrups

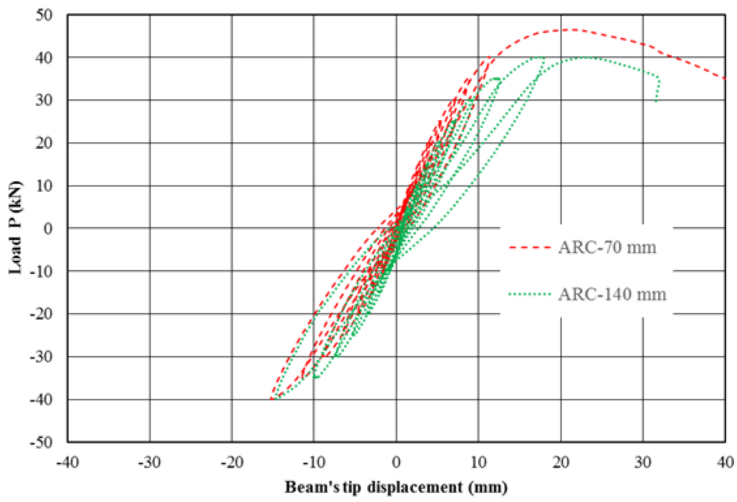

Figure 6. Load versus beam's tip displacement in cyclic load test of beam-column joints for ARC with 70mm vs 140mm spacing between the stirrups

In terms of the ultimate load, the load capacity of beam-column joint increased by 16 % when using ARC materials instead of conventional concrete in the same samples in terms of reinforcement arrangement. In addition, the peak load was not affected by increasing stirrups spacing twice when the ARC material was used. Larger stirrup spacing using ARC joints will save time and material without compromising the seismic capacity of the joint.

3. CONCLUSION

Two types of concrete were tested in RC beam-column joints with same arrangements of reinforcement and less transverse reinforcing bars. The tip of the beams was loaded cyclically and their structural performance including the crack location, load-deflection at the tip of the beam and the ultimate load capacity were investigated. Results revealed;

- The specimens ARC-70 mm and ARC-140 mm could complete more loading cycles compared to the CC-70 mm.
- ARC specimens showed stiffer behaviour under cyclic load test in comparison with CC specimens even after reduction of the transverse reinforcing bars at the joints by 50%.
- The ultimate load capacity of joints constructed with ARC material was higher than the same sample cast by conventional concrete.

However, more study is recommended in this regard before using this concrete in major structural applications.

4. ACKNOWLEDGMENTS

The authors would like to acknowledge the support of Advanced Materials Charactrisation Facility [AMCF] at Western Sydney University, the Centre for Infrastructure Engineering [CIE] at Western Sydney University, Structures laboratory at University of Technology [UTS] and Parchem for Construction Co/Dulux group, Australia.

5. REFERENCES

Corinaldesi, V., V. Letelier and G. Moriconi (2011). "Behaviour of recycled-aggregate concrete under cyclic loading." Constr Build Mater 25(4): 1877–1882.

Durrani, A. J. and J. K. Wight (1985). "Behaviour of interior beam-to-column connections under earthquake-type loading." ACI Journal 82(3): 343-349.

El-Amoury, T. and A. Ghobarah (2002). "Seismic rehabilitation of beam–column joint using GFRP sheets." Engineering Structures 24(11): 1397-1407.

Eslamihassanabadi, A. (2013). Investigating the earthquake performance of FRP strengthened reinforced concrete structures. Doctor of Philosophy, University of Queensland.

Geng, Z., M. Chajes, T. Chou and D. Pan (1998). "The retrofitting of reinforced concrete column-to-beam connections." Composites Science and Technology 58(8): 1297-1305.

Joshi, M. K., C. V. R. Murty and M. P. Jaisingh (2005). "Cyclic behaviour of precast RC connections." Indian Concrete Journal 79(11): 43–50.

Letelier, V. and G. Moriconi (2014). "The influence of recycled concrete aggregates on the behavior of beam–column joints under cyclic loading. ." Eng Struct 60: 148-154.

Metelli, G., F. Messali, C. Beschi and P. Riva (2015). "A model for beam–column corner joints of exiting RC frame subjected to cyclic loading’. ." Eng Struct 89: 79-92.

Mukherjee, A. and M. K. Joshi (2005). "FRPC reinforced concrete beam-column joints under cyclic excitation." Composite Structures 70(2): 185-199.

Nie, J., Y. Bai and C. Cai (2008). "New connection system for confined concrete columns and beams. I: Experimental study." J Struct Eng, ASCE 134(12): 1787–1799.

Ruiz-Pinilla, J., F. Pallares, E. Gimenez and P. Calderon (2014). "Ruiz-Pinilla JG, Pallares FJ, Gimenez E, Calderon PA. Experimental tests on retrofitted RC beam–column joints under designed to seismic loads. General Approach." Eng Struct 59(702-14).

Salek, S., B. Samali, V. Sirivivatnanon and G. Adam (2015). Development Of An Acid Resistant Concrete. Concrete 2015, Melbourne, Australia.

Proc. 1st International Conference on Structural Engineering Research (iCSER 2017)
20-22 Nov 2017, Sydney, Australia
ISBN: 978-0-6480147-6-8

Effect of Seasonal Weather on the Properties of Geopolymer Mortar

Balbir Singh[1], Zhu Pan[2], Ee Loon Tan[3], Olivia Mirza[3] and Youtam Mamo[4]
[1]Ph.D Student of Civil Engineering, Western Sydney University
[2]Post Doctorate Researcher, Western Sydney University
[3]Lecturer, Western Sydney University
[4]Undergraduate Student, Western Sydney University
Corresponding author's E-mail: balbir.singh@westernsydney.edu.au

Abstract

Despite proven to exhibit excellent mechanical properties, fresh geopolymer paste is highly viscous and displays low workability, which has become a major obstacle for it to be widely accepted for larger structural application. For cast-in-place applications, geopolymer concrete requires to be cured at ambient temperatures. Temperature and humidity varies in different seasons. The humidity variation has been found to have influence on the occurrence of white efflorescence on geopolymer samples. However, effects of temperature on efflorescence have received little attention, although temperature effects on strength are well-known. This paper will investigate the effect of a change in seasonal temperature on the properties of geopolymer mortars. The investigated properties include workability, compressive strength and efflorescence. Mini slump tests method will be carried out to determine the effect of adding extra water and commercially available superplasticisers (SP) on the flowability of geopolymer mortar. From the obtained test results, it was found that SIKA Visco Crete PC HRF – 2 has achieved the highest relative slump as compared to the reference mix RM8. Regarding strength development, it was observed those samples cured in hot (summer) conditions are more desirable to cure geopolymer mortar. Also, specimens cured under lower temperature curing conditions and low in humidity had formed white efflorescence after 7 days curing period, and rapid growth was observed over the period of 28 days curing cycle.

Keywords*:* Fly-ash, Geopolymer mortar, Seasonal weather, Workability, Compressive strength.

1. INTRODUCTION

Among the heavy consumer of natural resources and emitter of carbon dioxide (CO_2) into the atmosphere, the cement industry is one of the leading culprit of anthropogenic climate change emissions. World-wide, the production of cement contributes at least 5-7% of CO_2 emission (Turner and Collins (2013) and Kajaste and Hurme (2016), whereas, in Australia, production of cement accounts for approximately 1.3% of CO_2 emission Williams, McLellan et al. (2011).Thus, to tackle the presented situation, one suitable solution is to utilise fly ash based geopolymer concrete (GPC) that has proved to totally replace the usage of cement in the concrete industry Nuruddin and Malkawi et al. (2016).

According to research conducted by Albitar and Visintin et al. (2015) confirms that GPC exhibits excellent compressive strength, suffers very low drying shrinkage, resistance to sulphate attack and good acid resistance. However, fresh geopolymer concrete is very cohesive and displays poor workability Jindal et al. (2017). Nonetheless, to improve the workability, research conducted by Nematollahi, Sanjayan et.al (20114) observed that the addition of superplasticizer had a positive effect and increased the flowability of the geopolymer paste. Due to high alkality, superplasticizer does not work in fresh geopolymers as effectively as in fresh cement pastes. One potential solution is to add superplasticizer with extra water to improve its performance. Furthermore, another issue that has been overlooked in the research community is the occurrence of white efflorescence, and its effect on the properties of GPC cured at lower ambient temperatures. Research conducted by Zhang, Yang et al.

(2016) revealed that sample cured at room temperature of 20±5°C exhibited rapid occurrence of white efflorescence when exposed to humid conditions and efflorescence had a negative impact on compressive strength. However, there is very limited information about the subsequent occurrence of efflorescence and its effect on GPC when subject to a lower temperature during winter season and effect of a rapid change in humidity. Therefore, the aim of this study is to investigate the effect of the change in seasonal weather (temperature and humidity) on the properties of geopolymer and occurrence of white efflorescence and its influences on the properties of geopolymer mortar. Also, to investigate the effect of adding extra water and commercially available superplasticisers has on the flowability of the GPC mortar.

2. EXPERIMENTAL PROGRAM

2.1. Dry components

2.1.1. Supplementary cementitous material

The primary binder used for geopolymer mortar for the purpose of this research is fly ash. Also, grounded blasted furnace slag (GBFS) was utilised as an additive for fly ash based GPC.
The fly ash used is a low calcium Class-F fly ash obtained from Coal Power Plant in Queensland, Australia. The grounded slag used is provided by Australian Builders. The binder ratio of 90% fly ash content and 10 % slag was used. The chemical composition of fly ash and slag is presented in Table 1.

Table 1. Chemical composition of Fly Ash and Slag.

Material	SiO_2	Al_2O_3	Fe_2O_3	CaO	Na_2O	MgO	K_2O	SO_3	LOI
Fly Ash	52.2	24.0	13.7	3.18	0.65	1.32	0.78	0.18	1.08
Slag	32.6	13.4	0.35	43.0	0.20	5.5	0.25	3.41	0.14

2.1.2. Fine aggregates

The aggregates used for geopolymer mortar consisted of fine aggregates. The fine aggregates are Nepean River sand and are used by the local construction industry to prepare conventional mortar. For geopolymer mortar design ratio of binder to fine aggregate was 2:1.

2.2. Liquid Components

2.2.1 Alkaline Solution

The alkaline solution used to activate the binder content is a combination of sodium hydroxide (NaOH) and sodium silicate solution (Na_2SiO_3). The ratio of sodium hydroxide solution to Sodium silicate solution by mass is taken to be 2.5. The sodium silicate solution used is commercially available D-grade with SiO_2 to Na2O ratio of 2.0, that is the solution was comprised of 55.9% of water and 44.1% of sodium silicate (Na2O =14.7% and SiO_2 = 29.4%). For the purpose of this research, various NaOH concentrations are used to prepare an alkaline solution which includes 8M, 10M, 12M and 14M.

2.2.2. Superplasticisers (SPs)

A total of five commercially available superplasticisers were used to improve the workability of geopolymer concrete. To determine the most optimum SPs for geopolymer mortar various types of brands were used. Details of different SPs is provided in Table 2.

2.3. Mixture Proportions

To study the flowability of geopolymer mortar numerous mix design were prepared to incorporate different alterations such as NaOH molarity, a various brand of SPs and different combination dosage of superplasticisers and extra water. One reference mix for different NaOH concentration was prepared without the presence of SP and extra water. In addition to that, a mix design that has achieved the best relative slump value will be selected for cylinder testing. Mixture proportions are given in Table 2 and 3 for mini slump test and cylinder test, respectively.

2.4. Preparation of test specimens

To prepare the mortar, alkaline solution was prepared 24 hours before mixing. The alkaline solution was added during mortar mixing using a unique 50:50 method. Firstly, the dry component was mixed thoroughly, and 50 percent of alkaline solution was added to the mixing bowl and mixed for one minute. Followed by 50 percent of SPs into the mix and mixed for another thirty seconds. Next, rest of the alkaline solution and SPs was poured into the mixing bowl and mixed for one minute. Extra water was added at last if required and mixed for another two minutes.

2.5. Experimental Tests

2.5.1. Mini Slump Test

For mini slump test, three different sets of test were carried out to examine the flowability of the geopolymer mortar. First sets were carried out to determine the best commercially available SPs. Second test were carried out to determine the effect of SPs with extra water. Finally, the third set of test was carried out to determine the effect of extra water on the flowability of the mortar without the presence of SP.

2.5.2. Curing conditions for Compression Test

To study the effect of the change in seasonal temperature and humidity on strength development of geopolymer paste various for curing environment was adopted. To simulate realistic data, a mean maximum for hot season and a mean mini temperature for cold season were chosen for this research. Based on 21 years of past records from Bureau of Meteorology (2017), weather data for Kingswood, Sydney was studied. It was found that the average cold (winter) temperatures were 10-11 degree Celsius and the hot (summer) temperature conditions were 25-26 degree Celsius. Furthermore, to develop a high humidity curing environment, a method employed by Zhang, Yang et al. (2016) was used, where test samples were wrapped in a thin plastic sheet, submerged under water and kept at their relative cold and hot weather curing conditions until the testing day. Thus, cylinder test sample was cured under these four curing conditions.

2.6. Testing of Specimens

Mini Slump test is also known as the spread-flow test were conducted to determine the flowability of geopolymer mortar Nematollahi, Sanjayan et.al (2017). A freshly mixed mortar was poured into the cylindrical mould (top diameter of 20 cm, a bottom diameter of 38 cm and a length of 55 cm) and tampered with tamper rod. The excessive mortar was removed from the top surface and mould was lifted vertically, allowing the mortar to flow outwards in a circular pattern as shown in Figure 1. Three specimens were poured per mix design, and four perpendicular diameters on the dried mortar spread were measured as shown in Figure 2. The relative slump was calculated by the following equation:

$$\mathrm{r_p} = \left(\frac{d}{d_o}\right)^2 - 1 \tag{1}$$

Where, $\mathrm{r_p}$ = relative slump; d = average measured diameter; d_o = bottom diameter of the cylindrical cone.

The cylinders for compression test were prepared according to guidelines specified in standard RILEM 129-MHT (1995), where the specimen shall be cylindrical with length to diameter ratio between 3 and 4. Hence, the dimension of specimens is 30 mm diameter and 95 mm in length. Instron Universal testing machine with a 1000kN capacity was used to determine the compressive strength. The Compression test was performed in accordance with Australian Standard 1012.8.1:2014 (2006).

Figure 1. Fresh Mini Slump Test Sample.

Figure 2. Four Diameters on Dried Sample.

Table 2. Geopolymer Mix designs for Mini Slump Test.

<table>
<tr><th rowspan="2">Test Set No.</th><th rowspan="2">Test Objective</th><th rowspan="2">Mix ID</th><th colspan="4">Mix Proportions (g)</th><th rowspan="2">NaOH (M)</th><th rowspan="2">SP (%)</th><th rowspan="2">Extra water (%)</th><th rowspan="2">Different SP Brands</th></tr>
<tr><th>Fly Ash</th><th>Slag</th><th>Sand</th><th>Alkaline Solution</th></tr>
<tr><td rowspan="6">Set 1</td><td rowspan="6">Most Effective SPs</td><td>RM8</td><td rowspan="19">270</td><td rowspan="19">30</td><td rowspan="19">150</td><td rowspan="19">135</td><td rowspan="6">8</td><td>0</td><td>0</td><td>N/A</td></tr>
<tr><td>SPM1</td><td rowspan="5">6</td><td rowspan="5">0</td><td>MasterGlenium Sky 8100</td></tr>
<tr><td>SPM2</td><td>Superplastet-F</td></tr>
<tr><td>SPM3</td><td>MasterRheoBuild 1000</td></tr>
<tr><td>SPM4</td><td>SIKA Visco Crete PC HRF-2</td></tr>
<tr><td>SPM5</td><td>BASF HRL-0123</td></tr>
<tr><td rowspan="7">Set 2</td><td rowspan="7">The effect of SP and Extra water</td><td>RM10</td><td>10</td><td>0</td><td>0</td><td>N/A</td></tr>
<tr><td>8M1</td><td rowspan="3">8</td><td>1</td><td>6</td><td rowspan="6">SIKA Visco Crete PC HRF-2</td></tr>
<tr><td>8M2</td><td>4</td><td>6</td></tr>
<tr><td>8M3</td><td>3</td><td>3</td></tr>
<tr><td>10M1</td><td rowspan="3">10</td><td>1</td><td>6</td></tr>
<tr><td>10M2</td><td>2</td><td>9</td></tr>
<tr><td>10M3</td><td>1</td><td>10</td></tr>
<tr><td rowspan="6">Set 3</td><td rowspan="6">The effect of extra water only</td><td>8EW-M1</td><td rowspan="6">8</td><td>0</td><td>1</td><td rowspan="6">N/A</td></tr>
<tr><td>8EW-M2</td><td>0</td><td>3</td></tr>
<tr><td>8EW-M3</td><td>0</td><td>5</td></tr>
<tr><td>8EW-M4</td><td>0</td><td>6</td></tr>
<tr><td>8EW-M5</td><td>0</td><td>7</td></tr>
<tr><td>8EW-M6</td><td>0</td><td>10</td></tr>
</table>

		10EW-M1					10	0	3	
		10EW-M2						0	6	
		10EW-M3						0	10	
		10EW-M4						0	11	
		10EW-M5						0	12	

Table 3. Mini Cylinder Test Specimens.

Mix ID	Mix Proportion (g)				NaOH (M)	SP and Extra water dosage (%)	Specimen Dimensions (mm)	Curing Temperature Environment
	Fly Ash	Slag	Sand	Alkaline Solution				
10M2-C	2000	220	1100	990	10	2:9	95 x 30	10-11 Celsius Degree (Cold)
10M2-CW								10-11 Celsius Degree Water Bath (High Humidity)
10M2-H								25-26 Celsius Degree (Hot)
10M2-HW								25-26 Celsius Degree Water Bath (High Humidity)

3. RESULT AND DISCUSSION

3.1. Mini Slump Test

3.1.1. Best Commercially Available Superplasticiser

To ensure consistency with all the five mixes, the dosage of SPs and concentration of NaOH in alkaline solution was kept constant. The result of the relative slump and percentage increase are presented in Figure 3. It was observed that all the SPs had a positive effect on the workability of geopolymer mortar since all the SPs had improved the flowability of mortar in comparison to reference mix RM8. Mix design SPM3 consists of SIKA Visco Crete PC HRF – 2 has achieved the highest relative slump diameter of 12.59 cm and 70 % increase in the relative slump as compared to reference mix. Therefore, SIKA Visco Crete PC HRF – 2 will be used for rest of the geopolymer mortar mix designs.

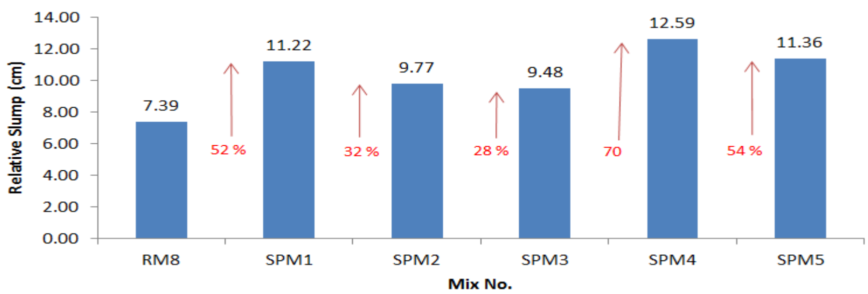

Figure 3. Relative Slump increase for most effective superplasticisers.

3.1.2. Effect of Superplasticisers and Extra Water combination on Workability

From the obtained test results, it was observed that specimens had experienced a reduction of flowability in geopolymer mortar when molarity of NaOH in alkaline solution was increased. Specimens with 12M alkaline solution had very low flowability and less setting time, therefore, the mortar dried within the mini cylindrical mould right after pouring the geopolymer mortar and no flowability was observed. Similarly, the test results for specimens with 14M alkaline solution had no flowability and zero setting time because the paste had dried with the mixing bowl.

However, the test results for alkaline solution comprised of 8M and 10M of NaOH observed good flowability in geopolymer mortar. As shown in Figure 4, mix deigns 8M2 comprised of SP and EW ratio of 4:6 has achieved 14.83 cm with 101% increase in the relative slump as compared to reference mix RM8. Furthermore, for specimens comprised of a 10M alkaline solution, mix design 10M2 with SP and EW ratio of 2:9 has achieved the highest relative slump of 17.97 cm with 113 % increase in the relative slump as compared to reference mix R10M. Overall, it was observed that increasing the dosage of SP while retaining constant water dosage yield less change in the relative slump as compare to increasing water dosage and retaining constant SP dosage.

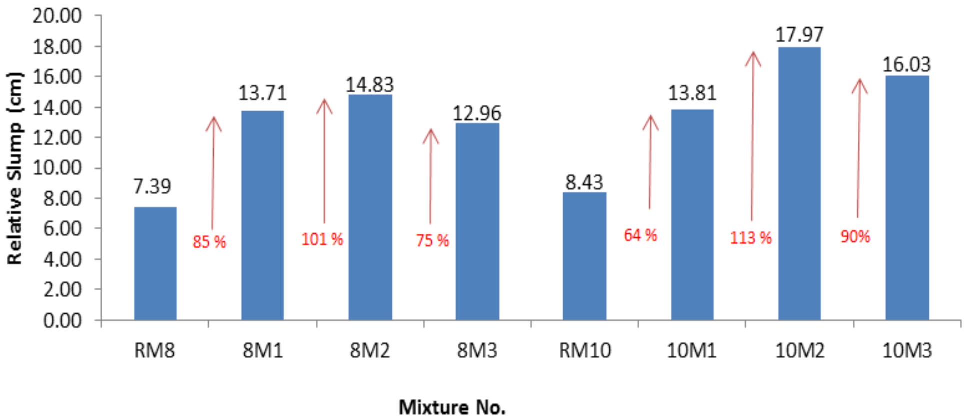

Figure 4. Relative slump increase for SP and Extra water.

3.1.3. Effect of Extra Water on Workability

The obtained test results revealed that in comparison to reference mix, the addition of extra water had a positive impact on the flowability. However, once an optimum level was achieved then increase of EW dosage had a negative impact. As seen in Figure 5, it can be observed that for 8M specimens mix design 8EW-M4 with 6 percent of extra water had achieved highest relative slump but increase in dosage of extra water had a reducing effect on the flowability. For instance, relative slump value achieved for 6% EW was 12.88 cm with 74 % increase from reference mix RM8. However, just by adding additional 1% of EW, the flowability was reduced to 31 %, that is a significant reduction of 58 %.

A similar pattern was observed for specimens comprised of a 10M alkaline solution. It was observed that upon achieving the optimum dosage of EW, there was a reduction in flowability, if higher EW dosage was added. From Figure 6, it can be seen that Mix design 10EW-M4 with 11 % of EW had the highest impact on flowability, however, by adding additional 1 % of EW, the flowability reduced. This behaviour of geopolymer mortar is new finding and has not been observed or reported previously. Furthermore, for 10M specimens, it was observed that 3 % and 6 % of EW had achieved the same relative slump value meaning having up to 6 % of EW had no significant change on the flowability and positive changes only occurred when a higher dosage of EW was added to the mix.

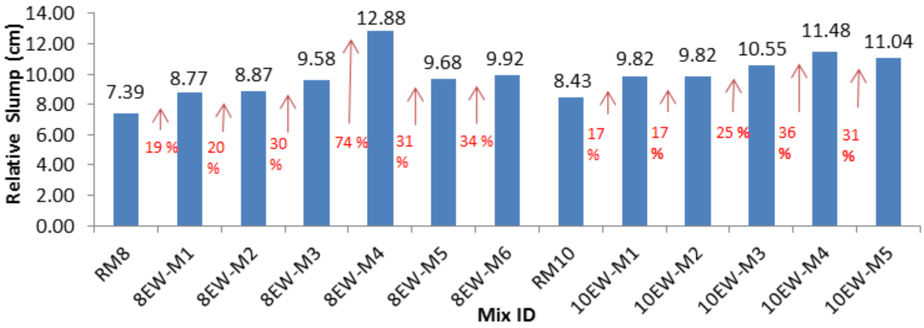

Figure 5. Relative slump increase for Extra water only.

3.2. Cylinder Compression Test

From the test results obtained, it was observed that different curing conditions based on seasonal weather changes had a great effect on the development of compressive strength and humidity also played an important role. Figure 6 illustrates the effect of temperature and humidity conditions on the strength development of geopolymer mortar. The results showed similar strength development pattern for various curing day. As expected geopolymer cylinder specimen (10M2-H) cured in for hot (summer) conditions with a temperature of 25-26 degree Celsius have developed relatively greater strength as compared to the cylinders specimens (10M2-C) cured in condition for cold (winter) temperature of 10-11 degrees Celsius. Over the curing period of 3, 7, 14, 21 and 28 days strength achieved by cylinder cured for cold weather condition was 5.4, 8.4, 12.8, 15.1 and 16.7 MPa, respectively. On the other hand, cylinders cured for hot weather conditions achieved 11.6, 22.8, 32.7, 37.6 and 40.4 MPa, respectively. Furthermore, in terms of the effect of high humidity on strength development of geopolymer mortar, it was observed that specimens cured under cold temperature had achieved the strength of 4.7, 6.6, 9.5, 10.0 and 14.6 MPa whereas for specimen cured under high humidity hot temperature had achieved strength of 9.6, 17.9, 27.2, 34.7 and 40.9 MPa. Overall, for both weather conditions, the compressive strength achieved by specimens kept under high humidity conditions was lower as compared to specimens cured in lower humidity curing conditions except for curing age of 28 days where mix 10M2-HW had achieved slightly higher strength as compare to mix 10M2-H. Nonetheless, it can be clearly seen that seasonal weather changes have a great effect on the strength development of geopolymer mortar where hot (summer) weather curing condition are more desirable as it has developed relatively high strength as compared to specimens cured under the cold (winter) weather curing conditions. Regarding strength development, it was observed that after 14 days of curing period the rate of strength increase was slower as compared to earlier curing days.

Another phenomenon that was observed for specimen (10M2-C) cured under the cold temperature at lower humidity is that cylinder specimens had formed white efflorescence after 7 days of curing period and at 28 days of curing age a larger surface area of the specimen was covered with white efflorescence as shown in Figure 7a and Figure 7b. However, specimen (10M2-CW) submerged under water did not show any occurrence of white efflorescence. Also, specimens (10M2-H and 10M2-HW) cured under hot temperature did not show any signs of efflorescence occurrence. This new finding certainly is unique since it is contrary to the findings observed by Zhang, Yang et al. (2017), where specimen submerged under water had shown efflorescence effect on the cylinder specimens and sample sealed in 25 degree Celsius exhibited a rapid development of efflorescence. Regarding strength development, the efflorescence had no impact on the compressive strength since there was no variation in strength development and a similar pattern of increase in strength was observed for all four mix specimens over the period of different curing age.

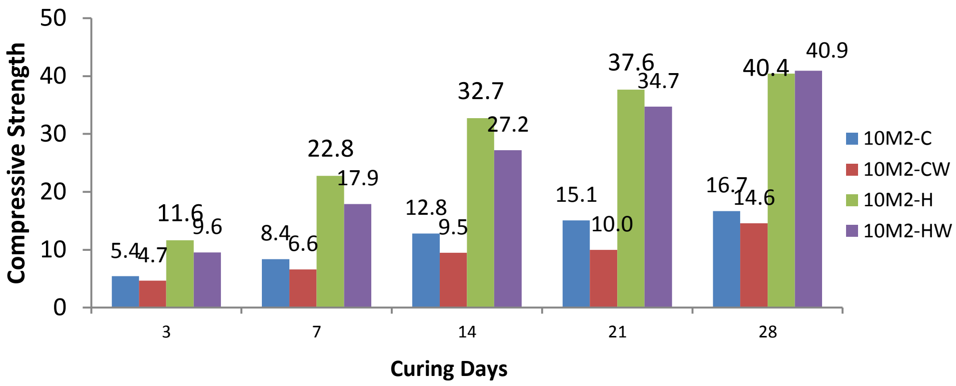

Figure 6. Mini Cylinder Compressive Strength Test Results.

(a) 7 days

(b) 28 days

Figure 7. Formation of white efflorescence on specimens cured under cold conditions with low humidity.

4. CONCLUSION

Consequently, several finding from this research has provided more insight to the effect of seasonal weather on the behaviours and properties of geopolymer mortar. Finding includes: [1] SIKA Visco Crete PC HRF – 2 had the most positive effect on the flowability of geopolymer mortar out of all the other commercially available superplasticisers; [2] specimens consists of 12M and 14M alkaline solution had no flowability and zero setting time, hence the paste dried within the mixing bowl, no relative slump was observed; [3] increasing the dosage of SP, whilst retaining constant water dosage yield less change in relative slump as compare to increasing extra water dosage with constant SP dosage; [4] specimens with different morality of NaOH behaved differently and different optimum dosage of extra water had achieved highest relative slump; [5] once optimum dosage was achieved, the increasing of EW in geopolymer mortar did not increase the flowability and had negative effect as it reduced the relative slump; [6] specimens cured under cold weather conditions had formed white efflorescence after 7 days curing period, and it rapidly grows as curing age increases, however specimen submerged under water did not show any sign of efflorescence; [7] in terms of strength development, hot (summer) weather curing condition with lower humidity are more desirable as compared to cold (winter) weather curing conditions.

5. REFERENCE

Albitar, M, Visintin P, Mohamed Ali M & Drechsler M (2015). Assessing behaviour of fresh and hardened geopolymer concrete mixed with class-F fly ash, KSCE Journal of Civil Engineering, 19, no. 5, pp. 1445-55.

Bureau of Meteorology, Australia., viewed March 17 2017, < http://www.bom.gov.au/climate/data/index.shtml?bookmark=200 >

Jindal BB, Singhal D, et al, (2017). Improving compressive strength of low calcium fly ash geopolymer concrete with alccofine, Advance in concrete construction, 05, pp. 17-29.

Kajaste R, Hurme M (2016). Cement industry greenhouse gas emission – management options and abatement cost, Journal of Cleaner Production, 112, pp 4041-4052.

Nematollahi, B., Sanjayan, J., et al. (2014). Effect of superplasticizers on workability of fly ash based geopolymer, ResearchGate.

Nuruddin MF., Malkawi AB, et al(2016). Geopolymer concrete for structural use: Recent findings and limitations, International conference on Innovative research.

Standards Australia Online (2006), "Methods of testing concrete - Method for making and curing concrete - Compression and indirect tensile test specimens", AS 1012-2014, viewed 17 March 2017, SAI Global database.

Turner LK, Collins FG, (2013). Carbon dioxide equivalent (CO_2-e) emissions: a comparison between geopolymer and OPC cement concrete, Construction and Building Materials, 43, , pp 125-130.

Williams RP, McLellan BC, et al (2011). Costs and carbon emission for geopolymer pastes in comparison to ordinary portland cement, Journal of Cleaner Production, 19, pp 1080-1090.

Zhang, Z.H., Yang, T., et al., (2016). The effect of efflorescence on the mechanical properties of fly ash-based geopolymer binders, 23rd Australian Conference on the Mechanics of Structures and Material, Byron Bay, Australia, pp 107-112.

129-MHT, R., (1985). *Compressive strength for service and accident conditions.* Materials and Structures, 28(7): p. 410-414.

Proc. 1st International Conference on Structural Engineering Research (iCSER 2017)
20-22 Nov 2017, Sydney, Australia
ISBN: 978-0-6480147-6-8

Effect of Temperature on Thermal Properties of Alkali-activated Fly Ash/Slag Binders

Zhu Pan[1], Zhong Tao[2], Yifang Cao[3], Neelam Bajracharya[4], Timothy Murphy[5] and Richard Wuhrer[6]

[1]Research Fellow, Western Sydney University, Penrith, Australia
[2]Professor, Western Sydney University, Penrith, Australia
[3]MPhil Candidate, Western Sydney University, Penrith, Australia
[4]Master by Research, Western Sydney University, Penrith, Australia
[5]Technical Officer, Western Sydney University, Parramatta, Australia
[6]Research Manager, Western Sydney University, Parramatta, Australia
Corresponding author's E-mail: z.pan@westernsydney.edu.au

Abstract

Geopolymeric binders exhibit high thermal stability and consequently it is believed that these materials can be extensively used in the construction of infrastructure, where fire safety is of major concern. For such applications, thermal properties play a fundamental role in the heat transfer calculation. This paper aims to provide a comprehensive experimental study of thermal properties of various geopolymeric binders at elevated temperatures. The binders were prepared using alkali-activated low calcium fly ash/ground granulated blast-furnace slag at ratios of 100/0, 50/50, 10/90 and 0/100 wt%. A transient plane source measurement technique was applied to assess the heat capacity and thermal conductivity at temperatures ranging from 23–600 ^{o}C. Data generated was utilised to develop analytical expressions for estimating thermal properties as a function of temperature. The simplified relationships can be used for estimating the fire resistance of structural elements made with geopolymeric materials.

Keywords: Geopolymers, Thermal conductivity, Specific heat, Elevated temperatures, Thermal property models.

1. INTRODUCTION

Alkali-activated slags and fly ashes (or refer to geopolymers) have emerged as innovative building materials with the potential to form an environmentally friendly alternative to ordinary Portland cement (OPC) concrete. These materials are produced by alkali activation of aluminosilicate raw materials (e.g., fly ash or metakaolinite) in a high pH environment and hydrothermal conditions. In comparison with OPC concrete, the greenhouse footprint of geopolymer concrete is 70% lower (van Deventer et al, 2012). Given correct mix design, these alternative binding systems could provide superior mechanical properties and durability to OPC concrete, and be highly profitable.

Research and development of geopolyermic materials started in the 1930s and the number of papers published in this field has grown exponentially in the last 20 years (Palomo et al, 2014). However, the transformation from academic research to on-site field work has been relatively slow. There is a lack of commercial drivers in the market as the benefits of geopolymeric materials are not fully realised by the industry practitioner. One such benefit is the excellent fire resistance of geopolymeric materials, which is attributed to its three-dimensional macromolecular framework (of alkali-activated fly ash) having high thermal stability (Pan et al, 2013).

A recent study has clearly indicated that geopolymeric materials have higher fire performance as compared to OPC materials (Pan and Sanjayan, 2010). When exposed to elevated temperatures, the strength of alkali-activated fly ashes (AAF) increased (due to further geopolymerisation) while the strength of OPC counterparts decreased (due to decomposition of calcium hydroxide). Sarker et al. (2014) studied the thermal spalling of AAF concrete and OPC concrete. When the specimens were exposed to elevated temperatures up to 1000 ^{o}C, the OPC concrete specimens suffered severe spalling, while no spalling was observed on AAF concrete specimens.

Besides mechanical properties and thermal spalling, thermal properties also have a significant influence on the fire response of a structural system. Material with a low thermal conductivity will reduce the amount of heat which flows through it, increasing the fire resistance of structures made from this material. While the effects of temperature on the performance of geopolymers have been investigated, there have been limited investigations into thermal properties of geopolymeric materials. A review of current literature (Subaer and van Riessen, 2007; Duxson, 2006) revealed that data on thermal properties of geopolymers have been preliminary and further research is required to understand these systems. Subaer and van Riessen (2007) investigated thermal expansion and thermal conductivity of geopolymers prepared by metakaolinite, and their results show a similar thermal conductivity obtained in geopolymers, as compared to OPC pastes. However, the specific heat of geopolymer was not reported and the measurement of thermal conductivity was only carried out at ambient temperature in this study. Duxson et al. (2006) studied the effect of humidity on thermal conductivity and specific heat of metakaolin-derived Na, NaK and K geopolymers in the temperature range of 40 to 100 ^{o}C. They found that the thermal conductivity of geopolymers is closely linked with the specific heat. As the specific heat of potassium is lower than that of sodium, the thermal conductivity of K-based geopolymers is also lower than that of Na-based geopolymers.

For a porous material, the thermal transport properties are affected by the pore structure (pore volume and pore interconnectivity) and moisture content. In geopolymerisation, water is required as a reaction intermediate and is released during condensation to form pores and create the biphasic structure (Subaer and van Riessen, 2007). Given that a significant volume fraction of geopolymer composite structures is comprised of water, the thermal properties of geopolymeric materials are expected to vary in a fire, as a result of evaporation. It is also noted that the pore structure varies greatly, depending on the raw materials for the synthesis of geopolymer, and curing regime. In the previous studies (Subaer and van Riessen, 2007; Duxson, 2006), geopolymers were prepared by using metakaolinite, and the samples developed strength under heat curing. Although this regime can easily be achieved in a typical precast concrete factory, it is hard to be implemented for cast in situ applications. In order to offset the limitation of heat curing, a typical method is to manufacture geopolymer by combing fly ash with slags. The fly ash/slag and pure fly ash involve entirely different reaction mechanisms and produce pore structure of distinct characteristics. The fly ash/slag system (Ca-Si system) undergoes a complex reaction that involves hydration of CaO in the presence of Al to form an aluminium-modified calcium silicate hydrate (C-(A)-S-H) gel as a major binding phase. On the other hand, alkali activation of fly ash or metakaolinite (Al-Si system) involves the dissolution of Si, coagulation, and a highly exothermic condensation reaction followed by crystallisation to produce zeolite-like polymers, with a three-dimensional sodium alumina-silicate hydrate (N-A-S-H) gel as a major binding phase (van Deventer et al, 2012). This is different from layered structure for calcium silicate hydrate (C-S-H) gel in Portland cement paste. Therefore, significant variation in thermal conductivity may be found for different type of binders.

This work aims to investigate the thermal properties of the Al-Si (mainly containing fly ash) system and Ca-Si system (slag or fly ash/slag). The thermal properties of the latter have received little attention. Moreover, the previous investigations (Subaer and van Riessen, 2007; Duxson, 2006) of geopolymers only studied the thermal properties over the range of 23–100 °C. In this study, thermal properties of both geopolymeric systems will be measured over the temperature range of 23–600 °C. Data obtained from this study will be used to develop simplified relations for expressing specific heat and thermal conductivity of geopolymers as a function of temperature. These relations are required for analysis of fire resistance of a structural system made with geopolymeric materials.

2. EXPERIMENTAL PROGRAM

2.1. Materials

In this investigation, for the purpose of comparison, cement paste was also prepared. The cement used meets the requirement of ASTM C150 Type I cement. The class F fly ash used in this investigation was mainly a glassy material with some crystalline inclusions of mullite, hematite and quartz. A granulated blast furnace slag was supplied with gypsum, which was pre-blended with slag. The oxide compositions of the binder materials are summarised in Table 1. It is noted that the fly ash has very low calcium content. As a result, the fly ash-based geopolymer mainly consists of calcium-free gel structures.

The alkaline activating agents used in this investigation included sodium hydroxide, sodium silicate and sodium metasilicate. Sodium hydroxide flakes of 98% purity were supplied by Orica Chemicals. Sodium silicate liquid and industrial grade-powdered sodium metasilicate were supplied by PQ Australia. Sodium silicate liquid (Grade D) has the chemical composition: 29.4% SiO_2, 14.7% Na_2O and 55.9% H_2O, with a molecular modulus of Ms=2.06. Sodium metasilicate has the chemical composition: 29% Na_2O, 28% SiO_2 and 43% H_2O, with the Ms=1.0.

Table 1. Chemical analysis by X-Ray Fluorescence of raw materials

Constituent	SiO_2	Al_2O_3	Fe_2O_3	K_2O	Na_2O	CaO	MgO	SO_3	Cl	Loss on ignition
Cement (wt%)	19.9	4.7	3.4	0.5	0.2	63.9	1.3	2.6	-	3
Fly ash (wt%)	48.4	30.6	12.1	0.3	0.2	2.7	1.3	-	-	1.7
Slag (wt%)	32.5	13	0.22	0.25	0.21	42.1	5.47	-	-	0.35

2.2. Mix proportion

Samples were prepared without aggregates, since this paper only focuses on one component of concrete, binding phase. Generally, concrete consists of 70% aggregates and 30% binding phase by volume. Although the binding phase constitutes a small fraction of the overall volume, it plays a major role in the determination of thermal properties of concrete because it acts as the continuous phase, whereas the aggregate acts as the dispersed phase.

The samples were prepared in fly ash/slag proportions of 100%/0%, 90%/10%, 50%/50% and 0%/100% (wt-%). The labels representing the above samples are F100, F90S10, F50S50 and S100, respectively. The liquid activator (a combination of sodium hydroxide solution and sodium silicate solution) was used to prepare F100 and F90S10. The concentration of sodium hydroxide solution was 8 M, and the mass ratio of sodium hydroxide solution to sodium silicate solution was 2.5. The ratio of liquid activator to the binder (fly ash + slag) was 0.45 for F100 and F90S10.

It was noted that the dissolution and reaction of slag in strong alkaline media were much faster, as compared to fly ash. As a result, the liquid activator could lead to the quick setting of fresh samples with a high content of slag (F50S50 and S100). To avoid the flash set, the powdered activator (sodium metasilicate) was used to prepare F50S50 and S100. The activator dosage used was 4 wt-% of the total mass of the binder and water to binder ratio was 0.5. The hydrated lime, with a 1 wt-% of the binder, was added to both mixtures of F50S50 and S100. OPC samples with a water to cement ratio of 0.5 were also cast for the purpose of comparison.

2.3. Specimen preparation

The mixing procedures used were summarised as follows. The binders (fly ash, slag or cement) and the liquid components (water or alkali liquid) were mixed in a Hobart mixer for 5 min. When making geopolymer samples, the powder ingredients were dry mixed for 2 min. Then the alkali liquid or water was added, and wet mixing was carried out for 4 min. For powdered activated samples, the dry silicate activator was pre-blended with slag and dry-mixed for 3 min to achieve a homogenous mixture. The hydrated lime was mixed with water in a ratio of 1:3. The lime slurry together with water was then added, and wet mixing was carried out for 4 min. The mixture was poured into the mould in three equal layers. Each layer was vibrated for 20-40 s on a vibration table.

The samples were sealed by using cling wrap and cured for one day in a laboratory environment. Then the samples were removed from the moulds and cured in an oven which was operated at a temperature of 23 ^{o}C and relative humidity of 100%. After 28 days, the samples were kept in the conditioning room until testing. This curing regime was conducted for all samples except F100. Regarding F100, the samples were kept in the moulds and covered by cling wrap and then placed immediately in a preheated oven at 60 ^{o}C. After one day, the samples were removed from the moulds and kept in the conditioning room until testing.

2.4. Test apparatus and procedure

The thermal properties were measured by using a commercially available thermal constants analyser which is illustrated in Fig.1 (a). The model thermal constants analyser is TPS 2500 S. The thermal properties measurements made by this model are reproducible within ±1%. A transient plane source probe is placed between two halves of the sample. When a constant heat source is applied, the temperature in the sensor rises and heat flow in the sample being tested. This measurement technique is described in ISO/DIS 220007 standard (2008). To measure thermal properties at elevated temperatures, the apparatus is connected with a tube furnace in which a specimen was heated to the target temperatures. The paste specimens of 65 x 65 x 25 mm size were sliced from the cylindrical samples before the measurement. Specific heat and thermal conductivity of various binder types were measured at seven temperatures: 23, 100, 200, 300, 400, 500, and 600 °C. In each test, the furnace temperature was raised to the desired temperature and remained at that temperature until the samples reached thermal equilibrium. Then the measurements were carried out.

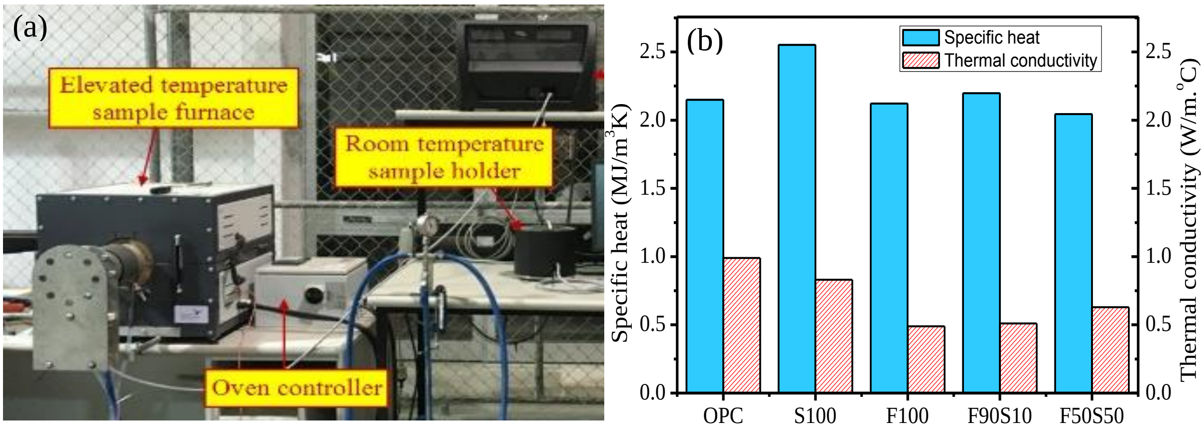

Figure 1. (a) Test apparatus and (b) Thermal properties at ambient temperature

3. RESULTS AND DISCUSSION

3.1. Thermal properties at ambient temperature

At ambient temperature, the variation of thermal conductivity of the cement paste and the geopolymers are demonstrated in Fig. 1(b). The thermal conductivity of slag-based mixture S100 activated with the powder-type activator is slightly lower than that of cement paste. When 50% of slag was replaced by fly ash, the thermal conductivity of F50S50 further decreased from 0.83 to 0.63 W/m·°C. The samples mainly containing fly ash exhibit lower thermal conductivity that is only half of the cement paste. These results suggest that fly ash replacement (in geopolymeric systems) leads to considerable reduction in thermal conductivity. The value of thermal conductivity of Al-Si system (F100) is within the range of thermal conductivity reported in the literature (Subaer and van Riessen, 2007; Duxson, 2006). Subaer and van Riessen (2007) reported that the values of thermal conductivity by using a hot wire method, were 0.55 and 0.91 W/m·°C for geopolymer pastes and mortar containing of 40 wt% quartz aggregates, respectively. Duxson et al. (2006) reported that the thermal conductivity of geopolymers (with different alkali cation) measured by using a laser flash method was between 0.3 to 0.52 W/m·°C. In comparison with the OPC system, the lower thermal conductivity of Al-Si system is due to the different skeletal framework between these two systems. Al-Si geopolymer consists of a three-dimensional alumino-silicate network that is configurated of SiO_4 and AlO_4 tetrahedrons united together by oxygen bridges. On the other hand, OPC system consists of either two or three layers of C-S-H gels, which could roll into fibres. The measured specific heat results of different binders are also illustrated in Fig. 1(b). The values of specific heat of different binder types are similar at ambient temperature, except S100. The specific heat of S100 is approximately 25% higher than that of other samples.

3.2. Effect of temperature on thermal conductivity

The variation of thermal conductivity for different binder types with temperature is presented in Fig. 2(a). The evolution of thermal conductivity shows distinct trends between Al-Si system and other systems. The overall trend of the Al-Si system is that the specific heat of all the samples increases up to 500 °C, then remains almost constant up to 600 °C. Although thermal conductivity for F100 and F90S10 follows a similar trend, a close examination of Fig. 2(a) shows the difference in the range of 200 to 300 ^{o}C. F90S10 shows an increase in thermal conductivity while F100 shows a decrease in thermal conductivity. In comparison with an increase in thermal conductivity of Al-Si system, Ca-Si geopolymers and OPC show a decrease in thermal conductivity with temperatures, and then the thermal conductivity remains almost constant at a higher temperature range. The influence of temperature on thermal conductivity is different between OPC and Ca-Si system. For OPC system, the thermal conductivity initially decreases with temperatures up to 400 °C. In the range of 400–600 ^{o}C, the variation of thermal conductivity is small. For Ca-Si system, a decrease in thermal conductivity can be observed on both S100 and S50F50 at elevated temperatures up to 200 °C. However, the slope of thermal conductivity for S100 is steeper than that for S50F50. At the higher temperature range, the thermal conductivity of these two binders becomes relatively stable. The above mentioned differences in the evolution of thermal conductivity reflect the different physiochemical processes taking place for different binder types at elevated temperatures. For OPC system, the correlation between these processes and the trend in thermal conductivity has been established (Khaliq and Kodur, 2011). The initial steep slope of thermal conductivity up to 400 °C can be attributed to moisture loss at a faster pace, resulting from the evaporation of free and pore water in concrete with a rise in temperature. The minor variation in thermal conductivity between 400 and 500 °C is attributable to the dissociation of small amounts of physically bound water present in concrete as a result of the phase change. Beyond 500 °C, there is a slow decrease in thermal conductivity because of the liberation of a small amount of strongly held moisture left within C-S-H layers. For geopolymeric systems, it has been observed a decrease in porosity at elevated temperatures (Irena et al, 2014). As the thermal conductivity of solid phase is much higher than that of air and water, the decrease in porosity will result in the increase in thermal conductivity of porous materials (e.g. geopolymers and cement pastes). At elevated temperatures, the strength gain of some geopolymers (F100) was observed in our previous study (Pan et al, 2016), indicating the decrease in porosity. A study has continued to investigate effects of temperatures on the porosity of geopolymers. The results will be presented at the conference.

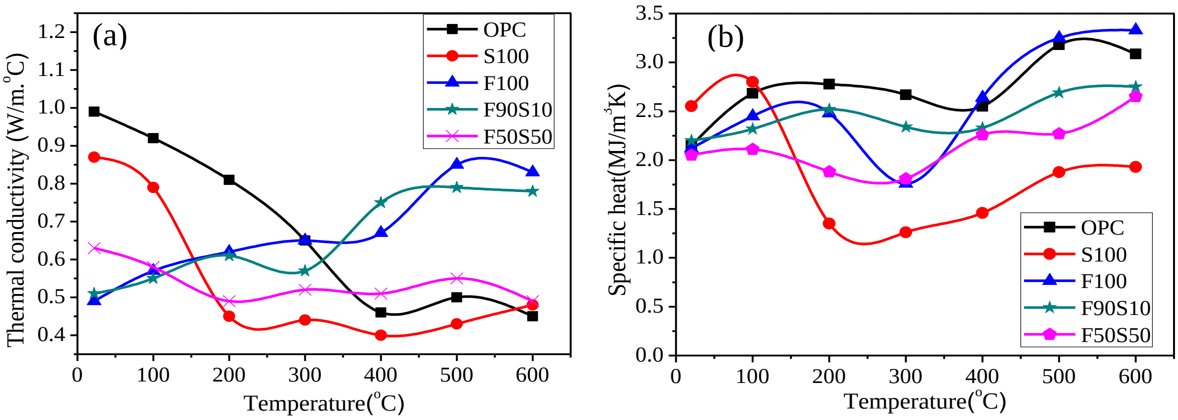

Figure 2. Effect of elevated temperatures on (a) thermal conductivity and (b) specific heat

3.3. Effect of temperature on specific heat

The specific heat of various binder types are presented in Fig. 2(b) as a function of temperature. The specific heat for all binder types shows an increasing trend up to 600 °C. This trend is attributed to the absorption of heat for bending and breaking of hydrogen bonds. Among the investigated binders, it is noted that S100 and F100 show an anomalistic change in specific heat at elevated temperatures. The change for the former is taking place in the range of 100–200 °C while the change for the latter is taking place in the range of 200–300 °C. A comparison of Fig. 2(a) and (b) shows that the thermal conductivity of S100 and F100 also exhibits a sudden change in the same temperature range. The consistency between the specific heat and thermal conductivity results again suggests that some phase transformations may take place in these binders at elevated temperatures. The decrease in specific heat is generally associated with either the heat release or increase in porosity, as a result of phase transformations. This requires considerable future research.

3.4. Empirical models

Data obtained from thermal properties was used to develop empirical models over a temperature range of 20–600 °C. The linear regression analysis was utilised to develop these models. As demonstrated in Fig. 2(a) and (b), both thermal conductivity and specify heat are affected by the type of binder and the range of temperature. Therefore, the empirical models are separately developed for each type of binders. At some temperature ranges, the thermal properties exhibit a sudden change, as a result of the phase transformations. In order to reflect this trend, the thermal property models are also developed in different ranges. The models for thermal conductivity and specific heat are summarised in Eqs. (1) through (5) and Eqs. (6) through (14), respectively. The typical linear regression models of geopolymeric systems, together with coefficient of determination R_2, are presented in Fig. 3.

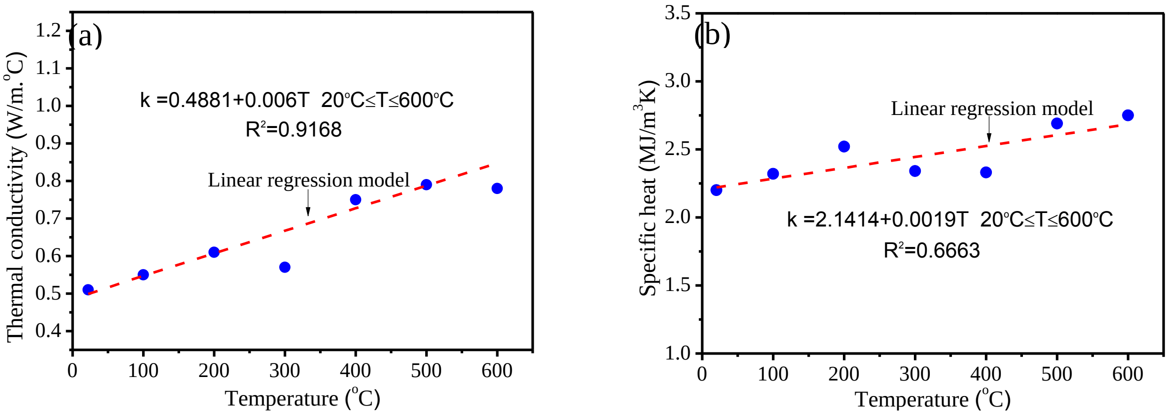

Figure 3. Effect of elevated temperatures on (a) thermal conductivity and (b) specific heat

Thermal conductivity

OPC

$$k = 0.9940 - 0.0010T \qquad 20°C \le T \le 600°C \tag{1}$$

S100

$$k = 0.7636 - 0.0007T \qquad 20°C \le T \le 600°C \tag{2}$$

F50S50

$$k = 0.5885 - 0.0002T \qquad 20°C \le T \le 600°C \tag{3}$$

F90S10

$$k = 0.4927 + 0.0005T \qquad 20°C \le T \le 600°C \tag{4}$$

F100

$$k = 0.4881 + 0.0006T \qquad 20°C \le T \le 600°C \tag{5}$$

Thermal conductivity

OPC

$$k = 2.1714 + 0.0034T \qquad 20°C \le T \le 200°C \tag{6}$$

$$k = 2.0235 + 0.0019T \qquad 200°C \le T \le 600°C \tag{7}$$

S100

$$k = 2.9971 - 0.0071T \qquad 20°C \le T \le 200°C \tag{8}$$

$$k = 0.8646 + 0.0018T \qquad 200°C \le T \le 600°C \tag{9}$$

F50S50

$$k = 2.1244 - 0.0010T \qquad 20°C \le T \le 300°C \tag{10}$$

$$k = 1.1090 + 0.0025T \qquad 300°C \le T \le 600°C \tag{11}$$

F90S10

$$k = 2.2067 + 0.0008T \qquad 20°C \le T \le 600°C \tag{12}$$

F100

$$k = 2.1414 + 0.0019T \qquad 20°C \le T \le 200°C \tag{13}$$

$$k = 0.3510 + 0.0053T \qquad 200°C \le T \le 600°C \tag{14}$$

4. CONCLUSIONS

At ambient temperature, the thermal conductivity of Al-Si geopolymer system is lower than that of OPC system. This is attributed to the different gel structure between these two types of binders. The C-S-H gel is believed to be the major reaction products for both S100 and OPC. As a result, the measured thermal conductivity for S100 and OPC is similar.

At ambient temperature, the results show a minor variation in the specific heat for all binder types.

At elevated temperatures, the thermal conductivity of Ca-Si geopolymeric system and the OPC system decrease with increasing temperature, while the thermal conductivity of the Al-Si geopolymeric system increases with increasing temperature.

At elevated temperatures, the specific heat for all the binder types generally increases with temperature. However, a sudden drop in specific heat is observed for F100 and S100 in the range of 200–300 °C and 100–200 °C, respectively.

The proposed relationships for thermal properties (at elevated temperatures) can be used for assessing the fire resistance of structures made with geopolymeric materials.

ACKNOWLEDGMENTS

The authors are grateful for the financial support provided by the Western Sydney University through an ECA award, and they would like to acknowledge the contributions from the laboratory staff Mr Murray Bolden and Mr Robert Marshall. The authors would also like to acknowledge the Advanced Materials Characterisation Facility (AMCF) of Western Sydney University for access to its instrumentation and staff, in particular Dr Shamila Salek.

5. REFERENCES

van Deventer JSJ, Provis JL, Duxson P (2012) Technical and commercial progress in the adoption of geopolymer cement, Minerals Engineering, 29, 89-104.

Palomo A, Krivenkob P, Garcia-Lodeiro I, Kavalerova E, Maltseva O, Fernández-Jiménez A (2014) A review on alkaline activation: new analytical perspectives, Materials, 64(315), http://dx.doi.org/10.3989/mc.2014.00314.

Pan Z, Feng KN, et al (2013) Damping and microstructure of fly ash-based geopolymers, Journal of Materials Science, 48(8), 3128-3137.

Pan Z and Sanjayan JG (2010) Stress–strain behaviour and abrupt loss of stiffness of geopolymer at elevated temperatures, Cement and Concrete Composites, 32(9), 657-664.

Sarker PK, Kelly S, Yao Z (2014) Effect of fire exposure on cracking, spalling and residual strength of fly ash geopolymer concrete, Materials & Design, 63, 584-592.

Subaer, van Riessen A (2007) Thermo-mechanical and microstructural characterisation of sodium-poly(sialate-siloxo) (Na-PSS) geopolymers, Journal of Materials Science, 42(9), 3117-3123.

Duxson P, Lukey GC, van Deventer JSJ (2006) Thermal Conductivity of Metakaolin Geopolymers Used as a First Approximation for Determining Gel Interconnectivity, Industrial & Engineering Chemistry Research, 45(23), 7781-7788.

ISO/DIS22007-2:2008 (2008) Determination of thermal conductivity and thermal diffusivity, Part 2: Transient Plane Heat Source (Hot Disc) Method, ISO, Geneva, Switzerland.

Khaliq W, Kodur V, (2011) Thermal and mechanical properties of fiber reinforced high performance self-consolidating concrete at elevated temperatures, Cement and Concrete Research, 41(11), 1112-1122.

Irena N, Ljiljana K, Ivona JC, Vuk R, Slavko M, Velimir R (2014) Improved compressive strength of alkali activated slag upon heating, Materials Letter, 133 (7), 251- 254.

Pan Z, Tao Z, Cao Y F, Bajracharya N, Murphy T, Wuhrer T (2016) Comparative performance of alkali-activated slag and fly ash at elevated temperatures, Proceedings, 24th Australasian Conference on the Mechanics of Structures and Materials, Perth, Australia, 415-420.

Proc. 1st International Conference on Structural Engineering Research (iCSER 2017)
20-22 Nov 2017, Sydney, Australia
ISBN: 978-0-6480147-6-8

Shear Response of Concrete with Nano-Materials

Pierre van Tonder and Morgan Dundu[3]

[1]Professor, University of Johannesburg, Department of Civil Engineering Science,
P O Box 524, Auckland Park, 2006, Johannesbrug, South Africa
Corresponding author's Email: pierrevt@uj.ac.za; mdundu@uj.ac.za

Abstract

Concrete exhibits excellent compression strength and durability properties; however, it is weaker in shear. The shear resistance of concrete is largely influenced by the strength of the interfacial zone between the aggregates and the mortar. To enhance the density and strength of the interfacial zone of the concrete, silica fumes have been mixed with the mortar and aggregates. This investigation focuses on the effect of multi-walled carbon nano-tubes (MWCNTs) and graphite nano-fibres (GNFs) on the shear strength of concrete. Since these nano-materials are small in size and possesses large surface areas and strong van der Waals interaction forces, it is expected that they can bridge the zone between the mortar and aggregate interface, thus limiting the formation and growth of micro-cracks. However, nano-materials tend to bundle up and form entangled clumps due to their strong van der Waals interaction forces. For this reason, the nano-materials were dispersed using gum arabic (GA). Two series were investigated; one incorporating GA and MWCNTs, and the other one incorporating GA and GNFs. In both series GA equivalent to 1% of the water was mixed with water and nano-materials (MWCNTs or GNFs) equivalent to 1% of the cement weight were mixed with the cement powder and subsequently mixed with the aggregates.

Keywords: Concrete, Nanomaterials, Shear strength, Graphite nano-fibres, Multi-walled carbon nano-tubes, Gum arabic, Functionalisation.

1. INTRODUCTION

Concrete is a heterogeneous material, consisting of different types of material (aggregates, hardened cement paste and aggregate-paste interface (interfacial transition zone)), which have different properties. This means that when concrete is loaded, the internal stresses and strains are not uniform; they are concentrated in certain areas. The aggregates are the strongest and least likely material to fail in the concrete, the hardened cement paste contributes greatly to the strength of concrete and is dependent on the porosity and the microstructure of the hardened cement paste, and the aggregate-paste interface (interfacial transition zone) is generally the weakest link in concrete. If concrete fails it is most likely that the interfacial transition zone will fail first, followed by the hardened cement paste. Failure of aggregate in concrete is very rare and is only encountered in high strength concrete applications or when inferior materials are used. The interfacial transition zone has a lower mechanical strength and a higher permeability than the rest of the surrounding concrete. It is unclear as to where the zone ends, and how thick it is, since it gradually blends into the surrounding concrete matrix. Decreasing the porosity of this zone will result in concrete having higher shear strength. The purpose of this investigation is to evaluate the influence of graphite nano-fibres and carbon nano-tubes on the shear strength of concrete, and to find out whether the properties of concrete could be enhanced so as to minimize the amount of shear reinforcement steel used in reinforced concrete structures. Silica fumes have been successfully used to increase the density and strength of the interfacial zone of the concrete. It is expected that the addition of carbon nano-tubes, which are much finer than silica fumes, could increase the strength of the interfacial transition zone of the concrete, and subsequently the overall strength of concrete, much more than silica fumes. In general the shear strength of concrete is approximately 50% of the compressive strength [1, 2].

1.1 Graphite nano-fibres (GNF)

Graphite nano-fibres (GNFs) are formed from carbon atoms, which are arranged in a hexagonal or honeycomb pattern as sheets and stacked one above the other. A single sheet is extremely strong, flexible, and stable, however, it is weakly bonded to neighbouring sheets of graphite [3]. GNFs consist entirely of sp^2 bonds [4]. Further, GNFs have diameters ranging from 1 – 2 nm and a length-to-diameter ratio exceeding 10 000, and are the strongest composites known to man (approximately three hundred times stronger than steel). Problems inhibiting the use of GNFs in the concrete mix are the tendency of the GNFs to stick together and form balls due to Van der Waals forces, the lack of cohesion between the GNFs and the concrete materials, the lack of reliable large scale production and the expensive cost of producing the GNFs. Cohesion between the GNFs and the concrete materials can be increased by the use of GA. A process called functionalization is used to aid in both the dispersion and the purification of the GNF.

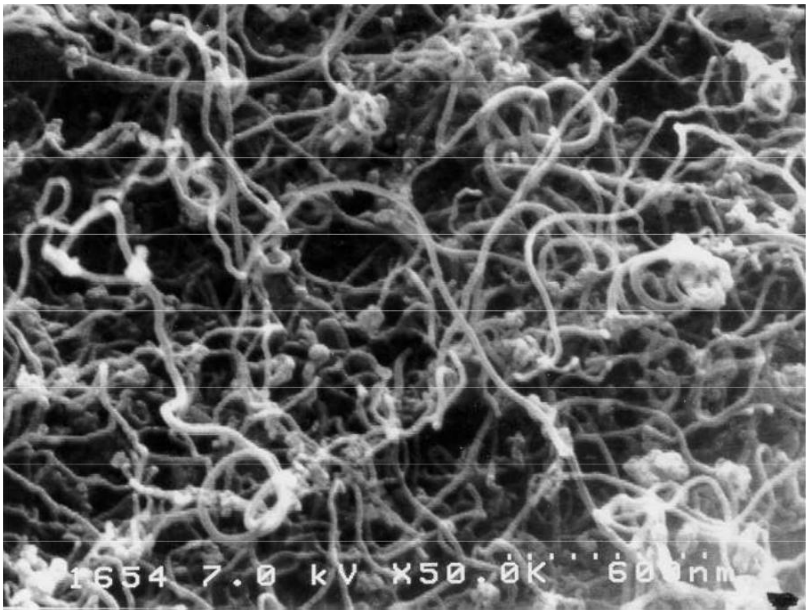

Figure 1 Graphite nano-fibres from a Scanning Electron Microscope [5]

1.2 Carbon nano-tubes

Carbon nano-tubes (CNTs) are allotropes of carbon, and are found as single-walled and multi-walled nano-tubes. A single-walled carbon nanotube (SWCNT) is a single layer or sheet of graphite, rolled into a long, thin seamless cylindrical tube of 1 – 2 nm diameter and has a length-to-diameter ratio exceeding 10 000 [4], as shown in Figure 2, while multi-walled carbon nano-tubes (MWCNTs) are cylindrical tubes made up of several layers of graphite sheets [6]. Unlike natural carbon nano-tubes, man-made nano-tubes are closed at both ends [7]. The mechanical properties of CNTs are astounding, but are still not yet fully standardised, because of the difficulty encountered in performing tests on the CNTs at nano-scale. Like GNFs, CNTs are composed entirely of sp^2-hybridized C-C covalent bonds and have approximately the same mechanical properties as GNFs. These are stronger than the sp^3 bonds found in diamond [8]. Carbon nano-tubes have been reported to have attained a strength of 150 GPa [6], and although mixed reports exist about the exact strength of CNTs, all agree it is far much than the strongest forms of steel available. Although carbon nano-tubes have extremely high tensile strength (150 GPa) and Young's modulus (1054GPa), their strength under compression, torsion and bending is poor due to their hollow structure and high aspect ratio (ratio between the longer dimension (length) and shorter diameter. Carbon nano-tubes are highly flexible and do not just fracture, but rather form kink-like ridges.

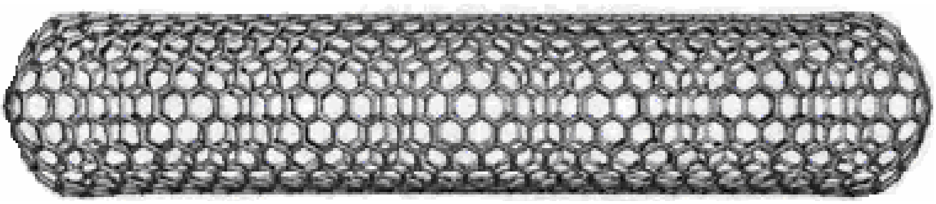

Figure 2: Closed single-walled carbon nano-tube [8].

2.0 Experimental procedure

2.1 Functionalization of GNFs and MWCNTs

As indicated before, in order to remove any impurities from GNFs, and to help in the dispersion of these nano-fibres, a process called functionalization was used. Impurities in graphite nano-fibres can potentially decrease the strength of the nano-fibres by up to 85%. Although MWCNTs are supplied clean, the cohesion between the MWCNTs and the concrete matrix still needs to be increased by functionalization (attaching carboxylic acid groups to the MWCNTs). Functionalization also assists in dispersing the MWCNTs through the concrete mix. Lack of cohesion between the CNTs and the concrete matrix results in "fibre pull-out" and sliding between the matrix and the CNTs at relatively low loads and thus do not allow the composite to reach high strengths [9]. It has been suggested that weak CNT-matrix cohesion results from the smooth surfaces and small diameter of CNTs. Currently there are two ways to resolve this problem, either by functionalising the CNTs or the aggregate particles [8].

(a) GNFs

(b) Mixing of the acids

(c) Refluxing of the nano-materials

(d) Filtering process

Figure 3 Functionalization process

To accomplish the functionalization process, the GNFs/MWCNTs were weighed and dissolved in an 80 ml acid mixture, containing a 3:1 ratio of sulphuric acid to nitric acid. In CNTs, a mixture of sulphuric acid and nitric acid is used to covalently attach carboxylic acid groups on the walls and ends of the MWCNT. The solution was refluxed at 55°C for 24 hours inside the fume cupboard, and left to cool down to room temperature. Functionalized GNFs/MWCNTs of 10-20 grammes were then placed in 2.5 litres of distilled water. The nano-materials were filtered using a 125 nm standard/normal filter paper, washed with more distilled water until the pH was in the range of 5-7, which gave the nano-materilas a neutral acidity. Figure 3 shows the functionalization process. Finally, the acid treated graphite nano-materilas were dried using the pump vacuum. They were then kept dry and sealed until used.

2.2 Casting of concrete cubes

The method of casting concrete followed the usually procedures of preparing concrete cubes. This included, creating the mix design, batching the concrete, checking the slump, casting the concrete in the moulds, curing after 24 hours and testing of the concrete specimens after 28 days. The concrete mix design was performed using the C & CI method [10]. Three different concrete test samples were mixed in each series; the first sample were merely a standard reference concrete mix, with nothing added to the mix, the second concrete mix included a soluble solution of GA, and the third and last batch included functionalized GNFs/MWCNTs and GA. The third test was the core part of this investigation. GA was mixed with water and added to the specimens to help improve the cohesion between the cement paste and the GNFs. Since GA had a tendency of decreasing the concrete strength and increasing the workability, the water cement ratio was adjusted from 0.73:1 to 5:1. The amount of GA and water was added to the concrete nano-material mix using in-situ trial concrete mixes. The nano-materials were functionalized, mixed directly with the cement powder, and subsequently added to the aggregate. The process of functionalization leaves nano-materials in flake-like structures. Before mixing the nano-materials with cement, the nano-materials were crushed into fine powder using a mortar and pestle. Safety equipment (goggles, gas masks, and latex gloves) was used to mitigate the health risks posed by crushing the nano-materials. The concrete was then cured as per the guidelines given in SANS 5861-1:2006 [11]. Table 1 provides the mix design used in each of the batches. Slump tests were performed on the three batches prior to filling the moulds. The slump tests were performed as per SANS 5862-1:2006 [12], and the results for the slump tests are also given Table 1.

Table 1 Concrete mix design for each series

Series 1	Materials	Batch 1 – Standard	Batch 2 – Gum Arabic	Batch 3 – Gum Arabic + MWCNTs
	Cement	8.558 kg	8.558 kg	8.558 kg
	Sand (7:3 blend)	23.18 kg	23.18 kg	23.18 kg
	Stone	15.41 kg	15.41 kg	15.41 kg
	Water	6.248 kg/*l*	6.186 kg/*l*	6.186 kg/*l*
	Gum Arabic	-	62.5 m*l*	62.5 m*l*
	MWCNTs	-	-	86 g
	Slump	40 mm	50 mm	10 mm
Series 2	Materials	Batch 1 – Standard	Batch 2 – Gum Arabic	Batch 3 – Gum arabic + Graphite Fibres
	Cement	8.558 kg	8.558 kg	8.558 kg
	Sand (7:3 blend)	23.18 kg	23.18 kg	23.18 kg
	Stone	15.41 kg	15.41 kg	15.41 kg
	Water	6.248 kg/*l*	6.186 kg/*l*	6.186 kg/*l*
	Gum Arabic	-	62.5 m*l*	62.5 m*l*
	Graphite Fibres	-	-	86 g
	Slump	45 mm	55 mm	20 mm

2.2 Shear tests of the concrete

Pure shear stress in concrete is never encountered in practise, as it is always accompanied by the compression and tension, caused by bending. There are no standard methods to determine the shear strength of concrete only. This is due to the fact that it is extremely difficult to set up a test which tests the concrete specimens purely for shear. Attempts have been made in the past to determine the shearing strength of concrete, using concrete beams of very short span. Loads were applied very close to the supports to try and replicate a pure shear scenario. Some of these tests showed the shear strength to be only slightly higher than the tensile strength; others showed it to be 50-90% of the compressive strength [13, 14]. The variation can attributed to the fact that either tensile or compressive stresses may have also been acting on the specimens [13, 14].

A mould in Figure 4, was constructed in order to test the shear strength of the concrete only [15]. Specimens developed from this mould was crushed in the same way as normal concrete cubes, at a standard crushing rate of 100 kN per minute. To achieve pure shear failure, the mould was placed at the centre and aligned vertically in an Avery Davison crushing machine, as shown in Figure 5 (a). The load was applied until the concrete failed in shear. The shear failure plane is illustrated as vertical section between the grooves in Figure 5 (b).

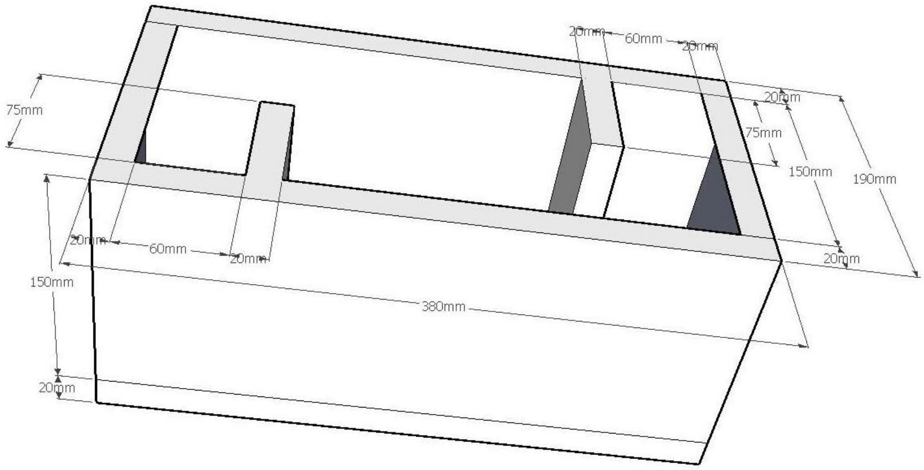

Figure 4: Shear mould dimensions

(a) Test set-up (b) Direct shear failure

Figure 5: Test set-up and shear zone

3.0 Compression results

The results obtained from the experiments are summarized in Table 2, and presented in the form of bar graphs in Figure 6. These graphs show the strength of each sample relative to other samples in the series, and the strength of samples in a series relative to other series. A full statistical analysis of the results was not performed because there are only a few results from each of the different samples. As opposed to the findings in the literature [16], the results show that the addition of GA in both series had a negative effect on the shear strength of concrete. As shown in Series 1 and 2, the results revealed that the addition of GA to the wet concrete decreased the shear strength of concrete by 5 - 6%.

When GA and MWCNTs were added to the wet concrete in Series 1, the strength of the concrete increased by 6%. Although not remarkable, effectively this means that MWCNTs have the potential to increase the strength of concrete by 11 – 12%. This increase may be attributed to the physical, cylindrical shape of the nanomaterials, because they retain a much stiffer and stronger elastic rod due to a rolling process. The addition of the MWCNTs to the concrete results in a loss of workability in the concrete mix as shown in Table 1. However, when both GA and GNFs were added to the wet concrete in Series 2, the strength of the concrete was reduced by 15%. This implies that the addition of GNFS to the wet concrete decreased the shear strength of concrete by a further 9 -10%. The further reduction of the strength may be attributed to the flat shape, and soft and slippery property graphite.

Table 2 Shear strength

Series	Specimen	Control (kN)	GA (kN)	GA + MWCNT/GNFs (kN)
Series 1	S1-1	4.6816	4.1388	4.8091
	S1-2	4.0839	4.0092	4.6688
	S1-3	4.2933	4.2112	4.6326
	Average	4.3529	4.1198	4.6326
	Std Deviation	0.3033	0.1023	0.1972
	CoV	0.0697	0.0248	0.0426
	% Increase/Decrease	0	-5	6
Series 2	S2-1	4.6800	4.2400	4.1600
	S2-2	4.2300	4.0400	3.5700
	S2-3	4.3500	4.2100	3.5800
	Average	4.4200	4.1633	3.7700
	Std Deviation	0.2330	0.1079	0.3378
	CoV	0.0527	0.0259	0.0896
	% Increase/Decrease	0	-6	-15

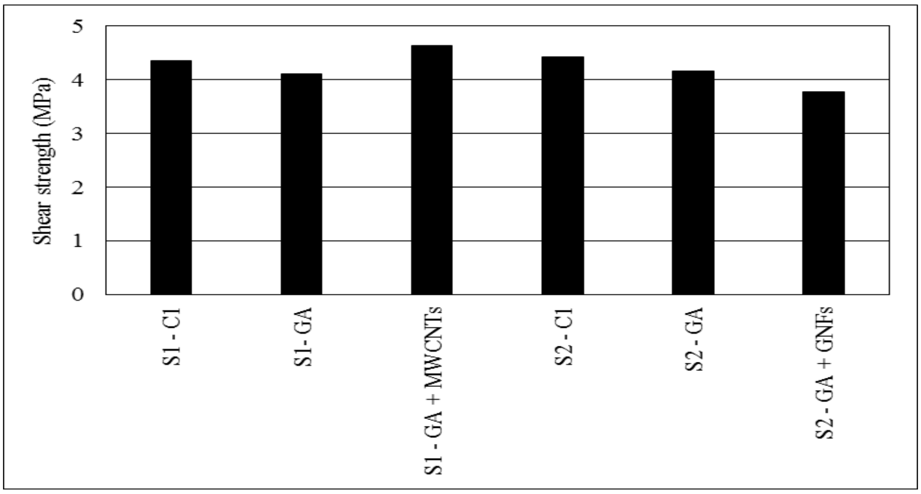

Figure 6 Shear strength of the concrete

4.0 Conclusion

When nano-materials were incorporated into the concrete in a quantity of 1% relative to the cement weight, a shear strength increase was evident. This increase may be attributed to the nano-materials bridging capabilities over the micro-cracks found within the mortar-aggregate interface and nanomaterials physical properties as they are much stiffer and stronger as compared to the softer graphene sheet of GNFs. GNF concrete displayed a decrease in shear strength, due to its soft and slippery properties. On average, the use of GA as a dispersion agent led to decrease in the strengths of concrete. This implies that alternative dispersion techniques should be investigated.

References

1. School of Concrete Technology. *Level 4: Concrete Technology and Construction*. Cement and Concrete Institute, 2001, Part 1 and Part 2.

2. Mindess, S and Young, J. *Concrete*. 1st edition. New Jersey: Prentice-Hall, 1982, pp. 381-406.

3. Crespi, V.H. 2006, Carbon Nanostructures [online], Penn State University, Available from:http://www.phys.psu.edu/people/display/index.html?person_id=202;mode=research;research_description_id=419

4. Wikipedia 2007, Carbon Nanotube [online], Available from:

   http://en.wikipedia.org/wiki/Carbon_nanotube.

5. Carbon NanoTube and Graphite Nanofibre [online], Available from:

   http://cedb.postech.ac.kr/~feel/research.php?view=1.

6. 7thWave, Inc. 2006, Nano-tubes and Buck balls [online], Available from:

   http://www.nanotech-now.com/nanotube-buckyball-sites.htm

7. Nalwa, H. S. 2000, Nanostructured Materials and Nanotechnology, Concise, Academic Press, San Diego.

8. Cheap Tubes, Inc. 2006, Carbon Nano-tubes 101 Presentation [online], Available from: www.cheaptubesinc.com/Carbon%Nano-tubes%20101.htm

9. Terry, R., Baker K. 1998, Synthesis, Properties and Applications of Graphite Nano-fibres [online], Available from: http://www.wtec.org/loyola/nano/US.Review/09_03.htm

10. Addis, B., Owens, G. 2001, Fulton's Concrete Technology, Eighth Edition, Cement & Concrete Institute, Midrand.

11. SANS 5861-1: 2006, Concrete tests – Mixing fresh concrete in the laboratory, Pretoria: South African National Standards, 2006.

12. SANS 5861-3: 2006, Concrete tests – Making and curing of test specimens, Pretoria: South African National Standards, 2006.

13. SANS 5862-1: 2006, Concrete tests - Consistence of freshly mixed concrete

    – Slump test, Pretoria: South African National Standards, 2006.

14. Mindess, S and Young, J. Concrete. 1st edition. New Jersey: Prentice-Hall, 1982, pp. 381-406.

15. Popovics, S. Strength and Related Properties of Concrete - A Quantitative Approach. 1st edition. Wiley, 1998, pp. 102-165.

16. Mac Gregor, J. G. 1988, Reinforced Concrete – Mechanics and Design, First Edition, Prentice Hall, New Jersey.

17. Saez de Ibarra, Y., Gaitero, J. J., Campillo, I. Atomic force nano identification of cement pastes modified by nanotube dispersions, Spain.

ISBN: 978-0-6480147-6-8

Classification and Characterization of Recycled Construction Aggregate (RCA)

Farzaneh Tahmoorian[1,1], Bijan Samali[2], John Yeaman[3]

[1]PhD Candidate, Centre for Infrastructure Engineering, Western Sydney University, Kingswood, Australia
[2]Director, Centre for Infrastructure Engineering, Western Sydney University, Kingswood, Australia
[3]Professor, Faculty of Science, Health, Education and Engineering, University of Sunshine Coast, Queensland, Australia

Corresponding author's E-mail: F.Tahmoorian@westernsydney.edu.au

Abstract

Construction projects use up large quantities of natural resources and produce tonnes of construction and demolition waste (CDW). Because of its growth, these quantities have increased in the last few years and it has now become necessary to create a sustainable method of development in civil construction. Therefore, recycling and utilization of recycled materials in construction projects can be the most promising solution for this problem. Due to important role and high portion of aggregates in asphalt concrete, utilization of recycled materials including recycled construction aggregates (RCA) can provide enormous benefits from the viewpoint of environmental sustainability and effective use of resources. In spite of the awareness of the importance of using RCA and much research being conducted, there is still a need for a deeper study about the characteristics of the RCA. The variability in behaviour and performance of RCA used in construction projects indicates the variability in their composition. This paper presents the results of a statistical study, image analysis and experimental study to evaluate the characteristics of RCA as an alternative for virgin aggregate in asphalt mixture. A series of characterization tests were conducted three times, using RCA collected at different dates.

Keywords**:** Asphalt, Igneous, Metamorphic, Recycled construction aggregate, Sedimentary

1. INTRODUCTION

The need for sustainable asphalt design and construction is becoming a priority within the asphalt industry. On the other hand, the large amount of construction and demolition waste generation around the world justifies the idea of using recycled construction aggregate (RCA) in new asphalt mixtures. RCA offers a good solution to design a sustainable asphalt mixture not only due to large amount of construction and demolition wastes but also providing a sound level of function for wearing course, because RCA is made up of three different aggregate types. However, it is important to understand the performance characteristics of RCA when specifying it for partial replacement of natural aggregates, since the overall performance and durability of the construction needs to be maintained. In addition, the level of RCA substitution achievable will depend upon the properties of the recycled aggregate, its availability in the market, the performance criteria of the mix, the whole-of-life sustainability of the product and the economic viability of its inclusion. This paper covers some RCA characteristics and the specifications of RCA required for producing sustainable asphalt with high standard.

1.1. Demand for aggregates and public infrastructure

Asphalt plays a vital role in global transportation infrastructure and drives economic growth and social well-being in developed as well as developing countries (Mangum, 2006). Asphalt contains approximately 95% aggregate and 5% bitumen. Referring to Ektas and Karacasu (2012), a layer of 15 cm thick and 10 m wide for one kilometre of road requires almost 3,750 tonnes of mixture containing aggregate and bitumen. In 2007, the latest year for which figures are available, about 1.6 trillion metric tonnes of asphalt were produced worldwide (EAPA & NAPA, 2009). Considering the important role and high proportion of aggregates in asphalt mixtures, it can be estimated that the large quantities of aggregates are required for road construction. Referring to the previous discussions and considering above mentioned statistics, application of waste materials in road construction, including the asphalt surface layer remains an attractive route to solve the problems associated with natural resource depletion and solid waste disposal. However, physicochemical and mechanical properties of recycled materials inevitably hinder the beneficial use of such materials in pavement construction, and particularly in asphalt mixtures because the application of waste materials should not influence the structural and functional aspects of the surface (wearing) course.

In general, the desired surface (wearing) course requires two major characteristics:

- Good Resistance to shear forces which depends on the bitumen quality and the aggregate skeleton of the asphalt mixture. In this regard, particle shape substantially affects interparticle friction and coarse aggregate shear resistance (White et al., 2016).
- Good Skid Resistance which depends on the microstructure and macrostructure of a pavement surface (Haas et al., 1994).

Therefore, the ability to design an adequate asphalt mix incorporating appropriate waste materials becomes a key issue in the design and construction of pavements, including surface course, in line with sustainable development concept.

1.2. Cost of aggregates for public infrastructure

Referring to the report by Macromonitor (2013) regarding the cost analysis of infrastructure construction in Victoria, the single biggest cost component in an infrastructure construction is materials. The Victorian example is an indicative of the cost of infrastructure throughout the world and it means that the cost of meeting future demand for public infrastructure will increase and that supplying construction materials to meet this demand will have a significant impact on this cost increase. It should be mentioned that to meet future demands for affordable public infrastructure, there must be efficient supply of construction materials. The efficiency of the construction materials supply is largely determined by location, as transportation equates to approximately 20 to 25% of the total cost of materials. This means that transportation costs have a significant impact on total construction cost. For example, according to a report from Access Economics (2006), in Melbourne, which has many quarries located in the metropolitan area and the average transport distance from quarry to asphalt plant is 30 km, the delivery cost of material is 70% less than Sydney in which there is one remaining metropolitan quarry, and the average transportation distance is 60 km (Access Economics, 2006). Therefore, it is essential to recognize the importance of locally supplied construction materials to the provision of affordable public infrastructure to ensure affordable supply. In addition, the identification of new and innovative resources of construction materials (like recycled aggregates) is of high importance in this regard.

2. A REVIEW ON RCA IN AUSTRALIA

As Australia's population grows, there will be an increasing demand for public infrastructure and construction materials. Today, the demand for aggregate materials is much greater than what could possibly be supplied using virgin aggregates alone. The Australian Quarrying Industry Estimates average consumption of aggregates across Australia at around 7 tonnes per person per annum.

The construction and demolition sector is Australia's biggest generator of waste who is responsible for around 40% of all Australian waste material with 19 million tonnes of annual waste by-products associated with our construction and demolition activities (CCAA, 2008a). If all the materials generated during Australian construction and demolition projects were treated as 'waste', it would keep at least 30 major landfill facilities operating all year round (Australia's Sustainable Aggregate Industry, 2013).

In Australia, RCA has been the most common construction and demolition waste used in construction projects as coarse and fine aggregates. RCA is available in Australian markets principally in Sydney and Melbourne. Figure 1 illustrates the sources of RCA in Australia, noting that Man Sand stands for "manufactured sand".

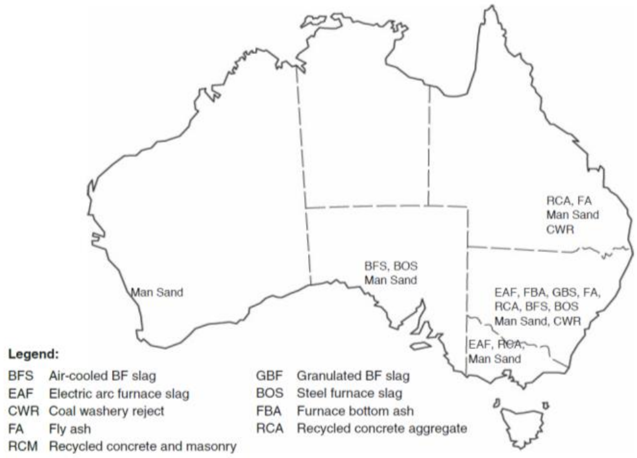

Figure 1. Sources of RCA in Australia (CCAA, 2008b)

Based on a life cycle analysis undertaken by the RMIT University, sustainable aggregates made from RCA have a 65% lower greenhouse emissions impact than similar products made from virgin rocks across the full product life cycle, largely due to avoiding the energy needed to quarry rock. Therefore, it will undoubtedly be required that a mixture of virgin and recycled materials be used, depending on the required performance and the relative availability of different materials.

2.1. Geological Study on RCA

The asphalt mixture performance can vary significantly depending on the type, percentages, and the properties of the materials. When it comes to aggregates, the physical, mechanical and chemical properties of the aggregates, resulting from the geological origin and mineralogy of the potential source and its subsequent weathering or alteration, play an important role on final product performance.

Aggregates can be classified in three groups reflecting the origin, formation and history of their rock:

- Igneous rocks which are generally of high strength.
- Sedimentary rocks constitute the greatest variation in strength and behaviour.
- Metamorphic rocks show a great variety in structure and composition and properties. Strength and resistance to weathering of metamorphic rocks make them suitable for use in construction projects.

Study on properties of all these rock groups indicates that each geological group has its own advantages and disadvantages in terms of engineering properties.

RCA is made up of these three different aggregate types in terms of geological classification, and hence can provide proper level of function for asphalt surface layer. For example, a matrix of portland cement concrete which will vary between basalt (i.e. Basic Igneous) and granite (i.e. Acidic Igneous) depending on the source of material and the age of the building from which it came, will form the igneous part of RCA. Sandstone or an agglomerate of sand and cement paste involves the sedimentary part of RCA, and metamorphic part of RCA could be quartz or hornfels depending on the source rock in the concrete, or could be "man-made" metamorphic rock such as ceramic, glass or brick.

As each of the aggregate types (i.e. igneous, sedimentary, and metamorphic) has different properties, their proportion in RCA significantly affects the properties of RCA, and subsequently the final performance of asphalt mixture. For instance, the aggregate proportion influences the bitumen absorption of asphalt mixtures. If RCA contains a lot of sedimentary rock, the RCA would be too absorbent and the binder content will be reduced by absorption. Consequently, the asphalt will be too dry and crack and ravel. In contrast, if the RCA contains a very large proportion of basalts and metamorphic group such as glass and ceramics, it would be very low in absorption, and subsequently the mix will be wet and lack shear strength and shove. It should be mentioned that crushed brick could be low or high in absorption depending on the amount of firing (clinker or callow).
Moreover, the skid resistance will be impacted by the aggregate composition. Asphalt concrete with crushed brick will provide differential wearing of the asphalt by creating a fresh and rugose surface and subsequently will enhance skid resistance (Chen and Liao, 2002). Therefore, RCA will positively affect the skid resistance of the asphalt concrete, as:

- Both the Igneous and Metamorphic groups will be generally hard and prone to polishing,
- The Sedimentary group and crushed brick will wear differentially and create an ever changing depth.

In light of this, asphalt surface layers provide unique opportunities for RCA reuse, as using RCA in asphalt surface layer can contribute to improvement of engineering characteristics of the asphalt pavement materials as well as the pavement performance, representing a value application for RCA. However, significant developmental limitations and many relevant considerations must be addressed in this regard.

2.2. Statistical study on RCA in Sydney

In spite of the awareness of the importance of using RCA and much research being conducted, there is still a need for a deeper study of the characteristics of RCA. The variability in the behaviour and performance of RCA used in different construction projects indicates the variability in RCA composition. Therefore, this research investigates the composition and variability of recycled construction aggregates through classification of aggregate samples collected from a recycling centre in Sydney. For this purpose, the RCA is collected at different dates over one year, and is categorized into different geological groups of igneous, metamorphic, and sedimentary, respectively (from left to right), as illustrated in Figure 2.

Figure 2: Classification of Recycled Construction Aggregate (RCA)

It is intended to create a database containing the composition and characteristics of RCA produced in Sydney in twelve months. The results of sorting RCA samples into different geological groups are presented in Table 1. As the results of classification shows, the sedimentary rocks in RCA are the greatest part and significantly influence the RCA properties. However, the man made metamorphic rocks such as bricks and ceramics involve about 20% of RCA. These types of man made aggregates can enhance both the strength (due to a good shape) and the durability due to low absorption as well as skid resistance.

Table 1. Summary of Statistical Study on the Classification of RCA

Average Percentage of Aggregate in the Sample	Aggregate Type		
	Igneous	**Sedimentary**	**Metamorphic**
	17	64	19

In an investigation by Yeaman (1976), it has been shown that the addition of small quantities of crushed brick to asphalt mixture, improves the skid resistance of this material (Yeaman, 1976). Therefore, the variability in RCA composition can result in making a superior hot mix asphalt (HMA) to Natural aggregate mixtures.

2.3. Study of RCA Characteristics

As discussed previously, the surface (wearing) course requires two major characteristics:

- Good Resistance to shear forces
- Adequate skid resistance

Aggregates with good particle shape will increase the wearing course resistance to shear forces (Mohajerani, 1997). In addition, the skid resistance is related to microstructure and macrostructure of aggregates. Microtexture is mainly dependent on aggregate shape characteristics and mineralogy, whereas; macrotexture is a function of mix properties, compaction method, and aggregate gradation (AASHTO, 1976). In this study, the particle shape of RCA is evaluated through the most commonly used tests including Particle Shape Test (AS 1141.14, 2007) and Flakiness Index test (AS 1141.15, 1999). The results of these tests on RCA and basalt are given in Table 2. As presented in Table 2, basalt materials show more of misshapen particles than RCA while still below the 35% limit of the Australian standard. Also, the results of flakiness index test show that RCA has less flakiness index than basalt which can positively affect the inter-particle interlock in asphalt mixture. This can subsequently lead to improvement in shear resistance of asphalt mix containing RCA.

Table 2: The Results of Particle Shape and Flakiness Index Test for RCA and Basalt and Australian Standard Limits for Dense Graded Asphalt

Test Name	Test Method	Aggregates		Australian Standards Limit (%)
		RCA	**Basalt**	
Particle Shape Test	AS 1141.14	6.2	18.3	35% (max)
Flakiness Index Test	AS 1141.15	6.9	19	25% (max)

Table 3: The Results of Particle Density and Water Absorption Test on RCA and Australian Standards Limit for Dense Graded Asphalt

Property	RCA	Sedimentary Rock in RCA	Igneous Rock in RCA	Metamorphic Rock in RCA	Basalt	Standards Limits
Water Absorption	6.30	7.64	2.03	5.86	1.64	2 % (max) heavy/ very heavy traffic
Particle Density	2.570	2.464	2.675	2.588	2.640	-

In addition, as mentioned previously, RCA is made up of different aggregates. Each of the aggregates will have different properties of which the most important is porosity that affects the absorption. The absorption is an indication of porosity in aggregate which demonstrates the pore structure of the aggregate. In asphalt mixtures, a porous aggregate increases the binder absorption, resulting in a dry and less cohesive asphalt mixture. Therefore, the determination of water absorption of individual groups of aggregates in RCA as well as RCA itself is of high importance when studying the RCA characteristics. To this end, water absorption and particle density test is considered as part of this research in order to obtain detailed information and data on this key property of RCA. The water absorption and particle density test is performed based on the procedure described in AS 1141.6.1 (2000), and the test results are presented in Table 3. The results of particle density and water absorption test on different rocks (i.e. igneous, sedimentary and metamorphic), as presented in Table 3, indicate the high absorption of sedimentary and metamorphic rocks in comparison with igneous rock. As can be observed, the RCA water absorption exceeds the limit set by the Australian Standard, mostly due to high proportion of sedimentary rocks in RCA.

3. CONCLUSION

From the study, it was determined that there are approximately 2,200 quarries operating across Australia that produce annually some 130 million tonnes of aggregates to be used in construction projects. If the current consumption rates are maintained, then the Australian industry will need to consider a 60% increase in production by 2050. On the other hand, construction projects produce large quantities of construction and demolition waste (CDW) including RCA. Even though there are many CDW management approaches to reduce the quantity of the generated CDW, it is impossible to stop its production. Therefore, a number of industry and academically based research projects have been undertaken to ascertain performance limits for recycled aggregates including RCA. However, the variability in RCA composition has led to the variability in the results of behaviour and performance of RCA used in construction projects. Therefore, the main aim of this research was to provide more insight into the contribution of aggregate types (i.e. igneous, sedimentary, and metamorphic) as different components of RCA as well as to create a data base containing the characteristics of RCA produced in nearest recycling units, over twelve months, that can be used in future research using RCA.

To this end, a series of characterisation tests have been conducted on different aggregate types of RCA samples collected at different dates over a twelve month period. The results of RCA classification reveals that RCA is composed of mostly sedimentary rocks, igneous rocks and metamorphic rocks. All these rocks, with their own properties and their weak and strong points, have made RCA a potential synthetic aggregate for pavement construction depending on the RCA percentage.

This paper presented the results of this statistical study and the associated experimental works conducted, as a component of a broader research project on designing an optimal asphalt mixture. Based on this research, it was concluded that RCA has lower value of flaky and misshapen particles in comparison with virgin aggregates. This implies that asphalt mixtures containing a certain amount of RCA can have better deformation resistance, compaction and, therefore, workability. In addition, the test results revealed that RCA exhibits comparatively more water absorption than conventional aggregate. Cracks and adhering mortar and cement paste can be significant reasons for the high water absorption of RCA. The high water absorption of RCA may result in high bitumen absorption in asphalt mixtures, and hence plays an important role in asphalt mixture design. Therefore, the selection of optimal combination of RCA and other aggregates is required to satisfy the relevant standards requirements while taking advantage of other strong points of RCA.

4. REFERENCES

Access Economics Pty Limited. (2006). Economic Contribution of the Extractive Industries in Victoria, Australia.

American Association of State Highway and Transportation Officials (AASHTO). (1976). Guidelines for Skid Resistant Pavement Design, Task Force for Pavement Design of the AASHTO Operating Subcommittee on Design (AASHTO), Washington, D.C., USA.

Australia's Sustainable Aggregrates Industry. (2013). Building Our Nation through Smarter Resource Use, Australia.

Cement Concrete and Aggregates Australia (CCAA). (2008a). Research Report: Manufactured Sand, Abrasion resistance and effect of manufactured sand on concrete mortar, Australia.

Cement Concrete and Aggregates Australia (CCAA). (2008b). Report: Use of Recycled Aggregates in Construction, Australia.

Chen, J.S., and Liao, M.S. (2002). Evaluation of Internal Resistance in Hot-Mix Asphalt (HMA) Concrete, Construction and Building Materials Journal, Vol. 16, No. 6, pp. 313-319.

Ektas, S., and Karacasu, M. (2012). Use of recycled concrete in hot mix asphalt and an ANN model for prediction of Resilient Modulus, Journal of Ekoloji, Vol. 21, No. 83, pp. 53-60.

European Asphalt Pavement Association (EAPA), the National Asphalt Pavement Association (NAPA). (2009). The Asphalt Paving Industry: A Global Perspective, USA.

Haas, R., Hudson, R., and Zaniewski, J. (1994). Modern Pavement Management, Krieger Publishing Company, Malabar, FL, USA.

Macromonitors. (2013). The Impact of Heavy Construction Materials Prices on Infrastructure Costs in Victoria, Australia.

Mangum, M. (2006). Asphalt Paving Sector Presentation. Health Effects of Occupational Exposure to Emissions from Asphalt/Bitumen Symposium. Dresden, Germany.

Mohajerani, A. (1997). A Study of Relationships between Polished Aggregate Friction Value, Aggregate Crushing Value, and Point Load Strength Index, Australian Geomechanics, December 1997, pp 62-65.

White, G., Tighe, S., Emery, S., and Yeaman, J. (2016). "Developing Framework for Diagnosis of Shear Distress in Asphalt Surfaces", International journal of pavement engineering, DOI:10.1080/10298436.2016.1141413.

Yeaman, J. (1976). Skid Resistance and Brick Making Materials, Master of engineering thesis, University of New South Wales, Australia.

Proc. 1st International Conference on Structural Engineering Research (iCSER 2017)
20-22 Nov 2017, Sydney, Australia
ISBN: 978-0-6480147-6-8

Structural Sandwich Panels: A State of the Art Review

Diana Makweche[1] and Morgan Dundu[2]

[1]Department of Civil Engineering Science, University of Johannesburg, Johannesburg, South Africa
[2]Department of Civil Engineering Science, University of Johannesburg, Johannesburg, South Africa
Corresponding author's E-mail: mmakweche@uj.ac.za

Abstract

Known for their structural efficiency, sandwich panels have evolved with advances in materials science. These panels are now used extensively in many fields including the construction industry to take advantage of their light weight and ease of construction. Metals and timber-based products, especially oriented strand board, have continued to be the facing materials of choice. However, plastic, polymer and concrete or other cementitious facings reinforced with glass, steel, carbon, natural fibres or textiles are finding increasing use. Core materials now include balsa and other types of wood, expanded polystyrene (EPS), rigid foams, and foamed or lightweight cements and concretes. Some cores incorporate various lattice, truss or pyramid-type structures while others have honeycombs. Such assemblies are fabricated using materials ranging from paper to aluminium and steel. The current review surveys structural sandwich panels with non-profiled faces and a range of innovative core composites and configurations. Specifically, it examines the properties that make them particularly suitable for their respective applications as well as any inherent weaknesses or peculiarities that require due consideration in design. Structural response under bending and compression, and typical failure modes are also considered.

Keywords: Sandwich panel, Structural insulated panel, Bending, Compression

1. INTRODUCTION

A *sandwich panel* is comprised of a thick internal layer of low density material, referred to as the *core*, which contributes to flexural stiffness, out-of-plane shear and compressive behaviour, and externally bound thin, stiff and fairly dense material, referred to as the *facings* or *face sheets*, which generally carry bending and in-plane loads (Figure 1). The methods of manufacturing sandwich panels are numerous, and depend on the materials and required shapes or configurations. Examples of these methods include injection moulding, air bubble-free resin vacuum infusion process, the seeman composites resin infusion moulding process (SCRIMP), which is a more economical vacuum-assisted resin transfer moulding (VARTM) process, vacuum bag technology, investment casting method, and hot-melt impregnation process. The structural applications of sandwich panels are as many and as diverse as the materials and the configurations used in their fabrication.

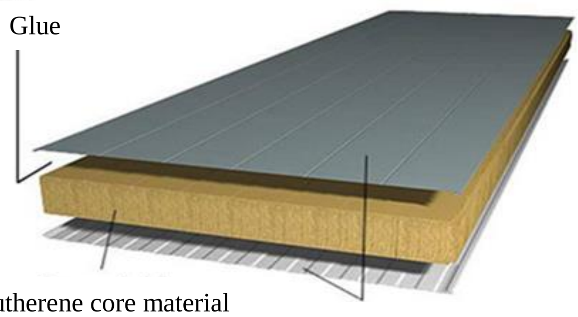

Figure 1 Typical sandwich panel (http://www.sovereignbd.com/sandwich-panel.html)

2. FACE SHEETS

It has been estimated by the Federation of American Scientists (2009) that metals are the most extensively used face sheets and make up approximately 50% of the market while wood, particularly oriented strand board, follows at approximately 42%. All other materials make up the remainder. The commonly used metals are steel (Szyniszewski et al (2012)) and aluminium (Ramakrishnan and Kumar (2016)), due to their relatively thin face sheets, which can be lightweight and non-flammable (Panjehpour et al (2013)). Oriented strand board, on the other hand is highly flammable, but tends to be much cheaper than metals (Panjehpour et al (2013)). Also in literature are concrete and other cement-based facings, such as precast concrete wythes, which are connected by concrete webs or steel connectors (Benayoune et al (2006)) and cellulose-fibre cement board (Dundu and Bukasa (2013)). Typically cement board is fire-resistant, but has the drawback of exhibiting brittle failure, especially in compression (Panjehpour et al (2013)). One group of materials that is now being used widely, as reflected in the growing body of research literature, is the fibre-reinforced polymers or plastics (FRP). A survey of literature reveals that the types of fibre ranges from Kevlar (Borsellino et al (2004)), fibreglass (Mamalis et al (2002)), electrical glass or E-glass (Borsellino et al (2004) and Abdi et al (2014)) to carbon fibres (Borsellino et al (2004) and Cartié and Fleck (2003)).

3. CORE MATERIALS

According to Daniel (2009), the core material properties have the greatest influence on failure initiation and failure mode, and this seems to be backed up by the huge range of materials that have been investigated. Balsa, which has a relatively high density of up to 150kg/m^3 (Avilés and Carlsson (2006)), and has been used in boat hulls and flooring over a long period of time has been found to have a static strength that is greater than polyvinyl chloride (PVC) foams (Ramakrishnan and Kumar (2016)). Today, this material is used as the core of modern facing materials, such as FRP (Avilés and Carlsson (2006)). However, PVC foams appear to enjoy the most widespread use, and this has been ascribed to their superior insulation properties (Ramakrishnan and Kumar (2016)). They can be found in densities ranging from 48kg/m^3 to 200kg/m^3 (Avilés and Carlsson (2006), Bezazi et al (2007) and Mamalis et al (2005)), depending on their intended use. Several researchers have investigated the effect of different types of foam and foam density on the structural properties of sandwich panels (Table 1). Other core materials found in literature include polyurethane (PUR) of densities ranging from 32kg/m^3 (Tuwair et al (2015)) up to 139kg/m^3 (Abdi et al (2014)), expanded polystyrene (EPS) (Borsellino et al (2004), and Mousa and Uddin (2011)), polymethacrylimid (PMI)(Mamalis et al (2005)), and syntactic phenolic foam(Mamalis et al (2002)).

Increasingly, these foams are being reinforced in various ways in order to improve their load-carrying capacity. A broad range of materials from simple fibres (Dawood et al (2010), and Cartié and Fleck (2003)) and pins (Abdi et al (2014)) to tubes (Mamalis et al (2002)), pyramidal shapes (Cartié and Fleck (2003)) or trusses (Benayoune et al (2006)) and honeycombs (Daniel (2009)) have been investigated in order to determine whether they are of structural benefit. Fibres extending from one facing to the other increased the shear strength, stiffness and flat-wise compression of the panel (Dawood et al (2010)). The problem of delamination was also dealt with to a certain extent (Abdi et al (2014)). It was found that cylindrical pins, made of glass-fibre/polyester resin laminate and encased in a polyurethane foam (69.5kg/m^3), and rigidly connected to the top and bottom sandwich faces increased the resistance to debonding and delamination. The pins also eliminated core crushing (Abdi et al (2014)). In one study (Cartié and Fleck (2003)), titanium alloy or carbon fibre pins were inserted into foam cores, at an angle of 30° to the sandwich panel mid-plane, resulting in a pyramidal structure. In another study (Mamalis et al (2002)), a phenolic foam core had additional reinforcement in the form of tubes made of the same material as the fibreglass facings. Located at the corners of the specimen, the axes of four of the tubes were aligned perpendicular to the plane of the facings, as shown in Figure 2. A fifth tube was positioned such that its axis was parallel to the facings and during edgewise compression test this tube was either vertical or horizontal (Mamalis et al (2002)). One conclusion drawn from the results was that the usefulness of such tubes as reinforcement was somewhat dictated by their orientation in relation to the loading direction (Mamalis et al (2002)).

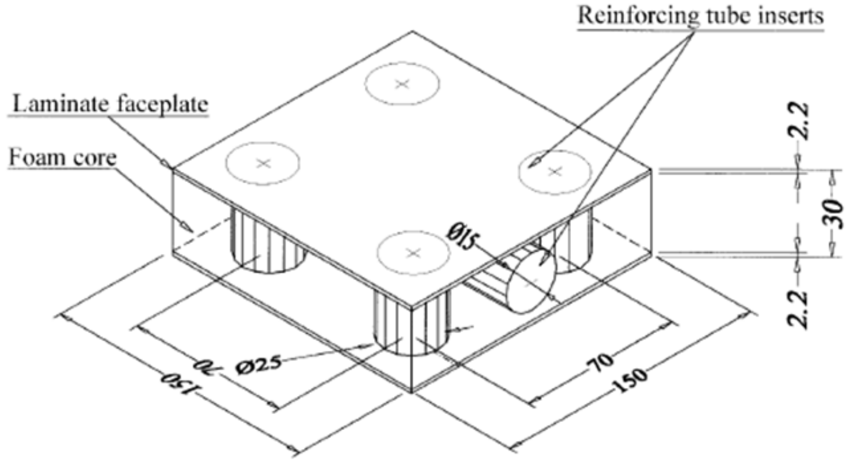

Figure 2 Schematic diagram showing tube orientation in foam core (Mamalis et al (2002))

4. STRUCTURAL RESPONSE OF PANELS IN BENDING

Flexural tests, in three or four-point bending, have been conducted on various combinations of facing and core materials. The deflections and ultimate loads sustained, and the failure modes were shown to be influenced by the choice of facing and core materials. A comparison between facings made up of several layers of either woven Kevlar, glass or carbon fibres with epoxy resin and hardener as the matrix (Borsellino et al (2004)) revealed that higher modulus of the carbon fibre facing translated into a slightly higher flexural strength when compared to the other two facing materials, but the maximum loads sustained by all three panels still remained within 10MPa of each other. The failure mode for all panels was wrinkling of the top facing (compression face) due to crushing of the underlying core. This was followed by a fracturing failure of that face, and this usually occurred under the load position. The failure of the Kevlar facing was found to be less sudden, a behaviour that was ascribed to its ability to absorb energy (Borsellino et al (2004)). In the same study, comparisons between two different densities of EPS foam (15kg/m^3 and 18kg/m^3) showed a 51% increase in elastic modulus and a 108% increase in ultimate flexural stresses for the higher density foam, compared to the one with the lower density (Borsellino et al (2004)). Similar results were obtained by Bezazi et al (2007). Specimens with the less dense core failed by upper facing rupture and indentation under the load position, while the denser core specimens experienced shear failure and delamination of both facings (Bezazi et al (2007)). In general, core failures occurred faster when compressive forces and shear stresses were working together than when either one is working in isolation. Indentation frequently occurred where the soft cores were subjected to concentrated loads. In such cases, the top facing deformed into the core (Daniel, (2009)).

Where the core had additional reinforcement in the form of pins, results showed that flexural stiffness and ultimate strength were increased by the presence of the pins. In fact, increasing the pin diameter was found to increase strength and stiffness (Abdi et al (2014)). When compared to plain foam core sandwich specimens, the samples reinforced with 2mm and 3mm diameter pins experienced an increase in the failure load-to-weight ratio of 44.9% and 48.6%, respectively, while the corresponding deflections increased by 98% and 42.6%, respectively. In addition, the maximum flexural stresses sustained by the 2mm and 3mm pin sandwich specimens were 77.2% and 97% higher, respectively (Abdi et al (2014)). In the plain foam core specimens, failure of the top face sheet resembled local buckling, at the load position, with no observable failure of the core (Figure 3 (a)). However, in the pin-reinforced specimens, the first sign of failure was cracking of the pins near the load position. The cracks happened at the top facing-core interface, propagated outwards towards the supports, and eventually traversed the core to the bottom interface, as illustrated in Figure 3 (b) (Abdi et al (2014)).

(a) Plain foam core panel (b) Pin reinforced foam core panel

Figure 3 Failure of the foam core material (Abdi et al (2014))

Truss cores were found to carry greater ultimate loads than similar tetrahedral cores (Wang et al (2003)). The failure mode was shearing of the core which took the form of tensile rupture of the core members. The compression members experienced yielding and no buckling. It was surmised that some of the truss member rupture was due rather to material imperfection which affected ductility (Wang et al (2003)).

Concrete and other cementitious composites have also been tested in four-point bending. Sandwich panels with FRP facings and polymer-concrete filled corrugated cores exhibited composite action and sustained greater ultimate shear and flexural loads when compared to equivalent conventional reinforced concrete wall panels (Wattick and Chen (2017)). The panels also exhibited greater stiffness and ductility than their conventional equivalents. At failure, the panels first experienced debonding between the core and facings and then finally failed in shear (Wattick and Chen (2017)). There was no evidence of such debonding or delamination of fibres of the face sheet in full scale panels made of cellulose fibre-cement board facings and EPS cement cores. Although the panels were found to be more than adequate in sustaining typical service loads, they experienced sudden catastrophic failure. The panels sustained very little deflection (Dundu and Bukasa (2013), and Bukasa and Dundu (2014)).

5. STRUCTURAL RESPONSE OF PANELS IN COMPRESSION

The behaviour of sandwich panels under compressive loads was examined either from tests on full-scale panels or from edge-wise or flat-wise compression tests of smaller specimens. Researchers investigated the effects of different cores on the compressive behaviour of sandwich specimens (Boyle et al (2001) and Daniel (2009)). Boyle et al (2001) examined the buckling and post-buckling behaviour of full scale panels with similar facings (glass/ vinylester FRP) and either PVC (69.5kg/m^3) or balsa (150kg/m^3) cores. With a panel aspect (length to width) ratio of 2, the specimens with balsa cores buckled in two half-sine waves, while those with PVC cores buckled in a single half-sine wave (Boyle et al (2001)). In addition, the failure load of the balsa core specimens was 1.75 times larger than the theoretical buckling load, compared to only 1.35 times for the PVC core. Face sheet delamination and subsequent shear failure of core were observed at failure for the balsa core panels (Boyle et al (2001)). In Daniel (2009)'s investigation panels with FRP facings and either aluminium honeycomb, 100kg/m^3 density PVC foam or 250kg/m^3 density PVC foam were tested. The specimens with aluminium honeycomb cores failed by compressive failure of the face sheet rather than by face sheet wrinkling. Theoretical equations had predicted that face sheet wrinkling would be the most likely failure at a stress of around 2850MPa but the panels actually failed at a stress of 1550MPa in compression. This ultimate compressive load was much lower than the critical wrinkling stress (Daniel (2009)). Both sandwich specimens with the PVC foam cores failed due to wrinkling of the facing, at stresses that were close to the theoretical values. Similarly, the effects of different facing materials have been investigated. In Borsellino et al (2004)'s study, panels with similar core material (EPS bounded by an outer layer of PVC foam)and FRP facings, reinforced with either Kevlar (aramid), glass or carbon fibres were subjected to either edgewise or flatwise compression tests. In edgewise compression, Kevlar was found to have lower strength than either glass or carbon (Borsellino et al (2004)).

Panels with circular or square debonds on one facing were tested under compressive loading (Avilés and Carlsson (2006)). The debonds were placed centrally and the core material was again varied (PVC foam (48kg/m^3, 100kg/m^3, 200kg/m^3) and Balsa (150kg/m^3)) while the facing material was kept constant. For the majority of panels, initial failure occurred by local buckling of the facing at the location of the debonds. After that the region of debonding spread as the load increased until compressive failure of the face sheet occurred (Avilés and Carlsson (2006)). A unique sandwich panel made up of solid steel face sheets and foamed steel core was the subject of an analytical study (Szyniszewski et al (2012)), to assess the local buckling strength of such an arrangement. It was shown that when between 30 and 90% of the initial solid steel plate thickness was foamed, the resulting bending rigidity was greater than that of both the solid plate and fully foamed plate. In fact, indications were that when only the central 30% of the panel was foamed strength increased by up to 200%. This assessment was based on a comparison with a solid steel panel of similar mass. However the effective modulus and yield decreased (Szyniszewski et al (2012)).

6. CONCLUSION

Sandwich panels have been in use for several decades and their behaviour is generally well understood. However, as advances continue to be made in manufacturing, and new materials and composites are developed and subsequently incorporated into sandwich panel design, there is an ongoing need to test their adequacy in carrying typical loads.

7. REFERENCES

Ramakrishnan, K.V., Kumar, P.G.S. (2016) Applications of Sandwich Plate System for Ship Structures. IOSR Journal of Mechanical and Civil Engineering (IOSR-JMCE). International Conference on Emerging Trends in Engineering & Management (ICETEM-2016) 83-90

Dawood, M., Taylor, E., Rizkalla, S. (2010) Two-way bending behaviour of 3-D GFRP sandwich panels with through thickness fibre insertions. Composite Structures 92, 950-963

Abdi, B., Azwan, S., Abdullah, M.R., Ayob, A., Yahya, Y., Xin, L. (2014) Flatwise compression and flexural behaviour of foam core composite sandwich panels. International Journal of Mechanical Sciences 88, 138-144

Borsellino, C., Calabrese, L., Valenz, A. (2004) Experimental and numerical evaluation of sandwich composite structures. Composite Science and Technology 64, 1709-1715

Mamalis, A.G., Manolakos, D.E., Ioannidis, M.B., Papapostolou, D.P., Kostazos, P.K., Konstantinidis, D.G. (2002) On the compression of hybrid sandwich composite panels reinforced with internal tube inserts: experimental. Composite Structures 56, 191-199

Sovereign Technology Ltd. http://www.sovereignbd.com/sandwich-panel.html.

Daniel, I.M. (2009) Influence of core properties on the failure of composite sandwich beams. Journal of Mechanics of Materials and Structures Volume 4 No. 7-8, 1271-1286

Bezazi, A., El Mahi, A., Berthelot, J.-M., Bezzazi, B. (2007) Experimental analysis of behaviour and damage of sandwich composite materials in three-point bending. Part 1. Static tests and stiffness degradation at failure studies. Strength of Materials Volume 39 No.2, 170-177

Boyle, M.P., Roberts, J.C., Wienhold, P.D, Bao, G., White, G.J. (2001) Experimental, numerical, and analytical results for buckling and post-buckling of orthotropic rectangular sandwich panels. Composite Structures 52, 375-380

Wang, J., Evans, A.G., Dharmasena, K., Wadley, H.N.G. (2003) On the performance of truss panels with Kagomé cores. International Journal of Solids and Structures 40, 6981-6988

Mousa, M., Uddin, N. (2011) Global buckling of composite structural insulated wall panels. Materials and Design 32, 766-772

Adaptations of Cementitious Structural Insulated Panels for Multistory Construction. A Report by The Federation of American Scientists for The Charles Pankow Foundation (2009), 41pp

Szyniszewski, S., Smith, B.H., Hajjar, J.F., Arwade, SR., Schafer, B.W. (2012) Local buckling strength of steel sandwich panels. Thin-walled structures 59, 11-19

Panjehpour, M., Ali, A.A.A., Voo, Y.L. (2013) Structural Insulated Panels: Past, Present, and Future. Journal of Engineering, Project, and Production Management 3(1), 2-8

Benayoune, A., Samad, A.A.A., Trikha, D.N., Ali, A.A.A.A., Ashrabov, A.A. (2006) Structural behaviour of eccentrically loaded precast sandwich panels. Construction and Building Materials 20, 713-724

Dundu, M, Bukasa, G.M. (2013) Compression and Flexural Tests of Mi Panels. International Conference on Civil and Environmental Engineering (CEE'2013) Nov 27-28 Johannesburg, South Africa, 206-208

Bukasa, G.M., Dundu, M. (2014) Flexural Tests of Mi Panels. Construction Materials and Structures. S.O. Ekolu et al. (Eds.). IOS Press, 893-898

Bukasa, G.M., Dundu, M. (2014) Compression Tests of Mi Panels. Construction Materials and Structures. S.O. Ekolu et al. (Eds.). IOS Press, 899-903

Wattick, J.A., Chen, A. (2017) Development of a prototype fibre reinforced polymer- concrete filled wall panel. Engineering Structures 147, 297- 308

Home Made Composites.
http://www.composites.ugent.be/home_made_composites/what_are_composites.html

Cartié, D.D., Fleck, N.A. (2003) The effect of pin reinforcement upon the through-thickness compressive strength of foam-cored sandwich panels. Composites Science and Technology 63, 2401-2409

Avilés, F., Carlsson, L.A. (2006) Experimental study of debonded sandwich panels under compressive loading. Journal of Sandwich Structures and Materials 8, 7-31

Tuwair, H., Hopkins, M. , Jeffery Volz, J. , ElGawady, M.A. , Mohaned Mohamed, M. , Chandrashekhara, K. , Victor Birman, V. (2015) Evaluation of sandwich panels with various polyurethane foam-cores and ribs. Composites Part B 79, 262-276

Mamalis, A.G., Manolakos, D.E., Ioannidis, M.B., Papapostolou, D.P. (2005) On the crushing response of composite sandwich panels subjected to edgewise compression: experimental. Composite Structures 71, 246-257

Wicks, N., Hutchinson, J.W. (2004) Performance of sandwich plates with truss cores. Mechanics of Materials 36, 739-751

Proc. 1st International Conference on Structural Engineering Research (iCSER 2017)
20-22 Nov 2017, Sydney, Australia
ISBN: 978-0-6480147-6-8

Behaviour of Axially Loaded Cold-Formed Steel Built-Up Stub Columns

Mohamed Ghannam[1]

[1]Lecturer, Structural Engineering Department, Faculty of Engineering, Mansoura University, Mansoura, Egypt
Corresponding author's E-mail: m.ghannam@mans.edu.eg

Abstract

This paper aims to study the behaviour of axially loaded innovative cold-formed steel (CFS) built-up stub columns. Four innovative CFS built up sections is presented in this paper. Each section is composed of combination of more than two elements as follows: channels, channels with lip, Sigma section and /or plates. The elements of each section are assembled together by using self tapping screws. The axial load capacity of each of the four sections was investigated numerically by using finite element (FE) model using ABAQUS program. The FE model was verified against previous test data. The FE model was used to study different parameters that affect the load capacities of the innovative CFS built-up stub columns, these parameters are: columns profile, steel thickness, steel grade and longitudinal spacing between screws (fasteners), cross sectional area.

Keywords: Cold-formed steel, Built-up stub columns, Axial load capacity.

1. INTRODUCTION

Cold-formed steel (CFS) sections have been increasingly used nowadays in different building construction, such as trusses members, floor joists and wall studs (Zhang and Young 2012), this is owing to the advantages of the CFS section that overcome the rolled sections which is mainly increasing the strength to weight ratio.

Other advantages of the CFS section are: easy construction and flexibility in fabrication, different shapes in cross section that suits different purposes (Z-section C-section Hat-section and ∑- section). Also from the reasons for increasing the use of CFS section are: improved rolling and forming technology, improved connection technology as using blind rivets and self-drilling, self-tapping screws (Davies 2000; Faridmehr et al. 2016).

It was stated that residential and low rise building made of cold formed steel was about 75 000 in 1994 in USA this number increased by five time in 2002 (Davies 2000). Nowadays, there are efforts and researches are being done to use cold formed steel section with larger spans and higher loads (Meza et al. 2015). Analytical study was presented by Dundu (2011) showing an analytical study for using CFS section in a portal frames with span of 12 m and a spacing of 4.5 m.

Using CFS built up section is one of the effective ways to meet the current demand of using cold-formed section. Previously, many researcher study the behaviour of CFS built up section made up of two element, mainly two C-channels back to back or face to face (Dobric et al. 2015; Faridmehr et al. 2016; Lau and Ting 2009; Whittle and Ramseyer 2009; Zhang and Young 2012) with no spacing between the two elements.

However limited researches are available on CFS built up section formed of more than two elements. Meza et al. (2015) presented an experimental investigation of CFS built up stub columns. The research focused mainly on studying the effect of the connector spacing on the behaviour of the built up columns and it was concluded that the connectors spacing has more significant effect on the column behaviour than on the ultimate load capacity. Bujňák et al. (2012) present a stud on the axial capacity of 4 CFS built up columns, the study shows the substantial increase in load capacity compared to other cold formed members.

This paper aims to cover the gap in the field of studying the behaviour of CFS build up section especially, those composed of more than two elements. Four innovative CFS built up stub columns is presented in this paper (0e of these section was presented by Meza et al. (2015). The axial load capacity of the four columns was investigated through numerical and analytical study. It should be mentioned that in this study, axial load capacity refer to the ultimate load capacity of the column where the column can no longer sustain any more load.

The numerical study was carried out by using FE model, which was verified against the test result obtained by Meza et al. (2015). It was very important to develop a FE model as there is a lack of research that provide an accurate FE model for CFS built-up stub columns. The FE model was built using ABAQUS (ABAQUS 2012) FE program. The verified FE model was used to study different parameter that affect the load capacities of the innovative CFS built-up stub columns, these parameters are: columns profile, steel thickness, steel grade, longitudinal spacing between screws (fasteners) and cross sectional area.

2. FINITE ELEMENT MODEL

It was very important to develop a simplified FE that predicts the axial load capacity of the CFS built-up stub columns, in order to use this model in the parametric study. This section gives a detailed description for the FE model that is developed in this paper.

2.1. Description

The FE model was developed using ABAQUS (ABAQUS 2012) general FE modelling programme. All the CFS built-up section elements are modelled using general-purpose 4 nodded shell elements (S4R) which was chosen from the ABAQUS program library. Fixed end boundary condition was applied to the columns end though two reference point located at the column ends. Each of these reference points is coupled with the adjacent column end as indicated in Figure1. Maximum size of 12 mm was used in meshing with maximum aspect ratio of 2.

The surface-to-surface contact in ABAQUS (ABAQUS 2012) was adopted to simulate the interaction between the CFS element that are composing the built up section. Hard contact in the normal direction and Coulomb friction in the tangential directions were defined in the surface-to-surface contact. Tie constraint was used at the location of fastener that are connecting CFS element together. Full details on the FE model can be found in Ghannam (2017).

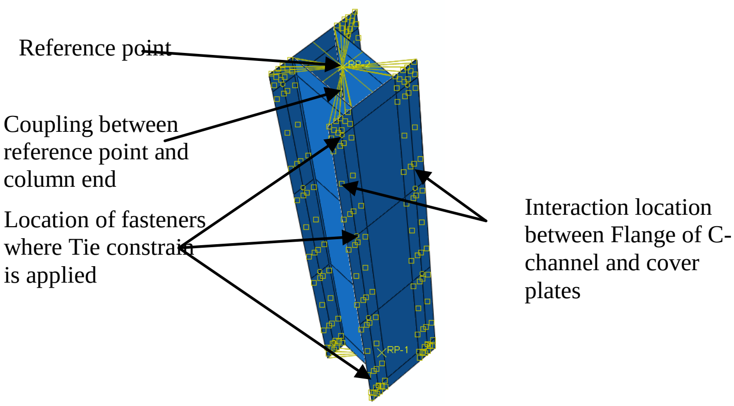

(a) Interaction and boundary conditions

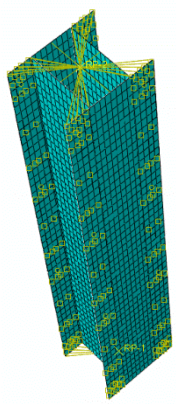

(b) Meshing

Figure 1. FE model adopted in this study

2.2. Verification of the FE model

The simplified FE model was verified against the test result performed by Meza et al. (2015). Brief details about the test performed by Meza et al. (2015), is introduced in this paragraph. The test program study the axial load capacity of two column profile of CFS built-up stub columns. Three stiffeners spacing were used in each column profile, each test was replicated twice, making a total number of twelve tested columns. The columns profile are indicated in Figure 2, test specimens matrix are shown in Table 1, it should be noted that Table 1 shows the details of specimens with no replication, that is why six columns are only shown in the table, these columns will be used for verifying the FE model. In Table 1, *L* is the columns length C-1 and C-2 is C-Channel no1 and C-channel no. 2 respectively as indicated in Figure 2, *a* is the longitudinal fastener spacing, it should be noted that the first fastener in all column is located at 50 mm from the columns end. $P_{U,Test}$ is the ultimate load obtained from the test (Meza et al. 2015) and $P_{U,FE}$ is the ultimate load obtained from the FE model developed by this study.

Figure3 shows a comparison between the load displacement curve of the test results and the FE model, and the Last column in Table 1 shows the ratio between ultimate test load ($P_{U,Test}$) and the ultimate load obtained from the FE model ($P_{U,FE}$). It can be observed that there is a good agreement between the test and the FE model up to the ultimate load. However, there is a difference between the test and the FE model at the failure zone, this can be explained due to the lack of data about the initial imperfection of each column, Meza et al. (2015) provide only the value of maximum and minimum value of imperfection which range from 0.1 and 0.69 for different CFS elements. Another reason, is the lack of information about the residual stress which was not provided by Meza et al. (2015) and was ignored in the FE model.

Figure4 shows a comparison between the failure modes in the test and the failure mode obtained by the FE model, good agreement can be observed between the test results and the FE model. As this study is concerned about the ultimate load value, this simplified FE model is considered to have a good agreement with the test result. If the full behavior of the column (pre and post ultimate stage) is under interest, initial imperfection, residual stresses and corner enhancement should be included in the FE model.

Table 1. Details of the test specimens (Meza et al. 2015) and results comparison.

Column	*L* (mm)	C-1, Web (mm)	C-1, Flange (mm)	Plate-width (mm)	C-2, Web (mm)	C-2, Flange (mm)	*a* (mm)	$P_{U,Test}$ (KN)	$P_{U,FE}$ (KN)	$P_{U,Test}/P_{U,Test}$
SC1-2	1100	154.12	53.75	199.78	-	-	333	183.97	180.75	1.02
SC1-3	1100	154.16	53.71	199.4	-	-	250	183.01	188.49	0.97
SC1-5	1100	154.17	53.62	199.79	-	-	167	201.72	225.45	0.89
SC2-2	800	154.09	53.38	-	79.00	36.28	233	213.32	240.88	0.89
SC2-4	800	154.04	53.44	-	79.17	36.45	140	238	245.89	0.97
SC2-6	800	154.24	53.73	-	79.05	36.26	100	232.62	263.71	0.88

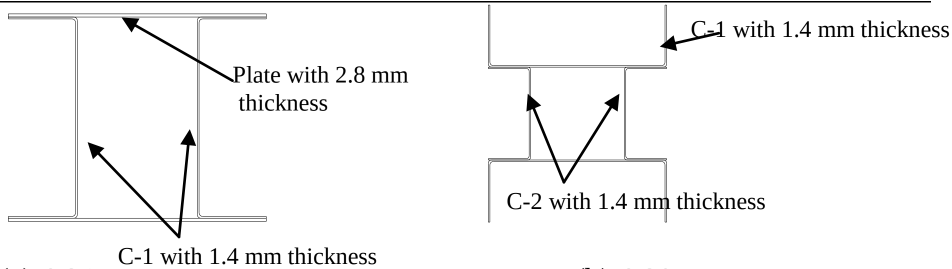

(a) SC1 (b) SC2

Figure 2. Columns profile used by Meza et al. (2015)

3. PARAMETRIC STUDIES OF COLD-FORMED STEEL (CFS) STUB COLUMNS

Parametric studies on axial load capacities were conducted for four columns profiles of cold-formed steel (CFS) built-up stub columns using the verified FE model as discussed in the previous section. Investigated parameters include, cross section profile (one profile were used as in Meza et al. (2015)

and another 3 innovate profiles), steel yielding strength (f_y) (240, 280 and 360 MPa as per ECP-205 (2008)), thickness of CFS section (t), vertical spacing between fasteners (a), cross sectional area (A). Table 2 gives details for each of the four Profiles. Figure5 presents a schematic diagram for each profile that was used in the parametric studies. It should be mentioned that, five cross sections (S1, S2, S3, S4 and S5) were used in each profile. Each cross section has equal area in the four profiles as indicated in Table 2. For instance, the cross sectional area of S1 = 5612 mm^2 , this cross section area is nearly the same in Profile: 1, 2 3 and 4.

Table 2. Different profiles and sections used in this study.

		Profile 1		**Profile 2**		**Profile 3**		**Profile 4**	
		Vertical	Horizontal	Vertical	Horizontal	Vertical	Horizontal	Vertical	Horizontal
Cross section	**S1**	C400x100x2.5	Pl 530x2.5	Σ 300x90x2.5	C360x100x2.5	C 400x100x2.5	Pl 530x2.5	C300x100x2.5	C360x100x2.5
	S2	C 400x100x4	Pl 520x4	Σ 300x90x4	C 360x100x4	C 400x100x4	Pl 520x4	C 300x100x4	C 360x100x4
	S3	C400x100x1.5	Pl 540x1.5	Σ 300x90x1.5	C360x100x1.5	C 400x100x1.5	Pl 540x1.5	C300x100x1.5	C360x100x1.5
	S4	C270x100x2.5	Pl 510x2.5	Σ 200x65x2.5	C360x100x2.5	C 270x100x2.5	Pl 510x2.5	C 200x71x2.5	C360x100x2.5
	S5	C400x100x2.5	Pl 380x2.5	Σ300x90x2.5	C 250x80x2.5	C400x100x2.5	Pl 380x2.5	C300x100x2.5	C 250x80x2.5

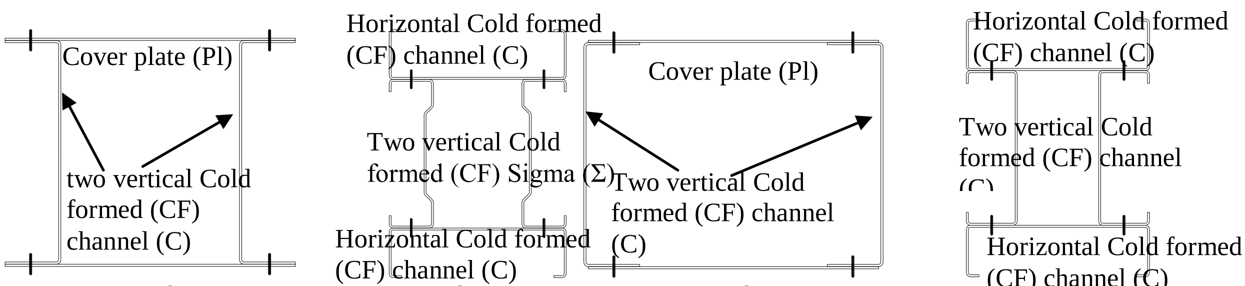

(a) Profile 1 (b) Profile 2 (c) Profile 3 (d) Profile 4

Figure 3. Four Different profiles used in the parametric study.

Different parameters that were used in this study are indicated in Table 3. Steel yielding strength (f_y) was used as in ECP-205 (2008) (240, 280 and 360 MPa). Three values of thicknesses were used; 1.5, 2.5 and 4 mm. Four different value of cross sectional areas were used in each profile as indicated in Table 2 and Table 3. It should be mentioned that sections S4 and S5 has the same cross sectional area but they are different in the value of the moment of inertia (I).

Five values of vertical spacing between the fasteners connecting different element of CFS built up stub columns were used. The locations of the spacing in the horizontal cross section in each profile are shown in Figure5. The value of spacing were chosen for different profiles such that two of the spacing are within the limits that is proposed by AISI-S100 (2007) in the section D1.3 and the other three spacing are outside this limit.

The influences of different parameters on the axial capacity (P_{FE}) of CFS stub columns which was calculated by using the verified FE model are presented in Figure6. As expected it was found that the axial capacity is directly proportional to steel yielding strength (f_y), CFS thickness (t) and the cross sectional area of different profiles.

By comparing the axial load capacity of section 4 and section 5 from different profiles which have the same cross section area but different in there moment of inertia, it was found that both sections give close result to each other, which shows that moment of inertia is not effective for the axial load capacity of stub columns, this is indicated in Figure6(b). This conclusion is verified in Fig.6(i) which shows moment of inertia's effect on the ultimate load capacity. No clear trend can be observed in this Fig.6(i). The main failure mode for stub columns is local buckling failure which depend on the plate slenderness (width to thickness ratio) as indicated in Figure4, for that reason, moment of inertia has no significant effect on the column's load capacity. Moment of Inertia might have a significant effect on the load capacity of the slender columns where the columns may fail due to one or combination of the following failure modes: local, distortional and flexural buckling mode

It can be noted from Figure6 (d, e, f and g), that increasing spacing between fastener decreases the Axial load capacity of the CFS built-up stub columns as a result of increasing the buckling of the individual elements forming up the built up section. Using the spacing within the limits proposed by AISI-S100 (2007) produce no reduction in the axial load capacity. Axial load capacity begin to decrease after increasing the spacing over the value proposed by AISI-S100 (2007) as indicated in Figure6 (d, e, f and g).

The effect of increasing the spacing is more pronouncing in profile 1 and 3 than profile 2 and 4 as indicated in Figure6 (d, e, f and g). This is as a result of using cover plate in profile 1 and 3 which has lower stiffness in x-direction compared to the horizontal C channels used in profile 2 and 4.

Figure6 (h) shows that profile 2 give the highest axial load capacity, followed by profile 4. Profile 1 and 3 give similar values of axial load capacity. This can be explained as profile 2 contains Σ section which has more stiffness compared to the C channel as the web of the Σ section is stiffened and the C channel web is not stiffened. Profile 4 gives higher axial load capacity compared to profile 1 and 3 because the flange of the C channel in profile 4 is stiffened with vertical lipped stiffener and the flange of the C channel in profile 1 and 3 is not stiffened.

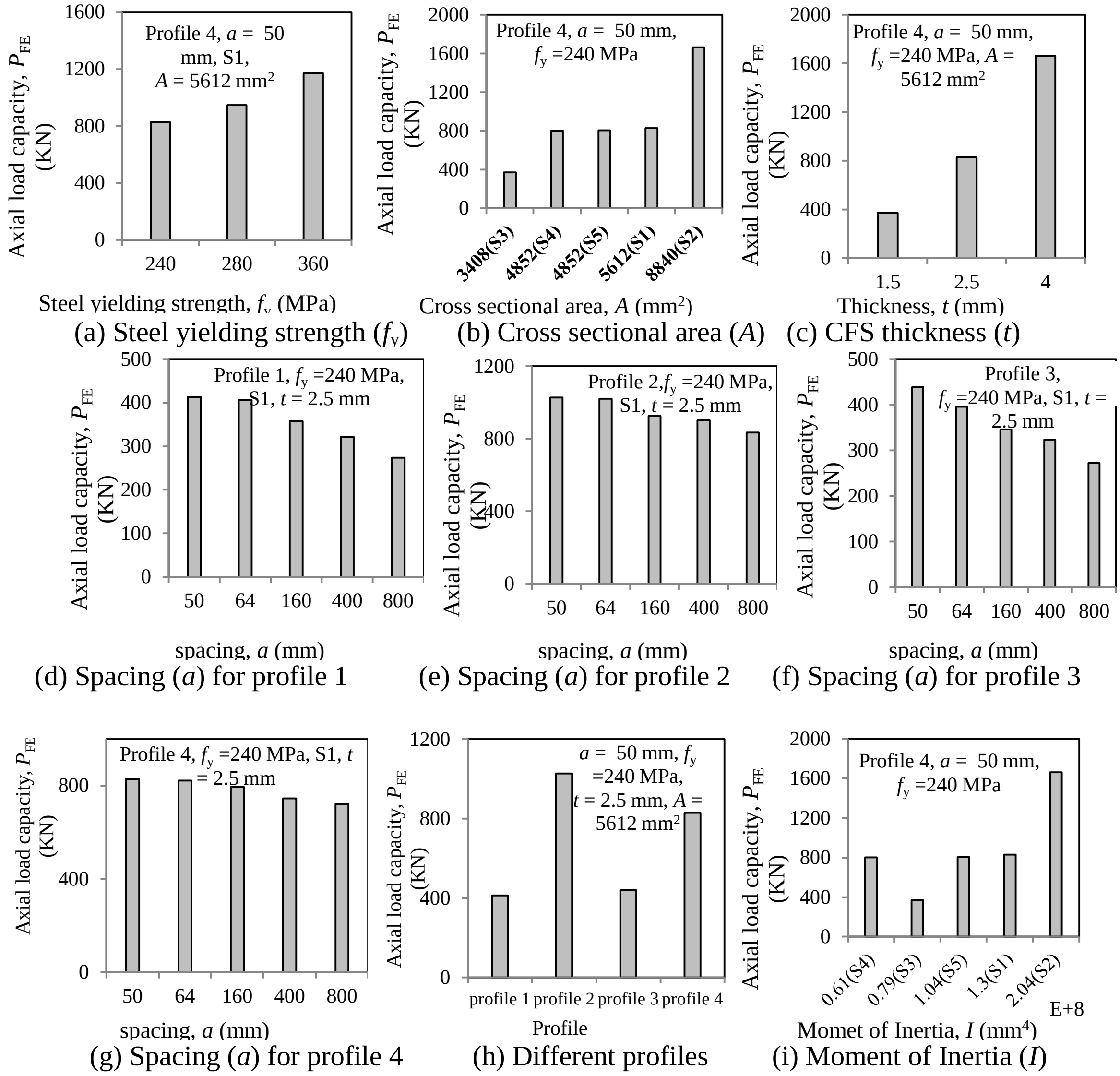

Figure 4. Effect of different parameters on CFS built-up stub columns.

4. CONCLUSIONS

In this paper, 4 innovative profile of CFS built-up stub columns (one of them is presented by Meza et al. (2015)) was presented and studied using verified FE model. Detailed parametric study have been carried out on the new profiles based on the axial load capacity of each column profile. Conclusions that are derived from this study are listed below:

1) Axial Load capacity is directly proportional to steel yielding strength (f_y), CFS thickness (t) and the cross sectional area of different profiles. Axial load capacity is inversely proportional with the vertical spacing between fasteners; this effect is more significant with section profiles which contain cover plates (eg. profile 1 and 3).
2) Axial load capacity of stub columns is greatly affected by the stiffened element within the cross section, increasing the stiffeners through the web and the flange increase significantly the axial load capacity.
3) From the profiles presented in this study, profile 2 gives the highest load capacity as the web and flange are both stiffened.
4) CFS built up stub columns can carry axial load more than 2000 KN based on the thickness and the steel type (as in profile 2), this conclusion gives encouragement to expand the use of CFS section in more structures type other than light loaded structure only.

5. REFERENCES

ABAQUS (2012). "ABAQUS standard user's manual, Version 6.12." Dassault Systèmes Corp., Providence, RI, USA.

AISI-S100 (2007). "North American Specification for the Design of Cold-Formed Steel Structural Members 2007 EDITION." American Iron and Steel Institute and Canadian Standards Association, Canada.

Bujňák, J., Vičan, J., Georgieva, I., Schueremans, L., Vandewalle, L., and Pyl, L. (2012). "Design of built-up cold-formed steel columns according to the direct strength method." *Procedia Engineering*, 40, 119-124.

Davies, J. M. (2000). "Recent research advances in cold-formed steel structures." *Journal of Constructional Steel Research*, 55(1–3), 267-288.

Dobric, J. D., Markovic, Z. A., Budjevac, D. V., Spremić, M. J., Fric, N. T., and Pavlovic, M. S. (2015). "Experimental investigation of flexural buckling of cold formed built-up stainless steel members." *Advances in steel structures*Lisbon, Portugal, 8.

Dundu, M. (2011). "Design approach of cold-formed steel portal frames." *International Journal of Steel Structures*, 11(3), 259-273.

ECP-205 (2008). "Egyptian code of practice for steel construction (load and resistance factor design) (LRFD)." Ministry of Housing, Utilities and Urban Communities, Housing and Building National Research Centre, Cairo, Egypt.

Faridmehr, I., Osman, M. H., Tahir, M. M., Azimi, M., and Gholami, M. (2016). "Behaviour and design of cold-formed steel C-sections with cover plates under bending." *International Journal of Steel Structures*, 16(2), 587-600.

Ghannam, M. (2017). "Axial load capacity of cold-formed steel built-up stub columns." *International Journal of Steel Structures*.

Lau, H. H., and Ting, T. C. H. "An Investigation of The Compressive Strength of Cold-formed Steel Built-up I Sections." *Proc., Sixth International Conference on Advances in Steel Structures*, The Hong Kong Institute of Steel Construction, 441-449.

Meza, F., Becque, J., and Hajirasouliha, I. (2015). "Experimental investigation of cold-formed steel built-up stub columns." *Advances in steel structures*Lisbon, Portugal, 10.

Whittle, J., and Ramseyer, C. (2009). "Buckling capacities of axially loaded, cold-formed, built-up C-channels." *Thin-Walled Structures*, 47(2), 190-201.

Zhang, J.-H., and Young, B. (2012). "Compression tests of cold-formed steel I-shaped open sections with edge and web stiffeners." *Thin-Walled Structures*, 52, 1-11.

Proc. 1st International Conference on Structural Engineering Research (iCSER 2017)
20-22 Nov 2017, Sydney, Australia
ISBN: 978-0-6480147-6-8

Experimental Investigation on Composite Steel and Precast Reinforced Concrete Transom under Impact Loading

Andrew Talos[1], Olivia Mirza[2] and Brendan Kirkland[3]

[1]Honours Student, Western Sydney University, Sydney, Australia
[2]Senior Lecturer, Western Sydney University, Sydney, Australia
[3]Associate Lecturer, Western Sydney University, Sydney, Australia
Corresponding author's E-mail: O.Mirza@westernsydney.edu.au

Abstract

Materials such as timber, concrete and steel have been utilised in the fabrication of transoms in railway bridges worldwide. Timber transoms are commonly used in Australia's railway network but frequently require maintenance and replacement due to the degradation of the timber. Therefore, they are not favourable for use in today's railway systems. To be a viable option for replacement, proposed transoms should provide practical, financial and structural benefits. This research outlines the structural benefits of composite steel-concrete transoms for ballastless tracks on the Sydney Harbour Bridge. The paper herein considers both reinforced concrete and prestressed concrete and simulates the derailment impact loading of a train through dynamic experimental testing. The paper also evaluates the potential use of 3 different shear connectors; welded shear studs, Lindapter bolts and Ajax bolts. The results of the experimental tests are used to determine whether each transom is a viable option for the replacement of the current timber transoms on the Sydney Harbour Bridge and whether they provide a stronger and longer lasting solution to the current transom problem.

Keywords: Composite Transom, Experimental Investigation, Impact Loading, Sydney Harbour Bridge.

1. INTRODUCTION

Transoms are one of the most important components of a railway system as they are designed as load carrying elements of a railway bridge which span under the roadway and transfer the loads of the railway to the trusses and beams. Current timber transoms are susceptible to biological and chemical degradation which reduces its service life and requires frequent maintenance and replacement. Alternative materials such as composite steel-concrete panels are starting to be implemented more as they provide a material which utilises the best attributes of each individual element providing higher strength, long service life and flexibility in design. Most research conducted thus far focuses on ballast tracks under static and dynamic loading but does not test derailment impact loading scenarios for transoms. Therefore, this research presents an experimental investigation of derailment impact loading for ballastless tracks determining the failure mode and ultimate capacity of the specimens. This will provide a guide for design engineers to use in the safe and economical design of railway bridges. The aim of this research is to determine the feasibility of replacing existing timber transoms with composite steel and precast concrete transoms for the Sydney Harbour Bridge when subjected to derailment impact loading. This research conducts an experimental study to determine the failure behaviour and ultimate capacity of composite steel and precast concrete transoms.

Existing research predominantly investigates the static and dynamic loading on railway bridge structures but are limited on investigations for derailment loading onto bridge structure itself. A case study conducted by Darwish (2015) conducted a site investigation of a railway bridge in Baghdad. This research applied actual static live loading and dynamic loads to the bridge by passing a heavy locomotive over it at different speeds and stopping it in selective spots to understand how the structure reacts and deflects to different loading scenarios. Similar studies conducted by Griffin et al. (2014) and Griffin et al. (2015) showed static tests on composite slabs, however, the studies did not investigate the derailment impact loading due to the locomotive.

Caglayan et al. (2011) studied the dynamic and seismic loading of a ballastless railway bridge system located in an earthquake prone region in Turkey. This research consists of two sections which are the field analysis, consisting of quasi static tests and free vibration tests, and the computer model analysis. These were undertaken to understand the behaviour of the bridge superstructure in different scenarios and to also calibrate the computer model. Design of these bridges is crucial for long term performance to determine the shortfall of existing structures.

A full scale of field tests of a railway bridge in Los Angeles was conducted by Maragakis, Douglas & Chen (1995) aiming to determine the seismic performance of a typical single span bridge quantifying the beneficial effects the rails provide between the structure. This research consisted of experimental studies conducted to identify the ultimate strength of railway bridges, dynamic properties and their responses due to earthquake excitations. This full range of testing was done as the bridge was scheduled for demolition providing a perfect candidate for testing. This research did look at how different sections of a railway track affect its overall performance however none of the tests performed study the effects caused by impact loading scenarios.

Researching derailment impact loading scenarios is crucial especially in bridge applications as failure to withstand these loadings can lead to tragic accidents. The available literature discussed the behaviour of ballast tracks however did not focus on the effects in ballastless tracks. Hence, the purpose of this paper is to fill the knowledge gap of ballastless tracks under derailment loading scenarios in the plastic region. This paper also aims to produce the failure modes and ultimate capacity of the specimen in order to provide a guide for engineers to use in designing railway bridges.

2. EXPERIMENTAL STUDY

2.1. Experimental Specimens

A total of 6 specimens (3 conventionally reinforced and 3 pre-stressed reinforced) of 2100 mm length were tested. The cross-sectional area of the transoms is 600 mm wide x 180 mm thick. The conventional transoms consist of N10 stirrups at 90 mm spacing, 2 N12 reinforcing bars of 2030 mm length at the bottom and 4 N28 reinforcing bars of 2030 mm length at the top. The pre-stressed transoms consist of N 10 stirrups at 90 mm spacing, 4 N12 reinforcing bars of 2030 mm long (2 at the top and bottom corners) and 3 pre-stressed strands of 15.7 mm diameter at the top. The types of connectors in the beams include 19 mm welded shear studs, 20 mm Ajax bolts and 29 mm Lindapter bolts. Table 1 shows the loading condition, reinforcement type and the shear stud connection type for each of the transoms. Composite steel-concrete panels are being implemented more in industry as they provide a material which utilises the best attributes of each individual element providing higher strength, long service life and flexibility in design hence why testing was conducted on these specimens. Figure 1 shows the location of the frame resisting the impact load and the location to the impact load on a longitudinal section view. The sides of the frame are first set up and bolted to the hardstand floor. From there the composite steel and precast concrete transom is loaded into the testing rig and aligned 500 mm from the edge to center of the drop hammer. The specimen was then bolted into place with the top member of the frame as shown in Figure 2. The strain gauges in the transom are then connected to the datalogger. The impact loading machine is also connected to the datalogger to record the loading applied. A displacement laser was then placed under the impact point and connected to the datalogger. To aquire measurements of the tip deflection a slo-motion camera and metre ruler are utilized for each of the tests. A rubber padding is placed at the impact zone of the specimen to reduce the initial peak load experienced. The drop hammer is then raised to the predetermined height with the data logger starting just before it was dropped. The results are recorded by the datalogger and later graphed and interpreted. Audible and visual inspections during and after the test are also recorded down.

Table 1: List of specimens and details

Specimen Name	Loading Condition	Reinforcement	Shear Studs
WSBC	Dynamic	Conventional	Welded
ABBC	Dynamic	Conventional	Retrofitted Ajax Bolts
LBBC	Dynamic	Conventional	Retrofitted Lindapter Bolts
WSBP	Dynamic	Pre-stressed	Welded
ABBP	Dynamic	Pre-stressed	Retrofitted Ajax Bolts
LBBP	Dynamic	Pre-stressed	Retrofitted Lindapter Bolts

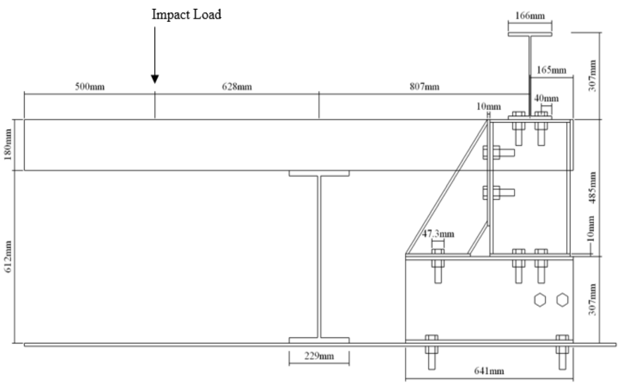

Figure 1: Frame and impact loading location on longitudinal sectional view

Figure 2: Frame setup

3. RESULTS AND DISCUSSION

3.1. Conventionally Reinforced Results

For the testing conducted on the specimens mentioned above, it can be concluded that all of the conventionally reinforced specimens behave similarly when subjected to impact loading. General observations showed that all tests experienced shear failures in the concrete around the impact zone region. All the specimens showed minimal cracking on the sides towards the supports with more significant cracks on the top face through the grouting. All the samples showed concrete crushing at the impact zone as a result of the repeated dynamic impact loading phenomenon between the drop hammer and the transom. It was also observed that all of the cross sections at the loaded end had delamination of the Bondek sheeting from the concrete transom. Figures 3 to 5 show the failure that occurred in the WSBC, LBBC and ABBC samples when the hammer was dropped from a height of 2 m.

Figure 3: WSBC concrete failure

Figure 4: LBBC concrete failure

Figure 5: ABBC concrete failure

For this comparative section, the data that is being compared is the real load experienced and the permanent damage deformation of the transom. The reason for the comparison of this data is because they are part of the critical information required for determining which shear stud provides the strongest and most reliable connection for the transom.

For the comparison of the results for the conventionally reinforced specimens, both the Lindapter and Ajax bolts will be compared to the welded shear studs as they are the most commonly used shear connection in industrial practice. The real load capacity observed for the welded shear studs was slightly higher than both the two bolts. The real load for WSBC was found to be 454.2 kN. The Lindapter and Ajax bolts showed a decrease in the real load of 4.9% and 10.2% respectively. The permanent damage deformation of the Lindapter bolts showed a 1.5 mm difference corresponding to an 11.3% decrease in comparison to the welded shear studs, whereas the Ajax bolts showed a displacement increase of 2.6 mm, corresponding to an overall permanent damage deformation increase of 19.5%. Figure 6 shows the comparison of the displacement versus time for the conventionally reinforced specimens.

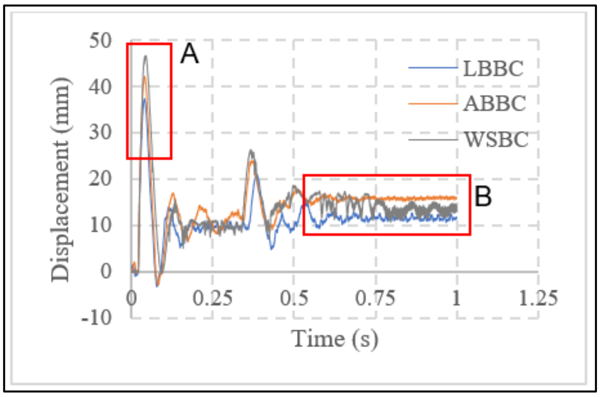

Figure 6: Displacement versus time comparison for conventionally reinforced specimens

Table 2: Conventional specimen summary data

	WSBC	LBBC	ABBC
Load (kN)	454.2	431.8	408
Strain	0.00015	0.0023	0.00219
Permanent Damage Deformation (mm)	13.3	11.8	15.9

From the strain results observed, the reinforcing steel for both the Lindapter and Ajax take more strain due to their bolt configuration. The reasoning why these reinforcing bars take more strain is because of the nut connection that these two have at the contact surface between the concrete and the supporting steel beam. Since the contact surface area for the welded shear stud is lower, it cannot take as much strain. Figure 6 segment A illustrated the initial displacement while segment B displays the permanent damage deformation experienced.

The results from this testing indicate that the Lindapter connector is the best in regards to maximum displacement and permanent deformation, however, the welded shear stud was found to be able to sustain a higher load. Table 2 shows the summary table of all the data discussed for the conventionally reinforced transom.

3.2. Pre-stressed Reinforced Results

General observations illustrate that three pre-stressed specimens showed some similarities in failure modes when subjected to impact loading. All the specimens had cracking form on the sides at the connection but only the Lindapter and Ajax had significant cracking in this region. This was because both of these specimens concrete failed towards the connection on the side nearest to the impact load, while the welded shear stud specimen failed due to concrete shear cracking at the impact zone. Both the welded shear stud and Ajax showed significant shear cracks towards the impact zone while the Lindapter only had minor cracks in this region. For all of these specimens, it was seen that there was significant cracking on the top face through the grouting. All of the samples showed concrete crushing at the impact zone as a result of the repeated dynamic impact loading phenomenon between the drop hammer and the transom. It was also observed that all of the cross sections at the loaded end had delamination of the Bondek sheeting from the concrete transom. Figures 7 to 9 show the failure that occurred in the WSBP, LBBP and ABBP samples when the hammer was dropped from a height of 2 m.

Figure 7: WSBP concrete failure

Figure 8: LBBP concrete failure

Figure 9: ABBP concrete failure

For the comparison of the results for the pre-stressed reinforced specimens, both the Lindapter and Ajax bolts will be compared to the welded shear studs following the same method as the conventional analysis. The real load capacity observed for the welded shear stud was larger than both the two bolts. The real load for the welded shear stud was found to be 486.8 kN. The Lindapter and Ajax bolts showed a decrease in the real load of 22.2% and 20.1% respectively. The permanent damage deformation of the Lindapter bolts showed a 27 mm difference corresponding to an 63.7% decrease in comparison to the welded shear studs, whereas the Ajax bolts showed a displacement decrease of 26.9 mm, corresponding to an overall permanent damage deformation decrease of 63.4%. Figure 10 shows the comparison of the displacement versus time for the conventionally reinforced specimens.

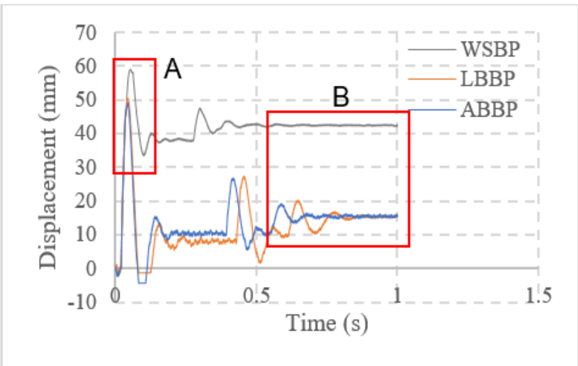

Figure 10: Displacement versus time comparison for pre-stressed reinforced specimens

Table 3: Pre-stressed specimen summary data

	WSBP	LBBP	ABBP
Load (kN)	486.8	378.6	389.1
Strain	0.00116	0.00196	0.00138
Permanent Damage Deformation (mm)	42.4	15.4	15.5

From the strain results observed, the reinforcing steel for both the Lindapter and Ajax take more strain due to their bolt configuration. The reasoning why these reinforcing bars take more strain is because of the nut connection that these two have at the contact surface between the concrete and the supporting steel beam. Since the contact surface area for the welded shear stud is lower, it cannot take as much strain.

The results from this testing indicate that the Lindapter and Ajax bolts are the best in regards to maximum displacement and permanent deformation, however, the welded shear stud was found to be able to sustain a higher load. Table 3 shows the summary table of all the data discussed for the pre-stressed reinforced transom.

4. CONCLUSION

The results showed that for the conventionally reinforced real load capacity, the welded shear stud was slightly higher than the Lindapter and Ajax bolts. The reasoning for this is because the welded shear bolt has a larger single surface area in comparison to the other two bolts resulting in a better resistance to loading. For the pre-stressed reinforced specimens, the real load capacity observed for the welded shear stud was significantly larger than the other two bolts.

For the conventional transoms, the Lindapter bolts showed the least permanent damage deformation in comparison to the weld shear studs and Ajax bolts. For the pre-stressed transoms, the permanent damage deformation of the Lindapter and Ajax bolts were very similar with minor differences.

The conventional results displayed through the graphs show that all three specimens display similar displacement results due to their similar shear failures that occurred in each transom. The pre-stressed results showed through the graph that the welded shear stud sustained shear failure of concrete by its higher permanent damage deformation while both the Lindapter and Ajax bolts displayed significantly lower permanent damage deformation as both these transoms failed towards the connection.

5. ACKNOWLEDGMENTS

I would like to express my sincere gratitude to my supervisor Dr. Olivia Mirza for her endless support and guidance throughout this paper. I would also like to thank my co-supervisor Dr. Brendan Kirkland and Mr. Matthew Hennessey for their collaboration and contributions. I would like to mention a special thanks to Mr. Zac White and the University of Wollongong's technical staff for their help during the testing stage. I would like to thank the industry partners Transport for New South Wales for sharing their technical knowledge, the School of Engineering at Western Sydney University for providing a productive environment for my studies and EJF Engineering for manufacturing the frame. I would lastly like to give a special thanks to my family for their constant support during this paper.

6. REFERENCES

Caglayan, O, Ozakgul, K, Tezer, O & Uzgider, E 2011, 'Evaluation of a steel railway bridge for dynamic and seismic loads', *Journal of Constructional Steel Research*, vol. 67, no. 8, pp. 1198-211.

Darwish, AM 2015, 'Static and dynamic loading test of a railway bridge', *Acta Technica Corviniensis - Bulletin of Engineering*, vol. 8, no. 2, pp. 145-8.

Griffin, D, Mirza, O, Kwok, K & Kaewunruen, S 2014, 'Composite slabs for railway construction and maintenance: a mechanistic review', *The IES Journal Part A: Civil & Structural Engineering*, vol. 7, no. 4, pp. 243-62.

Griffin, D, Mirza, O, Kwok, K & Kaewunruen, S 2015, 'Finite element modelling of modular precast composites for railway track support structure: A battle to save Sydney Harbour Bridge', *Australian Journal of Structural Engineering*, vol. 16, no. 2, pp. 150-68.

Maragakis, E, Douglas, BM & Chen, Q 1995, 'Full-scale field tests of a railway bridge', *Railway Age*, vol. 196, no. 9, pp. 101-3.

Proc. 1st International Conference on Structural Engineering Research (iCSER 2017)
20-22 Nov 2017, Sydney, Australia
ISBN: 978-0-6480147-6-8

Numerical Investigation of Composite Steel and Precast Reinforced Concrete Transom for Sydney Harbour Bridge under Static Loading

Matthew J Hennessy[1], Olivia Mirza[2] and Md Kamrul Hassan[3]

[1]Student, Western Sydney University, Sydney, Australia
[2]Senior Lecturer, Western Sydney University, Sydney, Australia
[3]Post Doctorate Researcher, Western Sydney University, Sydney, Australia
Corresponding author's E-mail: O.Mirza@westernsydney.edu.au

Abstract

The Sydney Harbour Bridge requires the replacement of the timber transoms that currently reside in the railway system. Composite steel and precast reinforced concrete transoms have been proposed as the replacement for the current timber counterparts. In existing studies, it is found that there is little investigation into the effect of derailment loading on reinforced concrete transoms. This paper provides a continuation on a previous study of static loading on reinforced concrete transoms and investigates the failure behaviour through means of finite element analysis. The FEA commercial software known as ABAQUS was used to investigate the effect of static loading on the composite concrete transoms. The FE data accuracy was verified by comparing the existing experimental results. The experimental study and numerical investigation, transoms using AJAX bolts was shown to perform better than the welded headed shear studs. Additionally, the FE models produced in this study were validated by the results of the experimental study; however, further investigation into the damage properties is required before proper evaluation of the failure behaviour is determined.

Keywords: Railway, Static, Failure, Finite element analysis, Concrete

1. INTRODUCTION

Through history, railway systems have incorporated large amounts of timber into the construction of various components. The most common component that utilises timber is the transom; mostly due to the availability of timber and simplicity with regards to construction and transportation. However, timber is susceptible to environmental and climate conditions, often leading to a low service life. For instance, the Sydney Harbour Bridge's railway network currently used timber transoms that require a high level of maintenance, hence, a more durable material is being sought after to replace the current transoms. To create a more consistent railway track in terms of quality and comfort for the passengers, and to provide the long-term functionality required, an alternative material must be found. In the modern era, railway locomotive speeds have been increasing as detailed by González-Nicieza et al. (2008) where it is stated that improvements in transom design is mainly focused upon increasing the durability of the sleeper around the loading produced by higher speeds of the locomotive. In recent studies, it is found that there is a lack of investigations with regards to numerical static railway loading scenarios on reinforced concrete. The purpose of this numerical investigation is to provide a detailed analysis of the performance of reinforced concrete transoms under static railway loading. This study provides a continuation on an existing experimental study conducted by Zaher (2016). This study aimed to explore the ultimate load capacity of conventionally reinforced composite concrete transoms. Experimental testing was conducted on two conventionally reinforced specimens using AJAX and welded headed shear studs. The experimental loading setup is illustrated in Figure 1. Since the numerical investigation herein simulated half the experimental specimen, the loading point used is the leftmost point of loading presented in Figure 1 with Point A. The loading of the transom consisted several stages; firstly, repeated increasing loads of 100 kN, 150 kN, 240 kN and 360 kN was applied to the transom at service load. Finally, a load of 900 kN was applied to determine the ultimate capacity of the transom. The failure behaviour is illustrated in Figure 2. From the results, it was concluded that the AJAX bolts perform better than the welded shear studs. Similarly, in a numerical and experimental investigation conducted by Johnston (2016), the same transom was analysed but being made of a glass fibre composite material. With the loading conditions being identical, it was also shown that the AJAX bolts outperformed the alternative shear connector.

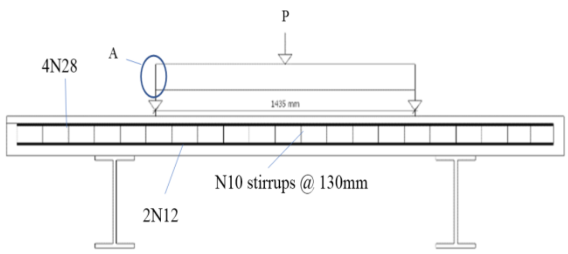

Figure 1. Numerical and experimental loading

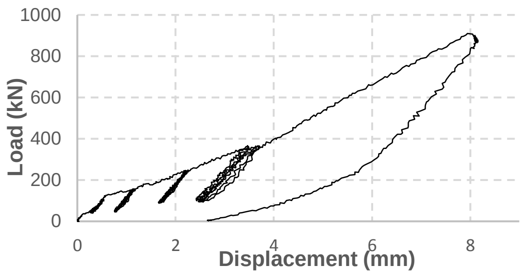

Figure 2. Experimental failure behaviour

2. FINITE ELEMENT MODEL

2.1. Element Type, Mesh and Contact Interactions

The elements used for the nodes in this investigation are the C3D8R element. As stated by Mirza (2008), this is derived from the five aspects of their behaviour; the family, degrees of freedom, number of nodes, formulation and integration. For the element utilised as stated above, the 'C' refers to the solid continuum family, the '3D' refers to the three degrees of translational freedom at each node, the '8' refers to the number of node for which the degrees of freedom are calculated and the 'R' refers to the reduced integration method for calculation purposes. The C3D8R element is used for all parts except for the conventional reinforcement where the truss element, T3D2 is used. Meshing, an important aspect in finite element analysis requires a mesh sizing to be applied to each part instance, this greatly induces the simulation time and accuracy of the results. Meshing is based upon a sensitivity analysis conducted by Griffin (2013) due to the similarity of FE models. For consistency, the same mesh size is used across all specimens presented herein.

The importance of contact interaction is greatly increased when the composite structure is considered since the load-bearing capacity of the structure is dependent upon the interaction between one or more elements. Surface to surface contacts are used for connecting the concrete to prestress tendons and Bondek II as well as connecting the Bondek II to the stringer beam. Complex interactions regarding the connection of the shear studs used the tie interaction to reduce simulation times.

2.2. Boundary Condition and Model Setup

The FE model consists of four specimens: Conventionally reinforced concrete transom with welded shear studs (CS-Welded), conventionally reinforced concrete transom with AJAX bolts (CS-AJAX), prestressed concrete transom with welded shear studs (PS-Welded) and prestressed concrete transom with AJAX bolts (PS-AJAX). All specimens are 2100 mm in length, 180 mm in depth with stiffened 610UB125 steel beams spaced 991 mm from the centre section of the transom.

3. RESULTS AND DISCUSSION

3.1. General

To keep results consistent, only the elasto-plastic region of the experimental and numerical results was considered. This is due to the concrete damage properties not yet being defined in the FE models. Hence, the presentation of the graphs was limited to 2 mm of displacement for clarity purposes. For deformation stress contour plots of the FE model, stress is limited to 10 percent of the characteristic strength of the concrete to observe the cracking failure of the concrete.

3.2. Conventionally Reinforced Transom with Welded Shear Stud (CSWelded)

To verify the numerical analysis, the results of the numerical static analysis were compared to the experimental results produced by Zaher (2016). Figure 3 shows the comparison of the experimental and numerical load versus displacement results. The graph shows a similar behaviour to experimental data and the discrepancy is with 10%. The failure behaviour of concrete is illustrated in Figure 4 through a deformation stress contour plot of the FE model.

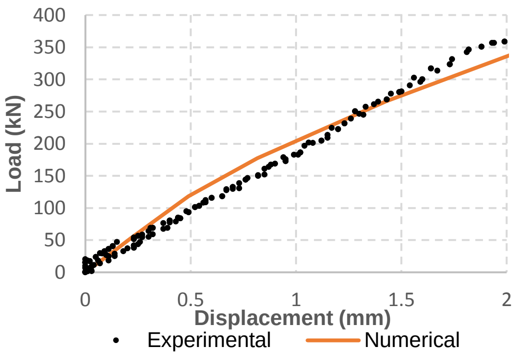

Figure 3: Comparison of numerical and experimental results for CSWelded

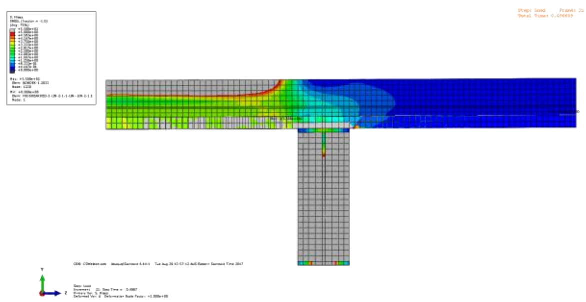

Figure 4: Stress contour plot of specimen CSWelded

From the numerical and experimental results, the loading produced to develop 2 mm of displacement was 336 kN and 360 kN respectively, corresponding to a 7% difference. Stiffness was also calculated to be 168 kN/mm for numerical analysis and 180 kN/mm for the experimental testing. These results are summarised in Table 4. From Figure 6, the cracking failure of the concrete is visualised through the red section of the stress contours. Cone shaped stress can also be observed around the support.

3.3. Conventionally Reinforced Transom with AJAX Bolts (CSAJAX)

Figure 5 shows the comparison of the experimental and numerical load versus displacement results. The failure behaviour of concrete is illustrated in Figure 6.

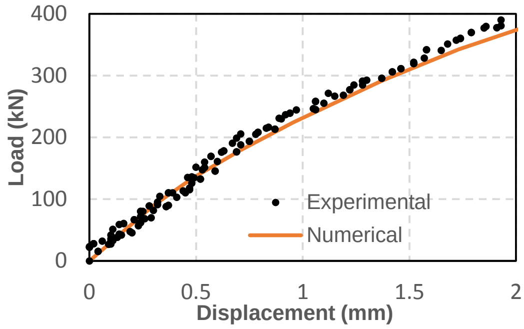

Figure 5: Comparison of numerical and experimental results for CSAJAX

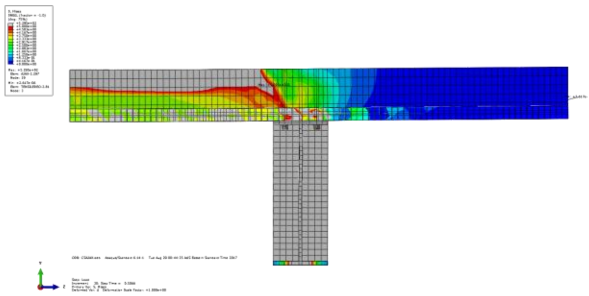

Figure 6: Stress contour plot of specimen CSAJAX

.

From the numerical and experimental results, the loading produced to develop 2 mm of displacement was 374 kN and 390 kN respectively, corresponding to a 4.3% increase. Stiffness was also calculated to be 187 kN/mm for numerical analysis and 195 kN/mm for the experimental testing. These results are summarised in Table 4. From Figure 8, the cracking failure of the concrete is visualised through the red section of the stress contours. Increased cone shaped stress can also be observed around the support when compared to the previous conventionally reinforced transom.

3.4. Prestressed Transom with Welded Shear Stud (PSWelded)

From the results of the comparison between the numerical and experimental investigation, the FE model can be assumed to be verified due to the minimal difference between the two sets of results. Hence, the numerical analysis of the conventionally reinforced transoms can be used as a baseline to evaluate the performance of the prestressed transoms. Figure 7 compares the performance of prestressed transom specimen with welded shear studs with its conventionally reinforced counterpart. Figure 8 also illustrates the failure behaviour of the PSWelded.

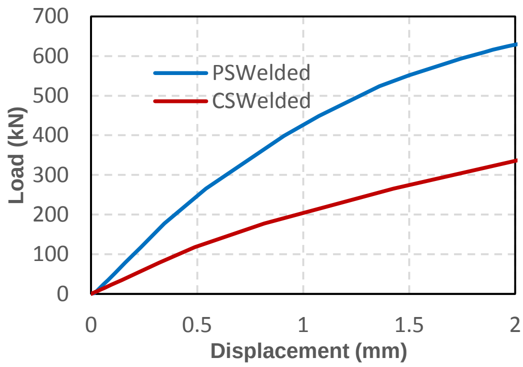

Figure 7: Comparison of specimens PSWelded and CSWelded

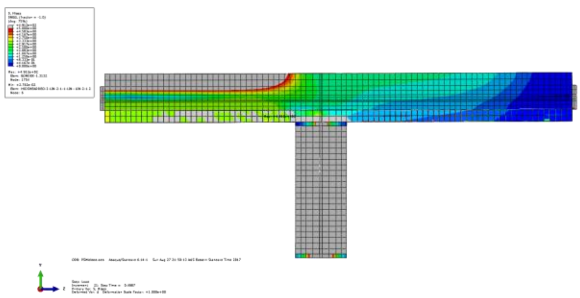

Figure 8: Stress contour plot of specimen PSWelded

From the results presented above, the loading at 2 mm of displacement was 628 kN for the prestressed transom comparing to 336 kN of loading at the same displacement resulting in an 87% increase in strength. The stiffness can also be calculated to be 314 kN/mm for the prestressed specimen. Table 4 also displays the results of the numerical investigation for specimen PSWelded. From Figure 10, the cracking failure of the concrete is visualised through the red section of the stress contours. Like the conventional specimens, cone stress distribution can be seen around the support. However, the stress around the support is noticeably less than the conventional counterpart.

3.5. Prestressed Transom with AJAX Bolts (PSAJAX)

Figure 9 compares the performance of the prestressed transom specimen with AJAX bolts with its conventionally reinforced counterpart. Figure 10 also illustrates the failure behaviour of the PSAJAX specimen.

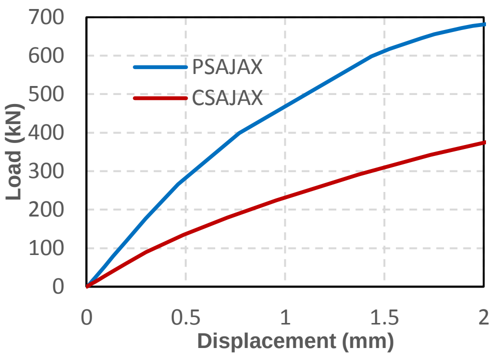

Figure 9: Comparison of specimens PSAJAX and CSAJAX

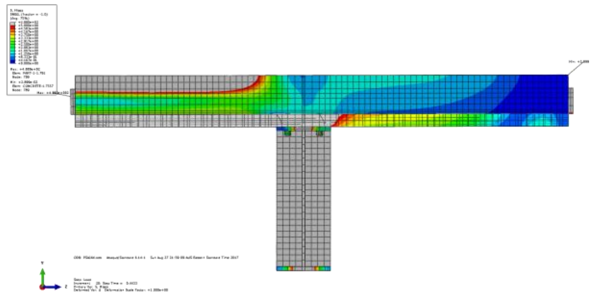

Figure 10: Stress contour plot of specimen PSAJAX

From the results presented above, the loading at 2 mm of displacement was 681 kN for the prestressed transom comparing to 374 kN of loading at the same displacement resulting in an 82% increase in strength. The stiffness can also be calculated to be 341 kN/mm for the prestressed specimen. Table 4 also presents the results obtained for specimen PSAJAX. From Figure 12, the cracking failure of the concrete is visualised through the red section of the stress contours. Also, visibly less cone stress distribution can be seen around the support when compared to the previous prestress section.

3.6. Result Comparisons

From the results, the existing experimental results produced by Zaher (2016) were compared to the numerical counterparts with the objective of validating these models. Once validated, they were then used as a baseline for which to compare the prestress specimens. Table 4 summarises all the results obtained from experimental and numerical investigation herein. The percentage difference was calculated between the results for welded shear studs and AJAX bolts. Throughout the results, transoms using the AJAX bolts perform better than transoms using the welded shear studs with an average percentage increase of 9.2%.

Table 4: Summary of experimental and numerical results

Experimental Results			
Specimen	**Loading at 2 mm displacement (kN)**	**Stiffness (kN/mm)**	**% Difference**
Conventional Welded Shear Stud	360	180	8.3
Conventional AJAX Bolt	390	195	
Numerical Results			
Specimen	**Loading at 2 mm displacement (kN)**	**Stiffness (kN/mm)**	**% Difference**
CSWelded	336	168	11
CSAJAX	373	187	
PSWelded	628	314	8.4
PSAJAX	681	341	

4. CONCLUSIONS

The research illustrates the validation of FE model and an understanding of the failure behaviour was made. The research concludes that: The discrepancies between the numerical and experimental results were less than 10%. Therefore, the FE models are reasonable accurate. The performance of these models will be able to be used as a baseline and provide the foundation for future numerical analysis on the same specimens. It was found that the prestressed models performed significantly better over the conventional models in terms of stiffness by an average of 84.7% as well as a higher resistance to cracking.

5. ACKNOWLEDGEMENTS

The authors would like to express RMS and Transport NSW for their technical supports and the Western Sydney University for providing conducive environment for this research.

6. REFERENCES

González-Nicieza C, Álvarez-Fernández MI, Menéndez-Díaz A, Álvarez-Vigil AE & Ariznavarreta-Fernández F (2008). Failure analysis of concrete sleepers in heavy haul railway tracks, Engineering Failure Analysis, 15, pp. 90-117.

Griffin D (2013). Design of Precast Composite Steel-Concrete Panels for Track Support: For Use on the Sydney Harbour Bridge, Honour thesis, University of Western Sydney.

Johnston J (2016). Feasibility Design of Transom Using Composite Fibre Technology for Sydney Harbour Bridge, Honour thesis, Western Sydney University.

Mirza O (2008). Behaviour and design of headed stud shear connectors in composite steel-concrete beams, Post Honours Doctorate Thesis, University of Western Sydney.

Zaher N (2016). Behaviour of Modular Precast Pre-stressed Concrete Panels for Sydney Harbour Bridge, Honour thesis, Western Sydney University.

Proc. 1st International Conference on Structural Engineering Research (iCSER 2017)
20-22 Nov 2017, Sydney, Australia
ISBN: 978-0-6480147-6-8

Experimental Study of Failures in Steel Tubular Bridge Structures due to Cyclic Loading

Feleb N Matti[1], Fidelis R Mashiri[2] and Idris Musa[3]

[1]PhD Candidate, School of Computing & Mathematics, Western Sydney University, NSW, Australia
[2]Associate Professor, School of Computing & Mathematics, Western Sydney University, NSW, Australia
[3]PhD Candidate, School of Computing & Mathematics, Western Sydney University, NSW, Australia
Corresponding author's E-mail: 17738907@student.westernsydney.edu.au

Abstract

Circular hollow sections (CHS) are widely used in most types of structures such as bridges, communication towers and offshore platforms that are subjected to different types of loading. The main girder for truss arch bridges and cabled stayed bridges can be made of CHS and concrete-filled circular hollow sections (CFCHSs) in large span bridges. Extensive experimental determinations of stress concentration factors (SCFs) on empty tube to tube T-joints have been previously investigated. These investigations resulted in the development of design guidelines for fatigue of CHS uniplanar T-joints such as CIDECT Design Guide No. 8. On the other hand, little research has been carried out on the determination of the SCFs of T-joints with concrete-filled chords. As a result, there is no design guide for T-joints with concrete-filled chords. An experimental investigation was performed at Western Sydney University (WSU), Kingswood Campus. The strain gauging process was used to install strip and single strain gauges onto two T-joint specimens with concrete-filled chords for the measurement of strains. The strain gauging enabled the measurement of strains in concrete-filled T-joints and determined the SCFs of two concrete-filled T-joints specimens under axial tension, axial compression and in-plane bending. The stress distributions around the weld joints for empty T-joints have been previously researched. Calculations of the SCFs for these empty T-joints under axial load and in-plane bending can be determined based on the CIDECT Design Guide No.8. The calculated SCFs values for empty joints are compared to the SCFs of the concrete-filled chord T-joints obtained from the results of the experiment. The purpose of this comparison is to find out if it is beneficial to use concrete- filled T-joints for fatigue design.

Keywords: SCFs, Concrete-filled T-joints, Experimental investigation

1. INTRODUCTION

Wang et al (2013) designed a CHS to CHS joint plus ten CHS to CFCHS joints to consider the effect of concrete strength grades on SCFs at joints as well as considering the effects of different non-dimensional geometric parameters. The CHS brace members were subjected to axial tensile and compressive force. Chen et al (2016) carried out the SCF testing of 4 large eccentricity N-joints under axial compression load in the vertical CHS brace, axial tension loading in the inclined CHS brace and without additional axial loading in the horizontal CHS chord. Jiao et al (2013) investigated fatigue behaviour of very high strength (VHS) circular steel tube to plate T-joints subjected to cyclic in-plane loading. Chen et al (2010) tested five tubular T-joint specimens with concrete-filled chords and three specimens of hollow steel tubular T-joints under in-plane bending and axial loading to determine and study SCFs. The stress distributions around the weld joints for empty T-joints have been previously researched. However, research on concrete-filled T-joints has not been much investigated previously. Therefore, more information on the behaviour of concrete-filled T-joints needs to be provided to practicing engineers.

The purpose of this research carried out is to investigate the stress distribution around the brace and chord intersection (welded connection) of the concrete-filled T-joints subjected to axial tension, axial compression and in-plane bending. Furthermore, the objective of this project is to determine SCFs and the hot spots' location in two concrete-filled T-joint specimens. In addition, the aim of this research is to compare the values of the SCFs of the concrete-filled T-joints and the values of the SCFs of empty joints based on the CIDECT Design Guide (Zhao 2001) to study the benefits of concrete-filled T-joints for fatigue design. Finally, this research carried out is also aimed to assist in identifying the parameters that may influence the fatigue strength of weld connection in joints with concrete-filled chord and to study the effects of cyclic loading on steel bridges and how cyclic loading can cause steel bridges to fail. The paper outlines the strain gauging process to enable the measurement of strains in T-joints. The test set-ups for axial load and in-plane bending are also described. The procedure of determining strain concentration factors (SNCFs) and SCFs of concrete-filled T-joints is also outlined.

2. EXPERIMENTAL INVESTIGATION

2.1. Specimens and Material Properties

Two concrete-filled T-joint specimens (T2 and T3) shown in Figure 2 and with sizes and non-dimensional parameters shown in Table 1 were tested in this investigation. The non-dimensional parameters are defined as follows: β, brace to chord diameter ratio (d_{br}/D_{ch}) ranging from 0.37 to 0.69, γ, chord radius to chord wall thickness ratio ($D_{ch}/2T_{ch}$) equal to 15.29, τ, brace to chord wall thickness ratio (t_{br}/T_{ch}) equal to 1 and α, chord length to chord radius ratio ($2L/D_{ch}$) equal to 16.84, see Table 1. Strip and single strain gauges were installed onto two concrete-filled T-joint specimens for the measurement of strains. The average compressive strength of the concrete used to fill the chords was 36MPa.

The strain gauging enabled the measurement of strains in T-joints that were carried out at Western Sydney University, Kingswood campus. Strain gauges were attached on the two concrete-filled T-joints specimens through the use of cyanoacrylate strain gauge glue. Single strain gauges were attached in the middle of the brace (around 285mm from the top) and at quarter points of the brace (around 142.5mm from the top plate) of both specimen T2 and T3 at 0°, 90°, 180°and 270°. However, the strip strain gauges were attached along the chord and the brace intersection at 0°, 45°, 90°, 135°, 180°, 225°, 270°, 315° and 360°. The first strain gauges of each strip strain gauge were located on the centerline of the marked location, 4mm from the toe of the weld as recommended by (Zhao et al 2001).

Figure 1. (a) T-joint specimens; (b) dimensions of T3 specimen

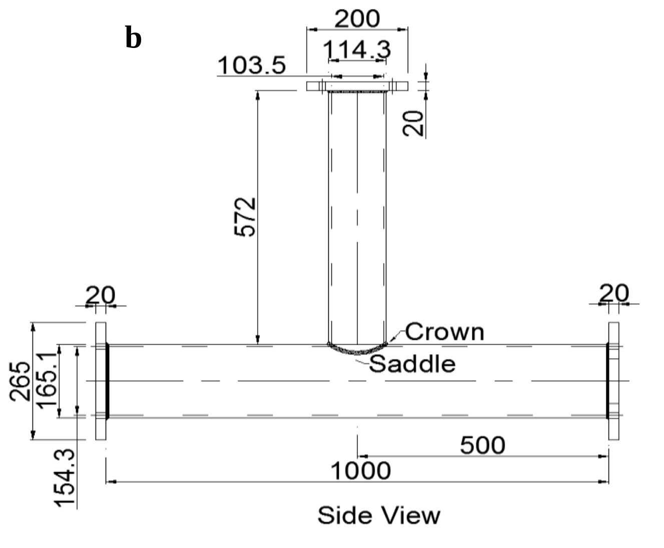

Figure 2. (a) T-joint specimens; (b) dimensions of T3 specimen

Table 1. Non-dimensional parameters

Concrete-filled T-joints specimens	Chord		Brace		Geometric Parameters			
	Diameter (mm)	Thickness (mm)	Diameter (mm)	Thickness (mm)	β	γ	τ	α
T2	165.1	5.4	60.3	5.4	0.37	15.29	1	16.84
T3	165.1	5.4	114.3	5.4	0.69	15.29	1	16.84

2.2. Test Set-Up for Axial Load and In-Plane Bending

The test of specimen T2 were set-up under axial tension and compression on the brace. The test set-up shown in Figure 3 was used in the measurements of strains under axial loads. Axial tension and then axial compression forces were applied to the specimen T2. About 10 cycles of loading were applied to the specimen to ensure the test set-up was stabilized. Each cycle included 4 quasi-static load levels. These loads fall within the elastic response region of the connection. The test of specimen T2 was then set-up under in-plane bending on the brace. The test-set up shown in Figure 4 was used in the measurements of strains for specimen T2 under in-plane bending. For in-plane bending, horizontal forces were applied to the brace. The procedure of the test set up for specimen T2 under axial load (tension and compression) and in-plane bending were repeated for specimen T3.

Figure 3. Test set-up for axial loading

Figure 4. Test set-up for in-plane bending

2.3. Determination of Strain Concentration Factors (SNCFs) and Stress Concentration Factors (SCFs) of Concrete-Filled T-Joints

The values of the nominal strain for specimen T2 and T3 under axial tension and compression were calculated by averaging the values of the four single strain gauges located in the middle of the brace at 0°, 90°, 180° and 270°. The nominal strain values for in-plane bending were calculated by averaging the values of the strains extrapolated to the weld toes based on the single strain gauges located at the crown points. The value of the SNCF for each graph was then calculated using the following equation:

$$\mathrm{SNCF} = \frac{\text{Hot Spot Strain (HSSN)}}{\text{Nominal Strain}} \tag{1}$$

Since strains were measured at four (4) load levels, four (4) SNCFs values were calculated for each strip strain gauge and for each location from 0^o to 360^o. The average value of the SNCFs is the strain concentration factor for the connection ($SNCF_{CHS}$)for each strip strain gauge or location from 0^o to 360^o.The value of the SCF_{CHS} was calculated using the following formula as recommended by Frater and van Delft et al, cited in Zhao et al (2001):

$$\mathrm{SCF_{CHS}} = 1.2 \times \mathrm{SNCF_{CHS}} \tag{2}$$

3. RESULTS AND DISCUSSION

3.1. SCFs under Axial Loading

As shown in Figure 5 and Figure 6, the hot spot location of both of the empty T-joint specimens at the chord and brace under axial loading occurred at the saddle points (90° and 270°). However, the hot spot locations of the concrete-filled T-joint specimens under axial tension or compression are not prominent but have SCFs of similar magnitude around the brace-chord intersections. The hot spot location at the chord and brace of concrete-filled T2 specimen under axial tension occurred at the saddle points. Furthermore, the hot spot location at the chord and brace of concrete-filled T3 specimen under axial compression occurred at the crown points (0°, 180° and 360°). The parameter that influences the fatigue strength was identified. As shown in Table 1, the change in dimensions of the brace diameters of both specimens T2 and T3 influence the non-dimension parameter (β). Since the non-dimensional parameter (β) of both of the specimens are not the same, different SCFs were obtained under different loading cases, showing that SCFs are influenced by the non-dimensional parameter, β**.**

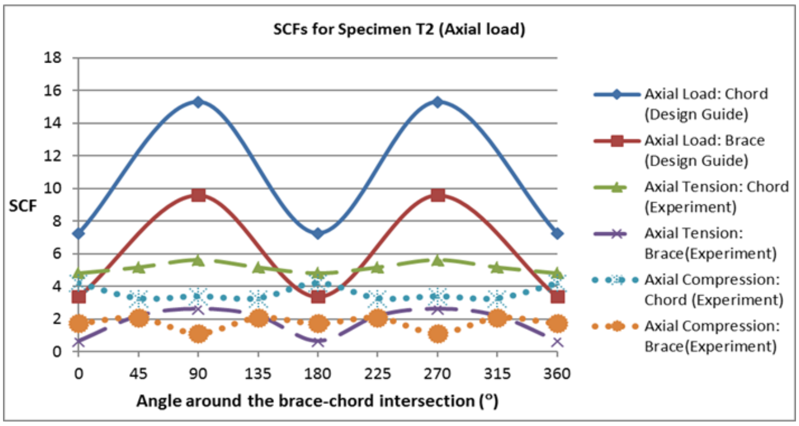

Figure 5. SCF distribution of specimen T2 under axial load along chord/brace intersection

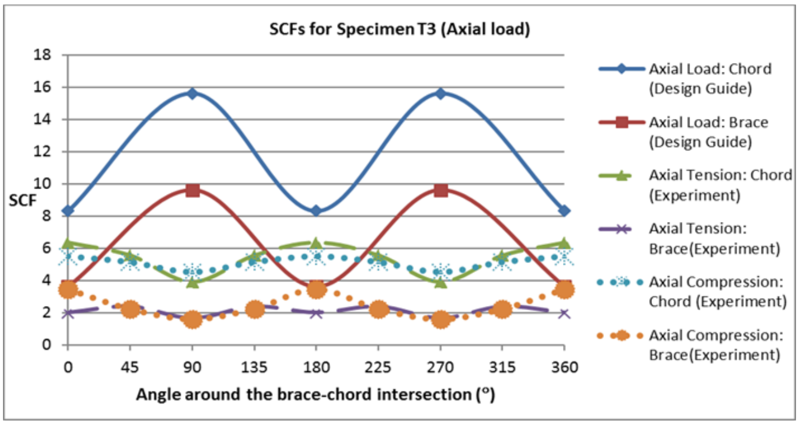

Figure 6. SCF distribution of specimen T3 under axial load along chord/brace intersection

3.2. SCFs under In-Plane Bending

As shown in Figure 7 and Figure 8, the SCF of both of the empty T-joint specimens at the chord and brace subjected to in-plane bending occurs at the crown points. However, the SCF of both of the concrete-filled T-joint specimens subjected to in-plane bending generally occurred at the crown point and in the middle of the crown and saddle points (45° and 315°). For example, the hot spots locations of the concrete-filled T2 specimen subjected to in-plane bending occurred at the chord crown points whereas T3 specimen occurred at 45° and 315°.

The SCF of the concrete-filled T2 specimen under in-plane bending is lower than the empty T-joint at the chord. Similarly, at the brace, the SCF of the concrete-filled T2 specimen under in-plane bending is also lower than the empty T-joint. However, the SCFs of the concrete-filled T3 specimen under in-plane bending are more than the empty T-joint. The maximum SCF of the concrete-filled T3 joint at the brace under in-plane bending occurred at 45°, however, the SCF of the concrete-filled T3 joint at 0° (Crown) is less than the maximum SCF of the empty T3 joint at 0°.

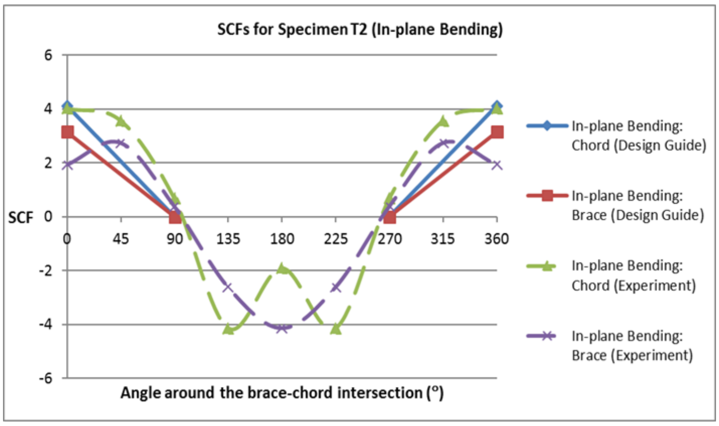

Figure 7. SCF distribution of specimen T2 under in-plane bending along chord/brace intersection

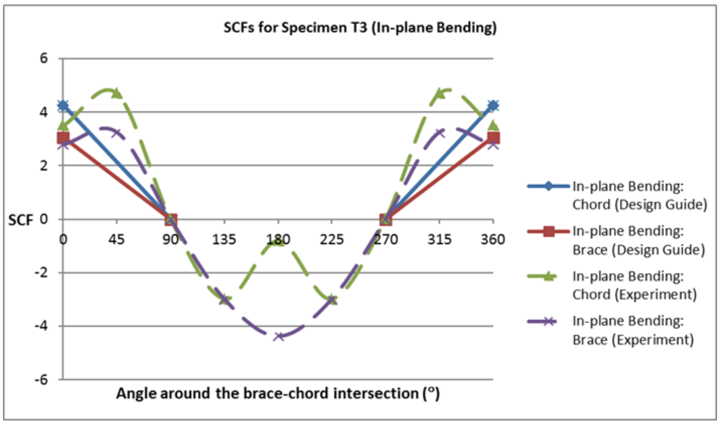

Figure 8. SCF distribution of specimen T3 under in-plane bending along chord/brace intersection

It is evident from all the graphs shown in Figure 4 to 7 that the Design Guide does not allow engineers to obtain the SCFs at 45°, 135°, 225° and 315°. These are the angles located in the middle of crown and saddle point. However, the Design Guide only allows engineers to obtain SCFs at the crown points (0°, 180° and 360°) and at the saddle points (90° and 270°). In this investigation, the SCFs have been determined at additional points: 45°, 90°, 135°, 180°, 225°, 270°, 315° and 360°. This project has therefore extended the understanding of SCFs distribution in the tubular connections in this respect. The change in dimensions of the brace diameters of specimens T2 and T3 influence the non-dimension parameter (β). Different SCFs were obtained as the non-dimensional parameter (β) of both of the specimens are not the same.

In this investigation, the SCFs between 90° and 270° are negative. This is because when the horizontal loads are applied to the brace of the specimens in the direction of the longitudinal axis of the chords, the region between 90° and 270° is under compression. This is shown in Figure 9. Hence, these SCFs are negative. The experiment shows both positive and negative SCFs whereas the CIDECT Design

Guide No. 8 shows only positive SCFs. This project has extended the understanding of the SCFs to that on the compression side of brace-chord intersections in tubular joints when compared to current standards which only give SCFs for the side under tension.

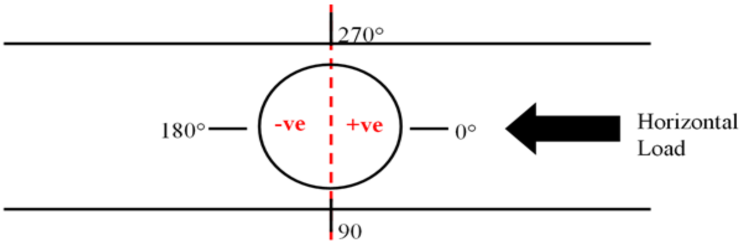

Figure 9. T-joint under in-plane bending

4. CONCLUSION

The experimental investigation provided more information on the behavior of T-joints specimens with concrete-filled chords which assisted in understanding the effect of concrete-filling on the reduction of stress around the welded joints. The stress distributions of concrete-filled T-joints were investigated. The hot spot location is different for each loading type. The locations of the hot spots generally occur at the crown and saddle points. Specimens with concrete-filled chords T-joints have lower SCFs compared to empty T-joints when subjected to axial tension or compression. Similarly, concrete-filled T2 specimen subjected to in-plane bending at the chord and brace has lower SCFs than the empty T-joint. However, the SCFs of the concrete-filled T3 specimen under in-plane bending are more than the empty T-joint. The maximum SCF of the concrete-filled T3 joint at the brace under in-plane bending occurred at 45°, however, the SCF of the concrete-filled T3 joint at 0° is less than the maximum SCF of the empty T3 joint at 0°. Therefore, it is beneficial to have concrete- filled T-joints for fatigue design as concrete filling efficiently decreases the peak SCFs. As a result, the life of the concrete-filled bridge will be longer and resulting in reduced maintenance cost. In the future, the effect of tube size (thickness) and the effect of different section shapes (square) will be studied.

5. REFERENCES

Chen J, Chen J, Jin W (2010). Experiment investigation of stress concentration factor of concrete-filled tubular T joints, Journal of Constructional Steel Research, vol. 66, no. 12, pp. 1510-5.

Chen Y, Yang J, Hu K (2016). Parametric study and formulae of SCFs for positive large eccentricity CHS N-joints, Journal of Constructional Steel Research, vol. 120, pp. 117-31.

Jiao H, Mashiri F, Zhao X-L (2013). Fatigue behavior of very high strength (VHS) circular steel tube-to-plate T-joints under in-plane bending, Thin-Walled Structures, vol. 68, pp. 106-12.

Wang K, Tong L-W, Zhu J, Zhao X-L, Mashiri F (2013). Fatigue Behavior of Welded T-Joints with a CHS Brace and CFCHS Chord under Axial Loading in the Brace, Journal of Bridge Engineering, vol. 18, no. 2, pp. 142-52.

Zhao, X-L, Herion, S, Packer, JA, Puhtli, RS, Sedlacek, G, Wardenier, J, Weynand, K, van Wingerde, AM, Yeomans, NF (2001). Design Guide for circular and rectangular hollow section welded joints under fatigue loading, Verlag TUV Rheinland.

Proc. 1st International Conference on Structural Engineering Research (iCSER 2017)
20-22 Nov 2017, Sydney, Australia
ISBN: 978-0-6480147-6-8

Behaviour of Shear Connectors for Sustainable Construction under Static Loading

Seyedeh Maryam Hosseini[1], Olivia Mirza[2], Fidelis Mashiri [3]

[1]PhD Student, [2]Senior Lecturer, [3]Associate Professor
[1,2,3] School of Computing Engineering and Mathematics, Western Sydney University, Sydney, Australia
Corresponding author's E-mail: f.mashiri@westernsydney.edu.au

Abstract

The purpose of this study is to identify structurally efficient and practical post-installed shear connectors for composite structures designed with a focus on sustainability. According to the Australian 2010 Infrastructure Report Card, a large number of Australian infrastructures are reaching the end of their design life. Therefore, there is a need for repair and strengthening of deteriorated, damaged and substandard infrastructures. The use of post-installed shear connectors to develop composite action in lieu of conventional headed shear studs and in strengthening and retrofitting of existing composite structures can be a structurally efficient and cost-effective approach. While composite beams that are retrofitted with post-installed shear connectors are potentially sustainable and recyclable elements, research contributions on these types of beams are very limited. In this paper a three-dimensional finite element model is developed to investigate the structural performance of a steel–concrete composite beam with post installed shear connectors and the factors that influence static strength of these types of connectors. The accuracy of the 3-D finite element model proposed in this work is validated by comparison with available experimental results.

Keywords: Composite beam, Post-installed shear connector, Finite element model

1. INTRODUCTION

Sustainability has become increasingly interested in civil engineering. Retrofitting existing structures has become a growing interest because of finite resources and expensive construction costs. The shear connection between the concrete slab and the steel section is an essential component of a composite beam. The use of post-installed shear connectors to develop composite action in lieu of conventional headed shear studs and in strengthening and retrofitting of existing composite structures can be structurally efficient and cost-effective approach. For strengthening an existing bridge, both the structural behaviour of shear connector and the installation problems are significant factors to select a post-installed shear connector. While composite beams that are retrofitted with post-installed shear connectors are potentially sustainable and recyclable elements, research contributions on these types of beams are very limited (Kwon, 2008).

More recently, Kwon (2008) continued the research conducted by Schaap (2004), Hungerford (2004) and Kayir (2006). They focused on the post-installed capacity for retrofitting existing structures. One recent research project on sustainability was conducted by Mirza and Uy (2010) using blind bolts as shear connectors. The objective of using blind bolts in the composite steel beams is to develop recyclable and sustainable structures. Consequently portable and sustainable structures can be developed since these bolts have the capability of being unbolted and bolted from one side only. The installation procedure of blind bolts is less complex and more rapid than that of conventional systems (Pathirana et al., 2016). In Figure.1, two blind bolt types referred to as Blind Bolt Type 1 (BB1) and Blind Bolt Type 2(BB2) are shown. The flexural performance of composite beams with two blind bolt types and headed stud connectors were experimentally evaluated by Pathirana et al. (2016) using full-scale beam specimens. Based on the experimental results, Pathirana et al. (2016) pointed out that these blind bolts have similar load capacity and behaviour to the welded stud.

(a) Blind Bolt 1 (BB1) (b) Blind Bolt 2(BB2)

Figure 1. Different Types of Blind Bolts (Pathirana et al., 2016).

The study of shear connector behaviour in composite beams using push-out tests is much more convenient than the use of beam tests; but in many cases these can be expensive and time-consuming. Therefore, numerical studies were undertaken to provide an effective alternative to the experimental procedures to investigate the structural behaviour of shear connectors. The performance of blind bolts under static loading condition still remains unknown; hence this study will focus on characterizing the static performance of the welded stud and the blind bolt connectors (BB2). The main purpose of the authors is to develop a three-dimensional finite element model using ABAQUS software to simulate the mechanical behaviour of different connector types. Subsequently, the simulation results are analysed and compared with results of selected push-off tests.

2. FINITE ELEMENT MODELING

2.1. General

The push-out test is the most common way used to investigate shear connector strength and behaviour. Concrete blocks, steel plates, reinforced bars and shear connectors are the four main parts in push-out tests. A series of push-out tests similar to the standard push-out test specimen in accordance with EC4 was conducted by Lam and El-Lobody (2005).The test setup of the push-out specimens is shown in Figure.2a. The test set up, instrumentation, test material and tests result were explicitly described in (Lam and El-Lobody, 2005). Experimental investigations undertaken by Lam and El-Lobody (2005) were used and compared with the finite element analysis to evaluate the mechanical behaviour of shear connectors in this study. Therefore, finite element modelling of the push-out tests was carried out to determine the load-slip behaviour of the shear connectors. Since the specimen is symmetric, only one half of the model was built using the Abaqus software, as shown in Figure.2b. Appropriate symmetrical constraints were applied to the models to simulate the real structure. Material nonlinearity is associated with the inelastic behaviour that was considered in the model. Abaqus/Standard analysis was used to analyse the three dimensional model for the push-out test. It is essential to model all details of the experimental test specimen to obtain accurate results and derive reliable conclusions (Wang et al., 2012). Therefore both the geometrical and material nonlinearities, including softening and yielding of material, were considered in the model. The concrete slab, steel beam and shear connectors were modelled using 8-node element with reduced integration (C3D8R) and each model has three translational degrees of freedom (DOF).The steel reinforcement was meshed with 2-node linear 3D truss elements (T3D2), which have three degrees of freedom. The whole model used coarse mesh and mesh sizes for critical zones such as shear connector and concrete slab around shear connector are carefully controlled to get accurate calculated results by using fine mesh.

Figure 2. (a) Push-out Specimen (Lam & El-Lobody, 2005.); (b) 1/2 FE model with ABAQUS

The actual connector geometries were modelled for this analysis; it should be noted that the collar and the nut of the bolted connector were not considered as separate parts. Figure 3. demonstrates the typical geometries and element types used to simulate the push out test specimens and different connector types.

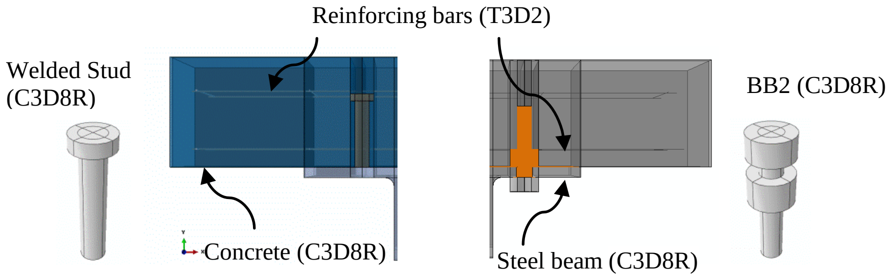

Figure 3. (a) Finite Element Model of Stud; (b) Finite Element Model of BB2

2.2. Material Models

The material properties used for finite element simulations are shown in Table 1.

Table 1. Steel properties for various steel components.

Material type	Material property		
	E-modulus (N/mm^2)	Yield strength (N/mm^2)	Ultimate strength (N/mm^2)
Reinforcing Steel	190,000	510	650
Steel beam	200,000	275	350
Welded Stud (19 mm dia.)	200,000	470	600
BB2 (M20,grade 8.8)	187,000	780	930

2.2.1. Material model of concrete

The concrete material behaves elastically up to the yield stress and will exhibit plasticity after yield point (See Figure 4.).

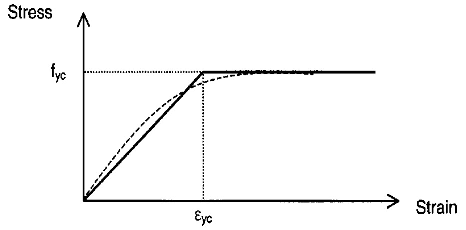

Figure 4. Stress–Strain Diagram for Concrete.

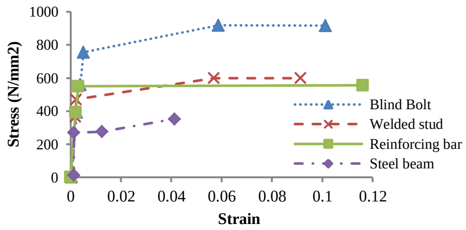

Figure 5. Stress–Strain Diagram for different Steel Materials.

The following relationships can be used to calculate average values of yield strain, yield stress and the Young's modulus of concrete in accordance to BS 8110 (BSI 1997) ((Lam & El-Lobody, 2005.)):

$$\varepsilon_{yc} = 0.00024\sqrt{f_{\mathrm{cu}}} \quad (1)$$

$$f_{yc} = 0.8 f_{\mathrm{cu}} \quad (2)$$

$$E_C = f_{\mathrm{yc}}/\varepsilon_{yc} \quad (3)$$

The used FE-model considers a nonlinear material behaviour for the concrete. The plastic region of the stress–strain curve for the concrete was defined using the concrete damaged plasticity model in ABAQUS. The tensile behaviour of concrete has been modelled by fracture energy to make the model in FEM less dependent on the element size. The compressive strength of the concrete used for the finite element models was 35 MPa.

2.2.2. Steel properties

In the finite element modelling, the stress–strain diagram of various steel materials was determined using material property test data. Prior to the yield point the steel material will deform elastically and this elastic range of behaviour is followed by further yielding and then by failure. In this study, the stress strain behaviours of these materials were transformed into piecewise linear curves. The stress–strain diagrams of the steel materials utilized to the push out test model; reinforcing bar, welded shear studs and the blind bolt connector respectively are shown in Figure 5.

2.3. Contact Properties, Loads and Boundary Conditions

The contact interaction and constraint methods available in ABAQUS were used to model the interactions between components of the push out test. The surface-to-surface contact algorithm was applied to the contact surface between the concrete slab, steel beam and connector to achieve practical structural design procedures for connections as listed in Table 2. In addition, Figure 6. describes the details and contact interaction between various parts of finite element model of the push-out test and each connector type. Penalty contact method was utilized to simulate the normal and tangential contact behaviour by using a tangential friction coefficient of 0.6.

Table 2. Contact interaction between various parts finite element model of the push-out test.

Part instance		Contact type	
1	**2**	**Welded Stud**	**BB2**
Concrete slab	Steel beam	Interaction	Interaction
Concrete slab	Reinforcing bars	Embedded	Embedded
Concrete slab	Connectors	Tie	Interaction
Steel beam	Connectors	Tie	Interaction

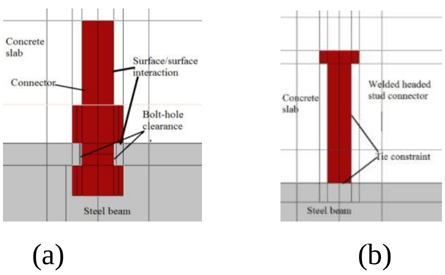

Figure 6. Details of The Interaction Between (a) The Bolted Connectors & (b)The Welded Stud Connectors and other Components of Finite Element Modelling .

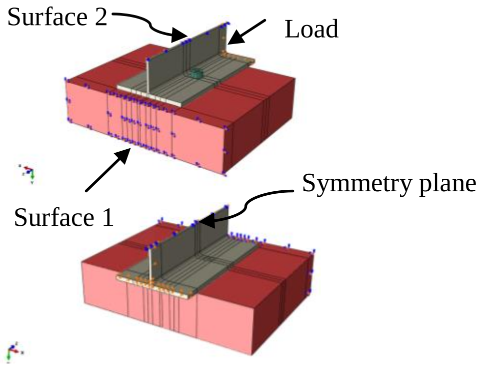

Figure 7.Boundary and Loading conditions.

The reinforcing steel model was embedded inside a concrete element using the embedded element method. The top surface of the beam is subjected to uniformly distributed load as shown in Figure 7. The bottom surface of concrete block in the opposite direction of loading (surface 1 in Figure 7.) was fixed in all directions. As 1/2 of the specimen was modeled, all nodes at the middle of the steel beam web (surface 2) are restricted to move in the X-direction because of symmetry as shown in Figure 7.

3. RESULTS AND DISCUSSION

3.1. Analysis Results

Figure 8 and 9 illustrate the stress and strain distribution of connectors and concrete. Under the action of a uniformly distributed load along the top of the beam, the connectors have obvious shear deformation. The concrete around the stud root has plastic strain as shown in Figure 8 (a); Figure 8 (b) and (c) demonstrate the static failure appearances at stud roots and stud shank embedded in concrete when the structure cannot take any more load. Furthermore, Figure 8 (c) also shows there is a good agreement between the observed failure mode of the stud and the FE model results. The experimental failure load recorded was 102.0 kN on each stud at a slip of 6.1 mm compared to 99.5 kN at a slip of 6.1mm evaluated by the finite element analysis with similar strength properties of concrete. These results also reveal that the model is able to capture the actual performance of the experimental push-out tests during loading. Consequently this model was used to study the load–slip behaviour of the demountable connectors.

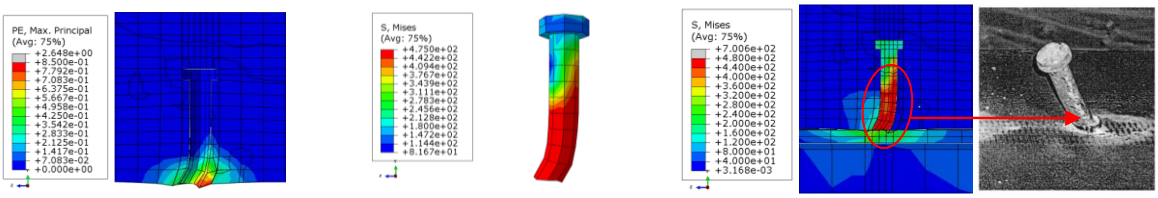

(a) Maximum Principle Plastic strain of concrete

(b) Mises stress of stud

(c) Failure elements on stud

Figure 8. Stress and strain distribution for Welded studs.

Figure 9(a) describes the region of plastic strain of concrete around the shank and nut of the blind bolt. The static failure appearances at the bolt shank embedded in the concrete slab and the steel beam is demonstrated in Figure 9 (b) and (c). In addition, at 6.1 mm slip, the maximum load was 146.8 KN for each blind bolt connector based on the finite element results. As shown Figure 10(b) these connectors have a slip of up to 14 mm before failure. Figure 9 (c) also shows the separation between the concrete and steel section at high loading stages, therefore, the current design of the blind bolt connector still needs improvement .

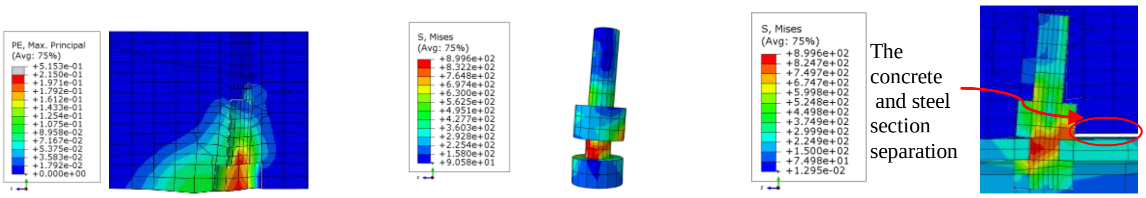

(a) Maximum Principle Plastic strain of concrete

(b) Mises stress of BB2

(c) Failure elements on BB2

Figure 9. Stress and strain distribution for Blind bolts.

3.2 Verification of Finite Element Models with the Experimental Results

The load-slip curve of each connector type obtained from finite element modelling was compared to the push-out test data, as shown in Figure 10. These load-slip curves have a clear elastic-plastic region. In the elastic portion, the load-slip curves show approximately linear behaviour for all connectors. It can be seen there is good match between the calculated load-slip curves of the welded stud and the experimental results.

In addition, the numerical simulation results indicated that with similar strength of concrete and failure mode, the blind bolt connector exhibits more ductility when compared with the welded headed stud. However, the conventional shear connectors demonstrated relatively large initial stiffness and the slip capacity than the blind bolt connectors. The blind bolt stiffness in practice may drop due to the bolt-hole clearance. Following the friction between the bolted connector and the steel beam is overcome, the connector slip may occur within the oversized holes. According to the numerical curve, the demountable connectors exhibited higher ultimate load capacity under static load when compared with the the headed shear stud connectors. Hence the reliability of the load–slip performance of the innovative blind bolts allows composite beams to be made demountable.

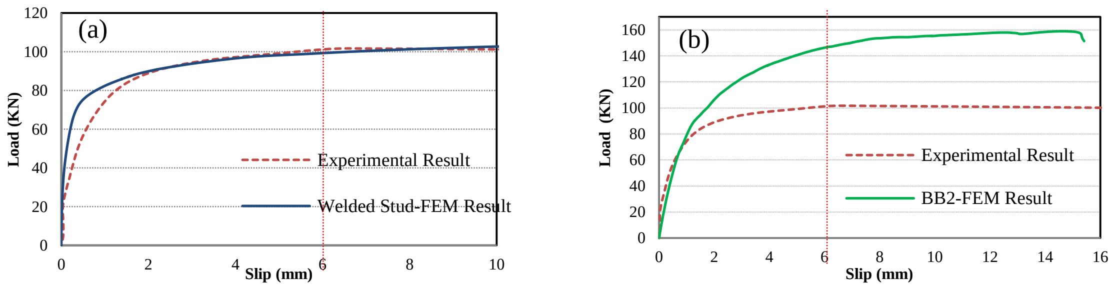

Figure 10. Comparison of FEM Calculated Results with Experimental Results.

4. CONCLUSIONS

The paper illustrates the development of a detailed finite element model that is capable of predicting load-slip behaviour and failure modes of different type of shear connectors in composite beam and could confidently replace some expensive experimental testing. Nonlinear, three-dimensional finite-element models were built in this study to evaluate the mechanical behaviour of different types of shear connectors utilising in composite steel–concrete beams. Abaqus software is used to investigate the load-slip behaviour of the blind bolt and welded shear connectors. The failure modes, stiffness and ductility have been compared in detail. Based on the finite element analysis the following conclusions can be made:

- The composite beam with the blind bolt connectors showed significantly higher strength and ductility.
- The results obtained from the finite element model suggest that the behaviour of the demountable connectors is comparable with that of the headed stud shear connectors to achieve composite action between the slab and the beam.
- A further investigation of the model results also reveals that these blind bolt connectors can be used as innovative shear connectors to develop recyclable and sustainable structures.

5. REFERENCES

Hungerford, B.,(2004). Methods to develop composite action in non-composite bridgefloor systems: Part II. M.S. thesis.. USA/Austin: Department of Civil, Architectural and Environmental Engineering, University of Texas at Austin.

Kayir, H., (2006). Methods to develop composite action in non-composite bridge floor systems: Fatigue behavior of post-installed shear connectors. MS thesis.. USA/Austin: Department of Civil, Architectural and Environmental Engineering, University of Texas at Austin.

Kwon, G. U., (2008) . Strengthening Existing Steel Bridge Girders by the Use of Post-Installed Shear Connectors. Austin: The University of Texas at Austin.

Lam, D. & El-Lobody, E., (2005). . Behavior of Headed Stud Shear Connectors in Composite Beam. Journal of Structural Engineering, 131(1), pp. 96-107.

Mirza, O. & Uy, B., (2010). Effects of the combination of axial and shear loading on the behaviour of headed stud steel anchors. Engineering Structures , Volume 32 , pp. 93-105.

Pathirana, S. W., Uy, B., Mirza, O. & Zhu, X., (2016). Flexural behaviour of composite steel–concrete beams utilising blind bolt shear connectors. Engineering Structures, Volume 114, p. 181–194.

Schaap, B., (2004). Methods to develop composite action in non-composite bridge floor systems: Part I. M.S. thesis. USA/Austin: Department of Civil, Architectural and Environmental Engineering, University of Texas at Austin.

Wang, Q., Liu, Y. & Lebet, J., (2012). Nonlinear Finite-Element Analysis of the Shear Behaviour of Stud Connectors. Stirlingshire, Scotland , s.n.

Proc. 1st International Conference on Structural Engineering Research (iCSER 2017)
20-22 Nov 2017, Sydney, Australia
ISBN: 978-0-6480147-6-8

Vibration Test of Circular Concrete-Filled Steel Tubular (CFST) Beams

Chuanchuan Hou[1], Linhai Han[2], Longbo Xie[3] and Feiyu Liao[4]

[1]Postdoc research fellow, Department of Civil Engineering, Tsinghua University, Beijing, China 100084
[3]Professor, Department of Civil Engineering, Tsinghua University, Beijing, China 100084
[3]Graduate student, College of Transportation, Fujian Agriculture and Forestry University, Fuzhou, China 35002
[4]Professor, College of Transportation, Fujian Agriculture and Forestry University, Fuzhou, China 35002
Corresponding author's E-mail: lhhan@tsinghua.edu.cn

Abstract

This paper studies the vibration properties of circular concrete-filled steel tubular (CFST) beams and their potential applications in determining the flexural stiffness of CFST and detecting steel-concrete interface debonding. A total of 8 specimens, 4 intact ones and 4 with circumferential debonding, were tested with impact hammer excitation. The frequency response function (FRF) curves of the specimens were calculated and the first few modes of natural frequencies and mode shapes of the specimens were extracted. Numerical model was established to predict the natural frequencies of the intact CFST beams. By comparing the predicted and extracted natural frequencies, the flexural stiffness of the beam was calibrated. It shows that employing the gross flexural stiffness in the numerical model could predict the natural frequencies of CFST with good accuracy. The major characteristics of debonded CFST vibration was also summarized, including the presence of extra modes and the reduction of natural frequencies of flexural modes. Such characteristics could be used as indicators of steel-concrete interface debonding in CFST structures.

Keywords: Concrete-filled steel tube (CFST), Modal test, Modal parameters, Flexural stiffness, Debonding.

ISBN: 978-0-6480147-6-8

Development of Engineered Cementitious Composites with Dune Sand

Richard Abubakar Shuaibu[1], Zhong Tao[2], Zhu Pan[3] Jian Zhou[4]

[1]PhD Candidate, Centre for Infrastructure Engineering, Western Sydney University, Penrith, NSW 2751, Australia

[2]Professor of Infrastructure Materials, Centre for Infrastructure Engineering, Western Sydney University, Penrith, NSW 2751, Australia

[3] Post-Doctoral Research Fellow, Centre for Infrastructure Engineering, Western Sydney University, Penrith, NSW 2751, Australia

[4]Head of Research Group in Advanced Cementitious Materials, Sinoma Research Institute, Sinoma International Engineering Co., Ltd, Beijing 100102, China

Corresponding author's E-mail: richard.shuaibu@westernsydney.edu.au

Abstract

In the last few decades, different studies have been conducted to develop high-performance fibre reinforced cementitious composites (HPFRCCs) exhibiting very high tensile strain. This type of material is designed based on micromechanics principles and is different from conventional concrete as it contains only very fine sand, usually silica sand with maximum aggregate size about 250µm. However, other types and sizes of aggregates have been successfully used to produce HPFRCCs. This study aims to develop ECC, which is a class of HPFRCCs, produced with a replacement of silica sand with dune sand at 0, 50 and 100% by weight. The presence of dune sand was seen to improve the strength of ECC by up to 50% at both early and later ages. The tensile strain at early age also was seen to improve in comparison to the control mix.

Keywords: ECC, Dune sand, Compressive strength, Tensile strength, Ductility.

1. INTRODUCTION

Engineered cementitious composite (ECC) is a group of high-performance fibre reinforced cementitious composites characterised by high ductility in the order of several hundred compared with that of normal concrete. This tensile property exhibited by ECC give it superior energy absorption capacity and impact resistance than ordinary concrete and fibre reinforced concrete (FRC). Unlike other high-performance fibre reinforced cementitious composites, the fibre volume content in ECC is normally not more than 2% Kanda et al (2000) and Li et al (2001). The composites are designed based on micromechanics principle by tailoring the interaction between fibres and cementitious matrix to produce desired tensile properties. In order to achieve good tensile properties, very fine silica sand with average size of 110µm and maximum size of 250 µm is often used Yang et al (2007). So far, the most popular fibre used in the production of ECC is polyvinyl alcohol (PVA) fibre, with length between 6-12mm and a diameter of 39 µm. Although aggregates play a key role in ensuring dimensional stability of cement composites, however, aggregates having a grain size bigger than the average fibre spacing may hinder the dispersion of fibre in the matrix Soroushian et al (1992) and Sahmaran et al (2009) and therefore result in poor fresh and hardened properties of the composites.

In order to produce sustainable ECCs, attempts have been made by different researchers using different types of supplementary cementitious materials Yang et al (2007) and Zhou et al (2010) and also using sand from different sources Sahmaran, et al (2009). This effort has led to the production of greener ECC with more robust tensile properties. For example, it was revealed that increasing the amount of fly ash in ECC led to reduced drying shrinkage, tighter crack width and more robust tensile strain ductility. Dune sand is a resource of very fine natural sand which is formed when blown sand is trapped by non-moving objects such as beach grass. It is one of the most untapped local materials in the construction industry, especially in Australia. The use of dune sand as an alternative to silica sand or river sand will bring benefits to the environment because of the various issues attributed to the mining of river sand and a lot of energy involved in the manufacture of silica sand. Studies have shown that very fine particles of dune sand have two major effects on cement hydration, which include heterogeneous nucleation and Pozzolanic effect. Luo et al (2013) amongst other studies have investigated the effect of dune sand particles on the properties of concrete. They found that dune sand can be beneficial in concrete production provided that sand-cementitious material ratio is less than 1.41. They further revealed that dune sand with a particle size less than 175 μm could affect cement hydration. Regarding the use of dune sand in the production of strain hardening cementitious material, Huang and Zhang (2016) developed a high-performance fibre reinforced cementitious composite with 7-day and 42-day average compressive strengths of 34.9 and 66.4 MPa, respectively. The average tensile strain capacities at 7 and 14 days were 1.96% and 1.22%, respectively.

This study proposes the use of dune sand particles in the development of ECC containing a high volume of fly ash. The strength and ductility properties of the developed ECC are investigated. The utilisation of dune sand, which is a locally sourced material abundant in Australia, will improve the material greenness of the composites.

2. MATERIALS AND METHODS

2.1 Materials

Ordinary Portland cement (OPC) and Class F fly ash were used as dual binders for all mixtures. The OPC complies with the requirements for Type General Purpose cement in Australian Standard AS3972. Silica sand with a maximum particle size of 300 μm and dune sand with a maximum aggregate size of 300 μm were used. High range water reducer (HRWR), MasterGlenium SKY 8100, supplied by BASF chemical company, Australia was used to adjust the workability. All ECC mixtures had a constant water-to-binder ratio (w/b) of 0.26, and fly ash-cement ratio (FA/C) of 1.2. PVA fibres were used at 2% volume fraction for all mixes. The fibres were sourced from Kuraray Co., Ltd, Japan, which is one of the major suppliers of coated PVA fibres for the production of ECC, The ratio of sand to cementitious material was kept at 0.36. Dune sand was added at 0, 50, 100% replacement levels of silica sand to the ECC mixtures. Table 1 summarises the size distributions of dune sand and silica sand used in this study, while Tables 2 and 3 show the properties of PVA fibres and proportions of the ingredients in various mixes respectively.

Table 1. Size distribution of silica sand and dune sand

Sand Type	**<300 (μm)**	**<150 (μm)**	**<106 (μm)**	**<75 (μm)**
Dune sand	100	47	24	10
Silica sand	93.3	67	32	11

Table 2. Properties of PVA fibre

Length (mm)	Diameter (mm)	Strength (MPa)	Young's Modulus (GPa)	Density (g/cm^3)	Elongation (%)
8.00	0.04	1560.00	41.00	1.30	6.00

Table 3. Mix design

Mix	Cement (Kg/m^3)	FA (Kg/m^3)	Silica sand (Kg/m^3)	Dune Sand (Kg/m^3)	Water (Kg/m^3)	HRWR (Kg/m^3)	PVA (Kg/m^3)
S100D0	571	685	456	-	332	6.8	26
S50D50	571	685	228	228	332	6.8	26
S0D100	571	685	-	456	332	6.8	26

2.1.1 Specimen Preparation and Curing

In this study, the mixing was done using a 15L mixer in the Structures Laboratory of Western Sydney University, Australia. Initially, all the solids such as cement, fly ash, silica sand and/or dune sand were mixed together at a low speed for one minute. Subsequently, water and superplasticizer were then added to the dry mix and mixed at a medium speed for one minute and at a high speed for another two minutes. The mortar was inspected to ensure that a uniform state was reached after which PVA fibres were added and mixed at a high speed for three minutes. The total time taken for the mix was seven minutes, where the mixing procedure used by Yang et al (2007) was adopted in this study. The fresh mix was then cast into various moulds and demoulded after 24 hours. After demoulding, the specimens were wrapped in plastics bags and cured under a controlled temperature of 23 ± 2oC and RH of 65 ± 5% until the testing date.

2.2 Methods

Compressive strength tests were conducted using Ø50x100 mm cylinders to determine 3, 7, 28-day compressive strengths using an Instron universal testing machine of 1000 kN capacity. On the testing date, the ends of the cylinders were grinded to ensure both surfaces are flat. The tensile coupon specimens were tested using a servo-hydraulic testing system under uni-axial tension with two external linear variable displacement transducers (LVDTs) attached on both sides of the specimen to measure the specimen deformation as shown in Figure 1(a). The coupon specimen was fixed to the machine with plates glued at both sides of the grip in order to avoid pre-mature failure of the specimen at the grip point. The gauge length used was 80 mm and the testing was done at a displacement control mode at a rate of 0.0025 mm/s to simulate quasi-static loading condition. Coupon dimensions are shown in Figure 1(b), where are recommended by the Japanese Society of Civil Engineers for high-performance fibre reinforced cementitious composites with multiple cracks.

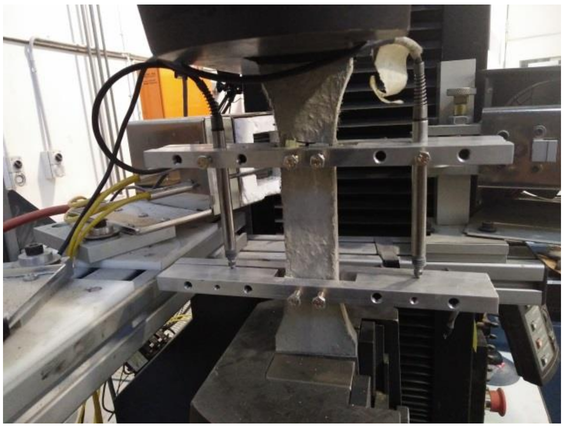

(a)

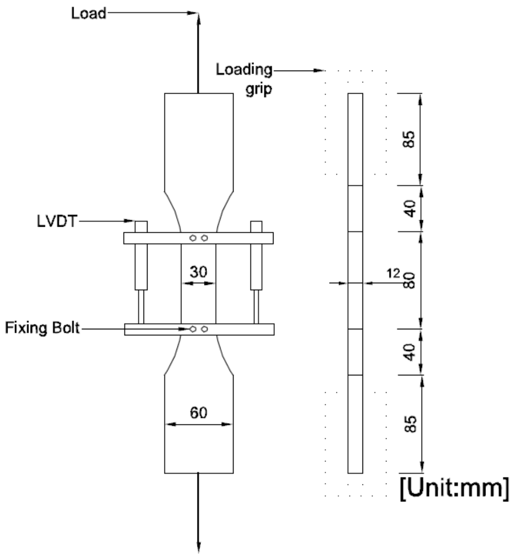

(b)

Figure 1. Uni-axial tensile test setup (a) and specimen details (b)

3. Results and Discussion

3.1 Tensile Properties

Prior to testing, the tensile coupons were sanded with sandpaper to ensure that the thickness was as uniform as possible. Figure 2 shows the representative 3-day tensile stress-strain curves for the three mixes. In the initial loading stage, all the specimens were seen to experience elastic straining up to the first cracking strength. After that, multiple micro cracks occurred as a result of bridging effects of the fibres with controlled crack width. In contrast, normal fibre reinforced concrete exhibits a localised crack when subjected to axial tension due to their brittle nature. The first crack strength of ECC as shown in Table 4 is predominantly the property of the matrix, which represents the matrix tensile strength. It is found that the first crack strength increases with increasing replacement level of dune sand, proving that the dune sand particles influence the fracture toughness of the matrix. Meanwhile, mix S50D50 with a dune sand replacement of 50% exhibited the highest ultimate strength and strain capacity. This mix has an ultimate tensile strength (σ_{tu}) to first cracking strength (σ_{fc}) ratio of 1.69, which is higher than the corresponding values of S100D0 (1.35) and S0D100 (1.36). The ratio of σ_{tu}/σ_{fc} is one of the critical parameters, determining the saturation of multiple-cracking of ECC. Accordingly, more multiple cracks were observed in mix S50D50, as shown in Figure 3. This is in line with the ECC theory that a specimen exhibits more cracks as the ratio of σ_{tu}/σ_{fc} increases. Figure 3 also shows the crack patterns of the three mixes. As the applied tensile load increased, the number of micro-cracks increased with decreasing distance between adjacent cracks until localised fracture occurred. The local failure was induced when the fibre bridging capability had been exceeded and the distance between neighbouring micro-cracks no longer reduced. The ultimate strain values are consistent with the values reported by Yang et al (2007). But the strain capacity exhibited by the control specimen, S100D0 is 2.4%, which is lower than 3.3-4.6% reported by Yang et al (2007). The reason for this discrepancy could be attributed to the different size distributions of silica sand or the difference in the properties of ingredients used in the two studies. The early age tensile strength was not reported in the same study for comparison.

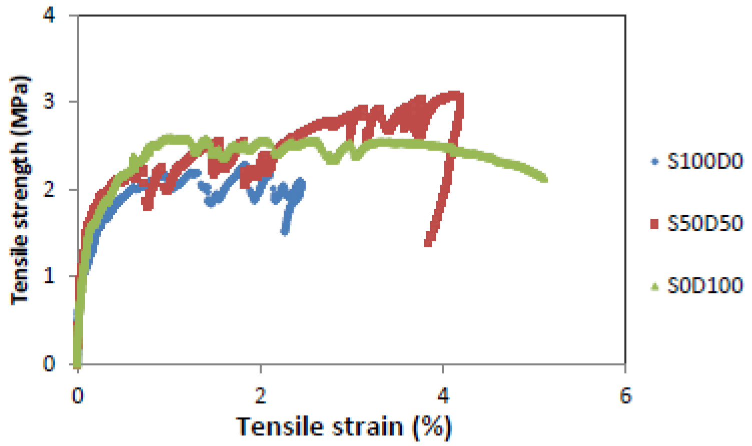

Figure 2. 3-day tensile stress-strain curve for all mixes

Figure 3. Crack patterns of the specimens

3.2 Compressive Strength

Table 5 shows the compressive strength of all the three mixes at different ages. Each representative value of compressive strength is an average of three cylinder tests with a respective standard deviation.

As observed from the values, it can be seen in Figure 4 that the strength increased with age for all the mixes. In addition, specimens with dune sand exhibited higher compressive strength both at early and later ages compared with the control sample S100D0 without dune sand. While S50D50 gained up to 10 MPa in compressive strength between 3 and 7 days, S100D0 only gained 5 MPa. It seems that the presence of dune sand in adequate proportion can catalyse the formation of cement hydration products, thereby improving the strength of the composites The values of compressive strength however were found to be comparable to those reported by Huang and Zhang (2016) for their developed dune sand HPFRCCs, which attained a 7 days and 42 days strength of 34.9MPa and 66.4MPa, respectively. Additional analysis of the strength development in Table 5 reveal that at 3 days, S50D50 and S0D100 attained up to 56.5% and 64.2% respectively of their 28-day compressive strength, whereas the corresponding value for the control sample is only 54.8%. Meanwhile, the 7-day strengths of S50D50 and S0D100 represent 77.3% and 75.9% of the 28-day strengths respectively. Once again, the percentages are higher than the corresponding percentage of 71.9% for the control sample. Thus, it might be concluded that the presence of dune sand influences the early formation of hydration products which leads to higher bonding and compressive strength. Further microstructure analysis is required to confirm this finding. From this investigation, 50% replacement of silica sand by dune sand gave the highest compressive strength at all ages. The 28-day compressive strength is 47.6 MPa for mix S50D50 whilst the corresponding compressive strength is only 29.2 MPa for the control sample S100D0.

Table 4. Compressive strength, MPa of Dune sand ECC with age

Mix	Compressive strength (days)			Strength ratio (%)	
	3	7	28	3/28	7/28
S100D0	15.96±1.35	21.01±1.86	29.2±1.2	54.8	71.9
S50D50	26.93±1.30	36.75±0.62	47.6±3.4	56.5	77.3
S0D100	24.21±1.00	28.62±2.01	37.7±3.8	64.2	75.9

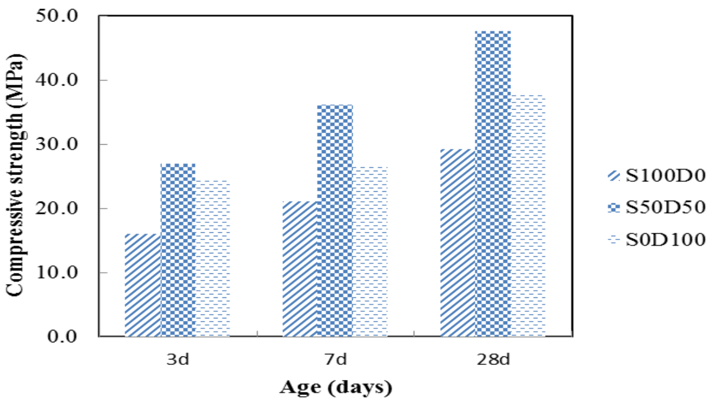

Figure 4. Comparative strength of ECC with age

4. CONCLUSION

Three ECC mixes with different replacement ratios of silica sand with dune sand were developed in this study to demonstrate the feasibility of using dune sand particles to produce ECC. The most common ECCM45 mix was used in this study. Tensile and compressive tests were conducted in order to determine the compressive strength and tensile properties of the developed dune sand composites. It was found that replacement of silica sand with dune sand particles by up to 50% gave better compressive and tensile properties compared to the control sample. This shows that dune sand particles in appropriate proportion could facilitate the formation of cement hydration products and improve the fibre matrix interfacial properties in ECC mixes. However, further research is required to find out the optimised replacement ratio of dune sand, and a microstructure analysis is also required to clarify the influence of dune sand on the mechanical behaviour of ECC.

5. ACKNOWLEDGEMENTS

The fist author would like to appreciate the generosity of Australian government and Western Sydney University for providing the International Postgraduate Research Scholarship and Western Sydney Postgraduate Research Award respectively to maintain my candidature, without which this research would not have been possible. We also want to recognise the contributions from the former Technical Manager at the Centre for Infrastructure Engineering, Dr Fernando Mithra towards the success of this investigation. The efforts of the Project Manager and other Technical Officers at the Centre are also highly appreciated.

6. REFERENCES

Kanda T, Li VC (1999). New micromechanics design for pseudo-strain hardening cementitious composites, ASCE Journal of Engineering Mechanics, 125 (4), 373-381.

Li VC, Wang S, Wu C (2001).Tensile strain-hardening behaviour of polyvinyl alcohol engineered cementitious composite (PVA-ECC), *ACI Materials J* , 98 (6), 483-492.

Yang E, Yang Y, Li VC (2007). Use of high volume fly ash to improve ECC mechanical properties and material greenness, *ACI Material Journal,* 303-311.

Sahmaran M, Lachemi M, Hossain KMA, Ranade R, Li VC (2009). Influence of aggregate type and size on ductility and mechanical properties of engineered cementitious composite, *ACI Materials Journal,* 106 (3), 308-316.

Soroushian P, Nagi M, Hsu J (2009). Optimization of the use of lightweight aggregates in carbon fiber reinforced cement, *ACI Materials Journal* , 89(3), 267-276.

Zhou J, Qian S, Beltran MGS, Ye G, Breugel K, Li VC (2010). Development of engineered cementitious composites with limestone powder and blast furnace slag, *Materials and Structures,* 43 (6), 803–814.

Luo FJ, He L, Pan Z, Duan WH, Zhao XL, Collins F (2013). Effects of very fine particles on workability and strength of concrete made with dune sand", *Construction and Building Materials,* 47, 131-137.

Huang T, Zhang, YX (2016). Mechanical properties of PVA Fibre reinforced engineered cementitious concrete", *Sustainable Solutions in Structural Engineering and Construction,* Perth, Australia, 439-444.

ISBN: 978-0-6480147-6-8

Experimental Study on the Behaviour of Headed Stud Shear Connectors for Composite Steel-Concrete Beams Incorporating Geopolymer Concrete

Youtam Mamo[1], Ee Loon Tan[2], Zhu Pan[3], Olivia Mirza[2] and Balbir Singh[4]

[1]Undergraduate Student, Western Sydney University
[2]Lecturer, Western Sydney University
[3]Post Doctorate Researcher, Western Sydney University
[4]PHD Student, Western Sydney University
Corresponding author's E-mail: balbir.singh@westernsydney.edu.au

Abstract

Recent academic research has focused on the need to develop an environmentally sustainable substitute for conventional Ordinary Portland Cement (OPC) based concrete. The need to develop such substitute stems from the global effort to reduce the consumption of natural resources and minimize carbon dioxide emissions. In this regard, the utilisation of Fly Ash (FA) based Geopolymer Concrete (GPC) within global construction applications can significantly reduce pollution and landfill issues associated with cement production and FA burial, respectively. However, essential additives such as Granulated Blast Furnace Slag (GBFS) and Superplasticizers (SPs) are required to achieve effective ambient temperature curing. Without effective curing within ambient temperature conditions, GPC behaves poorly with respect to important factors such as, strength development and workability Bakharev (2005). Consequently, this paper presents and discusses the methodology and results for both the fabrication and testing stages of eight push test specimens which incorporate GPC. A total of four specimens consist of standard Solid Slab (SS1, SS2, SS3, SS4) push tests and the remaining four specimens (B1, B2, B3, B4) consist of identical Solid Slab specimen dimensions with the additional implementation of Bondek (Profiled-Steel-Sheeting). Specimen SS1 outperformed all other Solid Slab (SS2, SS3) specimens which incorporated GPC in terms of maximum shear resistance capacity (MSRC) by achieving a value of 927kN, additionally, Bondek specimen B2 achieved a MSRC of 393.04kN, thus proving that outdoor temperature curing is superior than indoor temperature curing conditions and that the implementation of up to 30% recycled coarse aggregate (RCA) does not negatively impact the performance or durability of concrete with respect to 100% Natural Coarse Aggregate (NCA), respectively. Furthermore, the comparison of specimens SS1 and B2 to the control OPC based specimens, SS4 and B4 proves that GPC is capable of effectively replicating characteristics such as strength and durability of conventional OPC based concrete.

Keywords: Headed stud shear connector, Geopolymer, Fly ash, Slag, Alkaline solution, Push test.

1. INTRODUCTION

The demand for concrete within the construction industry is expected to have a 200% increase by the year 2050. Currently, 1 ton of OPC requires the consumption of 2.5 tons worth of raw materials and produces one ton worth of carbon dioxide emissions Xie & Ozbakkaloglu (2015). Due to the unsustainability of cement production, academic attention aims to substitute OPC based concrete with FA based GPC. Fly Ash is an increasingly abundant by-product produced when coal is burned within power pants. According to Hardjito and Wallah et al. (2004) the annual global production of fly ash exceeds 390 million tons, however less than 15% is utilised. Research conducted by Albitar and Visintin et al. (2015) affirms the benefits of FA based GPC, as the authors observed strong binding properties and high compressive strength in addition to minimal dry shrinkage, low creep and good resistance to sulphate attack. Hence, due to the abundance and 'cement-like' characteristics of GPC, research has intensified with the aim of finding an appropriate GPC mix design suitable for worldwide construction applications.

Thus, the aim of this experimental research is to effectively investigate the behaviour of headed stud shear connectors incorporating Geopolymer Concrete (GPC) within standard size composite steel-concrete push test specimens, as recommended by Eurocode 2005. The push test specimens within this experimental research represent beams with a degree of full shear connection. Ultimately, this paper will provide a comparison between the performance of GPC and OPC based concrete, whilst also comparing shear strength and shear stud behaviour within both Bondek and conventional Solid Slab specimens. Additional research objectives include the investigation of the superior curing condition i.e. indoor versus outdoor temperature curing and the influence of RCA on concrete compressive strength and durability within GPC in comparison to NCA.

2. EXPERIMENTAL PROGRAM

2.1. Materials

The type of FA used within this experimental research consists of low calcium Class-F FA. Since, an objective of this research is to develop a GPC mix design which possesses appropriate workability and strength development when cured at ambient temperature, the implementation of Grounded Blasted Furnace Slag (GBFS) was utilised as an additive for fly ash based GPC. GBFS is attributed with the ability to cure GPC within ambient temperature conditions. The GBFS used within this experimental research consists of 20kg paper packages produced by the Australian Builders company. The chemical compositions of FA, GBFS and Cement are presented in Table 1, where it can be observed that FA and GBFS complement each other to effectively replicate the composition of cement.

Table 1. Chemical composition of dry components.

Material	SiO_2	Al_2O_3	Fe_2O_3	CaO	Na_2O	MgO	K_2O	SO_3	LOI
Fly Ash	52.2	24.0	13.7	3.18	0.65	1.32	0.78	0.18	1.08
Slag	32.6	13.4	0.35	43.0	0.20	5.5	0.25	3.41	0.14
Cement	18.2	4.9	2.6	60.7	0.2	1.0	0.4	2.2	3.0

The alkaline activator solution (AAS) used to activate the binder content within the GPC mix designs is a combination of Sodium Hydroxide (NaOH) and Sodium Silicate solution (Na_2SiO_3). The pellets consist of 99% purity and have a specific gravity of 2.13, and are white in appearance. A D-Grade Sodium Silicate solution was used which consisted of a Silicon Dioxide ($SiO_{2)}$ to Sodium Oxide (Na_2O) ratio of 2.0. The solution was comprised of 55.9% of water and 44.1% of Sodium Silicate, whereby the latter component consisted of 14.7% of Na_2O and 29.4% of SiO_2. Overall, the ratio of Sodium Hydroxide solution to Sodium Silicate solution by mass is 2.5 and the concentration/molarity (M) of the Sodium Hydroxide used to prepare the GPC was 10M.

The fine aggregate used is Nepean River Sand whereas the natural coarse aggregate consisted of 20mm Basalt rock known as Blue Metal. The binder to fine aggregate ratio within the GPC mix designs was 2:1. The type of Superplasticiser brand utilised was SIKA Visco-Crete PC-HRF-2 Superplasticiser which is commercially available and designed for OPC based concrete applications. However, this experimental research utilised this brand of SP to improve the workability of GPC.

2.2. Mixture Proportions

A 90:10 (FA:GBFS) binder ratio was utilised for all the GPC mix designs. The total aggregate content consisted of 77% of the total volume of concrete, whereby the coarse aggregate was 63% and fine aggregate was 37%, however, within concrete mix design GPC2, 30% of the NCA was substituted for RCA. The amount of liquid in the form of components such as AAS, SPs and extra water was kept constant for all three mix designs. The OPC based concrete mix design was obtained from British Standards. Therefore, the recommended water to cement ratio was adopted as 0.55 and the total aggregate content was 76% of total volume of the concrete. The mixture proportions for both the GPC and OPC based concrete mix designs are provided in Table 2.

Table 2. Mixture proportion.

<table>
<tr><th rowspan="2">Mix (No.)</th><th colspan="9">Mix Proportion (kg)</th><th colspan="2">Push Test Specimen Type</th><th rowspan="2">Curing Conditions</th></tr>
<tr><th>Cement</th><th>Fly Ash</th><th>Slag</th><th>Sand</th><th>NCA</th><th>RCA</th><th>Alkaline Solution (10M)</th><th>Extra Water</th><th>SP</th><th>Solid Slab</th><th>Bondek</th></tr>
<tr><td>GPC1</td><td>-</td><td rowspan="3">92</td><td rowspan="3">10</td><td rowspan="3">184</td><td>312</td><td>-</td><td rowspan="3">45.91</td><td rowspan="3">3</td><td rowspan="3">2</td><td>SS1</td><td>B1</td><td>Outdoor Temperature Curing</td></tr>
<tr><td>GPC2</td><td>-</td><td>218</td><td>94</td><td>SS2</td><td>B2</td><td>30% RCA</td></tr>
<tr><td>GPC3</td><td>-</td><td>312</td><td>-</td><td>SS3</td><td>B3</td><td>Indoor Temperature Curing</td></tr>
<tr><td>OPC</td><td>85</td><td>-</td><td>-</td><td>188</td><td>248</td><td>-</td><td>-</td><td>47</td><td>-</td><td>SS4</td><td>B4</td><td>Control Mix</td></tr>
</table>

2.3. Mixing

The preparation of the GPC involved the mixing of all dry components together prior to the addition of any liquids. Therefore, dry materials were pre-mixed for approximately 2 minutes to ensure a uniform distribution of particles within the finished concrete. The liquid components are then added into the concrete mixer using a 50:50 method. This method was adopted to further ensure that all dry and liquid components are thoroughly mixed together. Hence, 50% of the AAS was added to the concrete mixer and allowed to mix for 2 minutes, followed by 50% of SP for an additional 2 minutes. Afterwards, the remaining 50% of the AAS and SP was poured into the mixer and mixed for 2 minutes. Extra water was added at last and was mixed for approximately 5 additional minutes. The completion of the mixing procedure allows for the finished concrete to be poured within the push test specimen formwork and various other sample testing moulds (i.e. compressive strength cylinders etc.).

2.4. Test Specimen

A total of 8 composite push test specimens were fabricated within this experimental study. The dimensions of the slab component for each push test specimen consist of 600x600x130mm. The steel beam component consists of a 700mm long 200UB29.8 section fabricated by stitch welding the flanges of two symmetrical T-sections together. Figures 1 illustrates the detailed dimensions of the Bondek push test specimens. The dimensions for the Solid Slab specimens are identical to those shown in Figure 1, withholding the presence of Bondek sheeting. These dimensions are slightly modified versions of the standard push test specimen dimensions outlined in Eurocode 2005.

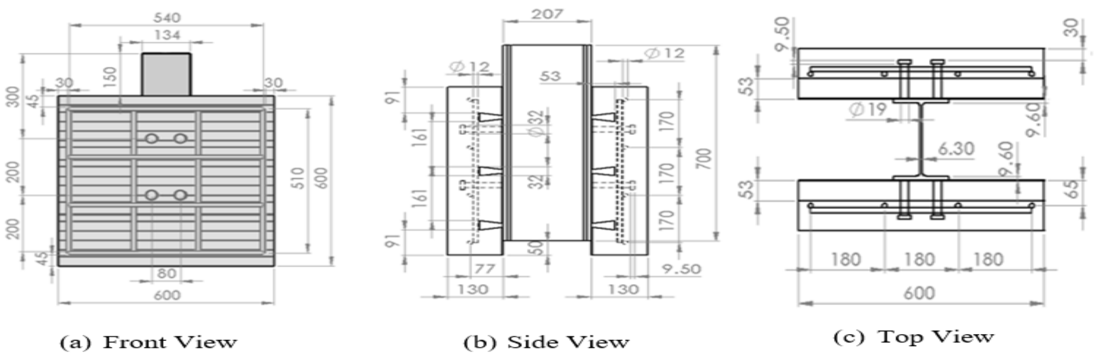

Figure 1. Detailed specimen dimensions.

2.5. Curing Conditions

Two pairs of push test specimens were cured within two different curing conditions to determine the effect of ambient temperature fluctuation. This was achieved by curing one pair of push test specimens (SS1 and B1) within an open environment and curing specimens SS3 and B3 within a closed environment. Specimens corresponding to design mix GPC2 (SS2 and B2) were also kept within the open environment curing condition, along with specimens SS4 and B4 which correspond to the control OPC design mix. The curing conditions used to cure each push test specimens and their corresponding concrete cylinder samples were designed to replicate both closed and open air room conditions found when typical OPC based concrete is cured within on-site building application. Hence, no water- bath curing was implemented within this study due to the unwanted chemical reaction which would occur in regards to specimen's incorporating GPC.

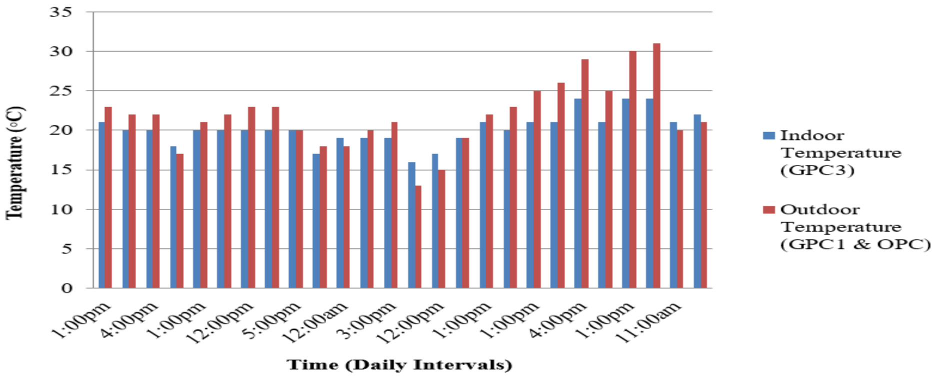

Figure 2. Temperature fluctuation graph.

2.6. Testing of Specimens

2.6.1. Overview of Test Procedure

The push test specimen design and arrangement utilised within this experimental study represents the behaviour caused by direct shear loading within full scale beam applications. The support condition consists of a fixed-roller support for the north and south slab, respectively. The specimens are placed onto a rigid steel plate which is supported by laboratory grade hard-floor concrete. Direct shear loading is then applied onto the steel section component of the specimen using an Instron Hydraulic Oscillator (IHO). The IHO has a maximum capacity of 1000kN.

2.6.2. Test Samples

The values for both the Compressive Strength and Young's Modulus of Elasticity of each concrete mix design were obtained by pouring small samples from each concrete mix into cylindrical moulds. These moulds are of 100 x200mm in dimension. The internal surface area of each mould is lubricated with engine oil prior to pouring of concrete to ensure swift demoulding at various stages within the curing period (i.e. 7, 14, 21 days etc.). An IHO was used to determine the compressive strength of the concrete cylinders, whereby each cylinder would be subjected to shear load at a constant rate of 20 MPa/min. The compressive strength test was performed in accordance with Australian Standard 1012.8.1:2014. Additional beam moulds of 100mm width and 400mm length were also poured to determine the concrete's Modulus of Rupture (Tensile Strength) values for each concrete mix design.

3. RESULT AND DISCUSSION

3.1. Compressive Strength

The compressive strength values for each concrete mix design were obtained by testing three individual samples at each curing stage as shown in Figure 3. The values achieved by the three GPC mix designs show slight variation in both the initial and final compressive strength recordings, however, samples attributed to GPC3 are slightly lower than GPC1 and GPC2. This can be attributed to the lack in strength development caused by indoor temperature curing which involves a lower maximum temperature value than outdoor curing.

The OPC based concrete mix possesses a significantly greater early strength development characteristic in comparison to all other GPC mix designs. However, the difference between the OPC based mix and most superior GPC mix at the final 28-Day strength curing stage is approximately 6MPa. This shows that the strength development rate for GPC is significantly more constant than conventional OPC based concrete and that the long term compressive strength values are similar.

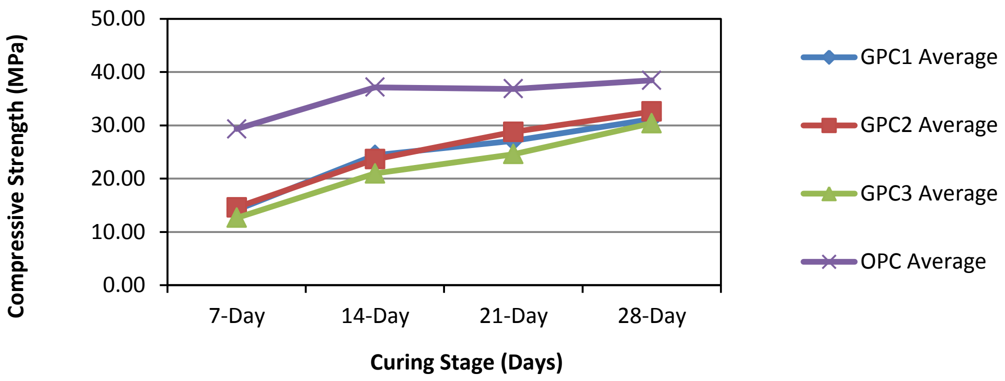

Figure 3. Average compressive strength values.

3.2. Young's Modulus of Elasticity

The Young's Modulus of Elasticity (***E***) values obtained during this experimental research reveal that GPC is less stiff and therefore more flexible than the conventional OPC based concrete mix design. A difference of approximately 15GPa exists between the OPC mix and the remaining three GPC mix designs, as shown in Figure 4. Based on this, the push test specimens utilising the GPC mix designs are expected to fail in a manner whereby signs of failure such as cracking and deformation appear gradually on the specimens. Whereas, the specimens utilising the OPC based concrete mix are expected to fail in a more sudden manner, whereby large cracks and brittle concrete failure occurs at a late stage within the push test loading procedure.

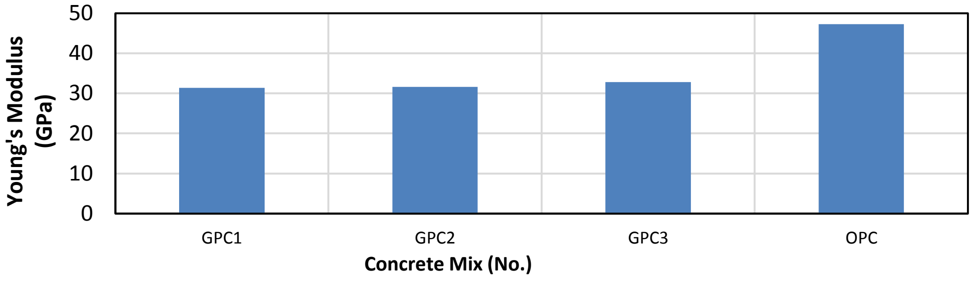

Figure 4. Young's modulus of elasticity.

3.3. Concrete Tensile Strength

The strong binding characteristic of GPC is validated based on the results obtained within this experimental research, as shown in Figure 5. All three GPC mix designs achieved greater tensile strength in comparison to the OPC based mix, however design mix GPC1 outperformed all other GPC mix designs. This can be attributed but not limited to the materials used and the curing conditions of GPC1 in respect to GPC2 and GPC3 respectively.

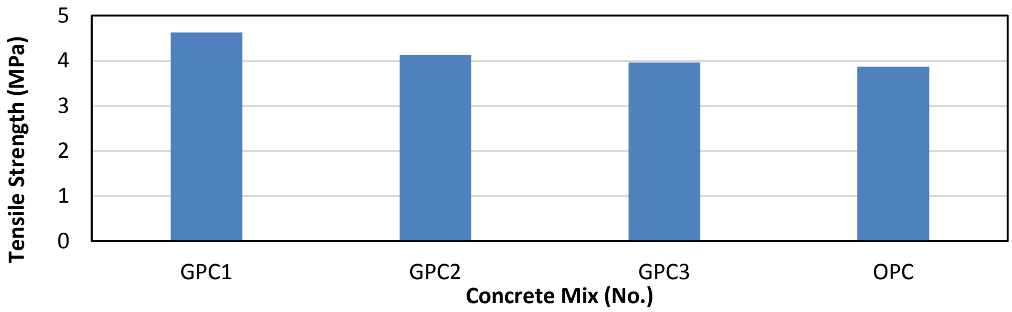

Figure 5. Concrete tensile strength.

Since GPC1 was subjected to outdoor temperature curing, the greater maximum temperature value of 31°C in comparison to 24°C allows for an improved geopolymerisation reaction to occur within GPC1 than GPC3 which causes greater binding between concrete particles. Furthermore, since GPC2 incorporated the use of 30% RCA, a lower concrete tensile strength can be attributed to the already depleted mineral structure and composition of particles within the RCA in comparison the mineral rich and uniform structure of particles within the NCA used within GPC1.

3.3.1. Push Test Results and Discussion

The overall MSRC achieved by each push test specimen represents the respective tensile, compressive and stiffness values obtained by each concrete mix type. Additionally, the dominant failure mode for both Solid Slab and Bondek type specimens is constant amongst all three GPC mix designs. Hence, Table 3 shows that the Solid Slab specimens all failed from concrete splitting type failure and the Bondek specimens failed from conical type failure, irrespective of the different concrete mix designs. However, the varying concrete mix designs effectively influenced the magnitude of shear loading required to cause specimen failure. Therefore, the durability and superior strength development of GPC1 is reflected by the MSRC achieved by specimen SS1 in comparison to specimen SS4, which possessed significantly greater compressive strength and stiffness values.

A comparison of the Bondek specimens shows that specimen B3 achieved the lowest MSRC of 329.84kN amongst all three Bondek specimens. Therefore, it can be deduced that specimen B1 outperformed specimen B3 in the same manner that specimen SS1 outperformed specimen SS3, which is based on the influences of outdoor and indoor temperature curing conditions. Consequently, specimen B2 has also outperformed specimen B3 based on the varying temperature conditions during curing. Furthermore, the superior performance of specimen B2 can be attributed to the fact that specimen B1 was subjected to an expected 40% failure load of 256kN. This may have caused the specimen to experience significant over-fatigue during cyclic loading, thus causing premature failure to weaken the specimen before the load-to-failure phase of testing commenced.

Therefore, the comparison of the MSRC values obtained by specimen B2, the optimum GPC specimen which implemented Bondek sheeting, and specimen B4, the control OPC based specimen, reveals that GPC can match the performance of conventional OPC based concrete withstanding the reduction in durability caused by the implementation of both 30% recycled aggregate and Bondek sheeting.

A performance pattern can be easily distinguished in regards to the significantly reduced MSRC of Bondek specimens in regards to Solid Slab specimens. This can be attributed to the presence of embossments, which ultimately reduce the amount of local concrete surrounding the shear connectors. Thus, causing the Bondek specimens to become increasingly prone to conical type concrete failure. Consequently, conical type concrete failure results in the significant separation of the concrete component from the steel section component which then reduces the amount of interaction between the concrete and steel components within the composite member and causes ineffectiveness in regards to shear load resistance.

Table 3. Push test results summary.

Specimen (*No.*)	Maximum Shear Resistance (*kN*)	Governing Failure Mode
SS1	927.56	Concrete Splitting Failure
B1	355.75	Conical Type Failure
SS2	705.44	Combination of Splitting and Cracking Failure
B2	393.04	Conical Type Failure
SS3	730.42	Concrete Splitting Failure
B3	329.84	Combination of Conical and Splitting Failure
SS4	947.46	Concrete Splitting Failure
B4	458.32	Conical Type Failure

Figure 6 (a) depicts an example of concrete splitting failure caused by significant outward and downward movement of the South (Roller-Support) slab. Whereas, Figure 6 (b) depicts an example of conical failure caused by the prevention of effective interaction between the local concrete surrounding the headed stud shear connectors and remaining volume of concrete. This reduction in effective interaction is attributed to the presence of embossments within the profiled steel sheeting (Bondek) which reduce the amount of concrete surrounding the shank of the headed stud shear connectors.

(a) Specimen SS3 (b) Specimen B2

Figure 6. Governing failure mode examples.

The Headed Stud Shear Connectors (HSSCs) within all the tested push test specimens within this experimental research experienced slight bending deformation. Additionally, none of the concrete compressive strengths within this experimental research was high enough to cause shear stud failure. Therefore, the results obtained for all the push test specimens within this research can be deemed favourable since early failure signs such as concrete cracking occurred for all specimens, rather than sudden failure without warning.

4. CONCLUSION

- Solid Slab push test specimens significantly outperform specimens incorporating Bondek sheeting due to the reduction in the amount of concrete surrounding each pair of shear studs caused by the presence of Bondek flanges. The Solid Slab specimens all failed due to concrete splitting type failure and Bondek specimens all failed from conical type separation of the local concrete surrounding each pair of shear studs.

- In regards to the implementation of up to 30% of Recycled Aggregate, a significant reduction in concrete durability occurs. Thus explain the lower MSRC achieved by specimen SS2 in comparison to specimen SS1. Therefore, GPC1 can be classified as the optimum GPC mix design.

- The expected calculations in regards to the shear resistance capacity of HSSCs installed within Solid Slab specimens in accordance with Eurocode 2005 are too conservative. Since the average shear resistance capacity of all three Solid Slab specimens equates to 98.5kN per stud in comparison to the calculated value of 74.4kN.

- The expected calculations in regards to the shear resistance capacity of HSSCs installed within Bondek specimens in accordance with Eurocode 2005 are extremely accurate. Since the average shear resistance capacity of all three Bondek specimens equates to 44.94kN per stud in comparison to the calculated value of 52.08kN.

- The high-performance expectation brought about by the results obtained by specimen SS1 (115kN per stud) resulted in overloading to cause premature failure in regards to specimen B1. Therefore, the accuracy of expected results calculated using Eurocode 2004 is again reinforced and the inaccuracy of expected calculations using AS2327.1 in regards to Bondek specimens is again reinforced.

5. REFERENCE

Albitar, M, Visintin, P, Mohamed Ali, M & Drechsler, M (2015). Assessing behaviour of fresh and hardened geopolymer concrete mixed with class-F fly as', KSCE Journal of Civil Engineering, vol. 19, no. 5, pp. 1445-55.

Bakharev, T (2005). Geopolymeric materials prepared using Class F fly ash and elevated temperature curing, Cement and Concrete Research, vol. 35, no. 6, p. 1224.

Hardjito, D, Wallah, SE, Sumajouw, DM & Rangan, BV (2004). On the development of fly ash-based geopolymer concrete, ACI Materials Journal-American Concrete Institute, vol. 101, no. 6, pp. 467-72.

Xie, T and Ozbakkaloglu, T (2015). Behavior of low-calcium fly and bottom ash-based geopolymer concrete cured at ambient temperature, Ceramics International, vol. 41, no. 4, pp. 5945-58.

ISBN: 978-0-6480147-6-8

Ultimate Capacity Estimate of Self-Compacting Concrete-Filled Small Diameter Steel Tubes under Axial Load

Faez Alhussainy[1], M. Neaz Sheikh[2] and Muhammad N. S. Hadi[3,*]

[1]Ph.D. Candidate, School of CME Engineering, University of Wollongong, Australia
[2]Associate Professor, School of CME Engineering, University of Wollongong, Australia
[3]Associate Professor, School of CME Engineering, University of Wollongong, Australia
*Corresponding author's E-mail: mhadi@uow.edu.au

Abstract

This study explores the effect of length to diameter (L/D) ratio on the axial load capacity of self-compacting concrete-filled small diameter steel tube (SCFT) specimens. The SCFT specimens with L/D ratio of 2, 4, 6, 8, 10, 12 and 14 were tested. Two different cold-formed steel tubes were used in the construction of the SCFT specimens. For each L/D ratio, two specimens were tested. For tension tests, three specimens were tested for each type of unfilled steel tube. A total of 62 steel tube specimens were tested which included 6 specimens under axial tension and 56 specimens under axial compression. The experimental results of the SCFT specimens were compared with the estimates from three design standards: American Standard, Canadian Standard and European Standard (Eurocode 4). It was found that Eurocode 4 provided the best estimate, whereas American Standard provided the most conservative estimate. Also, when the L/D ratio of SCFT specimens increased from 2 to 8, the parameter related to the effect of confinement concrete (η_c) which is calculated from Eurocode 4 decreased. Therefore, the decrease in η_c resulted in a decrease in the concrete enhancement factor. For SCFT specimens with L/D ratio ≥ 10 the parameter η_c was negligible and resulted in the concrete enhancement factor =1.

***Keywords**: Concrete-filled steel tube, Self-compacting concrete, Axial load, Length to diameter ratio.*

1. INTRODUCTION

In recent years cold-formed steel tubes have become more popular as a structural member due to its high yield stress (Alhussainy et al. 2017). One of the main applications of cold-formed steel tubes is concrete-filled steel tube (CFT). The CFT is constructed by filling steel tubes with concrete. The advantages of the CFT are high ultimate capacity, ductility, seismic resistance and fire resistance (Shanmugam and Lakshmi 2001; Huang et al. 2015). Due to the above mentioned advantages, CFTs have been widely used as columns for bridges and high-rise buildings (Abed et al. 2013). The CFT is also used in composite column that consists of inner CFT and outer reinforced concrete (Han and An 2014). Recently, Hadi et al. (2017) proposed using small diameter CFTs in lieu of longitudinal steel bars for reinforcing concrete columns. The innovative use of CFTs was found to be efficient due to the increase in the axial capacity and ductility (Hadi et al. 2017). In addition, CFT members can be effectively adopted for structural components where small cross-sections are required.

Li et al. (2015) compared experimental data of CFT columns with three design standards (American Standard ANSI/AISC 360-10 2010; European Standard Eurocode 4 2004 and Chinese Standard CECS 28-12 2012). Li et al. (2015) reported that all three design standards provided conservative estimates for both short and long CFT columns. Aslani et al. (2015) developed simplified relationships to predict the section capacity and ultimate buckling capacity of normal and high-strength concrete filled short and long CFTs. Aslani et al. (2015) considered that the slenderness reduction factor was modified based on the adjusted formula of section capacity.

The behaviour of steel tubes filled with concrete has been extensively studied and included in major design standards (American Standard ANSI/AISC 360-10 2010; Canadian Standard CAN/CSA S16-09 2009; and European Standard Eurocode 4 2004). A large number of studies were carried out on medium scale specimens with outside diameter between 100 mm and 200 mm using concrete of varying compressive strengths. However, research studies have seldom been conducted on small diameter concrete filled steel tubes. In this study, steel tubes with small diameters were used as CFT. The results of the axial load capacity of SCFT with different L/D ratios were compared to the estimates from three design standards. Also, experimental concrete enhancement factors of the SCFT specimens were calculated and compared with the estimates from the Eurocode 4.

2. EXPERIMENTAL PROGRAM

Two different types of cold-formed steel tubes were used to construct self-compacting concrete-filled small diameter steel tube (SCFT) specimens. The first cold-formed steel tube had 26.9 mm outside diameter, 2.6 mm wall thickness and 250 MPa nominal tensile strength. The second cold-formed steel tube had 33.7 mm outside diameter, 2 mm wall thickness and 350 MPa nominal tensile strength. The cold-formed steel tube specimens were divided into two groups: SCFT specimens and unfilled steel tube (UT) specimens. The behaviour of specimens under axial compression depends largely on the unsupported length to outside diameters (L/D) ratio. In the experimental program, specimens with L/D ratio of 2, 4, 6, 8, 10, 12 and 14 were tested under axial compression. For each L/D ratio, two specimens were tested under axial compression. The UT specimens were also tested under axial tension. Three specimens for each type of UT were tested under axial tension. A total of 62 specimens were tested which included 56 specimens under axial compression and 6 specimens under axial tension.

Self-compacting concrete (SCC) mix with a maximum aggregate size of 10 mm was used in casting the SCFT specimens. The average 28-day compressive strength of the SCC was 57 MPa.

A 500 kN universal testing machine in the High Bay laboratory at the University of Wollongong, Australia was used to conduct the tests for all specimens. The SCFT specimens were tested with the axial load applied on the entire section. The ends of steel tube specimens were milled for a flat surface. The specimens were tested under displacement controlled load applications at 1 mm/min.

Three samples of each UT26.9 and UT33.7 steel tubes were tested according to ASTM A370 (2014). Yield stresses of both unfiled steel tubes were determined using the 0.2% offset method, as clearly defined yield stress was not observed. The average yield stress and modulus of elasticity of UT26.9 steel tube were found as 355 MPa and 192 GPa, respectively. The average yield stress and modulus of elasticity of UT33.7 steel tube were found as 450 MPa and 196 GPa, respectively.

3. COMPARISON OF EXPERIMENTAL RESULTS WITH DESIGN STANDARDS

Three different design standards were used to calculate the axial load capacity of the self-compacting concrete-filled steel tube (SCFT) specimens under concentric axial load. The calculated results were compared with the experimental results. The design standards included in this study were the American Standard (ANSI/AISC 360-10 2010), Canadian Standard (CAN/CSA S16-09 2009) and European Standard (Eurocode 4 2004). The design standards for composite columns constructed with only two components: steel tube and concrete infill are briefly reviewed below.

In the American Standard (ANSI/AISC 360-10 2010), the nominal member capacity N_c is calculated by Eqs. (1) and (2).

$$N_c = N_o \left[0.658^{\left(\frac{N_o}{N_e}\right)}\right], \qquad \text{If } \frac{N_o}{N_e} \leq 2.25 \tag{1}$$

$$N_c = 0.877\, N_e, \qquad \text{If } \frac{N_o}{N_e} > 2.25 \tag{2}$$

$$N_o = f_y\, A_s + \alpha_1\, f_c'\, A_c \tag{3}$$

$$N_e = \frac{\pi^2\, EI_e}{(k_e\, L)^2} \tag{4}$$

where N_o is the squashing capacity of the cross-section, N_e is the Euler elastic buckling capacity, f_y is the steel yield stress, f_c' is the concrete compressive strength, A_s and A_c are the steel and concrete cross section areas, respectively, α_1 is the reduction factor for the filling concrete which is equal to 0.95 for circular section, k_e is the member effective length factor and L is the column length. The effective flexural stiffness EI_e of a cross section of a composite column is calculated by Eq. (5).

$$EI_e = E_s\, I_s + C_3\, E_c\, I_c \tag{5}$$

$$C_3 = 0.6 + 2\left(\frac{A_s}{A_s + A_c}\right) \leq 0.9 \tag{6}$$

where E_s and E_c are the elastic moduli of the steel and concrete, respectively, I_s and I_c are the second moment of area of the steel and concrete, respectively, and C_3 is the coefficient of concrete effective stiffness.

In the Canadian Standard (CAN/CSA S16-09 2009), the nominal member capacity is calculated by Eq. (7).

$$N_c = (\tau\ f_y\ A_s + \tau'\, \alpha_1\, f_c'\, A_c)\,(1 + \lambda^{2n})^{-1/n} \tag{7}$$

$$\alpha_1 = 0.85 - 0.0015\, f_c' \quad \geq 0.67 \tag{8}$$

where n =1.8 for a composite concrete filled steel tube, τ is the parameter of reducing steel capacity, τ' is the parameter of increasing concrete capacity due to confinement by steel tube.

$\tau = \tau'$= 1.0, except for circular steel tube sections with a length to outside diameter (L/D) ratio less than 25 for which:

$$\tau = \frac{1}{\sqrt{1+\rho+\rho^2}} \tag{9}$$

$$\rho = 0.02(25 - L/D) \tag{10}$$

$$\tau' = \left(\frac{25\ \rho^2\ \tau}{D/t}\right)\left(\frac{f_y}{\alpha_1\, f_c'}\right) + 1 \tag{11}$$

$$\lambda = \sqrt{\frac{N_o}{N_e}} \tag{12}$$

where t is the wall thickness of steel tube, λ is the relative slenderness, $N_o = N_c$ (computed with $\lambda = 0$), the Euler elastic buckling capacity N_e is calculated by Eq. (4). The effective flexural stiffness EI_e is calculated by Eq. (5) and the coefficient C_3 is calculated by Eq. (13).

$$C_3 = \frac{0.6}{1 + C_{fs}/C_f} \tag{13}$$

where C_{fs} and C_f are sustained and total axial load on the column, respectively.

The European Standard (Eurocode 4 2004) provides more detailed expression to estimate the effect of the confinement concrete due to steel circular tube. The nominal member capacity N_c is calculated by Eq. (14).

$$N_c = x\left[\eta_a\, f_y\ A_s + f_c'\, A_c\left(1 + \eta_c\, \frac{t}{D}\, \frac{f_y}{f_c'}\right)\right] \tag{14}$$

where η_a is a reduction factor for the steel strength and η_c is a factor related to the effect of confinement concrete. The factors η_a and η_c are functions of the relative slenderness λ which is calculated by Eq. (15). The squashing capacity of the cross-section N_o is calculated by Eq. (4) and by using the reduction factor for the filling concrete α_1 which is equal to 1. The Euler elastic buckling capacity N_e is calculated by Eq. (4). The effective flexural stiffness EI_e of a cross section of a composite column is calculated by Eq. (5) and by using the coefficient C_3 which is equal to 0.6.

For columns having slenderness λ > 0.5, there is no gain from confinement effect and η_a =1 and η_c =0. For columns having no eccentricity (e = 0), the coefficients η_a and η_c are calculated as:

$\eta_a = \eta_{ao} = 0.25(3 + 2\lambda)$, (but ≤ 1) (15)

$\eta_c = \eta_{co} = 4.9 - 18.5\lambda + 17\lambda^2$, (but ≥ 0) (16)

The function x provides the resistance reduction for slender columns, in terms of the relative slenderness λ, as shown in Eq. (12). For columns having relative slenderness $\lambda \leq 0.2$, the resistance reduction x =1.

$$x = \frac{1}{\varphi + \sqrt{\varphi^2 - \lambda^2}} \quad \text{(but} \leq 1) \quad (17)$$

$$\varphi = 0.5[1 + 0.21(\lambda - 0.2) + \lambda^2] \quad (18)$$

In order to compare the experimental results with prediction results based on the recommendations in the design standards, the partial safety factors for the design standards were taken equal to 1 in this study. The ratios of experimental results to the estimates from design standards (N_{SCFT}/N_c) for SCFT specimens are reported in Table 1. The values of average nominal member capacity N_c predicted by the design standards were found to be not very different from the experimental average ultimate load capacity N_{SCFT} for the SCFT specimens. The average N_{SCFT}/N_c ratios were close to 1 for the Eurocode 4 (2004), less than 1 for the CAN/CSA S16-09 (2009) and higher than 1 for ANSI/AISC 360-10 (2010). For the ANSI/AISC 360-10 (2010), the average N_{SCFT}/N_c ratios for the specimens in Group SCFT26.9 and Group SCFT33.7 were 1.167 and 1.134, respectively, with standard deviations of 0.061 and 0.075, respectively. For the CAN/CSA S16-09 (2009), the average N_{SCFT}/N_c ratios for the specimens in Group SCFT26.9 and Group SCFT33.7 were 0.933 and 0.888, respectively, with standard deviations of 0.018 and 0.024, respectively. For the Eurocode 4 (2004), the average N_{SCFT}/N_c ratios for the specimens in Group SCFT26.9 and Group SCFT33.7 were 1.060 and 1.018, respectively, with standard deviations of 0.057 and 0.048, respectively.

Table 1. Comparison of experimental results with design provisions in codes for SCFT specimens

L/D	N_{SCFT} (kN)[a]	N_c (kN)[b]			N_{SCFT}/N_c		
		ANSI/AISC	**CAN/CSA**	**EC4**[c]	**ANSI/AISC**	**CAN/CSA**	**EC4**[c]
Specimens constructed by using steel tube ST26.9							
2	117	90.2	122.5	119.4	1.297	0.955	0.98
4	104.2	89.2	116.2	106.4	1.168	0.897	0.979
6	103.4	87.7	110.3	95.5	1.179	0.937	1.083
8	97.9	85.6	104.9	88.0	1.144	0.933	1.112
10	93	83	100.1	84.4	1.121	0.929	1.101
12	90.9	79.8	95.9	82.8	1.139	0.948	1.098
14	85.8	76.3	92.3	80.3	1.124	0.929	1.068
Specimens constructed by using steel tube ST33.7							
2	164	126.6	175.2	170.5	1.295	0.936	0.962
4	143.1	125.1	165.7	150	1.144	0.864	0.954
6	137.2	122.7	156.9	132.9	1.119	0.875	1.032
8	132.9	119.3	148.8	122.3	1.114	0.893	1.087
10	125.9	115.1	141.5	119.1	1.094	0.890	1.057
12	117.8	110.1	135.1	114.6	1.070	0.872	1.028
14	115.3	104.6	129.6	114.0	1.103	0.889	1.011

[a] N_{SCFT} is the average ultimate load capacity of two SCFT specimens tested under axial compression.
[b] N_c is the nominal member capacity of SCFT specimens calculated from three design standards.
[c] EC4 is the Eurocode 4 (2004).

The experimental value for the concrete enhancement factor (O'Shea and Bridge 1996) was calculated by dividing the confinement concrete strength (f_{cc}) on the compressive strength of SCC. The confinement concrete strength f_{cc} was calculated by subtracting the unfilled steel tube capacity (N_{UT}) from the concrete-filled steel tube capacity (N_{SCFT}) and dividing the remainder by the infill concrete area (A_c). Also, Eurocode 4 was used to calculate theoretically the concrete enhancement factor of the SCFT specimens with different L/D ratios (Shanmugam and Lakshmi 2001; O'Shea and Bridge

1996). The theoretically concrete enhancement factor was calculated based on the term $\left(1+\eta_c \frac{t}{D} \frac{f_y}{f_c'}\right)$ in the Equation 14 (Eurocode 4 2004). Table 2 presents the experimental and theoretical values for the concrete enhancement factor of the SCFT specimens. When the L/D ratio of SCFT specimens increased from 2 to 8, the parameter η_c calculated from Eurocode 4 (2004) decreased and resulted in decreasing the concrete enhancement factor. For SCFT specimens with L/D ratio ≥ 10 the parameter η_c was negligible and resulted in the concrete enhancement factor =1. Also, the experimental concrete enhancement factor of SCFT specimens decreased when the L/D ratio increased from 2 to 10. However, for specimens with L/D ratio ≥ 12 the experimental concrete enhancement factor continued to decrease to a value less than 1, unlike the theoretical concrete enhancement factor which remained constant at 1. The concrete enhancement factor from Eurocode 4 (2004) is only valid for a relative slenderness lower than 0.5. Therefore, specimens with L/D ratio ≥ 12 tested in this study are considered out of scope.

Table 2. Experimental and theoretical values for the concrete enhancement factor of SCFT specimens

L/D	N_{UT} (kN)[a]	N_{SCFT} (kN)[b]	f_{cc} (MPa)[c]	f_{cc}/f'_c Concrete enhancement factor (Exp.)	Parameter η_c Eurocode 4 (2004)	Concrete enhancement factor (Theo.) $\left(1+\eta_c \frac{t}{D} \frac{f_y}{f'_c}\right)$
Specimens constructed by using steel tube ST26.9						
2	83.8	117	89.8	1.575	3.325	3
4	81.3	104.2	61.9	1.086	2.045	2.231
6	78.9	103.4	66.2	1.161	1.059	1.637
8	73.5	97.9	66	1.158	0.368	1.222
10	71.6	93	57.9	1.016	0	1
12	70.8	90.9	54.3	0.953	0	1
14	69.5	85.8	44.1	0.774	0	1
Specimens constructed by using steel tube ST33.7						
2	101.5	164	90.2	1.582	3.202	2.5
4	100.2	143.1	61.9	1.086	1.853	1.868
6	93.8	137.2	62.6	1.098	0.851	1.399
8	88.6	132.9	63.9	1.121	0.198	1.093
10	83.8	125.9	60.8	1.067	0	1
12	81.5	117.8	52.4	0.919	0	1
14	78.6	115.3	53	0.930	0	1

[a] N_{UT} is the average ultimate load capacity of two unfilled steel tube specimens tested under axial compression.
[b] N_{SCFT} is the average ultimate load capacity of two concrete-filled steel tube specimens tested under axial compression.
[c] f_{cc} is the confinement concrete strength.

4. CONCLUSIONS

Based on the experimental and analytical results presented in this study, the following conclusions can be drawn:

1. Based on the experimental results of self-compacting concrete-filled small diameter steel tubes (SCFT) and unfilled small diameter steel tube (UT) specimens, the SCFT specimens showed a higher increase of axial load capacity compared to the UT specimens due to the effect of the concrete infill.

2. The ratio of experimental results to the estimates from design standards (N_{SCFT}/N_c) for SCFT specimen was found to be close to 1 for Eurocode 4 (2004), less than 1 for CAN/CSA S16-09 (2009) and higher than 1 for ANSI/AISC 360-10 (2010).

3. When the L/D ratio of SCFT specimens increased from 2 to 8, the parameter related to the effect of confinement concrete (η_c) which was calculated from Eurocode 4 decreased. Therefore, the decrease in η_c resulted in a decrease in the concrete enhancement factor. For SCFT specimens with L/D ratio ≥ 10 the parameter η_c was negligible and resulted in the concrete enhancement factor =1.

4. The experimental concrete enhancement factor of SCFT specimens decreased when the L/D ratio increased from 2 to 10. However, for specimens with L/D ratio $\geq$ 12 the experimental concrete enhancement factor continued to decrease to a value less than 1, unlike the theoretical concrete enhancement factor which remained constant at 1.

ACKNOWLEDGEMENTS

The authors thank the University of Wollongong, Australia for research facilities. The first author thanks the Iraqi Government for the support of his PhD scholarship.

REFERENCES

Abed F, AlHamaydeh M, Abdalla S (2013). Experimental and numerical investigations of the compressive behavior of concrete filled steel tubes (CFSTs), Journal of Constructional Steel Research, 80, 429-439.

Alhussainy F, Sheikh NM, Hadi MNS (2017). Behaviour of small diameter steel tubes under axial compression, Structures, 11, 155-163.

ANSI/AISC 360-10 (2010). Specification for Structural Steel Buildings, American Institute of Steel Construction, Chicago, USA

Aslani F, Uy B, Tao Z, Mashiri F (2015). Predicting the axial load capacity of high-strength concrete filled steel tubular columns, Steel and Composite Structures, An International Journal, 19(4), 967-99.

ASTM A370-14 (2014). Standard Test Method and Definitions for Mechanical Testing of Steel Products, American Society for Testing and Materials, West Conshohocken, PA, USA.

CAN/CSA-S16-09 (2009). Limit States Design of Steel Structures, Canadian Standards Association, Mississauga, Canada

CECS 28:2012 (2012). Technical Specification for Concrete-Filled Steel Tubular Structures, China Engineering Construction Standard, Beijing, China

European Standard (2004). Design of Composite Steel and Concrete Structures- Part 1-1: General Rules and Rules for Buildings. European Standard, Eurocode 4, EN 1994-1-1, Brussels, Belgium

Hadi MNS, Alhussainy F, Sheikh NM (2017). Behavior of self-compacting concrete reinforced longitudinal with steel tubes, Journal of Structural Engineering ASCE, 143(6), 1-14.

Han LH, An YF (2014). Performance of concrete-encased CFST stub columns under axial compression, Journal of Constructional Steel Research, 93, 62-76.

Huang Y, Xiao J, Yang Z, Wang Q (2015). Behaviour of concrete filled-steel tubes under axial load, Proceedings of the Institution of Civil Engineers: Structures and Buildings, 169, 210-222.

Li N, Lu Y-Y, Liang H-J (2015). Statistical-based evaluation of design codes for circular concrete-filled steel tube columns, Steel and Composite Structures, 18(2), 519-546.

O'Shea MD, Bridge RQ (1996). Circular thin-walled tubes with high strength concrete infill. Composite Construction 3, Engineering Foundation Conference, Germany: 780-793

Shanmugam NE, Lakshmi B (2001). State of the art report on steel-concrete composite columns, Journal of Constructional Steel Research, 57(10), 1041-1080.

ISBN: 978-0-6480147-6-8

Strength and Ductility Behaviour of Steel Plate Reinforced Concrete Beams under Flexural Loading

Mazin M. Sarhan[1], Muhammad N. S. Hadi[2] and Lip H. Teh[3]

[1]Ph.D. Candidate, School of Civil, Mining and Environmental Engineering, University of Wollongong, Australia.
[2]Associate Professor, School of Civil, Mining and Environmental Engineering, University of Wollongong, Australia.
[3] Associate Professor, School of Civil, Mining and Environmental Engineering, University of Wollongong, Australia.
Corresponding author's E-mail: mms912@uowmail.edu.au

Abstract

Long-term durability is the main concern in the area of civil engineering due to safety considerations. This paper reports the strength and ductility behaviour of steel plate reinforced concrete beams under four-point bending. A total of three full-scale beams of 200 mm width, 300 mm height and 4000 mm length were cast and tested. All the beams had the same details of stirrups and compression reinforcement. The first beam was reinforced with ordinary reinforcement (2 deformed steel bars with a nominal diameter of 20 mm) and served as a reference beam. The second beam was reinforced with a chequer steel plate and provided with 20 steel bolts welded to the chequer steel plate at a regular distance of 200 mm centre to centre. The third beam was reinforced with a chequer steel plate and provided with 4 steel angles welded at the ends of the steel plate. Each plate reinforced concrete beam was designed to have an equivalent force to the ordinary reinforced concrete beam. The strengths, ductilities and analytical considerations of the beams are covered in this paper. The results showed no significant difference (less than 2%) between the strengths of ordinary and plate reinforced concrete beams. On the other hand, the steel plates significantly increased the ductility. The ductilities of plate reinforced concrete beams provided with steel bolts and angles increased by up to 3.7 and 2.3 times, respectively compared with the ordinary reinforced concrete beam. It was also observed, that the use of steel bolts in the plate reinforced concrete beam, improved the ductility by 43.2% compared to the steel angles.

Keywords: Steel plate, Concrete beam, Flexural behaviour, Ductility.

1. INTRODUCTION

In civil engineering investigations, understanding the behaviour of concrete members reinforced with steel bars has previously been the substantial aim of many researchers. On the other hand, only a few limited studies used steel plates as another concept of reinforcement, for example, Subedi and Coyle (2002), Su et al. (2008) and Su et al. (2009). The plate reinforced concrete beam (beam reinforced with an embedded steel plate(s)) is also a way to reduce the cross-section of the beam.

In the design of plate reinforced concrete beam, both the strength and ductility need to be recognized. The shear strength of reinforced concrete beam has been enhanced by using embedded steel plates. For instance, use of steel plate as shear reinforcement increased the shear resistance by about 75% compared to the conventional shear reinforcement (Subedi and Baglin 1999). The flexural strength of coupling concrete beams (with different depths) reinforced with vertical steel plates and steel bars together was investigated by Lam et al. (2013); the height of steel plates relied on the beam's depth. That study showed that the strength of beams was reduced with the use of the inadequate height of embedded steel plates. However, that study showed the combined effects of using steel bars and steel plates (only in vertical installation) on the flexural behaviour of concrete beams. Therefore, this study was conducted to investigate the flexural strength and ductility of the concrete beams reinforced with only steel plates installed in a horizontal way.

The performance of members reinforced with sections depends on the bond strength between the section and the surrounding concrete. The bond influences the serviceability aspects of the beam such as the width of cracks, the spacing of cracks and deflections. According to ACI-408R-03-Committee (2003), the interaction between the reinforcement and the surrounding concrete essentially relies on the mechanical anchorage of reinforcement. Thus, steel bolts, steel angles, and chequer surface of the steel plates were used as mechanical anchorages of reinforcement in this study.

2. EXPERIMENTAL PROGRAM

2.1. Beam design and preparation

In this study, three full-scale reinforced concrete beams were cast and tested under four-point bending. The dimensions of the beams were chosen to be 200 mm in width, 300 mm in height and 4000 mm in length. All the beams were reinforced with the same amount of stirrups and compression reinforcement. For stirrups, plain steel bars of 10 mm diameter (250 MPa nominal tensile strength) were used at 80 mm spacing centre to centre (R10 @ 80 mm). For compression reinforcement, two plain steel bars of 10 mm diameter were used. The clear cover of beams was maintained at 20 mm at the bottom and each side. The first beam (reference beam) was longitudinally reinforced with two deformed steel bars of 20 mm diameter (2N20) with 500 MPa nominal tensile strength. The second and third beams were longitudinally reinforced with chequer steel plates of 100 mm width and 10 mm thickness with 330-390 MPa typical yield tensile strength. One surface of the chequer steel plate was smooth, while the other had raised lozenges of 5.5 mm width, 26 mm length and about 1.5 mm height. In order to prevent or reduce the slippage between the steel plates and the concrete, steel bolts and equal steel angles were used. Twenty steel bolts of 20 mm diameter (460 MPa nominal tensile strength) were welded at 200 mm spacing to the steel plate of the second beam. Four equal steel angles (75 mm x 75 mm) of 8 mm thickness (480 MPa nominal tensile strength) were welded at the ends of the steel plate of the third beam. The second and third beams were designed to have an equivalent tensile force to the reference beam. Table 1 presents the main reinforcement details of the beams.

Table 1. Main reinforcement details of the tested beams

Beams	**Longitudinal reinforcement**				**Mechanical anchorage of steel plate**
	Type of reinforcement	Number of steel bars or steel plates	Diameter of steel bars (mm)	Dimensions of steel plate (mm)	
A	Steel bars	2	20	---	---
B	Steel plate	1	---	100x10	Steel bolts
C	Steel plate	1	---	100x10	Steel angles

2.2. Material properties

All the beams were cast on the same day with normal strength concrete provided by a local supplier. The average compressive strength was 42.3 MPa at 28 days. According to AS 1391-2007 (AS 2007), the tensile strengths of reinforcing steel bars (N20 and R10) and steel plate were found by using the 500 kN Instron testing machine. The average of yield tensile strengths were 365 and 540 MPa for R10 and N20, respectively, while it was 370 MPa for the steel plate. All the tests were carried out at the laboratories of the School of Civil, Mining and Environmental Engineering, University of

Wollongong, Australia.

2.3. Beam fabrication, casting and curing

Wooden formworks with inner dimensions of 200 mm wide, 300 mm height and 4000 mm length were used for casting the beams. The stirrups were prepared by forming a rectangle with 150 mm width and 250 mm height (centre to centre) by a local manufacturer. Steel chairs with a height of 20 mm were used to maintain the specified concrete cover (20 mm) at the bottom ends of the beams; these chairs were placed at a spacing of one meter. Small pieces of steel bars (20 mm length) were welded to the stirrups to obtain the specified cover at both sides. Before the concrete casting, the dust that may be inside the formworks was removed by using compressed air. The air bubbles inside the concrete were removed by using an electrical vibrator during the casting process. Thereafter, the beams were cured by covering them with wet hessian and a plastic sheet for 28 days.

3. TESTING PROCEDURE

All the beams were tested, under simply supported conditions, by a four-point bending test. The space between the two loading points (pure bending span) was 1200 mm. Four pieces of steel plates were used at the points of supports and loads to reduce stress concentration. The steel plate pieces had the dimensions of 100 mm width, 10 mm thickness, and 200 mm length. The deflection at the mid-span of each beam was measured by using a draw-wire transducer. The test was conducted using the 600 kN actuator. The actuator load was distributed into two applied loads by using a steel spreader of 870 N weight. The beams were tested under displacement control with a loading rate of 1 mm/minute. During the test, the data were recorded by a smart system installed on a computer.

4. EXPERIMENTAL RESULTS AND DISCUSSION

4.1 Failure modes

In this study, all the beams were tested until the failure. Figure 1 shows the failure modes of the tested beams at the end of tests.

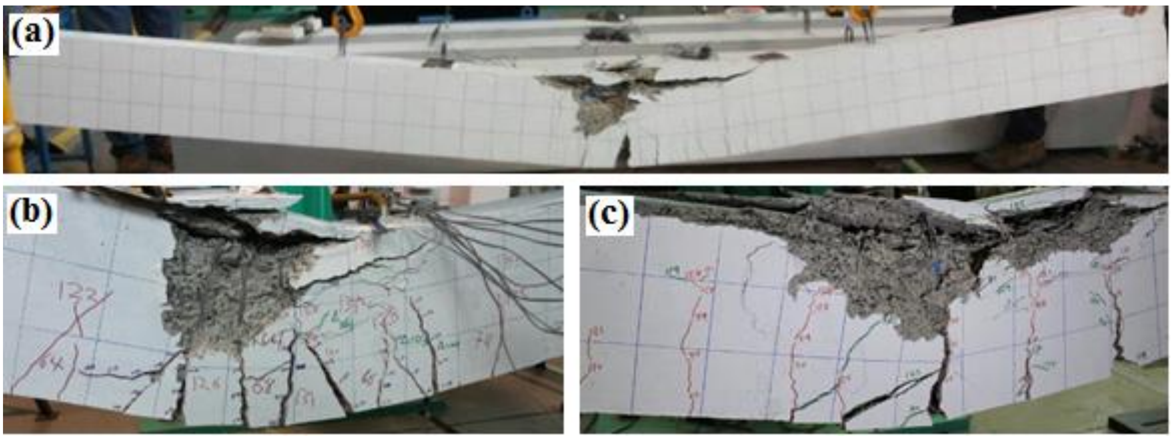

Figure 1. Failure modes of the beams; (a) Beam A; (b) Beam B and (c) Beam C

The failure modes relied on the type of reinforcement materials and the reinforcement details. During the loading, the behaviour of beams changed from elastic to plastic. The initial cracks formed at the tension zone of the pure bending span and then progressed towards the neutral axes. Before obtaining the load of failure, the tension reinforcement of all beams yielded; this indicates that the cross-sections of the beams were under-reinforced. It was also noticed that the yield took place before the concrete crush; this means that the beams' failure modes were flexural-tension. Afterward, the cracks exceeded the neutral axes of the cross-sections of the beams and became wider with the time of tests.

4.2 Load-midspan deflection behaviour

Figure 2 shows the load-midspan deflection curve of the tested beams. In general, all the beams approximately showed similar behaviour in the ascending part of the curve until the yield load. The ascending part of the curve was mainly controlled by the concrete stiffness. Yield loads of the beams are presented in Table 2. The yield loads of Beams B and C were similar, and they were higher than Beam A by 3%. After the yield loads, the beams showed different behaviour depending on the details of reinforcement of beams. The cover spalling approximately occurred at deflections of 65, 57 and 62 mm for Beams A, B and C, respectively. The maximum loads of the beams are also summarized in Table 2. It can be noticed that the maximum load of Beam A was 1.5% lower than Beam B and 1.2% higher than Beam C. This indicates that the tension forces of the beams are equivalent as were designed. However, there was a big difference in the ductility of the beams, as will be shown in the next subsection.

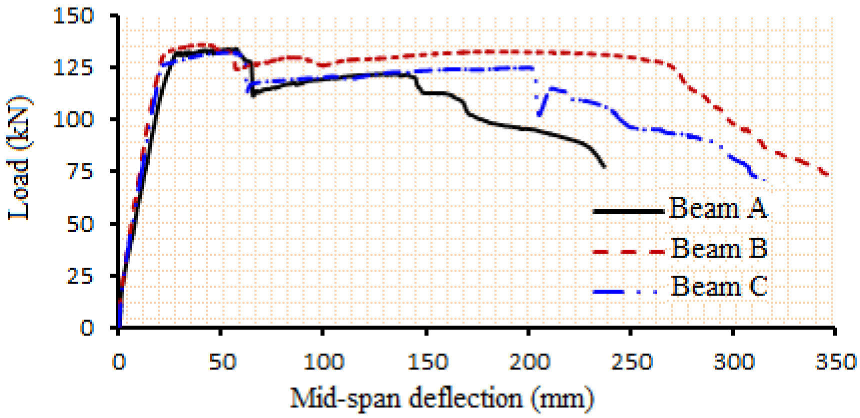

Figure 2. Load-midspan deflection curve of the tested beams

Table 2. Yield and maximum loads of the tested beams

Beams	Yield load (kN)	Maximum Load (kN)
A	122.8	134.2
B	126.5	136.2
C	126.5	132.6

4.3 Ductility of beams

Ductility can be defined as the ability of the member to undergo deflections without an essential reduction in the flexural capacity (Park and Ruitong 1988). The deflection can be influenced by some factors such as the compression/tension strength of concrete, the amount of tension and compression reinforcement and a number of stirrups (Xie et al. 1994). The ductility of beams (λ) can be presented as shown in Equation 1.

$$\lambda = \Delta_u / \Delta_y \quad (1)$$

where Δ_u represents the post-ultimate deflection at 85% of maximum load; Δ_y represents the deflection at yield load, Figure 3. Foster and Attard (1997) reported that the deflection at yield load can be obtained by three steps, as following:

(1) Draw a line from the origin point of the load-deflection curve passing through the point at 75% of the maximum load.
(2) Draw a horizontal line at the maximum load.
(3) The deflection at yield load represents the intersection point of those two lines.

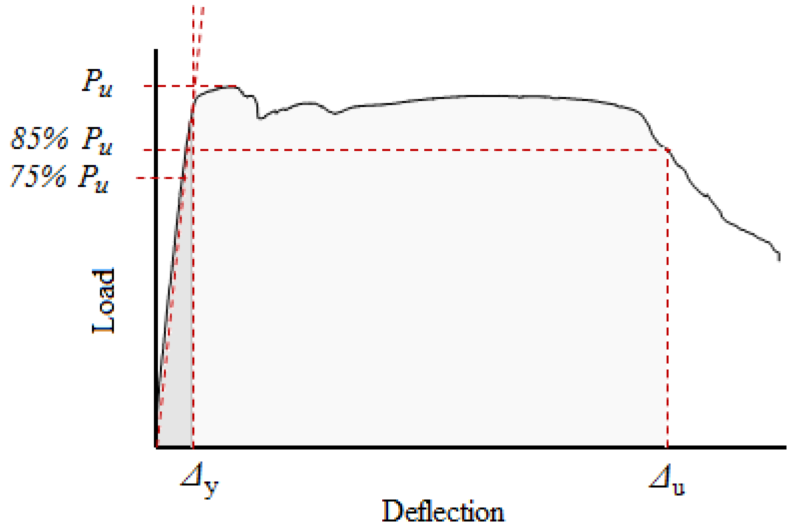

Figure 3. Ductility calculation of the tested beams

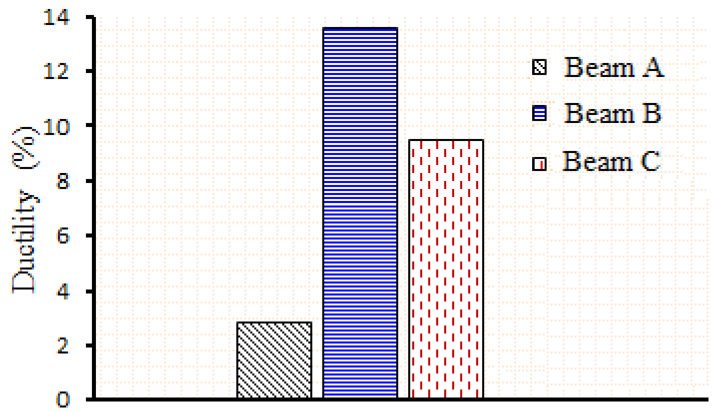

Figure 4. Ductility percentage of the tested beams

Figure 4 shows the ductilities of the tested beams. The ductilities of Beams A, B and C were 2.9, 13.6 and 9.5, respectively. It can be observed that the ductilities of Beams B and C (beams reinforced with steel plates) were higher than Beam A (beam reinforced with steel bars) by 3.7 and 2.3 times, respectively. This indicates that the use of steel plates, as the main reinforcement, makes the concrete beams more ductile. Furthermore, the ductility of Beam B was 43.2% higher than Beam C. This means that the use of steel bolts at regular distances along the beam better than the use of steel angles at the ends.

5. CONCLUSIONS

The behaviour of concrete beams reinforced with steel bars or steel plates was experimentally investigated. Three full-scale reinforced concrete beams were tested under four-point bending. Based on the results of this study, the following conclusions can be summarized:

1. All the test specimens failed in flexure with the reinforcement steel bars and horizontal steel plates fully yielded at the ultimate limit state.
2. The yield deflection of the specimen reinforced with steel bars was noticeably larger than that of the plate reinforced ones, even though their ultimate test loads are similar to each other.
3. The plate reinforced concrete beams showed much higher ductility in comparison with the ordinarily reinforced concrete beam.
4. The use of steel bolts welded at regular distances along the steel plate showed more ductile behaviour than the use of steel angles.

6. ACKNOWLEDGMENTS

The authors would like to thank the University of Wollongong for the research facilities. The first author also thanks the Iraqi Government for the support of his Ph.D. scholarship. The first author also wishes to express special thanks to his family for their support.

REFERENCES

ACI-408R-03-Committee (2003). Bond and Development of Straight Reinforcing Bars in Tension (ACI 408R-03). American Concrete Institute, Detroit, Michigan, US.

AS (Australian Standard) (2007). Metallic materials - Tensile testing at ambient temperature. AS 1391-2007, Sydney, NSW, Australia.

Foster SJ, Attard MM (1997). Experimental tests on eccentrically loaded high-strength concrete columns. ACI Structural Journal, 94(3), 295-303.

Lam WY, Li L, Su RKL, Pam HJ (2013). Behaviour of Plate Anchorage in Plate-Reinforced Composite Coupling Beams. The Scientific World Journal, 2013.

Park R, Ruitong D (1988). Ductility of doubly reinforced concrete beam sections. Structural Journal, 85(2), 217-225.

Su RKL, Lam WY, Pam HJ (2009). Experimental study of plate-reinforced composite deep coupling beams. The Structural Design of Tall and Special Buildings, 18(3), 235-257.

Su RKL, Lam WY, Pam HJ (2008). Behaviour of embedded steel plate in composite coupling beams. Journal of Constructional Steel Research, 64(10), 1112-1128.

Subedi NK, Coyle NR (2002). Improving the strength of fully composite steel-concrete-steel beam elements by increased surface roughness—an experimental study. Engineering Structures, 24(10), 1349-1355.

Xie Y, Ahmad SH, Yu T, Hino S, Chung W (1994). Shear ductility of reinforced concrete beams of normal and high-strength concrete. Structural Journal, 91(2), 140-149.

Proc. 1st International Conference on Structural Engineering Research (iCSER 2017)
20-22 Nov 2017, Sydney, Australia
ISBN: 978-0-6480147-6-8

Flexural Behaviour of Pre-cracked Reinforced Concrete Beams Repaired with Adhesive Bonded Steel Plates

Sandile D Ngidi[1] and Morgan Dundu[2]
[1]Postgraduate student, University of Johannesburg, Johannesburg, South Africa
[2]Professor, University of Johannesburg, Johannesburg, South Africa
Corresponding author's E-mail: sngidi@uj.ac.za

Abstract

The problem of cracked concrete structures is receiving considerable attention in the construction industry worldwide. Externally bonded steel plates are used to repair cracked reinforced concrete structures in a number of projects in various parts of the World, but their overall performance is still not fully understood. This investigation assesses the strength and deflections of 12 full-scale reinforced concrete (RC) beams of 175 mm wide x 300 mm deep x 3200 mm long that were pre-cracked, repaired with steel plate at its soffit, using strong epoxy glue and after that, tested to failure under a four-point loading. The beams were divided into three groups. Group 1 comprised of two control beams, which were tested until failure, and were not repaired with steel plates. Group 2 consisted of five beams which were pre-cracked up to the serviceability capacity of the control beams, and Group 3 consisted of five beams which were pre-cracked up to 85% of the capacity of the control beams. All the pre-cracked beams were repaired with steel plates of 6 mm thickness and widths which varied from 75 mm up to 175 mm, in increments of 25 mm. The structural behaviour of all the beams is reported in terms of flexural strength, stiffness, maximum deflections and failure modes. Finally, experimental results are compared with code-predicted results calculated using the EN 1992-1-1 (2004). Externally bonding the steel plate to the pre-cracked reinforced concrete beams resulted in increased stiffness and maximum load capacities and decreased in the maximum midspan deflections. The strength and rigidity of the repaired beams were found to increase with increasing the width-to-thickness ratio of the steel plate.

Keywords: Repairing, Flexural behaviour, Steel plates, Composite beams, Pre-cracking.

1. INTRODUCTION

Reinforced concrete structures often have to face modification and improvement of their performance during their service life. The reason for improvement of an existing structure may come from excessive deflections, cracking elements, structural damage by settlements, earthquakes and vehicle impacts. Repairing has become an acceptable way of improving their load carrying capacity and extending their service lives. In most cases, low carbon steel is used in repairing damaged concrete structures. This type of steel has a ductile stress strain properties and high deformation capacities which contribute to the overall ductility of the externally plated beam. The other advantage of using steel is low cost and wide availability of mild steel. External plating also does not require skilled labour. The epoxy bonded steel plates were extensively carried out by the researchers to strengthen and repair damaged concrete structures in a number of projects since the pioneering study of Hermite and Bresson in 1967. Macdonald (1978) reported that there is no adverse effect of pre-cracking on the structural behaviour of RC beams repaired by bonding the steel plates on their tension faces. Similarly, based on experimental study, Swamy at al (1989) reported that plate bonding can be used for repairing structurally damaged RC beams.

The present investigation focuses on the flexural behaviour of reinforced concrete beams repaired with steel plates. The aim of repairing cracked RC beams was to improve their serviceability and ultimate failure performance. This study investigates the pre-cracked reinforced concrete beams at both serviceability and ultimate loads. After pre-cracking these beams, they were then repaired with epoxy bonded steel plates to their soffits. Previous research has showed that the effectiveness of this repairing method strongly depends on the width-to-thickness ratio of the steel plates used to repair the damaged reinforced concrete structures, (Swamy et al (1989)). This investigation addresses that problem by changing the width-to-thickness ratio of the steel plates and observes the effect it have on the load carrying capacities, deflections and failure modes of the cracked specimens.

2. MATERIAL PROPERTIES

The experimental program consisted of casting 12 under reinforced concrete beams of 175 mm by 300 mm in cross-section and 3200 mm in length. The beams were under-reinforced on the tension side with 2, 12 mm high yield ribbed diameter bars of 451 MPa yield strength and 596 MPa ultimate strength, placed at an effective depth of 263 mm. In order to resist shear failure, 6 mm diameter shear links of 346 MPa yield strength and 425 MPa ultimate strength were provided at 150 mm centre to centre along the shear span. In order to hold the shear links in position, two compression bars of 8 mm in diameter were provided of 327 MPa yield strength and 389 MPa ultimate strength. The average compressive strength of concrete at 28 days was 31 MPa and the concrete cover was 25 mm.

3. SPECIMEN PREPARATION AND TESTING PROGRAMME

3.2 Testing of unrepaired beams

The beams were tested simply supported under a four point static loading system, over a span of 3000 mm. A linear variable displacement transducers (LVDT) was positioned at the mid-point of each beam in order to measure the vertical deflection. The testing configuration and instrumentation is shown in Figure 1. The tests were carried out using an Instron testing machine with an actuator capacity of 500 kN. The load was applied at a deflection rate of 2 mm/min to ensure that sufficient data was collected, until the beam failed. All measurements were recorded automatically at each load increment as the tests were performed. The control beams (Group 1) were loaded until failure attributable to the crushing of the concrete whereas the Group 2 and Group 3 beams were loaded up to their pre-cracking percentages of the load.

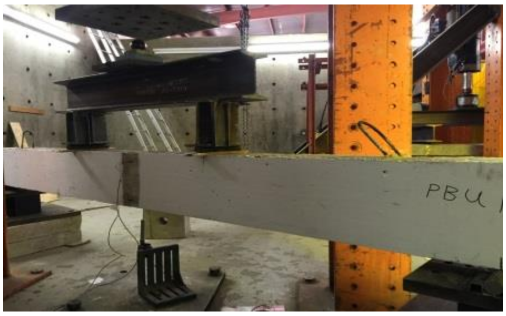

Figure 1: Test set-up

3.3 Surface preparation, bonding of the steel plates and final testing

The surface preparation of the concrete beams was achieved by removing the cement laitance on the soffit of the concrete beams, using a scabbling machine, in order to expose the aggregates and hence provide a good bonding surface for epoxy resins. The mild steel plates were sand-blasted to obtain a clean rough and white metal finish. The used epoxy resin consists of two parts, that is, a primer adhesive (Pro-Struct 618LV) and an epoxy adhesive (Pro-Struct 617NS). The primer adhesive was a two part product of base and activator component which were mixed in a ratio of 2:1, as recommended by the manufacture. It was then applied using a brush onto the prepared tension side of the beams, to allow it to penetrate through the small holes and thin hairline cracks. The epoxy adhesive is also a two part product of base and activator component. The components were mixed together for 5-10 minutes in a ratio of 1:1. The glue layer thickness of 1.5 mm was chosen for the experiment, as it has been proven to perform better by many eminent researchers (Swamy et al (1987), Swamy et al (1989), Basunbul et al (1990a), Hussain et al (1995), Olajumoke and Dundu (2015)). The steel plate was then placed on top of the prepared concrete surface and held in position using rectangular concrete slabs of dimensions of 700 x 700 x 200 mm. A minimum of 7 days of curing was allowed between plating and testing.

After 7 days of curing at ambient temperature, the repaired beams were instrumented and tested in similar fashion as the unrepaired beam. In this loading stage, electrical strain gauges were further used to measure the strain at the mid-point of the bonded steel plate. The distance between the support and the steel plate was kept constant at 35 mm for each beam. The test for each beam was stopped once the load showed a dramatic drop.

4. ANALYSIS AND DISCUSSION OF RESULTS

4.1 Experimental and theoretical maximum capacities

Table 1 shows the experimental and code-predicted results of the control and repaired beams. In this table, M_{rp} is the experimental pre-cracking moment of the repaired beams, δ_p is the experimental deflection at pre-cracking load of the repaired beam, $M_{emaxc/r}$ is the maximum experimental moment of the control/repaired beam, $M_{tmaxc/r}$ is the maximum theoretical moment of resistance, $\delta_{emaxc/r}$ is the experimental maximum deflection at failure of the control/repaired beam.

Table 1. Experimental and theoretical results

Group	Specimen	w/t	M_{rp} (kNm)	δ_p (kNm)	$M_{emaxc/r}$ (kNm)	$M_{tmaxc/r}$ (kNm)	$\delta_{emaxc/r}$ (kNm)	$\frac{M_{rp}}{M_{emaxr}}$	$\frac{\delta_p}{\delta_{emaxr}}$	$\frac{\delta_{emaxc}}{\delta_{emaxr}}$	$\frac{M_{emaxr}}{M_{emaxc}}$	$\frac{M_{emaxc/r}}{M_{tmaxr/c}}$	FM
Group 1	CB1	-	-	-	31.03	25.47	12.79	-	-	1	-	1.22	FY
	CB2	-	-	-	31.61	25.47	12.49	-	-	1	-	1.24	FY
Group 2	PBS1-75	12.50	19.47	10.57	68.07	70.61	10.58	0.29	0.99	1.21	2.17	0.96	PED
	PBS2-100	16.67	20.00	13.25	77.55	83.75	9.92	0.26	1.34	1.29	2.48	0.93	PED
	PBS3-125	20.83	19.78	9.26	79.07	95.94	9.32	0.25	0.99	1.37	2.52	0.82	PED
	PBS4-150	25.00	12.21	7.00	79.13	107.17	8.97	0.15	0.78	1.42	2.53	0.74	D
	PBS5-175	29.17	14.41	15.76	71.86	117.46	8.39	0.20	1.88	1.52	2.28	0.61	D
Group 3	PBU1-75	12.50	26.68	6.95	65.24	70.61	9.80	0.41	0.71	1.31	2.08	0.92	PED + D
	PBU2-100	16.67	25.92	6.66	73.86	83.75	9.61	0.35	0.69	1.34	2.36	0.88	PED
	PBU3-125	20.83	26.49	6.21	77.55	95.94	11.74	0.34	0.53	1.09	2.48	0.81	PED +D
	PBU4-150	25.00	26.13	11.11	77.74	107.17	9.52	0.34	1.16	1.33	2.48	0.73	D
	PBU5-175	29.17	25.99	10.48	78.04	117.46	7.83	0.33	1.34	1.63	2.49	0.66	D

FM: Failure mode; PED: Plate-end debonding; D: Delamination

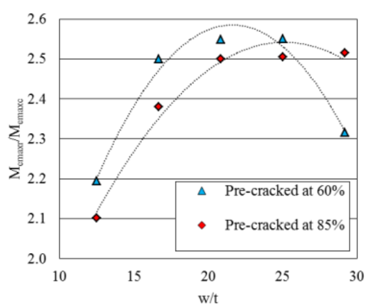

(a) (M_{emaxr}/M_{emaxc}) vs w/t ratio of plates

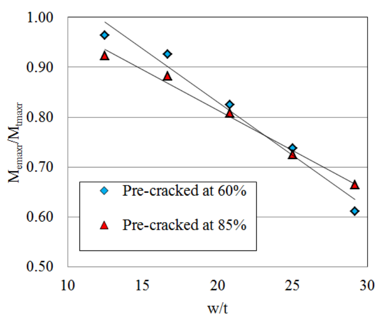

(b) (M_{emaxr}/M_{tmaxr}) vs w/t ratio of plates

Figure 2: The relationship between moment capacity and the width-to-thickness ratio

The repaired beams were able to achieve load capacities that are more than twice that of the control beams. Group 2 beams, PBS1-75 to PBS5-175, achieved a range of 117% to 153% increase in load capacity when compared to the control beams, whilst Group 3 beams, PBU1-75 up to PBU5-175, attained a range of 108% to 150% increase in load capacity when compared to the control beams. The repaired beams achieved a maximum strength that ranges from 2.17 to 2.53 and 2.08 to 2.49 as compared to the control beams, for beams in Group 2 and Group 3, respectively. Except for specimen PBS5-175, there is a generally increase in the capacity of both Group 2 and 3 beams with increase in the width-to-thickness ratios of the steel plates. It is clear that the beams that were pre-cracked at a lower load level (serviceability load) reached higher strengths than beams that were pre-cracked up to 85% of the ultimate load of the control beams. It can be concluded that the level of pre-cracking does affect the moment capacity of repaired beams. Although Group 3 beams were pre-cracked almost to failure, plating not only restored the beam's original capacity, but doubled it.

In Figure 2(a), both graphs of Group 2 and 3 beams increased gradually from a width-to-thickness ratio of 12.5 to a peak of M_{emaxr}/M_{emaxc} = 2.55 for Group 2 beams and a peak of M_{emaxr}/M_{emaxc} 2.50 for Group 3 beams, after that the graphs started decreasing gradually. This shows that there exists a limit in the width-to-thickness ratio of steel plates for which the load can increase. For the same width-to-thickness ratio, Group 2 repaired beams (pre-cracked at lower load) show greater maximum moment capacity as compared to Group 3 repaired beams (pre-cracked at higher load) for the first half of graph but quickly sheds the strengths much more than Group 3 beams. This behaviour was influenced by the stoppage of the Instron midway through the tests.

The theoretical moments of resistance of the beams were calculated using EN 1992-1-1 (2004) by assuming a rectangular stress distribution. Table 1 shows that the control beams, CB1 and CB2, were able to reach their full predicted flexural capacity since the ratio of the experimental maximum moment to the code-predicted moment of resistance of the control beam (Memaxc/Mtmaxc) was more than unity. Group 2 and Group 3 beams did not reach the code-predicted flexural capacity, as they all failed prematurely by debonding of the bonded steel plate. This means that no full composite action was achieved. Figure 2 shows that the ratio (M_{emaxr}/M_{tmaxr}) decreased as the width-to-thickness ratio increased, implying that debonding was more dominant in the beams with larger width-to-thickness ratios. Some inelastic behaviour was found in beams repaired with steel plates of smaller width-to-thickness ratios, such as PBS1-75, PBS2-100 and PBU1-75. Such beams had a ratio of experimental moment of resistance to the code-predicted moment of resistance (Memaxc/r/ Mtmaxc/r) of just less than 1.0.

4.2 Moment deflection curves

Figure 3 shows the moment-deflection curves of the beams tested in this study. The control beams shown in Figure 3 demonstrate stiffnesses that are similar to the repaired beams, which were maintained up to a moment of 28kNm. After this moment, the control beams experienced a significant drop in stiffness. These control beams' moment-deflection curves end with a horizontal line which indicates that the internal reinforcement was yielding. The high stiffness was maintained up to the maximum load in the repaired beams and this was caused by the increase in rigidity provided by the external bonded steel plate.

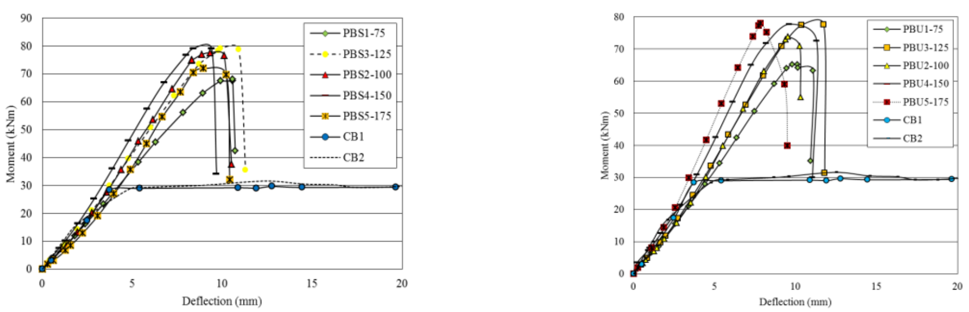

(a) Group 2 **(b) Group 3**

Figure 3: Moment-deflection curves of control and repaired beams

The steel plates provided additional stiffness for Group 2 and Group 3 beams to reach moment capacities that are 54% - 61% and 52% - 60% larger than the moments of the control specimens, respectively. This increase in the moment capacity is as a result of additional tensile forces and an increase in the lever arm provided by the external steel plate since it is bonded at an extreme position from the compression zone. The repaired beams show a reduction in deflections as compared to the control beams. The maximum experimental mid-span deflections was found to be 16% to 34% less than that of the control specimens for beams PBS1-75 to PBS5-175, respectively. The maximum experimental mid-span deflections for Group 3 repaired beams ranged from 7% to 38% less than that of the control specimens, for beams PBU1-75 to PBU5-175. The mid-span deflection is also observed to decrease as the width-to-thickness ratio of the steel plate increases, except for beam PBU3-125.

4.3 Failure modes

Four types of failure modes were observed in this experiment, as can be seen in Table 1. These are flexural yielding failure (FY), delamination (D) and plate-end debonding (PED) and a combination of PED and D. Both control beams, CB1 and CB2, failed by flexural yielding. These beams had flexural cracks only on the constant moment region. The cracks widened as the loading was increased, causing a loss in stiffness and strength of the beam. The beams failed by yielding of the tensile steel reinforcement and crushing of the concrete in the compression zone.

Two modes of failure were observed in the repaired beams, namely; plate-end debonding and delamination. Small diagonal shear cracks were observed, just before plate-end debonding occurred, due to interfacial shear and normal stresses at the plate-end curtailment (Oehlers (1992)). These cracks caused the end of the plate to separate from the concrete. As the plate separation propagated towards the mid-span, it transformed into shear diagonal cracks, which extended towards the loading point, at approximately 45º.

Similar to plate-end debonding, delamination started as a small diagonal crack at the plate-end curtailment, as a result of a change in stresses between the steel plate and concrete. In delamination, the crack extended to the tensile reinforcement. As the loading was increased, the crack propagated along the reinforcing bars towards the mid-span. Since the shear and bending stresses are high at the loading point, this forced the crack to change direction and to propagate at about 60º towards this point. Table 1 shows that, beams with a smaller width-to-thickness ratio failed by plate-end debonding and those with a larger width-to-thickness ratio failed by delamination. This means that the mode of failure was also dependent on the amount of external reinforcement used.

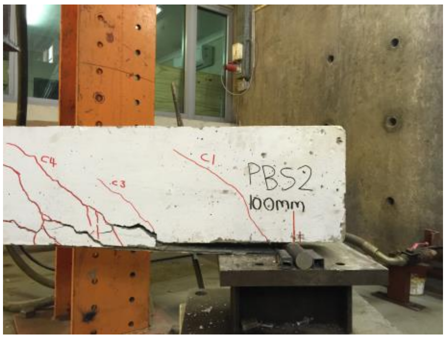

(a) PED (PBS2-100)

(b) Delamination (PBS1-150)

Figure 4: Plate-end debonding and delamination of the repaired beams

5. CONCLUSION

The maximum capacity of the beams, moment-deflection curves and failure modes were analysed and the following conclusions are drawn. The repaired beams were able to achieve load capacities that are more than twice that of the control beams. Except for specimen PBS5-175, there is generally increase in the capacity of the repaired beams with increase in the width-to-thickness ratio of the steel plates.

Beams that were pre-cracked at a lower load level (serviceability load) reached higher strengths than the beams that were pre-cracked at a higher load level (85% of the ultimate load capacity). The experimental results showed that there exists a limit in the width-to-thickness ratio of the steel plate for which the load can increase. The repaired beams showed high stiffnesses when compared to the control beams, due to the increase in rigidity provided by the external bonded steel plate. The rigidity of the repaired beams increased with increasing the width-to-thickness ratio of the steel plate. The use of external reinforcement reduced the maximum deflections of the beams and except for beam PBU3-125, this maximum deflections of the repaired beams decreased with increasing the steel plate width-to-thickness ratio. The repaired beams of smaller width-to-thickness ratio failed by plate-end debonding whereas those of larger width to thickness ratio failed by delamination.

6. ACKNOWLEDGEMENTS

The authors wish to acknowledge Bureau Veritas for financial supporting this research project and AfriSam South Africa for donating concrete used in this work.

7. REFERENCES

Basunbul IA, Gubati AA, A-L-Sulaimani GJ, Baluch MH (1990a). Repaired reinforced concrete beams, ACI Materials Journal, 87(37), 348-354.

Basunbul IA, Hussain M, Sharif AM, Al-Sulaimani G, Baluch MH (1990b). Repair of flexural cracked RC beams with bonded external steel plate, KFUPM Saudi Arabia, 81-92.

EN 1992-1-1 (2004). Eurocode 2. Design of concrete structures-Part 1-1: General rules and rules for buildings, The European Union.

Hermite RL, Bresson J (1967). Concrete reinforced with glued plates, RILEM International Symposium, Synthetic resins in building construction, Paris, 175 – 203.

Hussain M, Sharif A, Basunbul IA, Baluch MH, Al-Sulaimani GJ. (1995). Flexural behavior of precracked reinforced concrete beams strengthened externally by steel plates, ACI Structural Journal, 92(1), 14 -22.

MacDonald MD (1978). The flexural behaviour of concrete beams with bonded external reinforcement, TRRL Supplementary Report 415, Transport and Road Research laboratory, Department of the environment, Crowthone, 13.

Oehlers DJ (1992). Reinforced concrete beams with plates glued to their soffits, Journal of Structural Engineering, 118(8), 2023-2038.

Olajumoke AM, Dundu M (2015). Impact of adhesive thickness on the capacity of the surface mounting steel plates strengthening technique, International conference on structural and geotechnical engineering, December 20-22, Cairo, Egypt, ICSGE 14.

SANS 5863 (2006). Concrete tests-Compressive strength of hardened concrete, Pretoria, South African Bureau of Standard Division.

SANS 6892-1 (2010). Metallic materials-Tensile testing, Part 1: Method of test at room temperature. Pretoria, South African Bureau of Standard Division.

Swamy RN, Jones R, Bloxham JW (1987). Structural behaviour of reinforced concrete beams strengthened by epoxy-bonded steel plates, Structural Engineer, 65(2), 59 -68.

Swamy RN, Jones R, Charif A (1989). The Effect of External Plate Reinforcement on the Strengthening of Structurally Damaged R.C. Beams, Structural Engineer, 67(3), pp45- 54.

Proc. 1st International Conference on Structural Engineering Research (iCSER 2017)
20-22 Nov 2017, Sydney, Australia
ISBN: 978-0-6480147-6-8

Influence of Different Surface Preparations on the Capacity of Composite Steel-Concrete Beams

Sylvester M Rakgate[1] and Morgan Dundu[2]

[1]Lecturer, University of Johannesburg, Johannesburg, South Africa
[2]Senior Lecturer, University of Johannesburg, Johannesburg, South Africa
Corresponding author's E-mail: srakgate@uj.ac.za, mdundu@uj.ac.za

Abstract

External bonding of steel plates to structural concrete members has widely gained popularity in recent years, particularly for repairing and strengthening reinforced concrete beams. The success of this bonding technique depends on the effectiveness of the surface preparation of the steel and concrete beams. Studies have shown that most of the beams strengthened using this technique usually fail prematurely by debonding. In this study, concrete beams with different types of surface preparations were investigated, such as no surface preparation (NSP), wire brushing (WB), scabbling (SC) and hand chipping (HC). The quality of the surface preparation established was measured based on the flexural performance of the externally strengthened steel-concrete beams. Eight (8), 250x450x3600 mm reinforced concrete beams were prepared and strengthened with glued steel plates on their soffits. All the specimens were tested under two-point static loading and failure modes were observed. The results showed that beams with rougher surface preparation have a high bond strength as compared to smoother surface preparations. The increase in the average capacity of strengthened beams with the surface prepared by hand-chipping, scabbling, wire brushing was found to be 75.3%, 67.5% and 46.9% respectively, compared to the capacity of the beam strengthened without surface preparation.

Keywords: Concrete, Steel plate, Surface roughness, Strengthened, Adhesive, Debonding, Flexural capacity.

1. INTRODUCTION

Steel plates have been widely used to repair/strengthen many bridges and concrete structures in the United Kingdom, United States of America, South Africa, Japan, Poland, Belgium, France and Switzerland, because they are cheap and readily available, have uniform material properties (isotropic), have high ductility and high fatigue strength, can be secured easily whilst the structure is in use (Raithby, 1982), do not change the overall dimensions of the structure and can be secured without causing any damage to the structure (Swamy, Jones & Bloxham, 1987, Jumaat et al, 2011). The epoxy-bonded st;el plate (EBSP) technique has been reported by many eminent researchers to be the most effective and convenient method of enhancing the flexural performance under serviceability and ultimate limit states (Swamy, Jones & Bloxham, 1987, Jumaat et al, 2011). Despite these benefits, tests have shown that epoxy-bonded steel plates are prone to premature debonding, due to high interfacial shear stress concentration at the plate's ends (MacDonald, 1978; Jones, Swamy & Charif, 1988; Oehlers & Moran, 1990; Oh et al, 2003b). The interfacial bond failure takes place owing to the poor surface preparation of the steel plate and the concrete beams.

The bond strength in the steel plate-to-concrete interface is influenced by various factors such as the material properties of the epoxy, concrete substrate and steel plate, and surface preparation of the concrete and steel plate. (Lovinella et al., 2012, Ariyachandra and Gamage, 2013). For better results, the surfaces of the steel plate and concrete beams should be prepared so that it is clean, sound and suitable for the application of the adhesive and strengthening material (Lovinella et al., 2013). Some of the most common surface preparation methods are wire brushing, grinding, scarifying, bush-hammering, shot-blasting and sand-blasting, each with its own associated advantages and disadvantages, related to the desired roughness profile of the prepared surface, cost and processing time (Lovinella et al., 2013). Chajes et al. (1996) presented an experimental investigation on the study of the bond and force transfer of composite material plates bonded to concrete. The test results in this study suggested that an increased interfacial bond is achieved when the concrete surface is mechanically abraded using grinding wheel, creating porous concrete surface.

A strong bond is necessary between the steel plate and the concrete so that the concrete and the steel plate work monolithically when loaded, and shear forces are transferred from the concrete to the steel plate. Although the adhesive provides the bond, it is critical that the steel plate and the concrete are prepared sufficiently in order to maximise the bonding capabilities of the adhesive. A poorly prepared surface is a weak link, no matter how good the adhesive material might be. Adequate surface preparation produce a sound, clean, and suitably roughened surface on the bonded elements, and includes the removal of laitance (weak layer of cement and fines at the concrete surface), dirt, oil, films, paint, coatings, sound and unsound concrete, and other materials that will interfere with the adhesion or penetration of the adhesive.

A comprehensive roughness profile of the concrete surfaces is given in Technical Guidelines provided by the International Concrete Repair Institute (ICRI, 2013). Each concrete profile carries a CSP number ranging from CSP 1 (nearly flat) through CSP 10 (very rough). Grinding produces an abrasive force, which wears away the cement paste, fines, and coarse aggregate at a uniform rate to produce a nearly flat surface having little or no profile. In preparation for an investigation on strengthening and repairing of concrete beams, a decision was taken to re-visit the work on surface roughness profiles. Guided by the roughness profile of the concrete surfaces provided by the International Concrete Repair Institute (ICRI, 2013), eight (8) reinforced concrete beams were cast and their surface were roughened using four different mechanical surface preparation methods. The aim of this study is to determine the flexural performance of plated concrete beams with four (4) different types of surface preparations, namely; no surface preparation (NSP), wire brushing (WB), scabbling (SC) and hand chipping (HC).

2.0 Material properties

Two groups (Group A and Group B) of reinforced concrete beams of 3600x250x450 mm in size and four (4) concrete cubes were cast, using concrete of different strengths. The average 28-day compressive strength of the four cubes in Group A and Group B was 30 MPa and 27 MPa, respectively. Two, 10 mm diameter high yield strength bars with corresponding yield strength of 450MPa were used as both tension and compression reinforcement. All concrete beams were strengthened with mild steel plates of 6 mm thickness, 250 mm width and 3300 mm length, and of 351.73 MPa yield strength and 483.44 MPa ultimate strength. To ensure that the strengthened beams fails in flexure, 10 mm diameter bars were used as the shear links placed at 250 mm from centre-to-centre.

2.1 Experimental results and analysis

The experimental results regarding the flexural performance of strengthened beams, with different concrete surfaces, are given in Table 1. In this Table, P_{NSP} refers to the maximum load applied to the beams with no surface preparation (control beam), P_{NSP} refers to the maximum load applied to the beams with concrete surface preparation, P_t is the code-predicted yield load, P_{CSP}/P_{NSP} compares the maximum load of the beams that are roughened to that of the beams with no surface preparation and $P_{NSP/CSP}/P_t$ compares the maximum load of the beams to the code-predicted yield load. A code-predicted yield loads of 404.10kN and was calculated using the guidelines from SANS10162-1 (2011).

Tables 1: Experimental results.

Group	Specimen	Surface profile	$P_{NSP/CSP}$ (kN)	P_{CSP}/P_{NSP}	$P_{NSP/CSP}/P_t$	Failure mode
A	A-B1-27	NSP	199.21	-	0.49	De-bonding
	A-B2-27	WB	234.36	1.18	0.58	De-bonding
	A-B3-27	SC	252.47	1.27	0.63	Shear peeling
	A-B4-27	HC	264.10	1.32	0.65	Shear peeling
B	B-B1-30	NSP	221.34	-	0.55	De-bonding
	B-B2-30	WB	265.22	1.20	0.66	De-bonding
	B-B3-30	SC	294.13	1.33	0.73	Shear peeling
	B-B4-30	HC	314.31	1.42	0.78	Shear peeling

As indicated in Table 1, all the specimens in both Group A and Group B show an increase in flexural capacity as compared to the strengthened beam with no surface preparation. In Group A, an increase in flexural capacity of the prepared beams ranges from 18% to 32% as compared to the control beam whilst in Group B an increase in flexural capacity of the prepared beams ranges from 20% to 42%. The latter differences in the increase in flexural capacities of beams in Group A and Group B is due to the difference in the average 28-day compressive strength.

The comparison of increase in percentages of the flexural capacity of beams with roughened surface (WB, SC and HC) as compared to the control beams is well represented by Figure 1. Based on the results in Table 1 and Figure 1, it is clear that there is a correlation between the level of roughness, adhesion bond strength and the flexural capacity. In addition to that, beams that were prepared using hand chipping achieved higher load carrying capacity as compared to beams that were prepared using scabbling.

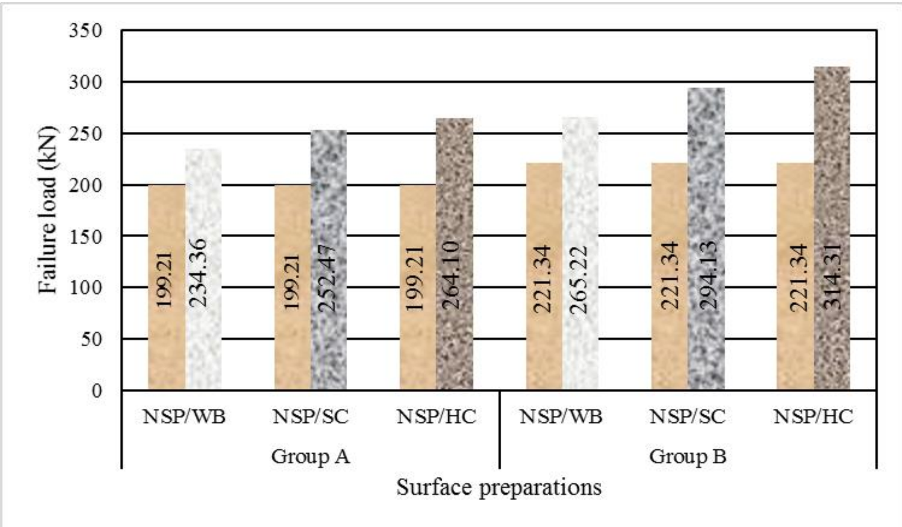

Figure 1: Comparison between the surface preparation methods

2.2 Moment-deflection curves

The moment-deflection response for each specimen is given in Figures 2 and 3. As illustrated both figures, the flexural strength of the concrete beams with improved surface roughness is significantly larger than the beam with no surface preparation (NSP). Beams with the concrete surface roughened before bonding the steel plate increased the overall stiffness of the strengthened sections, which results in high cracking load and maximum capacity as shown by various researchers.

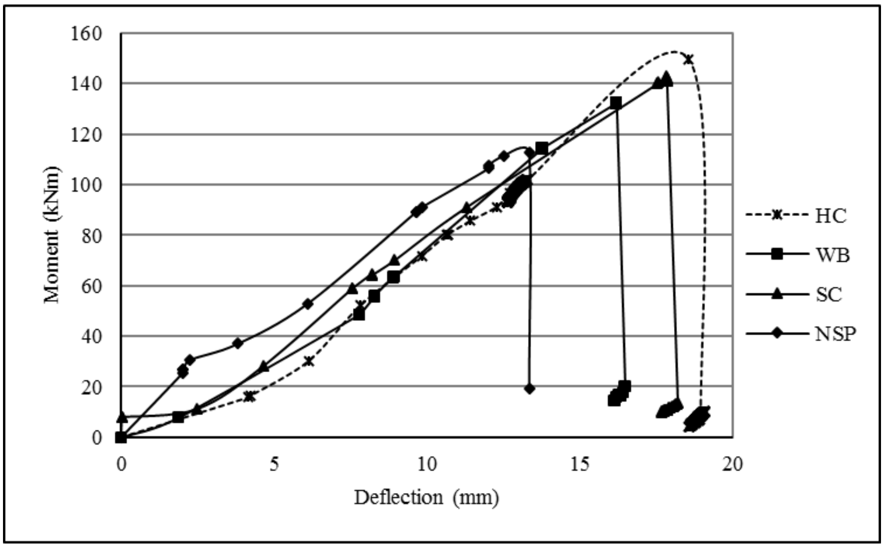

Figure 2: Moment-deflection response of the beams in Group A

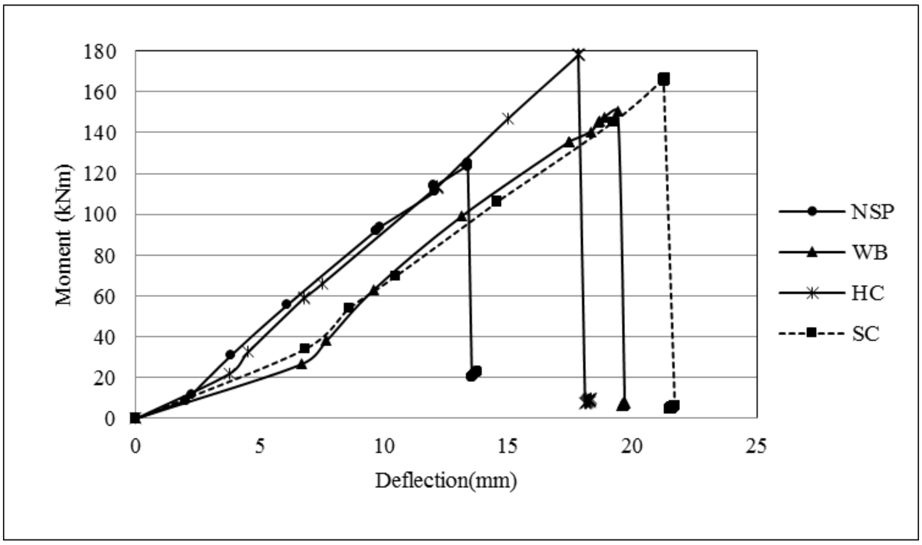

Figure 3: Moment-deflection response of the beams in Group B

2.3 Moment-steel strains curves

The moment-strain curves of beams with different concrete surface preparation are shown in Figure 4 and 5. Figure 4 and 5 shows that the steel plate of beams with concrete surface prepared by scabbling and hand chipping strained significantly as compared to beams that are prepared by wire brushing and not prepared. The latter is due to the high interfacial adhesion bond manifested between the epoxy-bonded steel and the prepared concrete surface, the two materials tend to act compositely for a longer time while being loaded, as compared to the specimens that are prepared using wire brushing and non-surface preparation which acted compositely for a shorter period of time. None of the steel plates shows any sign of yielding. From the tensile test, the yield strain of the 6 mm bonded steel plate was 0.0039, which is 64% and 59% higher than the maximum strains achieved by strengthened beams in both Group A(0.0014) and B(0.0016).

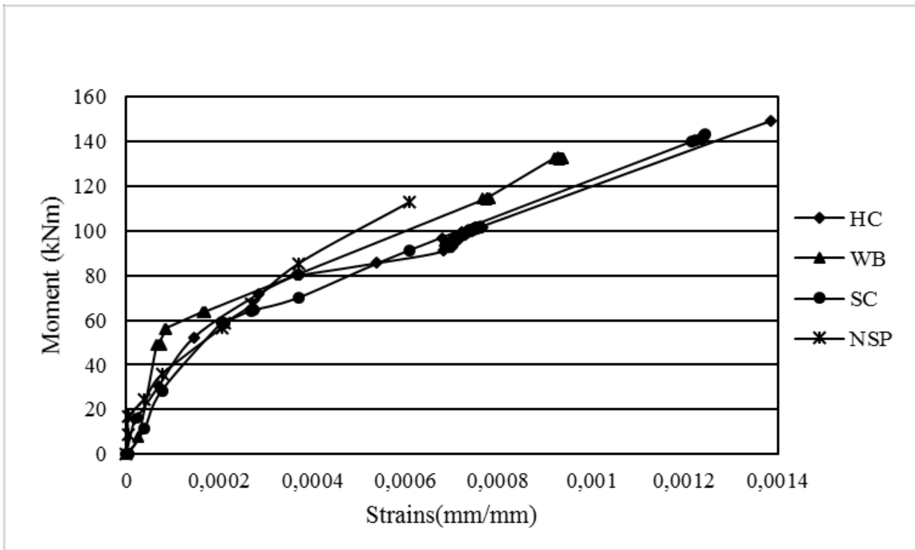

Figure 4: Moment-strain response of the beams in Group A

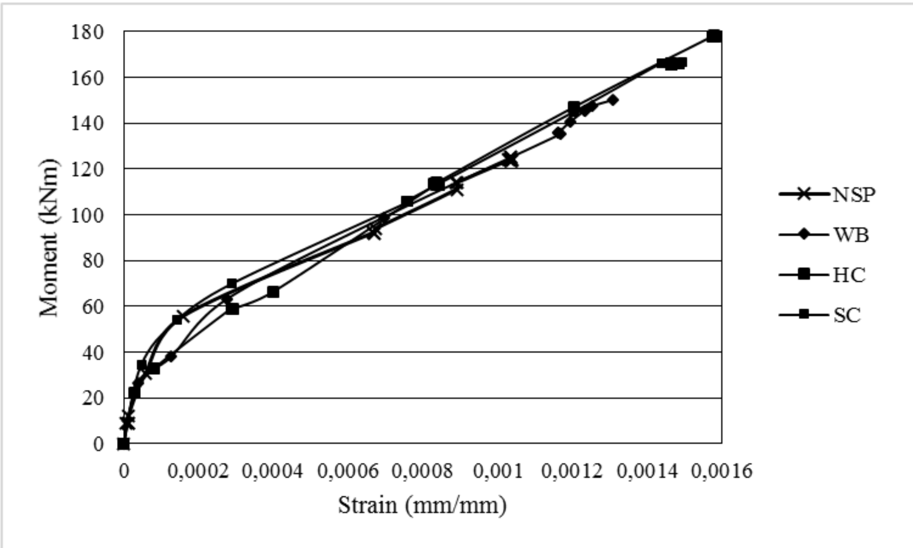

Figure 5: Moment-strain response of the beams in Group B

2.4 Failure modes

During testing of the strengthened specimen, different failure modes were observed. In both groups, the control specimens (NSP) failed prematurely, by peeling-off of the steel plate, due to lack of adhesion bond between the epoxy resin and the concrete. In addition to the latter, the control beam failed after exceeding the code predicted maximum capacity of the unplated beam of 50.28 kN. Figure 6(a) shows a debonded steel plate. The hardened epoxy resin on the steel plate clearly shows that there was no enough bond between the epoxy resin and the unprepared concrete surface. For concrete beams with wire brushed concrete surface, the premature failure of the strengthened beam was caused by the steel plate debonding in the shear zone, this is due to high shear stresses concentrated at the plate end.

For beams with scabbled and hand chipped concrete surface substrates, the mode of failure shifted from full flexural yielding to premature failure by plate-end debonding. This type of failure is common in strengthened beams, and is caused by diagonal shear cracks, in the zone of high interfacial normal and shear stresses, at the end of the plate (Oh et al., 2003; Olajumoke & Dundu., 2014). As evidence that shear stresses were dominant, as the plate separation propagated towards the mid-span, it changed into a diagonal crack, which extended towards the loading point at about 45°. The latter failure mechanism is called the critical diagonal crack (CDC) debonding and usually occurs after the formation of a large crack, which may be due to insufficient shear reinforcement (Olajumoke & Dundu., 2014, and Oehlers et al., 2003)

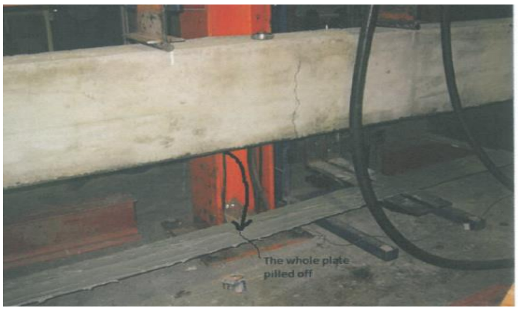

(a) No surface preparation (NSP)

(b) Wire brushing (WB)

Figure 6: Typical failure modes of the strengthened beams

3.0 CONCLUSION

Different surface roughening produces different interfacial bond strength, as reflected by different load capacities of the specimen. Bonding steel plates to the soffit of concrete beams increased their flexural strength and stiffness, particularly when the concrete surface is prepared by hand chipping and scabbling. Irrespective of the type of concrete surface treatment, roughening of the concrete surface increases the flexural performance, with hand chipping and scabbling being identified as the most effective surface preparation method. All the strengthened specimens achieved a flexural capacity higher than the code predicted maximum load of the unplated beam. One of the disadvantages of hand chipping is that, it is time consuming and difficult to create a uniform surface roughness throughout the length of one specimen, and on different specimens that require exactly the same roughness level. In most situations, the human skill and experience, required to achieve this might not be available. To create a balance between optimum roughness and practicality, scabbling, which achieves almost the same load capacity as hand chipping, should be adopted over hand chipping.

4.0 REFERENCES

Al-Tamimi, A.K., Ozkul, T.,Azzam, M.M., Sabetnia,M.R., Abdullah, M.B. and Hossieni, S.H. (2011) Investigation of the effect of surface preparation method and the degree of surface roughness on CFRP-concrete bonding and substrate strength, *The built & human Environment Review, Volume 4, no.1,pp. 33-44*

Barnes R.A, Baglin P.S., Mays C.G and Subedi N.K., (2001). The effects of plate system for the shear strengthening of reinforced concrete beams, *Engineering structures, vol. 23, no 2001, pp. 1162-1176*

De Lorenzis, L., Miller, B and Nanni, A. (2001). Bond of FRP Laminates to Concrete, *ACI Materials Journal, Vol 98, No.3, pp. 256-264*

ISBN: 978-0-6480147-6-8

Steel Contribution Effect on Beams Bonded With Steel Plates of Different Width-To-Thickness Ratios

Sylvester M Rakgate[1] and Morgan Dundu[2]

[1]Lecturer, University of Johannesburg, Johannesburg, South Africa
[2]Senior Lecturer, University of Johannesburg, Johannesburg, South Africa
Corresponding author's E-mail: srakgate@uj.ac.za[1] and mdundu@uj.ac.za[2]

Abstract

The concept of strengthening reinforced concrete (RC) beams using epoxy-bonded steel plates (EBSP) is a well-known solution in structural engineering. Experimental investigations conducted in the past has proved that strengthening RC beams with steel plates are the most efficient, effective, and cost-effective technique of increasing the flexural performance of these elements. However, the focus has been on effect of the external bonded steel plate, and not on the effect of the overall steel contribution ratio on the behaviour of the strengthened beams. Several codes give the minimum reinforcement ratios for concrete beams in order to encourage/improve their flexural behaviour such as cracking and ductility failure. The purpose of this present study is to investigate the effect of the steel contribution ratio on the flexural behaviour of concrete beams strengthened on their tension face with epoxy bonded steel plate, using the experimental results obtained by various researchers in this field. The outcomes of strengthening RC beams are decrease in mid-span deflections, decrease in crack-widths, and increase in first crack load, and consequently increase in both serviceability load and ultimate load, thus making it to be the most feasible strengthening technique

Keywords: Steel plates, Steel contribution factor, RC beams, Externally strengthened, Composite beams.

1. INTRODUCTION

Strengthening of beam elements in reinforced concrete (RC) structures is required when the strength of an existing structure is no longer adequate to resist the current design loads or when the structure is now required to resist larger ultimate loads. There are several methods for strengthening RC beams, however, strengthening of RC beams using epoxy-bonded mild steel plates on the tension face has proven to be the most effective, efficient, economical and convenient technique to enhance the flexural and shear performance of RC beams under service and ultimate loads. This technique has been applied successfully to strengthen RC structures such as buildings and bridges in various parts of the world, including South Africa, France, Switzerland, Japan, Poland, Belgium and United Kingdom (Bloxham, 1980). The technique has several advantages, compared to other strengthening methods, which include the fact that steel plates are relatively cheaper and readily available, has uniform material properties (isotropic), high ductility and high fatigue strength, can be secured easily whilst the structure is in use (Raithby, 1982), does not significantly change the overall dimensions of the structure, and can be secured without causing any damage to the structure (Swamy et al. 1987). However, much of the focus in these studies has been on the effect of the external bonded steel plate on the overall behavior of the strengthened beams and whether the width-to-thickness ratios of the bonded steel plate encourage ductility or not. The purpose of the present study is to investigate the effect of the steel contribution ratio (ρ) on the flexural behavior of rectangular concrete beams strengthened on their tensile with epoxy bonded steel plate. In this paper, the steel contribution ratio (ρ) is defined as the ratio of total area of the internal and external steel reinforcement to the area of the concrete.

2.0 SPECIMENS AND TESTS CONDUCTED.

A decision was taken to group all the material properties according to the author reviewed. The material properties of the reinforcement bars, steel plate, concrete and epoxy resin used in the various studies are given in Table 1, where f_y is the 0.2% proof yield stress of the steel reinforcement bars and steel plates, f_u is the ultimate stress, E is Young's modulus of elasticity, F_{cu} is the average 28-day compressive strength of the concrete cubes, and Cs, f_t and E_s are the compressive, tensile strength and Young modulus of the epoxy resin, respectively.

Table 1: Material properties

Author	Specimen	Steel and reinforcement bars			Concrete	Epoxy resin		
		f_y (MPa)	f_u (MPa)	E_s (GPa)	F_{cu} (MPa)	C_s (MPa)	f_t (MPa)	E_s (GPa)
Fleming and King (1967)	6Y14	No material properties provided						
	2Y6							
	SP0.6							
Huovinen (1996)	2Y9	No material properties provided						
	SP2							
	SP5							
	SP10							
Bloxham et al (1980)	3Y20	450.0	507.0	200	63.0	-	15.0	-
	R 6	250.0	336.0	-	73.0			
	SP 1.5	236.0	310.0	200	-			
	SP3.0	258.0	316.0	200	-			
	SP6.0	248.0	308.0	200	-			
Jones et al. (1982)	2Y10	530.0	597.0	200	63.4	44	5.3	6.0
	SP1.5	216.6	359.6	192	-			
	SP3.0	263.0	346.2	198	-			
	SP5	217.5	445.2	200	-			
	SP10	240.0	434.6	200	-			
Oh et al. (2003)	2Y16	365.0	536.0	200	28.7	180	70.0	2.3
	2Y13	345.0	503.0	200	-			
	R 8	420.0	600.0	200	-			
	SP2	292.0	410.0	200	-			
	SP3.0	292.0	410.0	200	-			
	SP4	292.0	410.0	200	-			
	SP5	292.0	410.0	200	-			
Neelamegam et al. (1998)	2Y9	475.0	-	-	44.0	No epoxy properties provided		
	R 6	275.0	-	-	-			

Fleming and King (1967) conducted an experimental investigation to determine the effect of strengthening RC beams by bonding steel plates on the tension side. To achieve this, a total of 2, 150 x 280 x 2800 mm beams, reinforced with 6, 14 mm tension reinforcement bars and 2, 6 mm compression bars were tested. Shear failure was limited using 5 mm shear links, spaced at 200 centre-to-centre mm. The author did not provide the properties of the materials. In a related study, Bloxham et al. (1980) examined the effect of epoxy-bonded steel plate on the structural deformations, serviceability loads, ultimate loads and first crack loads of RC beams. Twelve (12) RC beams of 155 x 255 mm in cross section and 2500 mm long were tested; one of the RC beams was used as a control beam. All beams were under-reinforced on the tension side with 3, 20 mm diameter placed at an effective depth of 220 mm. To avoid shear failures, 6 mm diameter shear links were provided at 75 mm center-to-center along the shear span. The shear links were held in compression by 2, 6 mm diameter bars.

Jones et al. (1982) tested 5 beams, one control beam and four (4) under-RC beams of 100 x 150 x 2400mm size, with glued mild steel plates of 80mm width, 2150mm length and varying thickness of 1.5, 3, 5, and 10mm. All the beams were internally reinforced on the tension side with 2, 10 mm diameter and 2, 8 mm diameter bars in compression. The beams were reinforced for shear with 6 mm shear links, spaced at 70 mm centre-to-centre, to ensure flexural failure. In order to establish the bond strength of glued steel plates and the effect of the steel plate on the overall flexural capacity of the strengthened beams, Huovinen (1996) tested 8 RC beams of 300 x 300 and 3200 mm in size. Two (2) were used as control beams and 6 beams were externally strengthened by bonding steel plates of 100 mm width, 2800 mm length and varying thicknesses of 2 mm, 5mm and 10 mm.

The RC beams were internally reinforced with two compressive bars and two tension-reinforcing bars of 9 mm in diameter.
In a wider study, Neelamegam et al. (1998) tested ten RC beams of 100 x 200 x 2400 mm in size, under incrementally two-point static loading, over a span of 2300 mm between the supports. The beams were internally reinforced on the tension side with 0.58% tension reinforcements and the shear links were of 6 mm diameter mild stirrups, spaced at 100 mm centre-to-centre. The bonded steel plates had a constant width of 100 mm, thicknesses varying from 0.8 mm to 6.8 mm, and length of 2200mm, 1800mm, 1400, and 800mm for S2-S7, S8, S9 and S10, respectively. Oh et al. (2003) tested 12 rectangular concrete beams under two-point static loading, with one (1) control beam and 11 strengthened beams. The beams were of 150 x 250 x 2100 mm in size, and each beam was strengthened internally with 2, 16 mm diameter tension bars and 2, 13 mm compression bars. To avoid shear failure, 8 mm diameter shear links, spaced at 110 mm centre-to-centre were provided. The bonded steel plate had constant length of 2000 mm, width of 150 mm and thicknesses varying from 2 to 5 mm. The adhesive thicknesses used and the shear-span-to-depth ratio (a/d) also varied from 1 to 7 mm and from 1.36 to 4.77, respectively.

Table 2: Details of the tested specimen

Author	Specimen	L/h	a/d	Steel plate	Reinforcement bars			
				Plate size	Gap	TBs	CBs	Shear links
Fleming and King (1967)	150x280x2800	10.0	0.50	150x6	-	6Y14	2Y6	R5
Huovinen (1996)	300x300x3000	10.0	3.33	100x2.0x2800	100	2Y9	2Y9	-
				100x5.0x2800				
				100x10x2800				
Bloxham *et al.* (1980)	155x255x2500	9.80	3.01	125x1.5x2200	50	3Y20	2R6	R6
				125x3.0x2200				
				125x6.0x2200				
Jones *et al* (1982)	100x150x2400	16.0	5.33	80x1.5x2150	50	4Y16	2R8	R6
				80x3.0x2150				
				80x5.0x2150				
				80x10x2150				
Oh *et al*. (2003)	150x250x2400	9.6	2.80	150x2.0x2000	50	2Y16	2Y13	R8
				150x3.0x2000				
				150x4.0x2000				
				150x5.0x2000				
Neelamegam *et al*. (1998)	100x200x2400	12.0	3.83	100x0.8x2200	50	2Y9	-	R6
				100x1.2x2201				
				100x2.3x2202				
				100x3.2x2203				
				100x4.3x2204				
				100x6.8x2205				

All beams were tested under two-point static loading over simply supported spans to simulate a distributed load, with equal point loads applied at a third of the effective length of the beam from each support. Almost all the beams were tested with a gap of 50 mm between the bonded plate end and the support to delay plate separation and maximize the strengthening effect.

3.0 EXPERIMENTAL RESULTS

The experimental results of the tested specimen are given in Table 3. In this table, ρ is the steel contribution ratio, $P_{ecrc/s}$ is the first experimental crack load of the control/strengthened beam, $P_{emaxc/s}$ is the maximum experimental load of the control/strengthened beam, $M_{emaxc/s}$ is the maximum experimental moment of the control/strengthened beam. Table 3 also compares the experimental first crack load of the strengthened beam to the experimental first crack load of the control beam (P_{ecrs}/P_{ecrc}), and the maximum experimental moment of the strengthened beam to the maximum experimental moment of the control beam (M_{emaxs}/M_{emaxc}). The failure modes of the respective specimen for each author are also recorded in Table 3.

Table 3: Experimental results

Author	Beam	ρ	t (mm)	$P_{ecrc/s}$ (kN)	$P_{emaxc/s}$ (kN)	$M_{emaxc/s}$ (kN)	$\delta_{c/s}$ (mm)	$\frac{P_{ecrs}}{P_{ecrc}}$	$\frac{M_{emaxs}}{M_{emaxc}}$	Failure modes
Fleming and King (1967)	C1	0.0220		40.0	86.0	80.27	-	-	1.00	Flexure
	B1	0.0430	-	90.0	98.0	91.47		2.25	1.14	Shear failure
Bloxham *et al* (1980)	C-1	0.0239	-	35.0	232.0	88.90	-	-	1.00	Flexure
	203	0.0286	1.5	50.1	270.0	103.50	-	1.43	1.16	Flexure
	204	0.0333	1.5	50.1	270.0	103.50	-	1.43	1.16	Shear failure
	205	0.0428	1.5	54.8	213.0	81.70	-	1.57	0.92	Delamination
	207	0.0286	3.0	55.0	262.0	100.60	-	1.57	1.13	Flexure
	208	0.0333	3.0	49.0	264.0	101.20	-	1.40	1.14	Shear failure
	209	0.0428	3.0	52.4	220.0	84.30	-	1.50	0.95	Delamination
	210	0.0428	3.0	50.1	215.0	82.40	-	1.43	0.93	Delamination
	216	0.0286	6.0	54.0	262.0	100.60	-	1.54	1.13	Flexure
	217	0.0333	6.0	48.0	257.0	98.60	-	1.37	1.11	Shear failure
	218	0.0428	6.0	51.1	194.0	74.50	-	1.46	0.84	Delamination
	219	0.0428	6.0	55.0	220.0	84.30	-	1.57	0.94	Delamination
Jones et *al* (1982)	URB1	0.0105	3.0	-	28.1	10.54	-	-	1.00	Flexure
	URB2	0.0185	3.0	-	40.0	15.00	-	-	1.42	Flexure
	URB3	0.0265	3.0	-	55.0	20.63	-	-	1.96	flexure+ plate separation
	URB4	0.0371	3.0	-	57.5	21.56	-	-	2.05	Plate separation
	URB5	0.0638	3.0	-	53.1	19.91	-	-	1.89	Plate separation
Neelamegam *et al* (1998)	CB	0.0058		8.0	30.0	23.00	7.5	-	1.00	Flexure
	S2	0.0098	-	20.0	37.0	28.37	3.4	2.50	1.23	Flexure
	S3	0.0118	-	24.0	43.0	32.97	2.8	3.00	1.43	Flexure
	S4	0.0173	-	28.0	59.9	45.92	2.1	3.50	1.98	Flexure
	S5	0.0218	-	36.0	60.0	46.00	1.7	4.50	2.00	Debonding
	S6	0.0218	-	44.0	48.0	36.80	1.8	5.50	1.60	Debonding
	S7	0.0273	-	48.0	56.0	42.93	1.3	6.00	1.87	Debonding
	S8	0.0398	-	36.0	42.5	32.50	1.8	4.50	1.42	Debonding
	S9	0.0218	-	20.0	35.0	26.83	2.1	2.50	1.17	Flexural peeling
	S10	0.0218	-	10.0	28.0	21.47	7.5	1.25	0.93	Flexural peeling
Oh *et al* (2003)	CB	0.0107	-	-	89.0	31.15	34.7	-	1.00	Flexure
	B23	0.0187	3	-	136.0	47.60	8.15	-	1.53	Flexure
	B33	0.0227	3	-	137.0	47.95	7.02	-	1.54	Flexure
	B43	0.0267	3	-	126.0	44.10	4.35	-	1.42	Plate separation
	B53	0.0307	3	-	142.0	49.70	5.00	-	1.60	Plate separation
	B41	0.0267	1	-	125.0	43.75	4.68	-	1.40	Plate separation
	B45	0.0267	5	-	134.0	46.90	4.97	-	1.51	Plate separation
	B47	0.0267	7	-	150.0	52.50	5.35	-	1.69	Plate separation
	B43B1	0.0267	3	-	132.0	69.30	5.94	-	1.48	Flexure
	B43B2	0.0267	3	-	128.0	57.60	5.61	-	1.41	Plate separation
	B43B3	0.0267	3	-	135.0	33.80	4.67	-	1.51	Plate separation
	B43B4	0.0267	3	-	221.0	33.20	5.13	-	2.58	Shear failure
Huovinen (1996)	CB1	0.00142	-	-	77.3	77.3	-	-	1.00	Flexure
	B1	0.00364	1	-	102.5	102.5	-	-	1.33	Flexure
	B2	0.00697	1	-	145.6	145.6	-	-	1.88	Flexure
	B3	0.0125	1	-	107.7	107.7	-	-	1.39	Plate separation

In the investigation reviewed, only three authors (Fleming and King (1967), Bloxham et al (1980) and Neelamegam *et al* (1998)) recorded the first experimental crack load of the control/strengthened beam. In Fleming and King (1967)'s work, the first crack of the control beam appeared at a load of 40.0kN, whilst that of the strengthened beam appeared at a load of 90 kN, to yield a mammoth increase of 125% compared to the crack load of the control beam. This shows a significant delay in the appearance of the first crack as compared to the control beam. In Bloxham et al's (1980) study, the first crack of the control beam appeared at a load of 35.0kN, whilst that of the strengthened beam appeared at loads varying from 48.0 – 55.0 kN. The increase of the cracking load of strengthened beams varied from 37% – 57%, compared to the control beams. This increase is much lower than the beam tested by Fleming and King (1967), despite the fact that the contribution ratio of this beam is the same as some of the beams tested by Bloxham et al (1980). No distinct trend could be established between steel contribution factor and the ratio of the first crack loads (P_{ecrs}/P_{ecrc}) or the modes of failure of the beams. Lastly, in Neelamegam et al's (1998) beams, the first crack of the control beam occurred at a load of 8.0kN, whilst that of the strengthened beam occurred at loads varying from 10.0 – 48.0 kN. The increase of the cracking load of strengthened beams varied from as little as 25% to as high as 500%, compared to the control beams. Except beams S8 – S10, the ratio of the first crack loads (P_{ecrs}/P_{ecrc}) increased with increase in the steel contribution ratio. It is also observed that beams with low steel contribution ratio failed by flexure, whilst those with high steel contribution ratio failed by debonding. The relationships between the ratio of the first crack loads (P_{ecrs}/P_{ecrc}) and the steel contribution ratios are shown in Figure 1. Although the trend is not clear in some results, it is clear from Table 3 and Figure 1 that the steel contribution influenced the initiation of the first crack in all the beams tested.

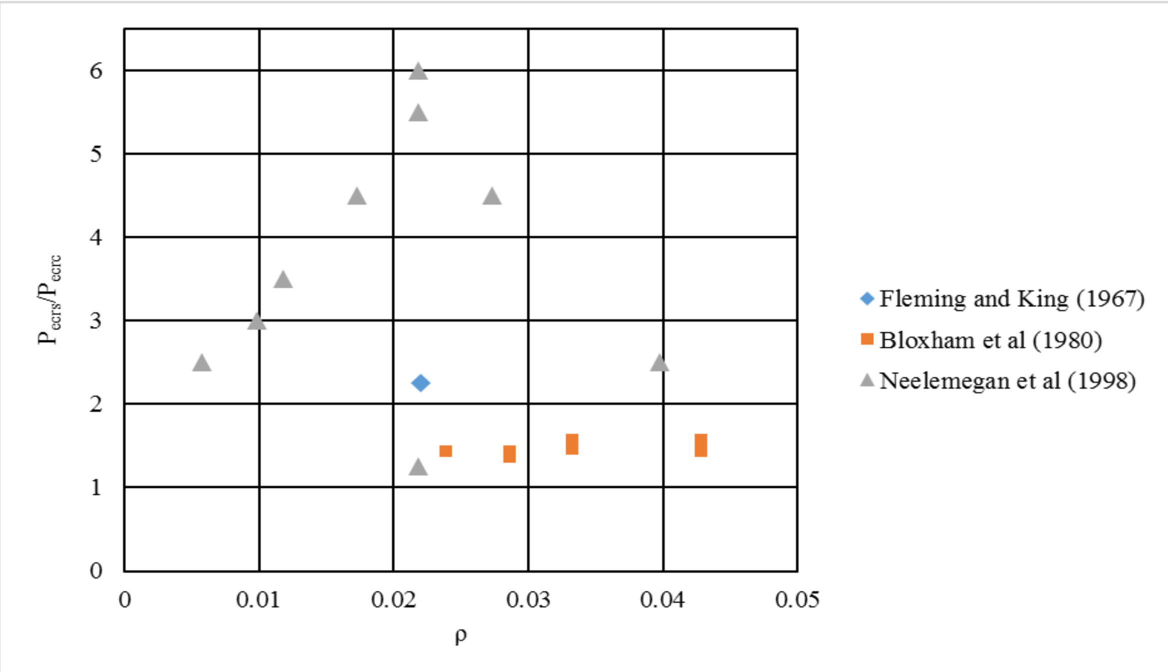

Figure 1: Ratio of experimental first crack loads vs the width-to-thickness ratio

As for Huovinen (1996), all the specimens with reinforcement ratio ranging from 0.00364 to 0.0125 registered a rise of 33 to 88% of ultimate capacity as compared to the control beam with reinforcement ratio of 0.00142, and this is due to the restraining effect offered by the bonded steel plate. Huovinen (1996) experimental result prove that, the load carrying capacity increases as the steel contribution factor increases. Furthermore, all the strengthened beams with steel contribution ratio (ρ) of 0.00364 and 0.00697 failed in flexure and the remaining beam with reinforcement ratio of 0.0125 failed prematurely by plate separation.

The drop in load of beam B3 with steel contribution factor of 0.0125 suggest that from the ductility and ultimate strength point of view, there is a limiting amount of reinforcement ratio that would be structurally reliable. It was concluded that the reinforcement ratio of the concrete beam that can encourages composite action until failure should not be more than 0.00697.
The author cannot conclude with such a bold statement after testing three epoxy bonded steel plate, to make a bold statement like that, a thorough and well defined experimental investigation must be done. In addition to that, the results obtained in this investigation, are only adequate to conclude about the increase in stiffness offered by the bonded steel plate as compared to the control.

4.0 CONCLUSIONS

From the literature conducted, it is apparent that epoxy-bonded steel plate can be successfully used as the strengthening and repairing technique provided the operation be cautiously implemented. Based on the results obtained in the literature, the epoxy-bonded steel plate can increase the flexural stiffness at all load levels and thus reducing the mid-span deflections significantly, it can increase the ductility at failure, increase the maximum flexural capacity, it delays the appearance of the first visual cracks thus resulting in increased service loads, it increases the range of elastic behaviour. Provided the surface preparation and the gluing process are carried out properly, under a given load the epoxy-bonded steel plate can decrease the tensile strains in the concrete due to the composite behaviour of the bonded steel plate, adhesive resin and concrete, in comparison with those in the unplated concrete beam.
Regardless of the advantages the epoxy-bonded steel plate offers, only a limited amount of efficient research has been done regarding the reinforcement ratio (ρ) that must be provided to encourage yielding of the externally bonded steel. Several investigators compliment the effectiveness of the epoxy-bonded steel plate technique by comparison of the manner at which the strengthened beams perform as compared with the unplated beams, however, there is lack of experimental investigation regarding the various reinforcement ratio (ρ) that can lead to composite action to be maintained until failure. The reported range of reinforcement ratio (ρ) that can encourage composite action until failure can be confusing as there is no agreement among the researchers regarding the primary factors that controls the behavior of composite beams

5.0 REFERENCES.

Fleming CJ, King GEM. The development of structural adhesives for three original uses in South Africa. BULLETIN RILEM 1967; 37:240-251.

L'Hermite R, Bresson J. Concrete reinforced with glued plates. RILEM International Symposium. Synthetic resins in building construction, Paris. 1967. p.175 – 203.

Bloxham JW. Investigation of the Flexural Properties of RC Beams Strengthened by Externally Bonded Steel Plate. PhD thesis, Sheffield University; 1980.

Jones R, Swamy RN, Ang TH. Under- and over-RC beams with glued steel plates. International Journal of Cement Composite and Lightweight Concrete 1982; 4:19–32.

Swamy RN, Jones R, Bloxham JW. Structural behaviour of RC beams strengthened by epoxy-bonded steel plates. The Struct. Engr. 1987; 65A (2):59–68.

Proc. 1st International Conference on Structural Engineering Research (iCSER 2017)
20-22 Nov 2017, Sydney, Australia
ISBN: 978-0-6480147-6-8

Time-Space Hybrid Dynamic Integration Algorithm for Inelastic Earthquake Time-History Analysis of Building Structures

Zhinan Ren[1] and Zheng He[2,3]

[1]Postgraduate, Dalian University of Technology, Dalian, China
[2]Professor, Dalian University of Technology, Dalian, China
[3] State Key Laboratory of Coastal and Offshore Engineering, Dalian University of Technology, Dalian, China
Corresponding author's E-mail: hezheng1971@126.com

Abstract

To solve the convergence problem of the building structures under the strong nonlinear condition, this paper develops a series of hybrid algorithms for strong nonlinear analysis of the building structures, which combine the advantages of explicit and implicit algorithms. In the time-domain hybrid algorithm, the switch between the implicit algorithm and the explicit is decided by the occurrence of iteration non-convergence when the implicit algorithm is used for the analysis of the whole building structure. And in the space hybrid algorithm, the whole structure is divided into several floor areas and interface areas to decouple the independent dynamic balance equation of each floor area by predicting the dynamic responses of interface, so that the proper dynamic integral algorithm of each area could be confirmed through its real state. The time-space hybrid algorithm, using the occurrence of the implicit algorithm iteration non-convergence as the switch criterion for the dynamic algorithm in the time domain and referring to the displacement difference vector of the iteration failure moment, can determine the area in the state of strong nonlinear and automatically partition the building structure according to the freedom number, then switch to the space hybrid algorithm to calculate the current time step. The hybrid dynamic algorithm realized in the self-development finite element analysis platform presents the superiority in solving the strong nonlinear problems over the Newmark algorithm when it is applied to the nonlinear time-history analysis of strong earthquake for building structures.

Keywords: Hybrid dynamic algorithm, Earthquake, Inelastic analysis, Building structures.

1. INTRODUCTION

The whole dynamic process simulation can effectively reveal the catastrophic behavior of the building structure under the collapse level earthquake, but the computational efficiency problem of the explicit algorithm and the convergence problem of the implicit algorithm constrain the simulation. Therefore, the study of hybrid dynamic integration algorithm is meaningful as suggested by Cai et al. (2012). The earliest implementation of the hybrid algorithm is usually used in the stamping springback simulation which achieves the switching of different algorithms in the time domain. Jung and Yang (1998) use the implicit algorithm in the initial calculation and the algorithm is switched to the explicit algorithm when the number of iterations of the implicit algorithm exceeds the limit after the impact contact. Narasimhan and Lovell (1999) employ the explicit algorithm in the stamping process and the implicit algorithm in the springback process and other processes. The research about the algorithm automatic switching derives from Ludovic et al. (2002), who takes the CPU time-consuming of algorithm as the selection basis of the implicit and explicit algorithm. The space hybrid algorithm is mainly used for the analysis of fluid-solid coupling problem began with Belytschko and Mullen (1978). And different integration schemes including asynchronous algorithm of explicit-explicit partition and asynchronous algorithm of implicit-explicit partition as suggested by Liu and Belytschko (1982) are adopted in different partitions. Smolinski (1996) proposes an explicit sub-cycle algorithm that the time step ratio can be a non-integer for structural dynamic calculations. Then Daniel (1997) proposes an implicit sub-cycle algorithm based on Newmark's discrete format, whose numerical stability is superior to the explicit sub-cycle algorithm. Based on the explicit and implicit Newmark algorithm, Zhang and Jin (2014) propose an arbitrary explicit and implicit hybrid asynchronous algorithm. It could be concluded that there is certain research basis in the time-domain and space hybrid algorithm, and the time domain hybrid algorithm has been applied into some commercial FE software. The space hybrid algorithm, at the same time, can realize the multi-partition synchronous analysis and show good stability. However, these studies don't focus on the problem of the strong nonlinear analysis of the building structure. This paper focuses on the hybrid dynamic algorithm applied to the nonlinear analysis of building structures, and the time hybrid dynamic algorithm, space hybrid dynamic algorithm and time-space hybrid dynamic algorithm (hereinafter referred to as THDA, SHDA and TSHDA) are used to carry out the seismic inelastic time-history analysis respectively. Considering the consistency of dynamic analysis parameters, the explicit Newmark algorithm and implicit Newmark algorithm are selected to implement the hybrid dynamic algorithm. Based on the finite element analysis platform DUT2014 as suggested by Fu et al. (2015), three kinds of hybrid dynamic algorithms are achieved.

2. THE TIME-DOMAIN HYBRID DYNAMIC ALGORITHM

THDA is a mixture of implicit and explicit algorithms in the time domain, which employs the implicit algorithm to calculate with large time step when the implicit algorithm can converge, and uses the explicit algorithm to analyze with subdivided time step when the implicit algorithm can't converge. The schematic diagram of THDA is shown in Figure 1.

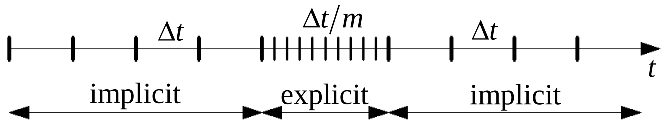

Figure 1. Schematic diagram of the time-domain hybrid algorithm

The following is the detailed description of the THDA calculation process. (1) The implicit Newmark algorithm is used to start the time-history analysis. (2) In the process of analysis, whether the implicit algorithm converges is set as switching criteria. (3) The response vectors of the structure are reset to the vectors at the beginning of the time step. (4) The time step of the explicit Newmark algorithm should be subdivided. (5) The load calculation of the explicit Newmark algorithm: in the cycle of subdivided m steps (the loop variable is i), the calculation method of the full load at i step is $P_0 + (i/m)\times(\Delta p + F_p)$, where P_0 is the full seismic load at $i = 0$, Δp is the incremental seismic load at current time step, and F_p is the imbalance force generated in the previous step. (6) After the time step analyzed by explicit Newmark algorithm, the analysis algorithm is switched back to the implicit Newmark algorithm to continue calculation.

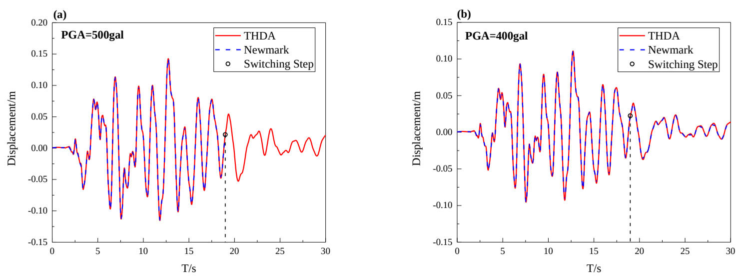

Figure 2. Comparison diagram of time-history displacement of vertex

The Newmark algorithm and THDA are used to carry out the earthquake time-history analysis of a 6-

story frame structure. The structure has a span of 5.1m in both X and Y direction, the story height is 3m, the column size is 0.6m×0.6m, the beam size is 0.5m×0.3m, and the floor thickness is 0.12m. The implicit Newmark algorithm is used to do the analysis, where γ=1/2, β=1/4, the analysis time step is taken as 0.01s, the convergence tolerance is 1.0E-4, and the maximum number of iteration is 20. When the PGA level reaches 500 gal, the implicit Newmark algorithm does not converge at 1899 step. Then the structure is re-analyzed by THDA, where the explicit time step subdivision *m* is 10000. It can be seen from Figure 2(a) that the displacement calculation results are not deviated at the switching step and the results are not divergent at the follow-up time steps. In order to verify the accuracy of THDA, the implicit Newmark algorithm and THDA are used to do the time-history analysis of this structure where PGA=400gal, and the implicit Newmark algorithm is forced to switch to the explicit Newmark algorithm at step 1899. The comparison diagram of the complete displacement time-history curve of Newmark and THDA in Figure 2(b) shows that the calculation results of THDA are credible.

3. THE SPACE HYBRID DYNAMIC ALGORITHM

Under the earthquake load excitation, most areas in the building structure are in the state of weak nonlinearity, and only some local areas enter the state of strong nonlinearity which may lead to the convergence problem. This paper has developed SHDA shown in Figure 3, which divides the entire building structure into multiple sections according to the state of nonlinearity. It takes the explicit algorithm with small time step to analyze strong nonlinear regions, and the implicit algorithm with large time step to analyze weak nonlinear regions, and couples the interaction between partitions through the interface.

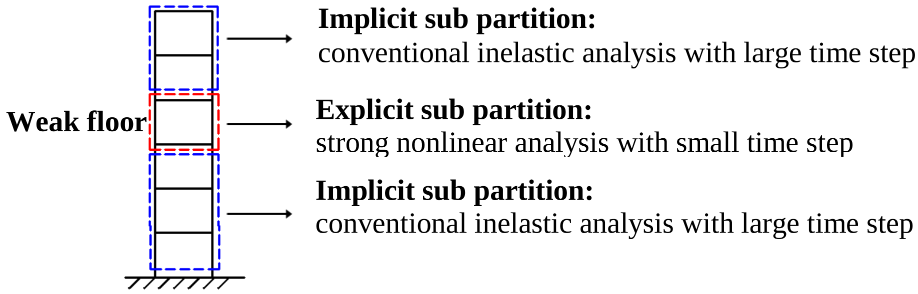

Figure 3. Schematic diagram of the space hybrid algorithm

The system is divided into a number of substructures, where **I** and **E** represent the degree of freedom of the partition and the interface, respectively. Then the system dynamic equilibrium Equation 1 where can be expressed as Equation 2 which can deduce partition dynamic balance Equation 3 and interface dynamic balance Equation 4 through the equation rearranging.

$$\boldsymbol{M}\boldsymbol{x}'' + \boldsymbol{C}\boldsymbol{x}' + \boldsymbol{K}\boldsymbol{x} = \boldsymbol{P}$$
(1)

$$\begin{bmatrix} \boldsymbol{M}_{\mathrm{II}} & \boldsymbol{M}_{\mathrm{IE}} \\ \boldsymbol{M}_{\mathrm{EI}} & \boldsymbol{M}_{\mathrm{EE}} \end{bmatrix} \begin{bmatrix} \boldsymbol{x}''_{\mathrm{I}} \\ \boldsymbol{x}''_{\mathrm{E}} \end{bmatrix} + \begin{bmatrix} \boldsymbol{C}_{\mathrm{II}} & \boldsymbol{C}_{\mathrm{IE}} \\ \boldsymbol{C}_{\mathrm{EI}} & \boldsymbol{C}_{\mathrm{EE}} \end{bmatrix} \begin{bmatrix} \boldsymbol{x}'_{\mathrm{I}} \\ \boldsymbol{x}'_{\mathrm{E}} \end{bmatrix} + \begin{bmatrix} \boldsymbol{K}_{\mathrm{II}} & \boldsymbol{K}_{\mathrm{IE}} \\ \boldsymbol{K}_{\mathrm{EI}} & \boldsymbol{K}_{\mathrm{EE}} \end{bmatrix} \begin{bmatrix} \boldsymbol{x}_{\mathrm{I}} \\ \boldsymbol{x}_{\mathrm{E}} \end{bmatrix} = \begin{bmatrix} \boldsymbol{P}_{\mathrm{I}} \\ \boldsymbol{P}_{\mathrm{E}} \end{bmatrix}$$
(2)

$$\boldsymbol{M}_{\mathrm{II}}\boldsymbol{x}''_{\mathrm{I}} + \boldsymbol{C}_{\mathrm{II}}\boldsymbol{x}'_{\mathrm{I}} + \boldsymbol{K}_{\mathrm{II}}\boldsymbol{x}_{\mathrm{I}} = \boldsymbol{P}_{\mathrm{I}} - \boldsymbol{M}_{\mathrm{IE}}\boldsymbol{x}''_{\mathrm{E}} - \boldsymbol{C}_{\mathrm{IE}}\boldsymbol{x}'_{\mathrm{E}} - \boldsymbol{K}_{\mathrm{IE}}\boldsymbol{x}_{\mathrm{E}}$$
(3)

$$\boldsymbol{M}_{\mathrm{EE}}\boldsymbol{x}''_{\mathrm{E}} + \boldsymbol{C}_{\mathrm{EE}}\boldsymbol{x}'_{\mathrm{E}} + \boldsymbol{K}_{\mathrm{EE}}\boldsymbol{x}_{\mathrm{E}} = \boldsymbol{P}_{\mathrm{E}} - \boldsymbol{M}_{\mathrm{EI}}\boldsymbol{x}''_{\mathrm{I}} - \boldsymbol{C}_{\mathrm{EI}}\boldsymbol{x}'_{\mathrm{I}} - \boldsymbol{K}_{\mathrm{EI}}\boldsymbol{x}_{\mathrm{I}}$$
(4)

In the above equations, $\boldsymbol{x}$, $\boldsymbol{x'}$ and $\boldsymbol{x''}$ are the displacement, velocity and acceleration vector of the system respectively, $\boldsymbol{K}$, $\boldsymbol{M}$ and $\boldsymbol{C}$ are the stiffness, mass and damping matrix of the system respectively, $\boldsymbol{P}$ is the external load vector of the system, the subscript II and I represent the matrix and vector of the implicit sub partition, the subscript EE and E represent the matrix and vector of the explicit sub partition, and the IE and EI represent the matrix Coupled with the implicit and explicit sub partition.

If the responses of system at i step are known, the responses at i+1 step can be solved as the following calculation steps: (1) The responses of interface at i+1 step are predicted through assuming that the acceleration of the interface at this time step is constant. (2) The right-hand term for each partition dynamic balance Equation 3 can be obtained. (3) Each partition is calculated independently using the appropriate algorithm and the analysis step, and then the responses of each partition at i+1 step can be obtained. (4) The responses of interface at i+1 step can be got through taking the responses of each partition into Equation 4. (5) The predicted responses of interface should be corrected. (6) After the responses of system at i+1 time step are obtained, the responses at i time step, the system matrix $\boldsymbol{K}$, $\boldsymbol{C}$, and the restoring force vector $\boldsymbol{f}_s$ should be updated to carry out the calculation at next time step.

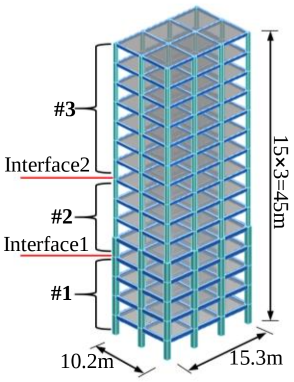

Component parameters	1-5F		6-7F		8-15F	
	beam	column	beam	column	beam	column
Section size(m)	0.6×0.3	0.7×0.7	0.45×0.2	0.45×0.45	0.5×0.25	0.5×0.5
Concrete strength (N/m^2)	3.0E+07	4.0E+07	3.0E+07	4.0E+07	3.0E+07	4.0E+07
Elastic modulus of concrete (N/m^2)	3.0E+10	3.3E+10	3.0E+10	3.3E+10	3.0E+10	3.3E+10
Steel strength (N/m^2)	4.0E+08	4.0E+08	4.0E+08	4.0E+08	4.0E+08	4.0E+08
Elastic modulus of steel (N/m^2)	2.0E+10	2.0E+10	2.0E+10	2.0E+10	2.0E+10	2.0E+10
Steel ratio	0.873	1.025	1.543	1.005	1.005	2.011
Note: Floor thickness at 1-5F is 0.12m, Floor thickness at 6-15F is 0.10m						

Figure 4. Schematic diagram of a 15-story reinforced concrete frame structure

In the inelastic time-history analysis of the structure shown in Figure 4, beam-column members are modelled with fiber-beam-column element, floors are modelled by the layered shell element, failure and removal of the beam-column element are considered and the norm of the displacement increment vector should be less than the convergence tolerance. The input is a seismic wave which lasts for 30s. The implicit Newmark algorithm is used to analyze with analysis parameters γ=1/2, β=1/4, step size of 1/100s, convergence tolerance of 0.001, maximum iterations of 20. The PGA level of seismic wave will gradually increase from 100gal to 700gal, when PGA is greater than 400gal, Newmark algorithm will fail to obtain complete time history analysis results owing to failure of iteration. In order to solve the convergence problem, SHDA is used to do the analysis. As shown in above, the #2 partition adopts the explicit algorithm with time step of 1/50000s; the #1 and #3 partitions adopt the implicit algorithm with time step of 1/100s. Figure 5 shows that the results of the two algorithms are in good agreement in the time domain that the implicit Newmark algorithm can converge and SHDA can carry on the stronger nonlinear analysis compared with the Newmark algorithm.

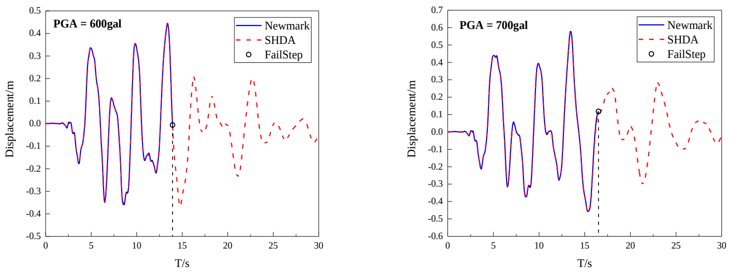

Figure 5. Comparison diagram of inelastic analysis results of the Newmark and SHDA

4. THE TIME-SPACE HYBRID DYNAMIC ALGORITHM

THDA is limited by the stability condition, and SHDA needs to determine the location of the weak position of the structure in advance. Therefore, combined with THDA and SHDA, the time-space hybrid dynamic algorithm (TSHDA) is proposed. As shown in Figure 6, the implicit algorithm with large time step Δt is used to calculate the whole structure at first, when the implicit algorithm doesn't converge, it is possible to determine the strong non-linear part to partition the structure into different parts. Then the current time step is analysed by SHDA that the strong non-linear part is analysed by the explicit algorithm with time step of Δt/m, and the time step of other sub-partitions is still Δt. After the current time step is calculated, the algorithm is switched back to the implicit algorithm to calculate the whole structure until the end of the seismic wave.

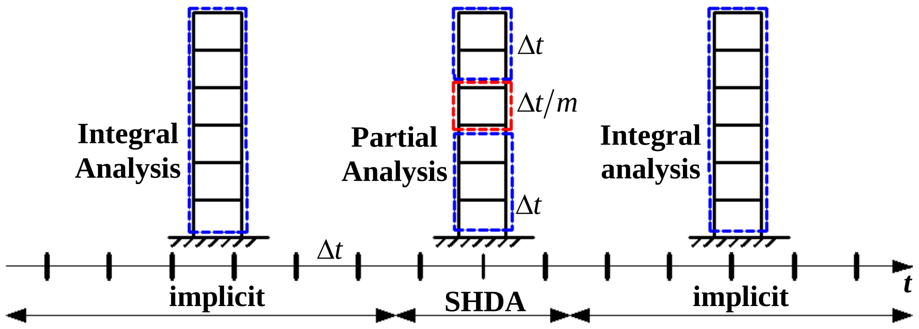

Figure 6. Schematic diagram of the time-space hybrid dynamic algorithm

The detailed calculation flow of the space-time hybrid dynamic algorithm is shown in Figure 7. On the one hand, TSHDA improves the computational efficiency of SHDA and on the other hand enhances the versatility of the hybrid algorithm. For the general nonlinear analysis, TSHDA uses the implicit Newmark algorithm to complete the time-history analysis in the whole time domain. As for the strong nonlinear analysis, the Newmark algorithm tends to fail in some time steps, and SHDA can be used to solve it in those time steps.

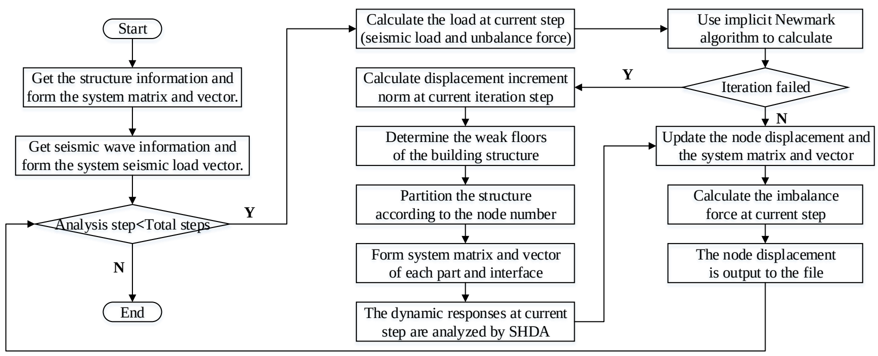

Figure 7. The calculation flow diagram of the time-space hybrid dynamic algorithm

As for the structure shown in Figure 4 with the same PGA level and dynamic parameters in SHDA analysis, the vertex time history displacement and algorithm switching time step obtained by TSHDA are shown in Figure 8. It can be seen that the calculation results of SHDA and TSHDA are basically identical, and the error is within 0.03m. When PGA=600gal, the calculation time of SHDA is 12346s compared with 817s of TSHDA; When PGA=700gal, the SHDA is 12886s compared with 1449s of TSHDA. It can be seen that TSHDA is more efficient.

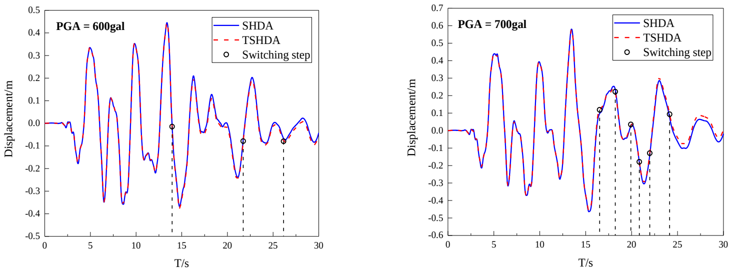

Figure 8. Comparison chart of inelastic analysis results of the SHDA and TSHDA

5. CONCLUSION

It could be obtained from the reinforced concrete frame structures' inelastic time-history analysis that the hybrid algorithm proposed in this paper overcomes the convergence problem of implicit algorithm and the computational efficiency problem of explicit algorithm, which could be used to do the strong nonlinear analysis when the structure suffers collapse scale earthquake. THDA is more suitable for the small structures subject to its stable condition. The problem of pre-specified partition of SHDA makes it suitable for the structure with definite stiffness distribution characteristics. TSHDA achieves mixing of algorithms in different time stages and regions, and has larger time step and higher efficiency, so it is fit for the analysis of the large scale structure.

REFERENCES

Cai Y, Li G, Wang H, Zheng G, Lin S (2012). Development of parallel explicit finite element sheet forming simulation system based on GPU architecture. Advances in Engineering Software, 45(1), 370-379.

Jung D W, Yang D Y (1998). Step-wise combined implicit–explicit finite-element simulation of autobody stamping processes. Journal of Materials Processing Technology, 83(1–3), 245-260.

Narasimhan N, Lovell M (1999). Predicting springback in sheet metal forming: an explicit to implicit sequential solution procedure. Finite Elements in Analysis and Design, 33(1), 29-42.

Ludovic Noels, Laurent Stainier, JeanPhilippe Ponthot, & Jérôme Bonini (2002). Combined implicit-explicit algorithms for non-linear structural dynamics. Revue Européenne Des Éléments Finis, 11(5), 565-591.

Belytschko T, Mullen R (1978). Stability of explicit-implicit mesh partitions in time integration. International Journal for Numerical Methods in Engineering, 12(10), 1575-1586.

Liu W K, Belytschko T (1982). Mixed-time implicit-explicit finite elements for transient analysis. Computers and Structures, 15(4), 445-450.

Smolinski P (1996). Subcycling integration with non-integer time steps for structural dynamics problems. Computers and Structures, 59(2), 273-281.

Daniel W J T (1997). The subcycled Newmark algorithm. Computational Mechanics, 20(3), 272-281.

Zhang W, Jin X (2014). An arbitrarily mixed explicit-implicit asynchronous integration algorithm based on uniform discretization format. Chinese Journal of Theoretical and Applied Mechanics, 46(3), 436-446.

Fu S, He Z, Li Z, Tu X, Tao Q (2015). Shared memory parallel computing procedures for nonlinear dynamic analysis of super high rise buildings. International Conference on Performance-based and Life-cycle Structural Engineering, 1629-1637 pp.

Proc. 1st International Conference on Structural Engineering Research (iCSER 2017)
20-22 Nov 2017, Sydney, Australia
ISBN: 978-0-6480147-6-8

Numerical Investigation on Impact of Bushfire Enhanced Wind on Building Structures

Christophe Camille[1], Olivia Mirza[2], Kenny Kwok[3] and Yaping He[4]

[1]Honours Student, Western Sydney University, Sydney, Australia
[2]Senior Lecturer, Western Sydney University, Sydney, Australia
[3]Professor, The University of Sydney, Sydney, Australia
[4]Senior Lecturer, Western Sydney University, Sydney, Australia
Corresponding author's E-mail: o.mirza@westernsydney.edu.au

Abstract

Most researches about bushfire and wind, individually focuses on the origins, impacts and reconstruction process which are systematically studied after a devastating event. Indeed, it can reveal a lack of research as both bushfire and wind are interrelated and subsequently referred as 'bushfire enhanced wind'. This phenomenon has long been acknowledged by researchers, however it's understanding about the different interactions and effects still remain relatively limited. Therefore, this research addresses the impacts of bushfire enhanced wind over residential structures by numerical investigation using a finite element commercial software known as Abaqus. The model first simulates the most common type of wall system (i.e. masonry: double brick) in Australia with the results presented as pressures and stress distribution. Secondly, the finite element analysis emphasises on the critical sections (i.e. wall and roof connections) when the model contains an opening (i.e. window). The outcomes generated by the finite element analysis are expected to provide valuable understanding into the fire-wind interaction and subsequently impact the Australian Standards aimed at improving structural design within bushfire prone areas.

Keywords: Bushfire, Wind, Finite element modelling, Brick masonry, Double brick connections

1. INTRODUCTION

The combined effects of bushfire enhanced wind on building structures have long been acknowledged, but unfortunately the Australian Standards: AS 3959-2009 'Construction of buildings in bushfire-prone areas', AS/NZS 1170:2:2011 'Structural design actions-Part 2: Wind actions' and AS 4055-2012 'Wind loads for housing' do not reflect that design criteria. For instance, when bushfire enhanced wind effects are considered, the factors affecting the response of the structures are the material properties (i.e. strength masonry & concrete), induced external/internal pressures and the strength of critical connections. Therefore, this paper herein presented used Abaqus to develop an accurate finite element model analysing the different impacts (i.e. strength reduction & stresses) and behaviour of building structures experiencing bushfire enhanced wind. Wherein, the main objectives of this paper are to understand and identify the critical sections within building structures, develop finite element models of Double-Brick residential structure (including opening) to analyse the pressure and stress distribution for providing design recommendations in bushfire prone areas.

Most of the previous researches investigating the complexity of fire-wind interactions on structures were limited to dangerous and costly experimental testing revealing real gaps between the Australian Standards and the actual behaviour of structures. An important factor to be considered during a bushfire enhanced wind event is the fire resistance of the construction materials used. One advantage of masonry (i.e. double brick wall) over concrete and steel structures is its ability to maintain a structural adequacy, integrity and insulation for approximately 240 minutes when equally loaded as represented in Figure 1. As a result, masonry structures (i.e. clay bricks) are typically recommended for bushfire prone areas (AS3700-2011: Standard Australia Online 2011). Similarly, wind is an essential part of the structural members design where engineers primarily focus on three of its major effects identified as: out-of-plane bending, in-plane shear and uplift (AS 4055-2012: Standard Australia Online 2012). These wind pressures can be either external or internal (due to an opening) and typically vary from 0.7 to 6.0 kPa characterising the net wind effects on the structure. Therefore, it is important to numerically analyse these correlation behaviours specially at critical locations (i.e. roof-to-wall connections) to further provide structural recommendations for bushfire prone areas. Figure 2 highlights four critical connections which will be further researched and modelled within Abaqus.

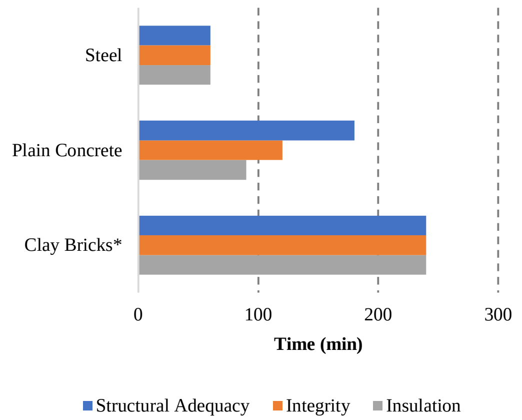

Figure 1: Fire resistance levels of construction materials

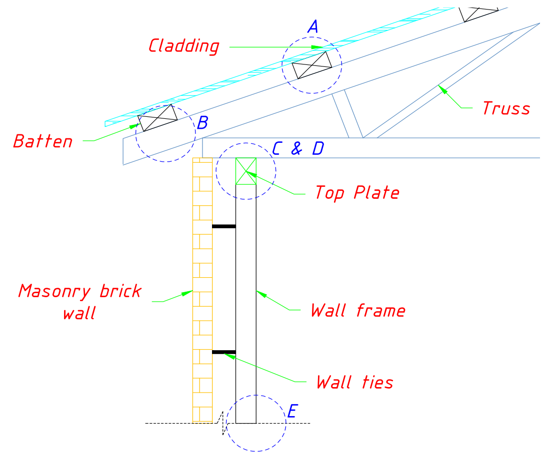

Figure 2: Cladding-to-batten (A), batten-to-truss (B), truss-to-top plate (C), top plate-to-wall frame (D) and wall-to-foundation (E)

2. FINITE ELEMENT MODEL

2.1 General

The numerical investigation herein presented used the finite element software Abaqus to simulate the interaction of bushfire enhanced wind on building structures and their connections to an exposure of 9MW/m (fire-front) and a 9.52m/s wind. These effects are represented in terms of forces and material properties reduction affecting the behaviour of the double brick walls and the concrete roof. Therefore, to achieve accurate results from the finite element analysis, these crucial components must be thoroughly researched and their mechanical properties precisely imputed towards the generation of a three-dimensional model.

2.2 Concrete

The models mainly consist of load bearing double brick walls supporting a concrete roof, wherein the behaviour of concrete in compression is assumed to be linear up to 40% of its strength (f'_c). Exceeding that stress, a non-linear behaviour is observed for which the stress-strain relationship of concrete in compression can be expressed using Equation 1 (Carreira & Chu 1985).

$$\sigma_c = \frac{f'_c . \gamma . (\varepsilon_c / \varepsilon'_c)}{\gamma - 1 + (\varepsilon_c / \varepsilon'_c)} \qquad (1)$$

where $\gamma = \left|\frac{f'_c}{32.4}\right|^3 + 1.55$ $\qquad \varepsilon'_c = 0.002$ (peak strain)

f'_c = Compressive strength, ε_c = Strain of the curve, γ = Dimensionless material parameter

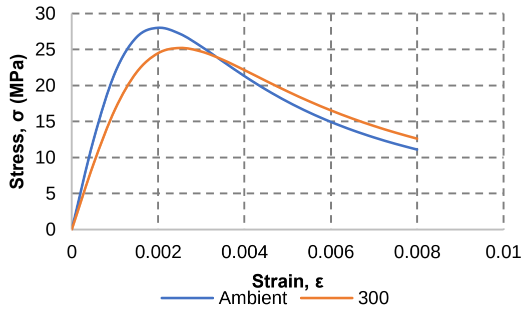

Figure 3: Stress-strain relationship of concrete at elevated temperature (Carreira & Chu 1985; Kodur 2014)

In addition, it is essential to simulate the performance of concrete when exposed to elevated temperatures (i.e. 300°C), as it usually experience a compressive strength reduction of approximately 10% (Kodur 2014). As result, the stress-strain relationship of the concrete roof imputed within Abaqus is illustrated in Figure 3.

2.3 BRICK MASONRY

In order to provide an efficient numerical analysis, the research herein presented has adopted the macro-numerical approach simplifying the masonry unit, mortar and unit-mortar interface to one homogenous element. As a result, the masonry stress-strain curve can be expressed by Equation 2 which has provided a good fit to numerous past experiments (Kaushik, Rai & Jain 2007).

$$\frac{f_m}{f'_m} = \left(2 * \frac{\varepsilon_m}{\varepsilon'_m}\right) - \left(\frac{\varepsilon_m}{\varepsilon'_m}\right)^2 \quad (2)$$

where $\varepsilon'_m = 0.0018$ (peak strain at ambient temperature)

f_m = strength (stress) of masonry unit

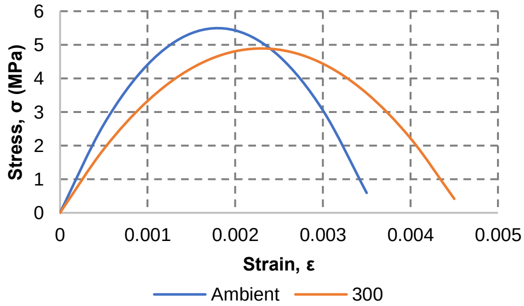

Figure 4: Stress-strain relationship of clay bricks at elevated temperature (Russo & Sciarretta 2013)

Similar to concrete's mechanical behaviour, the masonry bricks experienced a strength reduction of 11% when exposed to a bushfire temperature of 300°C corresponding to the peak measurement at the surface of the walls. Figure 4 summaries the deformation of clay bricks within the finite element model through its stress-strain relationship.

2.4 MESH, BOUNDARY & LOADING CONDITIONS

Three-dimensional solid elements commonly abbreviated to C3D8R were used to model the double brick walls and the roof as shown in Figure 5. That specific element uses the Continuum solid element, 3-Degree of freedom as well as 8 nodes with Reduced integration to efficiently reduce computational time and enhanced the convergence towards accurate results. For the boundary condition, the bottom edge of the double brick walls (highlighted in red) were set to 'encastre' simulating a fixed connection to the ground.

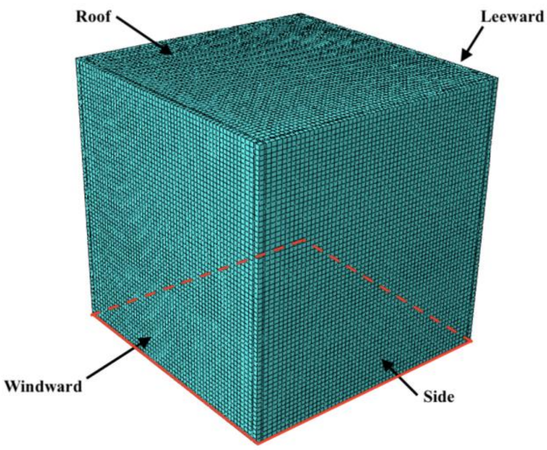

Figure 5: Finite Element Model of a Silsoe cube

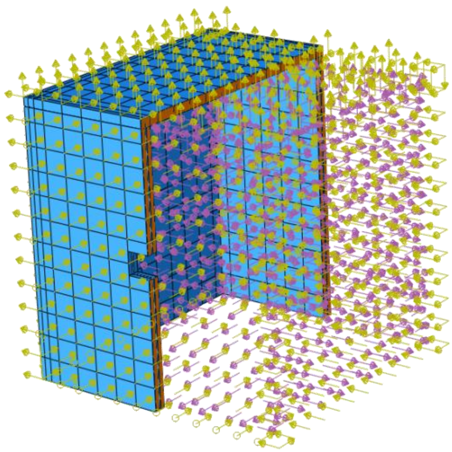

Figure 6: Finite Element Model with all the forces

Additionally, all the loads applied towards the Abaqus model were generated from a Fire Dynamics Simulator (FDS) analysis conducted by Baker (2017), wherein the surfaces on both the external and internal walls of the Silsoe cube were exposed to the effects of a typical 9MW/m bushfire and 9.52m/s wind. The loading conditions herein described involve two cases of which the first one simulates the exposure of the surfaces to the maximum positive and/or negative pressures. On the other hand, case two precisely followed the FDS simulation in terms of average pressure on every single side. However, two cases include the simulation of the model under both the influence of opening and no opening expose to either fire or no fire. Figure 6 represents the internal and external forces acting on both the walls and roof due to the presence of an opening being 1m wide and 0.5m high.

3. RESULTS & DISCUSSION

3.1 OVERVIEW

The results generated from the finite element analysis herein presented summarised the fire-wind interaction onto a building structure and its connections. Eight Abaqus models were analysed for the following scenarios focusing on the maximum/minimum stresses, forces, pressures and critical connections:

1. No opening subjected to only wind effects of 9.52m/s;
2. No opening structure exposed to a 9MW/m fire front and a 9.52m/s wind;
3. Windward wall opening (1m wide and 0.5m high) affected only by a 9.52m/s wind.
4. Windward wall opening (1m wide and 0.5m high) exposed to a 9MW/m fire front and a 9.52m/s wind.

Similarly, case 2 investigate the same fire, wind and opening arrangement, yet based on the average FDS results compared to case 1 which consider the highest positive/negative effects.

3.2 SCENARIO 1

Figures 7 and 8 below represent the stress distribution under wind actions with no reduction in materials properties. The numerical analysis revealed that the average pressures resulting from the wind actions on both cases were negative indicating a suction effect. In accordance with the Australian Standards: AS 4055:2012 'Wind Loads for Housing', this structural response is expected where only the windward wall experienced positive external pressures with roof corner and wall edges being critical.

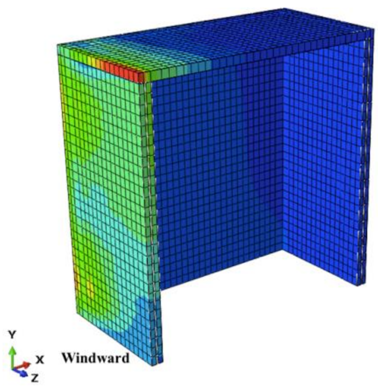

Figure 7: Stress distribution of the Abaqus model with no opening under wind actions (Case 1)

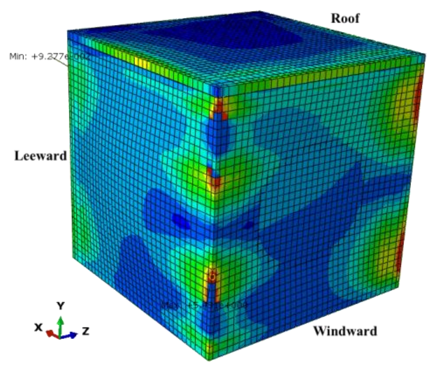

Figure 8: Stress distribution of the Abaqus model with no opening under wind actions (Case 2)

3.3 SCENARIO 2

The stress distribution for both the fire and wind effects are highlighted in Figures 9 and 10. For this second scenario with the addition of fire, it was observed that the critical sections were situated on the windward side with the wall edges and roof-to-wall connections initially failing. In terms of average external pressures, both cases mainly experienced positive pressure due to the fire surrounding the structure.

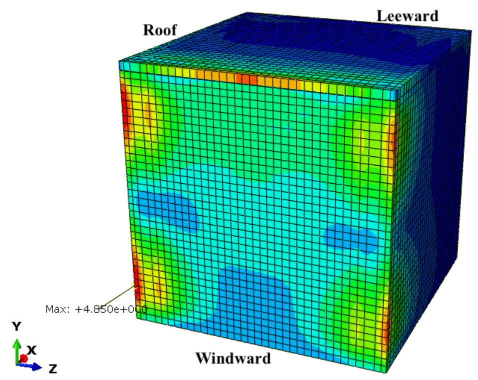

Figure 9: Stress distribution of the Abaqus model with no opening under fire and wind effects (Case 1)

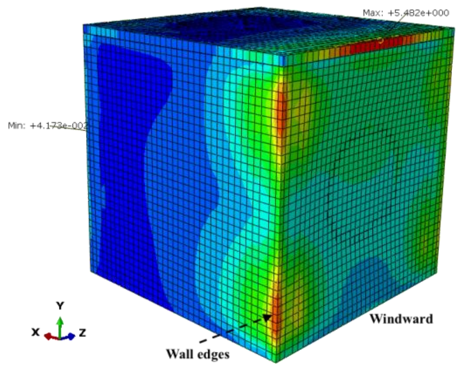

Figure 10: Stress distribution of the Abaqus model with no opening under fire and wind effects (Case 2)

3.3 Scenario 3

The stress distribution under wind actions only is represented in Figure 11 and 12. In both cases, the wall corners and roof edges experienced significant deformation on the windward side as justified in the Australian Standards: AS 4055:2012 'Wind Loads for Housing'. However, when subjected to the average wind pressures (Case 2), the finite element model displayed a critical stress at the roof-to-wall connection on the left-side wall describing a higher wind actions on that side of the structure.

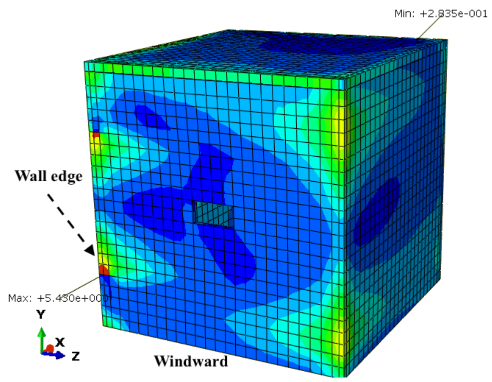

Figure 11: Stress distribution of the Abaqus model with windward opening under wind actions (Case 1)

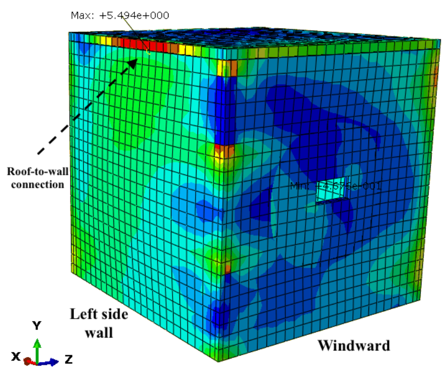

Figure 12: Stress distribution of the Abaqus model with windward opening under wind actions (Case 2)

3.3 Scenario 4

Figure 13 and 14 represent the stress distribution under the interaction of fire and wind which produced a reduction in materials properties and an increase in pressures due to the elevated temperatures. These last finite element models also represent the bushfire enhanced wind interaction with opening (1m wide and 0.5m high) and are considered to generate the most realistic effects a structure will endure.

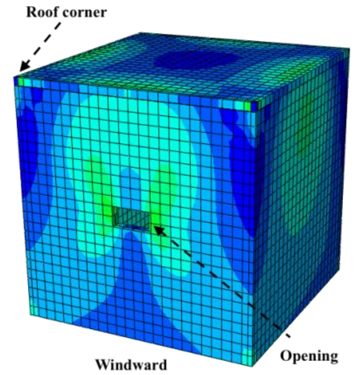

Figure 13: Stress distribution of the Abaqus model with windward opening under fire and wind effects (case 1)

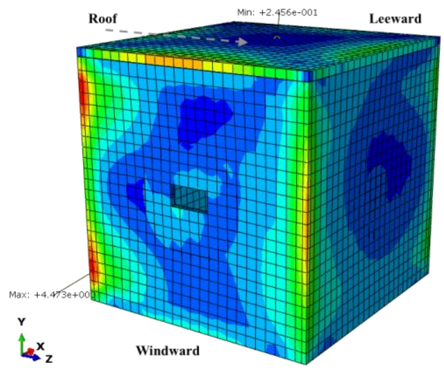

Figure 14: Stress distribution of the Abaqus model with windward opening under fire and wind effects (case 2)

This increase in pressure validate the accuracy of the finite element models which conformed to the pressure law as the temperature increases.

4. CONCLUSIONS

This paper discusses eight different bushfires enhanced wind scenarios and their effects towards buildings structures. The reasonable accurate finite element models have been developed to interpret the influence of fire and wind both individually and in combination, wherein the materials deterioration have been taken into account. Subsequently, the finite element analyses conducted on eight models include two cases and four possible scenarios from which the following conclusions were achieved:

- The effects of fire tend to reduce the peak stress experienced by the building, implying a strength reduction capacity of the structure;
- The presence of opening induced a drastic change in the net pressures configuration as the internal pressures may in certain circumstances resist or facilitate the failure of the structure;
- In specific arrangement, Case 2 which uses the average FDS pressures has been identified as the critical loading case inducing the highest stresses throughout the connections;
- The interaction of bushfire, wind and opening generated the worst situation as structures are exposed to elevated temperatures as well as high internal and external pressures. The pressure difference may vary by ± 50 to 130%.

5. FURTHER STUDY

Further research into the following areas will be conducted to improve the accuracy and understanding of bushfire enhanced wind effects:

- Perform finite element modelling for roof-to-wall and wall edges connections;
- Perform a time-dependant finite element analysis to evaluate different combinations of varying pressures.

6. ACKNOWLEDGEMENT

The authors acknowledge Australia Research Council Discovery Project DP160103248 which provided the catalyst for undertaking this research as well as Western Sydney University through the School of Computing, Engineering and Mathematics for their support to the authors work described herein.

REFERENCES

Baker, K, He, Y, Kwok, K & Mirza, O 2017, 'Numerical investigation of Bushfire-Enhanced wind profiles', Penrith, Western Sydney University.

Carreira, D & Chu, K 1985, 'Stress-strain relationship for plain concrete in compression', *Journal of ACI Structural*, vol. 82, no. 11, pp. 797-804.

Kaushik, HB, Rai, DC & Jain, SK 2007, 'Stress-strain characteristics of clay brick masonry under uniaxial compression', *Journal of materials in Civil Engineering*, vol. 19, no. 9, pp. 728-39.

Kodur, V 2014, 'Properties of Concrete at Elevated Temperatures', *ISRN Civil Engineering*, vol. 2014, p. 15.

Russo, S & Sciarretta, F 2013, 'Masonry exposed to high temperatures: Mechanical behaviour and properties—An overview', *Fire Safety Journal*, vol. 55, pp. 69-86.

Standard Australia Online 2011, *Masonry Structures, AS 3700-2011*, SAI Global database.

—— 2012, *Wind Loads for Housing, AS 4055-2012*, SAI Global Database.

Proc. 1st International Conference on Structural Engineering Research (iCSER 2017)
20-22 Nov 2017, Sydney, Australia
ISBN: 978-0-6480147-6-8

Numerical Investigation of the Impact of Bushfire-Enhanced Wind Profiles on Structures

Kallan Baker[1], Yaping He[2], Kenny Kwok[3], Olivia Mirza[2]

[1]Honours Student, Western Sydney University, Sydney, Australia
[2]Senior Lecturer, Western Sydney University, Sydney, Australia
[3]Professor of Engineering, The University of Sydney, Australia
Corresponding author's E-mail: y.he@westernsydney.edu.au

Abstract

It has long been known that extreme bushfire circumstances are always associated with violent winds. There has been a wealth of research devoted to investigating the effect of wind on bushfire spread, but only recently is attention being paid to the enhancement wind by fire and the subsequent impact on buildings. Previous studies have focused on building blocks with simple configurations, however, building structures in reality can be quite complex. This research examines the effects of bushfire-enhanced wind on a typical structural configuration, that is, a building with openings. The computational fluid dynamics approach was employed to reveal pressure distributions, wind velocity, and temperature profiles. The numerical simulations also revealed an interior flow within the building, which is believed to have been caused by the stack effect. Consequently, fire-generated wind pressure loading on the building is different to that on a building with no opening. The analytical information obtained will assist in research on structural response during intense bushfire, furthering the development of relevant standards for better protection of building structures against bushfire attacks.

Keywords: Buoyancy, Bushfire, Wind, Computational fluid dynamics (CFD), Stack effect

1. Introduction

Bushfire is a type of natural disaster that is heavily influenced by a range of environmental factors that combine to create catastrophic conditions. Bushfire affects vast populations across the world, particularly within Australia, which is recognised globally as the most fire-prone continent on Earth (Bryant 2008). Wind is another significant environmental aspect that can have a detrimental impact on modern infrastructure. It has long been known that wind and bushfire interact to form more aggressive bushfire conditions, however there appears to be severe lack of research regarding their combined properties. The destructive nature of a bushfire event should therefore not be solely attributed to apparent bushfire attack mechanisms such as flame contact, radiant heat and ember attack that are identified in the relevant standard (AS3959–2009).

Several extreme cases of bushfire have highlighted the significance of the need to fully understand the phenomenon of fire-generated wind, such as the 2009 Victorian Bushfires which claimed the lives of 173 people and in excess of 4,500 structures (Mannakkara and Wilkinson 2013). It was indicated by Lambert (2010) that excessive quantities of wind were being drawn to the base of the bushfires to replace the displaced air, creating increased pressure conditions great enough to prise main structural components (mainly roofs) from their fixtures. As a consequence, structures were left unprotected from flame and ember attack, which ignited buildings from within the interior. Furthermore, the 2003 Canberra Bushfires which killed 4 people and destroyed approximately 500 houses was another instance of intense bushfire-enhanced wind damage. According to McRae *et al.* (2013), the intense bushfires coupled with extreme winds resulted in a powerful pyro-convective atmospheric event, which essentially formed a 'fire tornado', the first ever recorded in Australia.

Earlier research attentions to bushfire-wind structure interactions were reported in the works by He *et al.* (2011) and Kwok *et al.* (2012), followed by Ly (2012). Their studies focused on a simple intact building block and demonstrated significant variations in pressure distributions that could have more detrimental effects on the building structure than the wind that is not affected by bushfires.

It has been identified through various research projects that ember attack, rather than radiant heat or flame exposure, is the primary cause of building ignition during and after a bushfire event *(Whittaker et al.* 2013). However, embers by themselves do not pose much threat to buildings, it is the wind damage that creates opportunities for embers to attack. Furthermore, a partially damaged structure could be subjected to even greater wind generated pressure load, hence greater devastation. The objective of the current study is to investigate bushfire-enhanced wind effects on a structure with partial damage that is represented by an opening in the windward wall. The results of this study will play a critical role in future structural response analysis projects aimed at improving stability and protection for buildings during bushfire-enhanced wind scenarios, such as the research conducted by Camille *et al.* (2017).

2. Numerical Simulation

The numerical investigation presented within this research has been conducted from a computational fluid dynamics (CFD) approach to examine to the effects of bushfire-enhanced wind on a building structure containing an opening. The software program used to undertake this investigation is the Fire Dynamics Simulator 6 (FDS), which has been developed by the National Institute of Standards and Technology (NIST), USA (McGrattan *et al.* 2013). The program is designed to model fire-driven fluid flow, particularly for heat and/or smoke transfer from fires. It numerically calculates a form of the Navier-Stokes equations to resolve turbulent flow using the large eddy simulation (LES) scheme.

2.1. Domain Modelling and Boundary Conditions

The domain for the FDS modelling is a three-dimensional rectangular prism with *XYZ* dimensions of 73 m × 30 m × 24 m as shown in Figure 1. This domain layout has been based upon previous studies by He *et al.* (2011), Kwok *et al.* (2012) and Ly (2012). The domain parameters have been verified within the aforementioned studies, which focused on a 6 m × 6 m × 6 m building block with no opening known as the Silsoe cube (Richards *et al.* 2001). The mesh sizing applied to the domain is 0.1667 m × 0.25 m × 0.15 m. The bushfire front is 3 m in width in the *X*-direction, and extends across the domain in the *Y*-direction at a height of *Z*=0 m. The origin of the coordinate is set at the base of the building block which is placed at the centre plane across the transverse direction. The wall of the block has a thickness of 0.26 m and a roof thickness of 0.2 m in accordance with works conducted by Camille *et al.* (2017).

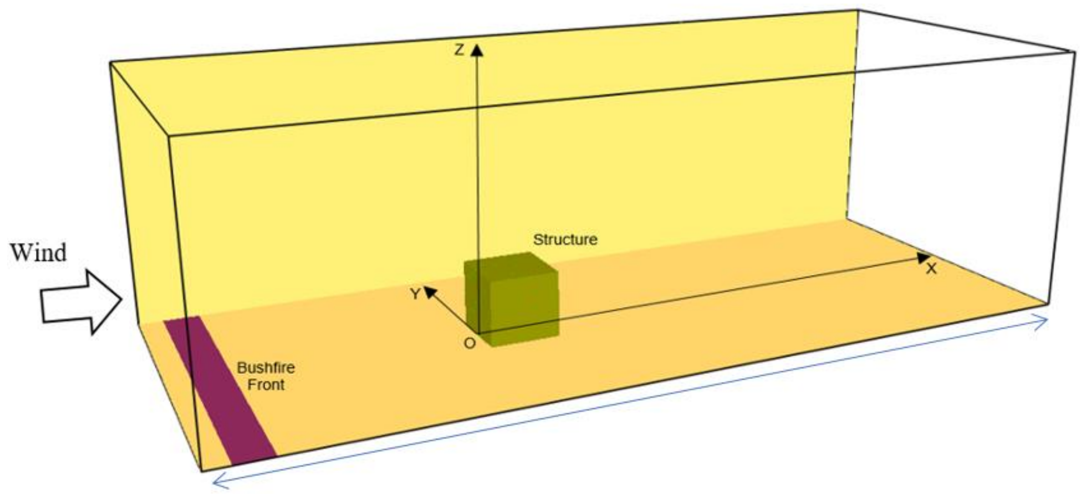

Figure 1. Layout of computation domain.

The following boundary conditions were set in order to achieve the most accurate simulation for the investigated scenario. The domain essentially forms an open roof tunnel, whereby wind travels from the left (X= –25m) boundary across the domain to the exit point at X=48 m. The velocity profile at the entrance follows a power function (He *et al.* 2011). The boundaries at Y= –15 m and Y=15 m are specified as slip surfaces. The ground at Z=0 m is a no-slip surface and the top at Z=24 m is specified as in the open condition.

2.2. Windward Wall Opening and the Simulation Output Point Distribution

A window opening is specified at the centre of the windward wall of the building block. The dimension of the window opening was a control parameter in the simulation. Figure 2 below illustrates the location of the opening when the dimension is set at 1 m × 0.5 m. Also identified in Figure 2 are the pressure output points which record the relative pressure acting on the interior and exterior surfaces of the structure. They are equally spaced at 0.5 m across and down the face in a 13 by 13-point grid.

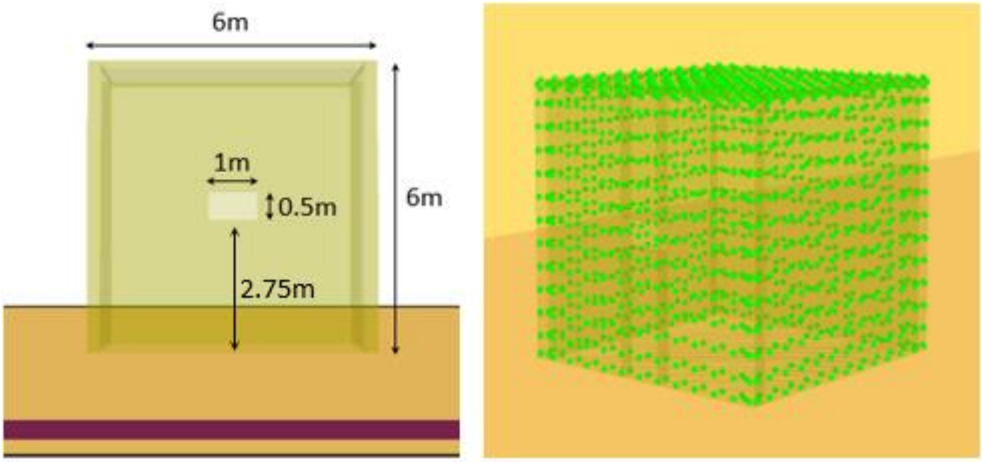

(a) **(b)**

Figure 2. (a) windward wall opening dimensions and location and (b) pressure output points (green dots) over the exterior and interior surfaces of the structure.

3. Results & Discussions

The numerical investigation of this research was based upon a number of scenarios in which the opening configuration was altered to examine the role of the opening for structural response studies. The presence of the bushfire was also altered. Two control scenarios containing no opening in the windward face, one with fire and the other without fire, were established as reference cases for comparisons with the investigations by He *et al.* (2011) and Ly (2012). Both of these scenarios were also reproduced without a bushfire front to highlight the significance of the fire-generated wind. A summary of the simulation scenarios is given in Table 1 below.

Table 1. Summary of the simulation scenarios.

Scenario number	Bushfire intensity (MW/m)	Opening size, $h \times w$ (m × m)
1	0	0 × 0
2	9	0 × 0
3	0	0.5 × 1
4	9	0.5 × 1
5	0	1 × 2
6	9	1 × 2

The following parameters were employed as the input across all six scenarios based on the aforementioned studies, the wind velocity has been referenced as an average value taken from the field testing on the Silsoe cube conducted by Richards *et al.* (2001);

- Building Block Dimensions, $L \times W \times H$ = 6 m × 6 m × 6 m;
- Characteristic Wind Velocity, u_r = 9.52 m/s;
- Bushfire Front Intensity, Q_m = 9 MW/m;
- Simulation Running Time, t = 50 s

He *et al.* (2011) also investigated the velocity profile across the domain for the simulation, concluding that it takes approximately 20 seconds for the flow field to establish a quasi-steady state. Therefore, the data averages presented throughout this research are based upon the average values for the quasi-steady period, which in all cases is the range between 20 and 50 seconds.

3.1. Opening Configuration Comparison

An analysis comparing each scenario regarding the pressure coefficient C_p acting on the exterior and interior vertical centreline (Y=0 m) of the structure was conducted to verify the output data from the simulations. Figure 3 below shows the predicted C_p distributions for all six scenarios. The non-dimensional distance parameter S^* is defined by $S^*=s/L$, where s is the distance measured from the base of the block and L is the characteristic length of the building block (=6 m).

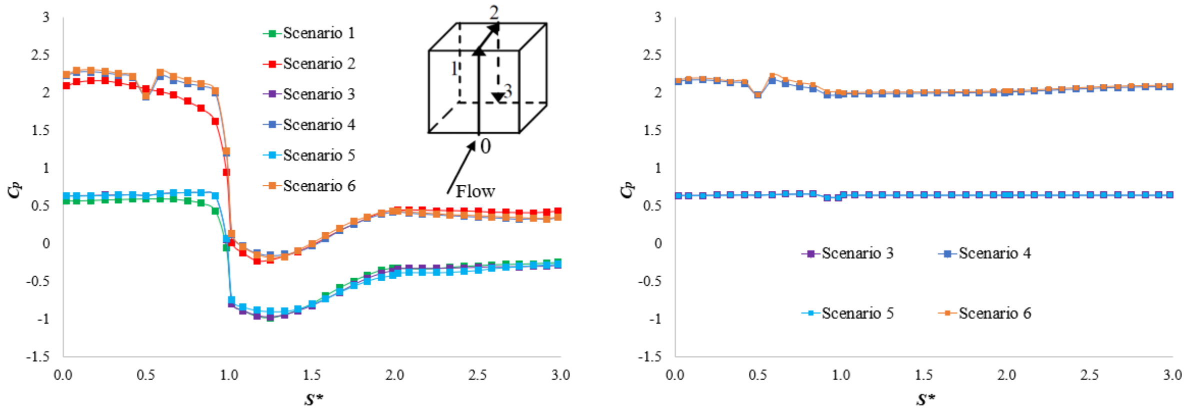

(a) (b)

Figure 3. Pressure coefficient variation along the centreline of (a) exterior and (b) interior of the building.

As it can be seen from Figure 3(a), several key points can be drawn from the results. Firstly, the C_p distribution for Scenario 1 (no opening, no fire) appears to be in accordance with that produced by Ly (2012). Only minor discrepancies exist between C_p distributions of Scenario 1 and Scenario 3 (0.5 m × 1 m opening, no fire). When the fire of 9 MW/m intensity is introduced, the entire distribution curves are shifted upwards significantly. The exterior C_p variation on the structure is not affected by the sizing of the opening. It is apparent that the bushfire contributes significantly to the pressure on the structure with increase of approximately 350%.

A similar upwards shift is evident in the interior C_p in Figure 3(b), where the curves for the scenarios with bushfire are increased significantly compared to the scenarios without bushfire. The similar nature of the data values for Scenarios 3 and 4 and Scenarios 5 and 6 indicate that the size of the windward wall opening does not significantly alter the interior C_p and is therefore considered negligible. The data from the interior C_p distributions appears to confirm that the wind entering through the single opening pressurises the interior of the structure and the C_p is therefore constant throughout the building.

3.2. Temperature Variance

One difference between ordinary wind and bushfire affected wind is that the latter has a much higher temperature and poses additional attack to building structures. Figure 4 shows the predicted temperature planar distribution across the domain at Y=0 m and at time of t = 40 s. The flow immediately in contact with the building façade is estimated to have reached the temperature range of approximately 300-320°C. It can be seen that a minor portion of the temperature profile is entering the building through the opening at approximately 100°C. This provides more evidence for the velocity flow phenomenon inside the structure, as air with a higher temperature is more buoyant, which may be the main driving force causing the fluid flow within the building.

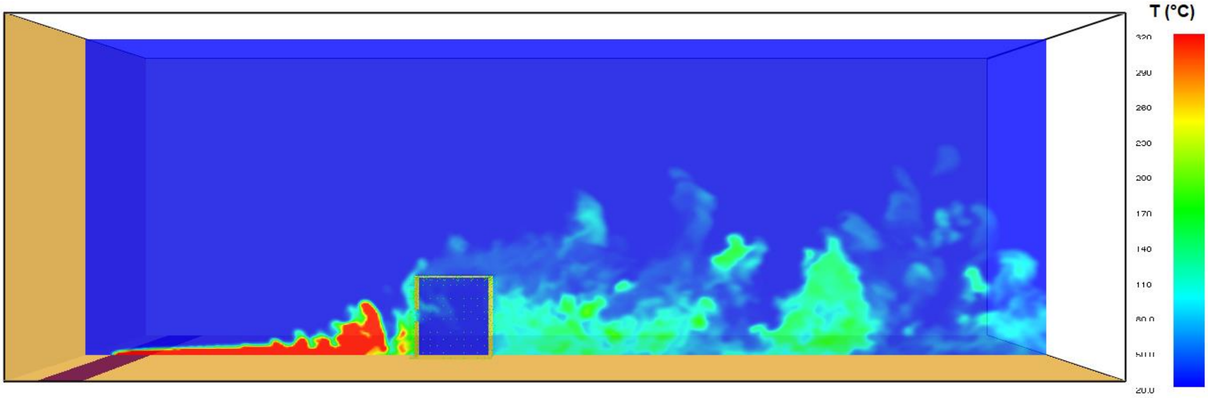

Figure 4. Temperature distribution across the domain (*Y*=0 m) in Scenario 6 at *t* = 40 s.

3.3. Evidence of Interior Flow

The expected to allow the attainment of pressure equilibrium between the exterior and interior of the building block. However, the temperature differential between the exterior and interior helped the creation of the stack effect (Klote and Milke 2002) which induced a counter-current flow phenomenon at the opening. Figure 5 compares two simulations with the 1 m × 2 m opening, (a) is from Scenario 5 with no bushfire effect and (b) is from Scenario 6 with 9 MW/m bushfire intensity. It is evident that the temperature from the bushfire is the main factor behind this flow.

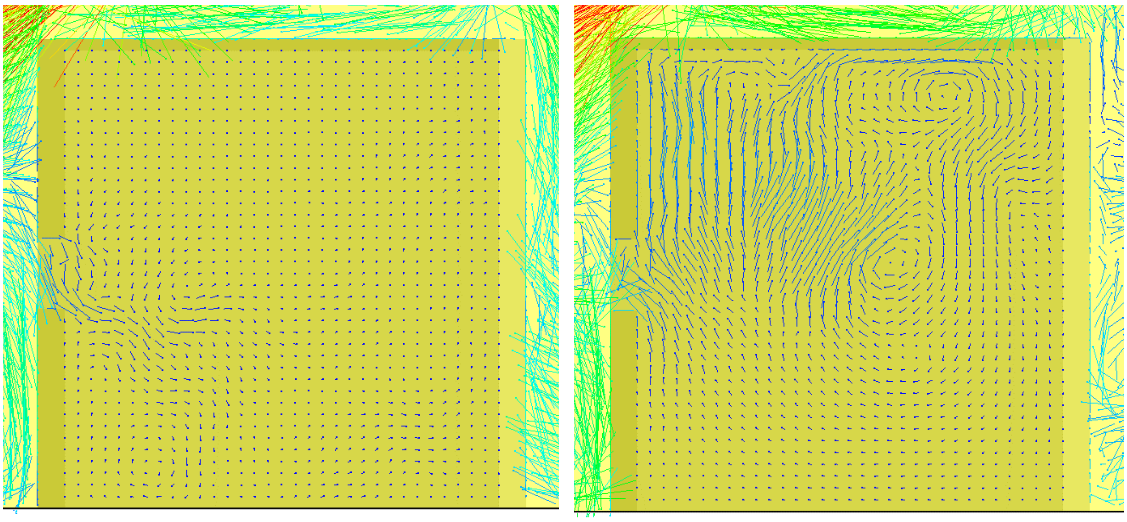

(a) (b)

Figure 5. Interior flow within the structure with a 1×2 m opening (a) no fire; and (b) with fire.

4. Conclusion and Further Research

It has been confirmed through the numerical simulations that the fire-generated wind pressure loading acting on the structure with an opening is vastly different to a similar structure with no opening. The numerical simulations revealed that fire-enhanced winds can induce severe pressure loading conditions that have the potential to ultimately cause structural failure during a bushfire event. Furthermore, the numerical investigation revealed a distinctive phenomenon of the fire-driven fluid flow within the building enclosure. The key parameter that controls this interior flow is the temperature difference between the exterior and interior of the enclosure. Although there is adequate evidence provided to suggest this interior flow phenomenon is occurring, a greater depth of study is required to determine the major contributing factor. Future research focusing on various independent parameters such as bushfire front intensity and the characteristic wind velocity would provide explanations to distinguish the main cause of the internal flow.

The results of this report can be used in future research to determine the structural response of the building block to support developments within the bushfire protection field. Other future investigations for this work include modifying the positions of the opening(s), as this research focused solely on openings in the windward wall. In conclusion, further investigation is required to confirm the interior flow within the building structure, although substantial evidence has been provided.

6. Acknowledgement

This work is supported by Australian Research Council grant ARC-DP160103248.

7. References

Bryant C (2008). Understanding bushfire: trends in deliberate vegetation fires in Australia, Vol. 27, Technical and Background Paper, Australian Institute of Criminology, Canberra.

Camille C, Kwok K, Mirza O, He Y (2017). Numerical Investigation on Impact of Bushfire-Enhanced Wind on Building Structures, Western Sydney University, Penrith.

He Y, Kwok K, Douglas G, Razali I (2011). Numerical Investigation of Bushfire-Wind Interaction and its Impact on Building Structure, Fire Safety Science - Proceedings of the Tenth International Symposium, pp. 1449-62.

Klote JH, Milke JA (2002). Principles of smoke management, American Society of Heating, Refrigerating and Air-Conditioning Engineers (ASHRAE), Atlanta.

Kwok K, He Y, Douglas G (2012). Bushfire-enhanced wind load on structures, Proceedings of the Institution of Civil Engineers: Engineering and Computational Mechanics, 165(4), pp. 253-63.

Lambert K (2010). Extreme bushfire/firestorm impact and the bush/urban interface, Black Saturday 7th February 2009, Submission to the 2009 Victorian Bushfires Royal Commission.

Ly J (2012). Numerical Investigation of Aerodynamic Impact of Bushfire-Enhanced Wind, Honours thesis, Western Sydney University, Penrith.

Mannakkara S, Wilkinson S (2013) Build Back Better principles for post-disaster structural improvements, Structural Survey, 31(4), pp. 314-27.

Mcgrattan K, Mcdermott R, Hostikka S, Floyd J, Weinschenk C, Overholt K (2016). Fire Dynamics Simulator User’s Guide, 6th ed.: NIST Special Publication 1019, National Institute of Standards and Technology.

McRae R, Sharples J, Wilkes S, Walker A (2013). An Australian pyro-tornadogenesis event, Journal of the International Society for the Prevention and Mitigation of Natural Hazards, 65(3), pp. 1801-11.

Richards PJ, Hoxey RP, Short LJ (2001). Wind pressures on a 6 m cube, Journal of Wind Engineering & Industrial Aerodynamics, 89(14), pp. 1553-64.

Whittaker J, Haynes K, Handmer J, McLennan J (2013). Community safety during the 2009 Australian 'Black Saturday' bushfires: an analysis of household preparedness and response, International Journal of Wildland Fire, 22(6), pp. 841-9.

Proc. 1st International Conference on Structural Engineering Research (iCSER 2017)
20-22 Nov 2017, Sydney, Australia
ISBN: 978-0-6480147-6-8

Base Isolation Systems in Multi-Storey Structures

Keoagile Kerileng[1] and Morgan Dundu[2]

[1]Botswana International University of Science and Technology,
Department of Civil and Environmental Engineering
Private Bag 16, Palapye, Botswana
Email: kerilengk@biust.ac.bw
[2]University of Johannesburg, Department of Civil Engineering Science,
P O Box 524, Auckland Park, 2006, South Africa
Email: mdundu@uj.ac.za

Abstract

Base isolation (BI) systems have been found to be effective tools to safeguard multi-storey buildings and other structures from severe earthquake excitations. It requires the structure to be separated from the ground by isolation devices which can dissipate energy. This is proven technology which may add a little to the initial cost of the building, but will prove to be less expensive in the long term. Base isolation technology introduces flexibility into the connection between the structure and the foundation. In addition to allowing movement, the isolators are often designed to absorb energy and thus add damping to the system. Furthermore reduces the seismic response of the building and also enables a building or non-building structure (such as a bridge) to survive a potentially devastating seismic impact, following a proper initial design. This study discusses the concept of base isolation and reviews existing base isolation systems

Keywords: Base isolation systems, Multi-storey buildings, Earthquake excitations, Mitigation, seismic risk, Three degrees of freedom.

1. INTRODUCTION

Structures respond to earthquake ground shaking in different ways. When the forces on a building or the displacement of the building exceeds certain limits, damage is incurred in different forms and to different extents. If a brittle building is designed to respond elastically with no ductility, it may fail when the ground motion induces a force that is more severe than the building strength. On the other hand, if the building is designed with ductility, it will be damaged but will still be able to weather severe ground shaking without failure. Since the motion of earthquakes is vibrational in nature, the principle of vibration isolation can be utilised to protect a building (i.e., it is decoupled from the horizontal components of the earthquake ground motion by mounting isolation between the building and its foundation). Such a system not only provides protection to the building but also to its contents and occupants. Base isolation is a passive structural control technique where a collection of structural elements is used to substantially decouple a building from its foundations resting on shaking ground, thus protecting the building's structural integrity. For several decades, engineers have focused on ways of designing structures that are capable of withstanding earthquake effects. This was achieved by using diagonal bracing and installation of shear walls. Flexible buildings on the other hand use isolators and dampers to minimize the level of excitation (Morgan (2007)). Rigid techniques are preferred to flexible techniques because they are more mature. However, in the case of large-scale earthquake events, considerable inter-storey floor accelerations and drift of highly stiff buildings raises risks of brutal devastations.

2. CONCEPT OF BASE ISOLATION

Seismic action generates ground displacements, which are then transferred to the supports of the structure. As a result, the structure experiences deformations and accelerations, often larger than the one of the ground. Among the structural mitigating technologies available to earthquake is the base isolation technique. Base isolation decouples the structure vibration from the ground vibration, preventing most of the horizontal movement of the ground from being transmitted to the buildings (Figure 1). The base isolation technique is based on the principle that during earthquakes, the vibration natural period is shifted from a short time range to long time range, which effectively reduces the damaging effects. The most important feature of this technique is that it introduces elasticity into the connection between the foundation and the structure itself. Only a few devices can reduce both horizontal and vertical responses of structures at the same time (Lu & Lin (2008)).

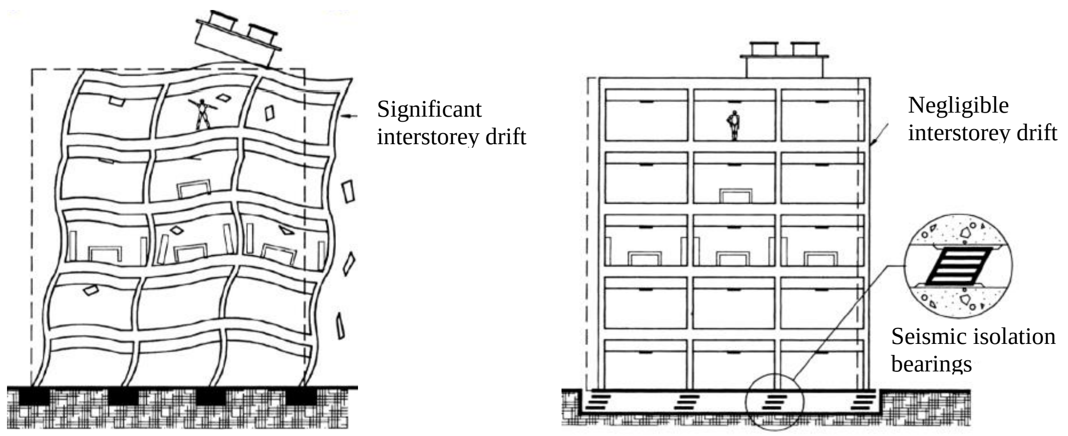

(a) Fixed base (b) Isolated base

Figure 1. Fixed base and isolated base (Lu & Lin (2008))

In a structure with fixed base, lateral deformations are distributed along the building height Multi Degree of Freedom (MDOF) system, whilst in a base-isolated structure lateral deformations are concentrated in the isolation devices, the structure behaving essentially as a SDOF system. Seismic isolation is achieved by inserting devices between the foundation and structure that has small lateral stiffness (increases period), large vertical stiffness and large damping. A base-isolated structure has a substantially larger period of vibration than a structure with fixed base (Figure 2 (a)). The effect of increasing the period is to reduce accelerations (and related forces) and increase displacements. To reduce displacements, it is important that the isolating device can offer significant damping (Figure 2 (b)).

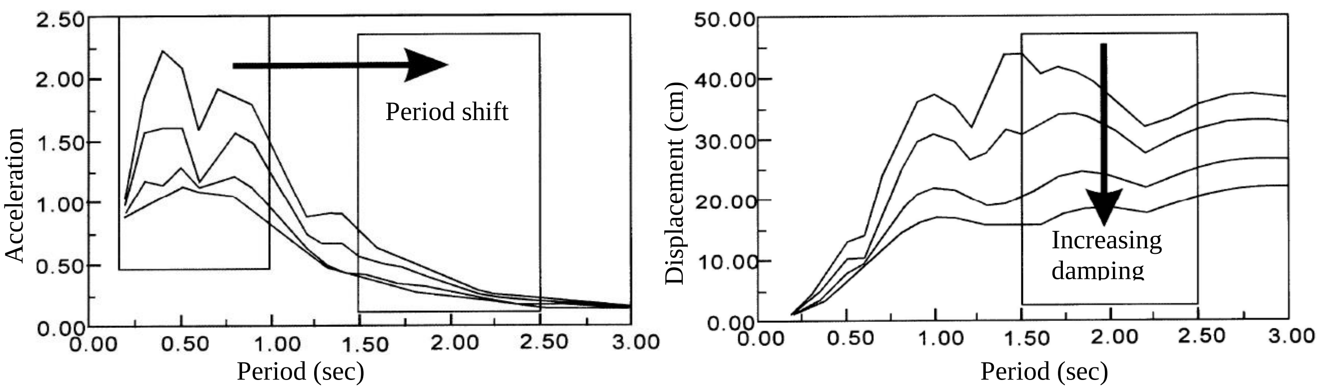

(a) Period shift (b) Increasing damping

Figure 2. Principles of seismic isolation

Base isolation is efficient in rigid structures (low-rise and medium-rise buildings), with periods of vibration below 1 sec. Using isolator devices, the period can be increased to 1.5-2.5 seconds, which is an important reduction of seismic forces induced in the structure. High-rise buildings have large period of vibration, their design being often governed by wind loading. Base isolation is efficient for structures with a low ratio between the height and largest dimension of the building. Overturning leads to difficulties in operation and design of isolators in high-rise structures.

3. A BRIEF HISTORY OF BASE ISOLATION SYSTEMS

Although the first patents for base isolation were in the 1800's, and examples of base isolation were claimed during the early 1900's (e.g. Tokyo Imperial Hotel) it was the 1970's before base isolation moved into the mainstream of structural engineering. Isolation was used on bridges from the early 1970's and buildings from the late 1970's. Bridges are a more natural candidate for isolation than buildings because they are often built with bearings separating the superstructure from the substructure. The first bridge applications added energy dissipation to the flexibility already there. The lead rubber bearing (LRB) was invented in the 1970's and this allowed the flexibility and damping to be included in a single unit. About the same time the first applications using rubber bearings for isolation were constructed. However, these had the drawback of little inherent damping and were not rigid enough to resist service loads such as wind.

In the early 1980's developments in rubber technology lead to new rubber compounds which were termed "high damping rubber" (HDR). These compounds produced bearings that had a high stiffness at low shear strains but a reduced stiffness at higher strain levels. On unloading, these bearings formed a hysteresis loop that had a significant amount of damping. The first building and bridge applications in the U.S. in the early 1980's used either LRBs or HDR bearings.The development of the friction pendulum system (FPS) shaped the sliding bearing into a spherical surface, overcoming this major disadvantage of sliding bearings. As the bearing moved laterally it was lifted vertically. This provided a restoring force. Although many other systems have been promulgated, based on rollers, cables etc., the market for base isolation now is mainly distributed among variations of LRBs, HDR bearings, flat sliding bearings and FPS.

3.1. Elastomeric Bearings

The base isolation system that has been adopted most widely in recent years is typified by the use of elastomeric bearings, where the elastomer is made of either natural rubber or neoprene. In this approach, structure is decoupled from the horizontal components of the earthquake ground motion by interposing a layer with low horizontal stiffness between the structure and the foundation. Elastomeric bearing comprises of bonded alternating rubber and steel layers, as shown in Fig 3 (a), and is most common base isolation system to date. The steel layer keeps the rubber layer from bulging laterally and provides the rigidity so that the bearings can support high vertical loads in bridges and buildings, whilst the rubber layer, which is made out of either natural rubber or synthetic rubber (such as neoprene) provides the required flexibility when subjected to horizontal loads. Elastomeric bearing allow the super-structure to move significantly during earthquake motions without facing any form of disfigurement. Since elastomeric bearings experience consistent expansion and contraction they may require constant replacement. The pads used for the elastomeric bearings are made of laminated steel. Elastomeric bearing can be damaged through tearing of rubber under severe earthquake. The bearing force generated by lead rubber bearing can be represented by Equation 1.

$$F_b = C_b \dot{U}_b + \alpha_b K_b U_b + F_z \tag{1}$$

where, C_b is the damping coefficient , $\dot{U}_b$ is the velocity, α_b is computed by the following expression $\alpha_b = \alpha_b^2 m_t q / f_y$, f_y is yield strength of the isolator, K_b is the stiffness, U_b is the displacement, $F_z = (1-\alpha_b) f_y q z_b$ is the restoring force as a result of presence of lead core , α_b is computed by the following expression $\alpha_b = \alpha_b^2 m_t q / f_y$, f_y is yield strength of the isolator, m_t is the mass of the superstructure, q is characteristics strength of the lead core and z_b is the non-dimensional hysteretic displacement component. Due to low critical damping (typically 2%-3%), elastomeric bearings have little resistance to service load, and additional damping devices are required in order to control higher lateral displacement. Elastomeric bearings has a relatively low manufacturing cost compared to other types of bearings, their mechanical properties are independent of temperature and aging and do not exhibit creep under long-term loading.

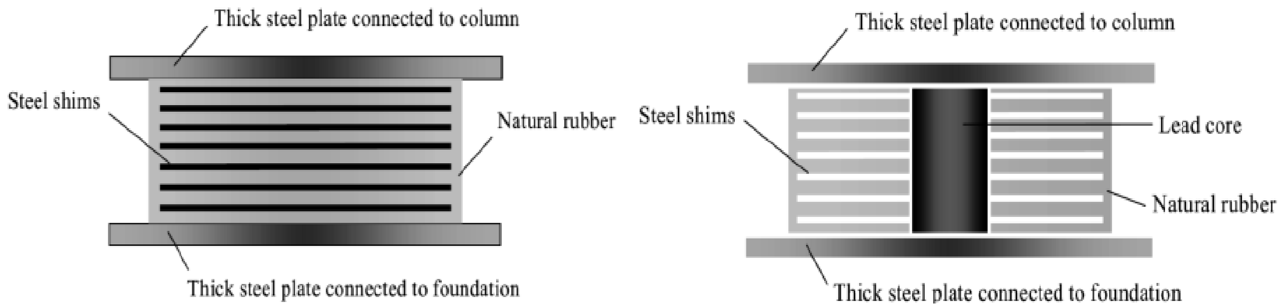

(a) Elastomeric bearing (b) Lead-rubber bearing

Figure 3. Elastomeric and lead-rubber bearing

3.2. Lead-rubber bearings

Lead-plug bearings are fabricated by plugging a lead core into the elastomeric bearing. The solid plug in the middle absorbs energy and adds decamping (Jung, Eem, Jang, & Koo (2011)), while natural rubber is useful in facilitating flexibility through its ability to move and return to its normal position. The performance of the lead-plug bearing depends on the imposed lateral force. If the lateral force is small, the movement of the steel shims is restrained by the lead core, and the bearing displays higher lateral stiffness. As the lateral force becomes larger, the steel shims force the lead core to deform or yield, and the hysteretic damping is developed with energy absorbed by the lead core. The equivalent damping of the lead-plug bearing varies from 15% to 35%.

3.3. Sliding systems

A sliding system is a combination of levers that allow two adjacent solids slide past each other or on each other with minimum friction (Usman et al (2009)). This system is based on the hypothesis that the lower the friction coefficient, the less the shear transmitted [2]. The horizontal frictional force offers resistance to motion and dissipates energy. For sliding to occur the intensity of exciting force must be more than frictional force of isolator. The technology of sliding systems was applied in the United States of America at the start of the 20th century. Many wooden structures in America are developed with a three-layered base that comprises the foundation (concrete), a sliding steel system, and a floor on top of it. The sandwiched steel base allows the house to sway from side to side during relatively strong quakes and indeed holds the structure intact [28]. The movement involves little inertia with minimal implications for occupants (house) and users (bridge), and thus is often unnoticed. Sliding systems are also used in bridges to allow the bridge withstand strong winds and tremors, however, it is not easy to apply these systems in structures that carry a lot of weight. If effectively applied, the swinging or sliding of the structure effectively minimizes the susceptibility of a structure to shear and thrust forces (Usman et al (2009)). Due to the fact that they tend to shake earlier than most of the structures under a quake, they are effective base-isolation systems. Sliding systems are nonetheless dangerous where the structure is old (over 5 decades) as it may have loose bolts that may give way in the wake of tremors.

3.4. Friction Pendulum

A similar system is the Friction Pendulum Bearing (FPB), another name of Friction Pendulum System (FPS). It is based on three aspects: an articulated friction slider, a spherical concave sliding surface, and an enclosing cylinder for lateral displacement restraint (Zayas, 1990). The bearing material of the friction pendulum is provided in between the base and the slider, and it is hardly used separately from sliding systems and elastomeric bearings. The principle of the friction pendulum is that during an earthquake, the slider slides over a concave surface so as to provide the isolation. To facilitate easy sliding, the spherical surface is normally coated with Teflon of approximately 3% friction coefficient. At the end of earthquake, the slider moves back to its original position under action of gravitational force, due to concavity of the base, thereby restoring the structure at its original position and minimizing residual displacement. During an earthquake, the slider moves on the spherical surface lifting the structure and dissipating energy by friction between the spherical surface and the slider. Increasing the sliding period reduces the base shear and increases the displacement, and decreasing the friction coefficient reduces the base shear and increases the displacement. Thus the friction coefficient should be such that it should provide enough rigidity as well as the isolation by shifting the effective period from the duration of pulses. The main limitation of this system is that it is designed for a specific level (intensity) of ground excitation, since the spherical surface has a constant time period, which solely depends upon the radius of curvature. In addition, if the excitation period and isolator period coincides then the friction pendulum system faces the problem of resonance (Weisman & Warn (2012)).

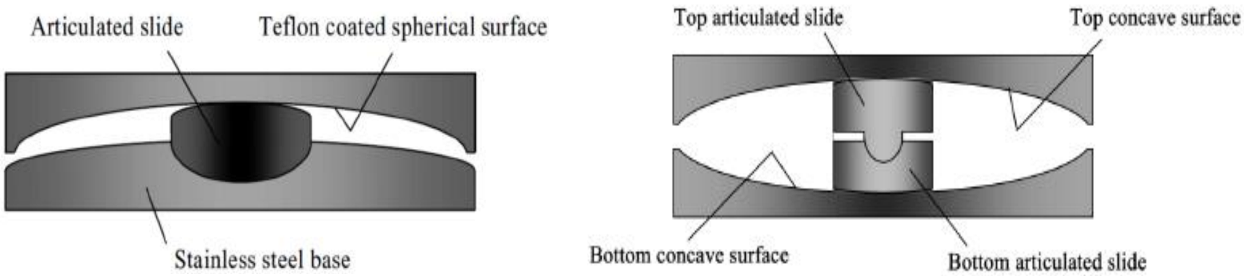

Figure 4. Friction pendulums

Pendulum systems (friction pendulums) are difficult to construct and quite expensive to maintain. The measurements concerning the particular angles of tilt, the pulley structures as well as the general design of the material such as weight specifications and the handling of the CoG (Centre of Gravity) makes it among the most expensive base isolation structures[43]. Figure 2.2 presents an illustration of the friction pendulum concept that is utilized in base isolation of buildings

3.5. Pot Bearings

Pot bearings have been applied mostly in bridges to restrict both vertical and horizontally induced motion. These bearings can accommodate very high loads of up to over 45 000 kN. In a pot bearing an encased natural rubber pad is placed in a steel pot under high pressure which makes the pad work like a liquid. The flexibility of the rubber facilitates tilting of the piston along the horizontal axis (Rabiei & Khoshnoudian (2011)). The entire structure of the pot bearing is detachable since parts require occasional repair and replacement.

4. CONCLUSION

This paper discusses the concept of base isolation and reviews existing base isolation systems. Most of the base isolation systems reviewed can absorb earthquake energy in 2 dimensions. In conclusion, the friction pendulum is observed to be the only base isolation that is capable is absorbing earthquake energy in both three principal directions. The observed research results , it shows that the structural deformations going into the inelastic/plastic range and the consequent is likely to be completely eliminated in FPS, and the structure needed to to designed for much smaller acceleration. In addition, the relative sotrey displacement (drifts) tend to be reduced hence less damage to walls, cladding etc is minimized or eliminated. Also the response acceleration at higher floors tends to be reduced much hence the damage are minimized. Investigation on this aspect are still on-going, as 3-dimensional systems are new technologies for absorbing earthquake energy.

5. REFERENCES

Ariga, T, Kanno, Y &Takewaki I (2006), "Resonant behaviour of base isolated high-rise buildings under long-period ground motions". *Structural Design Tall Special Buildings*, 15, pp 325-338.

Cheng, F, Jiang H & Lou, K (2008), "Smart structures, innovative systems for seismic response control," *CRC Press*. pp 672-680.

Contento, A& Di Egidio, A (2009),"Investigations into the benefits of base isolation for non-symmetric rigid blocks".*Earthquake Engineering & Structural Dynamics*, *38*(7),pp 849-866.

Elgamal, A, Yan, L, Yang, Z, & Conte, J. P (2008),"Three-dimensional seismic response of Humboldt Bay bridge-foundation-ground system".*Journal of Structural Engineering*, *134*(7),pp 1165-1176.

Fenz, D.M & Constantinou, M.C (2008),"Spherical sliding isolation bearings with adaptive behavior: Theory", *Earthquake Engineering and Structural Dynamics,* 37(2): pp163-183.

Jung, H. J, Eem, S. H, Jang, D. D & Koo, J. H (2011),"Seismic performance analysis of a smart base-isolation system considering dynamics of MR elastomers". *Journal of Intelligent Material Systems and Structures*, *22*(13), pp1439-1450.

Kaptan, K (2013), "Seismic base isolation and energy absorbing devices".*European Scientific Journal*, (18), pp41-45.

Kouadio, IK, Aljunid, S, Kamigaki, T, Hammad, K & Oshitani, H 2012, "Infectious diseases following natural disasters: prevention and control measures", *Expert review of anti-infective therapy*, vol.10, no.1, pp.95-104.

Lu, L& Lin, G.L (2008), "Predictive control of smart isolation system for precision equipment subjected to near-fault earthquakes". *Eng. Struct.*, 30: pp3045-3064.

Lu, L, Lin, G & Kuo, T (2008), "Stiffness controllable isolation system for near-fault seismic isolation". *Engineering Structures*, *30*(3), pp 747-765.

Ming, L, Xuemin, T, Duguo, W &Liyuan, L. (2006), "Research and application of building structure base isolation technology".*Journal ofTechnology for Earthquake Disaster Prevention*,(1),pp4-12.

Monfared, H, Shirvani, A &Nwaubani, S (2013), "An investigation into the seismic base isolation from practical perspective".*International Journal Of Civil & Structural Engineering*, (3), pp451-464.

Morgan, T. A (2007), *The use of innovative base isolation systems to achieve complex seismic performance objectives*. ProQuest.

Narasimhan, S &Nagarajaiah, S (2005), "A STFT semiactive controller for base isolated buildings with variable stiffness isolation systems". *Engineering structures*, *27*(4), pp514-523.

Oliveto, N. D, Scalia, G &Oliveto, G (2010),"Time domain identification of hybrid base isolation systems using free vibration tests".*Earthquake Engineering & Structural Dynamics*, *39*(9),pp1015-1038.

Rabiei, M &Khoshnoudian, F (2011), "Response of multistorey friction pendulum base-isolated buildings including the vertical component of earthquakes". *Canadian Journal Of Civil Engineering*, *38*(10), pp1045-1059

Proc. 1st International Conference on Structural Engineering Research (iCSER 2017)
20-22 Nov 2017, Sydney, Australia
ISBN: 978-0-6480147-6-8

Fire Resistance of Fly Ash-Based Geopolymer Concrete Blended with Calcium Aluminate Cement

Yifang Cao[1], Zhong Tao[1], Zhu Pan[1], Timothy Murphy[2] and Richard Wuhrer[2]

[1] Centre for Infrastructure Engineering, Western Sydney University, Penrith, NSW 2751, Australia
[2] Advanced Materials Characterisation Facility, Western Sydney University, Parramatta, NSW 2116, Australia
Corresponding author's E-mail: Z.Pan@westernsydney.edu.au

Abstract

Geopolymer has been known as an eco-friendly alternative to Portland cement-based concrete. Geopolymer concrete usually uses alkali-activated fly ash as the binder, and develops desirable strength within 8 hours when a heat-curing regime is used. Due to its ceramic-like properties, geopolymer concrete is believed to have high fire resistance. When heat-cured geopolymer concrete is exposed to high temperatures, a strength gain is often reported. However, the heat-curing procedure limits the future of geopolymers for on-site applications. To solve this issue, suitable additives (e.g., ground granulated blast-furnace slag and calcium aluminate cement) can be used in the binder which can develop the desirable strength of geopolymer concrete. It is important to understand the high-temperature performance of ambient-cured geopolymer concretes which have received little attention. This paper presents a study on the high-temperature performance of fly ash-based geopolymer concrete cured at ambient temperature. Compression tests were carried out on geopolymer mortars at temperatures of 23, 600 and 800 °C. As an outcome from this work, the authors have proposed a geopolymer concrete mixing design based on the parameter analysis, and the fire performance of the geopolymer concrete are compared with that of the reference OPC concrete at different temperatures.

Keywords: CAC, Fire resistance, Geopolymer, Concrete.

1. INTRODUCTION

Concrete has been known as a fire-resistant material. Conventional concrete contains ordinary Portland cement (OPC) as a binder material. However, the binder of conventional concrete suffers severe damage under fire conditions. Due to increasing population, high rise buildings have become prevalent in megacities. Extremely high residential density has increased the probability of fire hazard as well as the severity of consequence. The threat of fire has raised the interest into studies on fire-resistant binders as such geopolymer has been considered as a promising alternative to OPC in construction applications.

At 100–200 °C, the free water evaporation causes the mass loss of OPC binder. For the OPC binder, the strength loss starts to fleet after approximately 400 °C. The dehydration and decomposition of C-S-H gel and other hydrates under high temperatures are probably responsible for failure of OPC binders (Seleem, Rashad & Elsokary 2011). The hydrated OPC contains a considerable amount of $Ca(OH)_2$ which releases water after 400 °C, and this water-release reaction causes the volume to expand which is responsible for the spalling phenomenon of OPC concrete at high temperatures from 350 to 450 °C (Guerrieri & Sanjayan 2010). The thermal response of OPC is evaluated by performance-based fire engineering method which

has been widely adopted among the world (Wang et al. 2012), and the strength reduction of normal weight concrete is supposed to be 85% after 800 °C exposure in the performance-based design method.
Ceramic-like properties of alkali aluminosilicate materials are the reason why some geopolymer binders exhibited better fire performance than OPC. The properties of geopolymers are dependent on compositions of raw material. Regarding compositions, Al_2O_3, SiO_2, and the calcium content have an important role in determining the mechanical properties and fire performance. In Australia, the majority of fly ash produced is low calcium (class F) fly ash. The low calcium content leads to slow strength development at ambient temperature. Thus, elevated temperature curing regime was used to improve the mechanical properties of geopolymer in former researches (Mendes, Sanjayan & Collins 2008), (Pan, Sanjayan & Rangan 2009). The heat curing procedure inhibits the application of geopolymer in the construction industry. Some researchers have found the addition of calcium aluminate cement (CAC) (Cao et al. 2016), OPC (Nath & Sarker 2015) or ground granulated blast-furnace slag (GGBFS) was able to improve the mechanical properties at ambient temperature (Khan et al. 2016). These three additions are considered as a solution for curing geopolymers at ambient temperature. However, the addition of OPC introduced the hazard of spalling into geopolymer under high temperature, while the GGBFS blended geopolymer was reported to have strength decrease when exposure to temperatures of 50 °C and above (Jambunathan et al. 2013). In contrast, CAC is known for its high early strength and fire performance. The mechanical properties of geopolymer blended with CAC at ambient temperature have been studied by the authors in the former paper (Cao et al. 2016). The study of using geopolymer blended with CAC in fire-resistance application will be conducted in this paper.

To the Authors' best knowledge there has been no reported literature on the fire resistance of fly ash-based geopolymer blended with CAC. In order to investigate fire performance of geopolymer, the hot strength of geopolymer mortar tested at 600 and 800 °C are reported in this paper. The crack patterns of geopolymer under fire are compared to typical failure pattern proposed by ASTM, C (1996). Influence of three different factors including activator concentration, CAC replacement ratio and activator to binder ratio on the hot strength of geopolymer is analysed. Based on results obtained in mortars, one optimised mix has been selected for casting concrete. The fire performance of this geopolymer concrete mix is compared with OPC concrete at 23, 200, 400, 600 and 800 °C.

2. MATERIALS AND EXPERIMENTS

2.1 Materials

The raw materials used in mortar mixing were divided into three parts (activator, binder and sand). Activator was uniform solution composing of sodium hydroxide, tap water and sodium silicate. The majority of the binder was low calcium fly ash from a power plant in Victoria, and 5-20% of fly ash by mass was replaced by CAC. Locally available river sand which fits the grading curve was used by ASTM (2003). Nine (No. 1 to No. 9) mixing designs were made based on three different factors at three levels. The mixture design was shown in Table 1. The mixture No. 10 was concrete mixing design which used lime stone as coarse aggregate, and the maximum nominal size was 20 mm which fits the grading curve suggested in the ASTM (2003).

The binder materials include fly ash, CAC and OPC (ASTM type I cement) of which chemical compositions are shown in Table 2. The SiO_2 content of fly ash was the major, followed by Al_2O_3. The sum of the oxides Al_2O_3+SiO_2+Fe_2O_3 was more than 70% while the content of CaO was only 2.8%. The CAC used in geopolymer has an alumina content of around 68.5%. The alumina and calcium contents of fly ash were improved by replacing fly ash with 5% to 20% CAC. Geopolymers made with fly ash blended with CAC does not require heat curing for strength development.

Table 1. Mixture proportions (kg/m^3).

Mixture No.	Activator			Binder		Sand	Lime stone	Extra water
	NaOH pellet	Water	Sodium silicate	Fly ash	Calcium aluminate cement			
1	40.7	89.0	324.3	1232.4	64.9	648.6	-	-
2	45.3	99.0	360.9	1136.8	126.3	631.6	-	-
3	49.7	108.6	395.6	984.6	246.2	615.4	-	-
4	52.1	92.2	360.9	1200.0	63.2	631.6	-	-
5	57.1	101.1	395.6	1107.7	123.1	615.4	-	-
6	46.8	82.9	324.3	1037.8	259.5	648.6	-	-
7	63.9	94.3	395.6	1169.2	61.5	615.4	-	-
8	52.4	77.3	324.3	1167.6	129.7	648.6	-	-
9	58.3	86.0	360.9	1010.5	252.6	631.6	-	-
10	21.1	31.1	130.3	467.9	52.1	586.3	1080.2	31.1

Table 2. Chemical compositions by X-Ray Fluorescence of binder materials.

Constituent (%)	Al_2O_3	SiO_2	Fe_2O_3	CaO	MgO	SO_3	K_2O+ Na_2O
Fly ash	30.5	48.3	12.1	2.8	1.2	0.3	0.6
CAC	68.5	0.8	0.4	31	0.5	0.3	0.5
OPC	4.7	19.9	3.4	63.9	1.3	2.6	0.7

2.2 Specimen preparation

Three factors (activator concentration, CAC replacement ratio and activator to binder ratio) at three levels were investigated with nine mixture designs. These three factors were designed from the knowledge of preliminary experiments. The sodium silicate to sodium hydroxide ratio was kept constantly at 2.5 which was an optimised value concluded in the former research (Cao et al. 2016). The key factors of the nine mixture designs are shown in Table 3.

Table 3. Experimental factors.

Level	**Experimental factors**		
	Activator concentration	CAC replacement ratio	Activator to binder ratio
1	10 M	5%	35%
2	12 M	10%	40%
3	14 M	20%	45%

The alkali activators were prepared 24 hours before the geopolymer mortar mixing. The sodium hydroxide pellets were dissolved into tap water to form uniform solution. After the sodium hydroxide solutions cooled down to room temperature, the sodium silicate, known as grade D water glass, was added into the sodium hydroxide solutions and mixed and stored in corrosive chemical cabinet 24 hours before the casting of geopolymer.

The binders and sand were dry-mixed in a mixer for 3 minutes before the alkali activator was added into the mixer. The mixing proceeded for 6 minutes until the mixture formed homogenous slurry. The fresh mortar was casted into 60 × 180 mm cylinder moulds in three layers. A vibrating table was working all the process of casting fresh mortar into moulds. Each layer was kept vibrating for 15 seconds to 30 seconds to chase the bubbles out. The specimens were demoulded after one day and then they were cured at room temperature constantly. A CIVILAB core facing grinder was employed to grinder both ends of each cylinder to get smooth and flat surfaces.

2.3 Testing method

After 28 days of curing, compression tests and fire performance tests were conducted. The concrete cylinders were tested with an INSTRON 8036 universal testing machine in accordance with the requirement in ASTM, C (1996). The loading rate was 0.25 ± 0.05 MPa/s. The testing was conducted in Structural Research and Testing Laboratory at Western Sydney University in which the temperature was constantly around 23 °C. The cross-sectional area of each cylinder was measured to calculate the stress.

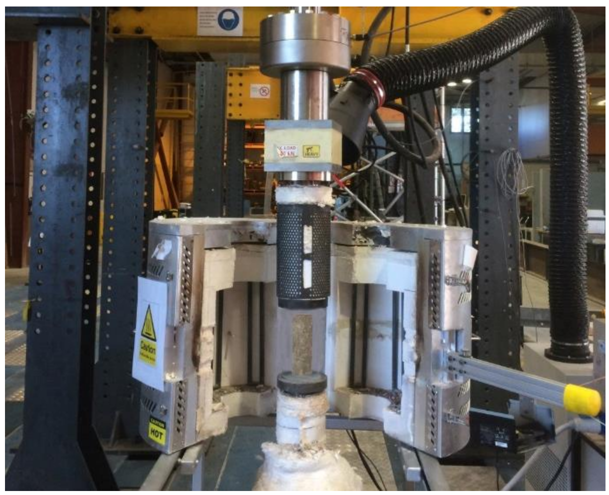

Figure 1. Vertical tube furnace

A vertical electric tube furnace, as shown in Figure 1, was employed to heat the specimens. A hydraulic loading jack which had 1000 kN capacity was located at the top of the vertical tube furnace. The upper and lower holders were cast by 253MA high temperature stainless steel. The steel casing was installed after the cylinder sample was steadily put on the lower holder. Then, the furnace temperature was increased to the target temperature of 600 or 800 °C with a heating rate of 5 °C/min. To investigate the ultimate strength of geopolymer mortars in hot status, the hydraulic jack started loading when the furnace had held the target temperature for 2 hours. Two specimens were conducted in the same condition to get an average compressive strength. The furnace was cooled naturally to ambient temperature to avoid thermal shock.

3. RESULTS AND DISCUSSION

3.1 Visual appearance

The geopolymer specimen was dark grey in appearance after 28 days curing. After heating at 600 °C for 2 hours and cooled down, the colour had turned light grey, whereas at 800 °C the sample turned yellow ochre.

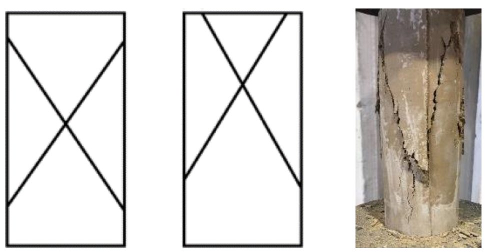

(a) Type 1

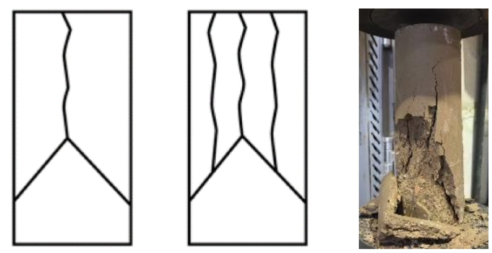

(b) Type 2

(c) Type 3

(d) Type 4

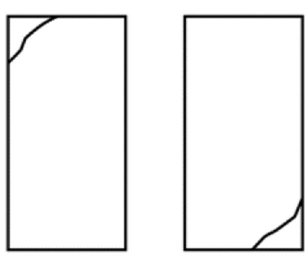

(e) Type 5

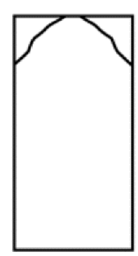

(f) Type 6

Figure 2. Typical fracture patterns of specimens subjected to elevated temperature exposure

The crack patterns of the specimens after compressive strength testing for high temperature exposure are presented in Figure 2. The crack patterns are compared with typical fracture patterns defined in ASTM, C (1996). Type 1 (reasonably well-formed cones on both ends, less than 25 mm cracking through caps) was found very common in geopolymer mortars. Type 2 (well-formed cone on one end, no well-defined cone on the other end, vertical cracks running through caps) was least common among the three fracture patterns appeared. Type 4 (Diagonal fracture with no cracking through ends; tap with hammer to distinguish from type 1) was the most common fracture pattern in geopolymer mortar specimens exposed to high temperature. No type 3 fracture pattern (columnar vertical cracking through both ends, no well-formed cones) was observed among all the specimens recorded. Neither type 5 nor type 6 fracture pattern was observed because the compression was conducted with bonded caps.

In conclusion, the fracture patterns of geopolymer mortar were easier to form cones or diagonal fracture. Vertical cracks were fewer than shear failure cracks to be observed.

3.2 Compressive strength

The results were calculated based on at least two samples after 28 days curing. A third specimen was tested if the deviation exceeded 5%. Table 4 shows the compression testing results of different geopolymer mortar mixes at 23, 600 and 800 °C. The average strength at ambient temperature was 79.4 MPa, while the strength tested at 600 and 800 °C were 33.0 MPa and 48.1 MPa, respectively. The compressive strength of geopolymer blended with CAC tested at high temperature was lower than its ambient temperature strength.

Geopolymer mortar exhibited ideal mechanical properties and fire resistance in general. After exposed to 600 °C for two hours, the strength of mortar specimens decreased by 58.4% on average, while geopolymer subjected to 800 °C decreased only 39.4% of ambient compressive strength. In temperature range of 600 to 800 °C, the geopolymer samples regained their strength, indicating a phase transformation taking place in this temperature range. Further research is required to provide evidence for such transformation.

At ambient temperature, the highest compressive strength achieved was 118.9 MPa in mix 8 which was two times more than the weakest mixture, mix 3. At 600 °C, the highest compressive strength was 49.5 MPa (mix 6), while the highest strength retain ratio was 87.3% (mix 9). The highest strength of specimens tested at 800 °C was 67.7 MPa (mix 8), and the best strength retain ratio was 91.5% (mix 4).

Table 4. Compressive strengths of geopolymer mortars at different temperatures

Mixture No.	**Mixture factors**			**Compressive strength (MPa)**		
	Activator concentration	CAC replacement ratio	Activator/binder ratio	23 °C	600 °C	800 °C
1	10 M	5%	35%	62.5	26.4	52.9
2	10 M	10%	40%	107.6	25.8	58.5
3	10 M	20%	45%	50.4	40.9	23.1
4	12 M	5%	40%	63.5	23.1	58.1
5	12 M	10%	45%	101.1	26.2	41.1
6	12 M	20%	35%	80.0	49.5	38.5
7	14 M	5%	45%	75.1	25.6	55.4
8	14 M	10%	35%	118.9	31.2	67.7
9	14 M	20%	40%	55.7	48.6	38.0

3.3 Parameter analysis on high temperature performance of geopolymer mortars

The variations of compression results regarding to the three key factors are shown in Figures 3–5. Most of the samples exhibit lower strength at 600 °C than that at 800 °C. However, geopolymers with 5% CAC at 600 °C had higher strength than 800 °C. In the following, parameter analysis is conducted by changing one factor while keeping other two factors consistent, where the compressive strength of heated geopolymer is referred to its ambient temperature strength. The test result of one level is the averaged compressive strength of 3 results, and three levels of other two parameters all appear once. For example, the compressive strength result of 12 M is calculated from mixing design Nos. 4, 5 and 6, while 14 M parameter is the averaged value of mixing design Nos. 7, 8 and 9.

3.3.1 Activator concentration

As shown in Figure 3 (a), the compressive strength of geopolymer mortar increased as the alkali activator concentration increased before fire exposure. Geopolymer specimens with 14 M concentration had higher compressive strength than others. At 800 °C, the strength increase of 14 M geopolymer was as high as 18.6% compared with 10 M and 12 M geopolymers.

Strength ratios of different geopolymer samples at specific temperatures were almost the same. The results in Figure 3 (b) show the strength of geopolymer decreased by 60% when heated to 600 °C, while the strength decrease was only about 40% for geopolymers heated at 800 °C.

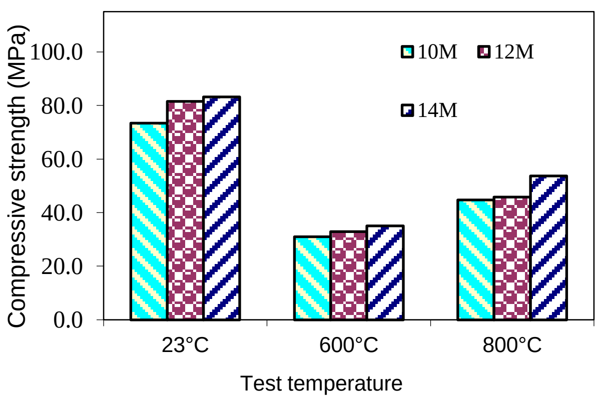

(a) Compressive strength vs. activator concentration

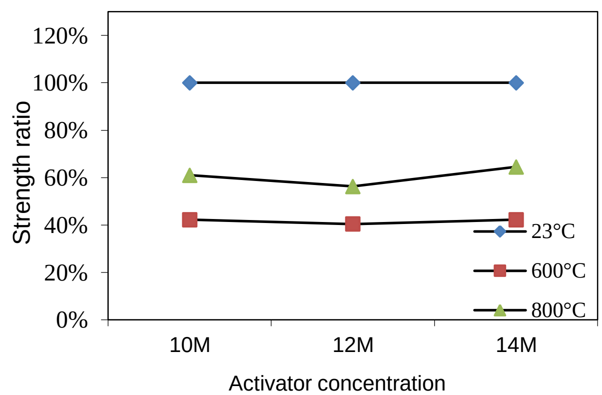

(b) Strength ratio vs. activator concentration

Figure 3. Influence of activator concentration

3.3.2 CAC replacement ratio

CAC replacement ratio is the most important parameter on the fire performance of geopolymer mortar, shown in Figure 4(a). The geopolymer mortar with 10% CAC exhibited highest compressive strength at ambient temperature. Geopolymer with 5% CAC had the lowest compressive strength under fire condition which was 25 MPa. The compressive strength of geopolymer at 800 °C was higher than strength at 600 °C when the CAC addition was 5%.

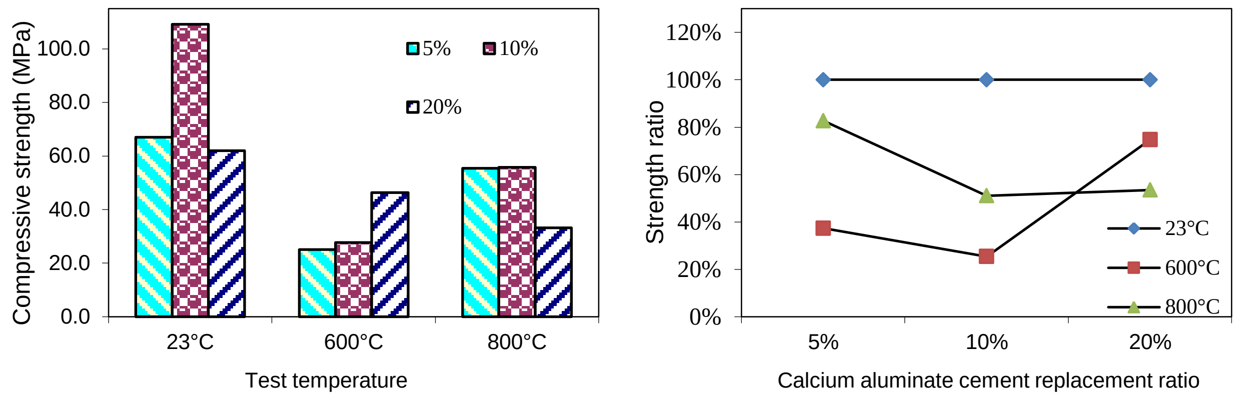

(a) Compressive strength vs. CAC replacement ratio

(b) Strength ratio vs. CAC replacement ratio

Figure 4. Influence of CAC replacement ratio

As can be seen from the results in Figure 4 (b), geopolymer with 20% CAC only decreased 15.3% in compressive strength at 600 °C, while 46.5% of strength was lost at 800 °C. The addition of 5% CAC improved the fire performance of geopolymer at 800°C which remained 82.7% compressive strength compared to the strength results tested at room temperature.

3.3.3 Activator to binder ratio

The increasing of liquid in geopolymer mortar caused the decreasing of strength at all temperatures. For specimens tested at 23 and 600 °C, the average strengths dropped 15.4% and 15.5% respectively when the activator content was increased from 35% to 45%. When the activator increased from 35% to 45%, the strength loss increased 33.0% for geopolymer exposed to 800 °C, as shown in Figure 5 (a).

Changing activator to binder ratio had negligible influence on strength ratio of geopolymers at 600 °C which was around 41% of that at ambient temperature, as shown in Figure 5(b). At 800 °C, the relative changes of strength for geopolymers with activator contents ranging from 35% to 45% were 60.7%, 68.2% and 52.8%, respectively.

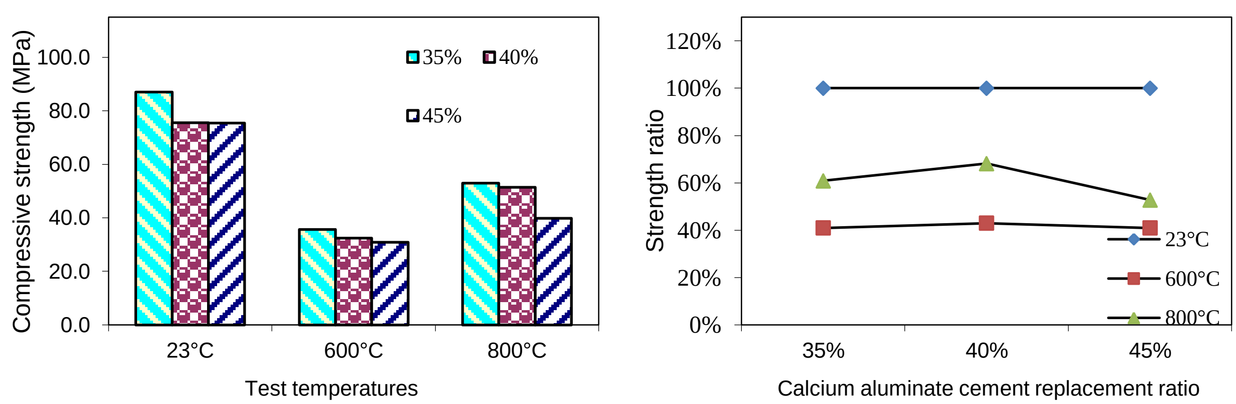

(a) Compressive strength vs. activator to binder ratio

(b) Strength ratio vs. activator to binder ratio

Figure 5. Influence of activator to binder ratio

3.4 Fire performance of concrete

Performance-based fire engineering design method requires a full analysis of structures. In order for geopolymer to be applied in construction, the material properties at elevated temperatures should be understood. However, many researchers reported only residual strength of small geopolymer samples (Hussin et al. 2015). In this section, the investigation of geopolymer concrete at temperatures ranging from 23 to 800 °C is conducted. Reference OPC concrete samples with similar strength have also been tested at the same conditions.

The key factors of geopolymer concrete mixing design are alkali concentration, CAC replacement ratio and activator to binder ratio. The 14 M alkali solution and 35% activator to binder ratio were chosen because high concentration geopolymer binder exhibited best fire performance and ambient performance. The CAC was added into geopolymer concrete with the ratio of 10%. Although the performance of this mix at 600 °C is not the best, the ambient strength is extremely high and the performance at 800 °C is reasonable. Extra water was added into geopolymer concrete mixing to improve the workability of fresh concrete.

As shown in Figure 6, CAC geopolymer concrete exhibited higher fire performance than the OPC concrete at all temperatures. The strength reduction of concrete was calculated by dividing the strength at the elevated temperature to the initial strength (at ambient temperature). By comparing the relative changes of strength, it is found that geopolymer had much higher strength over OPC at the temperatures of 200 and 800 °C. The strength decreasing at 200 °C was accounted for an increase in porosity caused by evaporation. The geopolymer also had a mild drop of strength at 400 °C which was possibly caused by the evaporation. At the temperature of 800 °C, the strength of geopolymer dropped slowly because of the ceramic-like property of matrix. Some researchers even reported strength gain of geopolymers at high temperature (Pan, Sanjayan & Rangan 2009). However, OPC concrete exposed to 800 °C suffered a severe decrease in the mechanical properties which was accounted for the chemical decomposition of its matrix.

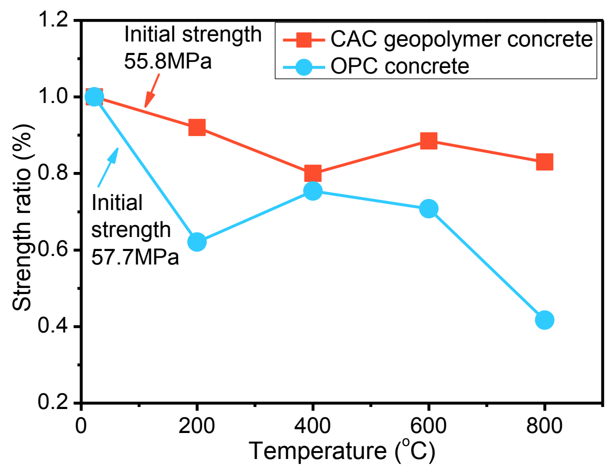

Figure 6. Fire performance of concrete

In conclusion, geopolymer concrete exhibited better fire performance than OPC concrete among the whole range of temperatures. This was accounted for the matrix of geopolymer which was much more stable and durable than OPC.

4. CONCLUSIONS

This research investigated the feasibility of using geopolymer to improve the fire performance of concrete. Nine mortar mixing designs were tested to conduct a parameter analysis of geopolymers at three different temperatures. Three parameters (activator concentration, CAC replacement ratio and activator to binder ratio) were analysed at three levels respectively.

1. The failure patterns of geopolymer mortars were investigated. The results showed geopolymer mortar mainly formed cones or diagonal fracture, while vertical cracks were seldom observed.

2. The influence of three parameters on the compressive strength of geopolymer mortar at elevated temperatures was studied. Geopolymer with the addition of CAC could achieve very high strength (118.9 MPa) before heating. This mix still had 67.7 MPa residual strength at 800 °C. CAC addition among all three factors is the most important factor on the fire performance of geopolymer.

3. The fire performance of geopolymer concrete was studied by comparison with OPC concrete with the same aggregates except for the binder. Geopolymer concrete blended with CAC exhibited better fire endurance than OPC concrete at all tested temperatures. This is due to the fact that the matrix of geopolymer concrete was much stable and endurable than the matrix of OPC concrete.

5. ACKNOWLEDGEMENTS

The mechanical testing was conducted in Structural Research and Testing Laboratory at Western Sydney University (WSU). The authors wish to acknowledge the technical support from the laboratory manager Mr. Robert Marshall and laboratory staff Mr. Murray Bolden. The access to the WSU Advanced Materials Characterisation Facility (AMCF) and the assistance of Dr Shamila Salek are also greatly appreciated.

6. REFERENCES

ASTM (2003), *C09. ASTM C33-03, Standard Spesification for Concrete Agregates*, ASTM International.

ASTM, C (1996), '39, Standard test method for compressive strength of cylindrical concrete specimens', *Annual book of ASTM standards*, vol. 4.

Guerrieri, M & Sanjayan, JG (2010), 'Behavior of combined fly ash/slag - based geopolymers when exposed to high temperatures', *Fire and materials*, vol. 34, no. 4, pp. 163-75.

Hussin, M, Bhutta, M, Azreen, M, Ramadhansyah, P & Mirza, J (2015), 'Performance of blended ash geopolymer concrete at elevated temperatures', *Materials and Structures*, vol. 48, no. 3, pp. 709-20.

Jambunathan, N, Sanjayan, JG, Pan, Z, Li, G, Liu, Y, Korayem, AH, Duan, W & Collins, F (2013), 'The role of alumina on performance of alkali-activated slag paste exposed to 50° C', *Cement and Concrete Research*, vol. 54, pp. 143-50.

Khan, M, Shaikh, F, Hao, Y & Hao, H (2016), 'Workability and compressive strength properties of high strength geopolymer mortars', in *Mechanics of Structures and Materials: Advancements and Challenges*, CRC Press, pp. 393-400.

Mendes, A, Sanjayan, J & Collins, F (2008), 'Phase transformations and mechanical strength of OPC/Slag pastes submitted to high temperatures', *Materials and Structures*, vol. 41, no. 2, p. 345.

Nath, P & Sarker, PK (2015), 'Use of OPC to improve setting and early strength properties of low calcium fly ash geopolymer concrete cured at room temperature', *Cement and Concrete Composites*, vol. 55, pp. 205-14.

Pan, Z, Sanjayan, JG & Rangan, B (2009), 'An investigation of the mechanisms for strength gain or loss of geopolymer mortar after exposure to elevated temperature', *Journal of materials science*, vol. 44, no. 7, pp. 1873-80.

Seleem, HEDH, Rashad, AM & Elsokary, T (2011), 'Effect of elevated temperature on physico-mechanical properties of blended cement concrete', *Construction and Building Materials*, vol. 25, no. 2, pp. 1009-17.

Wang, Y, Burgess, I, Wald, F & Gillie, M (2012), *Performance-based fire engineering of structures*, CRC Press.

ISBN: 978-0-6480147-6-8

Influence of Boundary Condition on Cold-Formed Column-Channel Bases Subjected to a Moment and Axial Load

Saeid Sheikholarefin Bafghi[1] and Morgan Dundu[2]

[1]PhD Student, University of Johannesburg, Johannesburg, South Africa
[2]Professor, University of Johannesburg, Johannesburg, South Africa
Corresponding author's E-mail: ssheikholarefin@uj.ac.za

Abstract

The aim of this study is to explore the initiation of stress concentrations around the base connections of columns made of cold-formed channels, and its influence on the combined ultimate axial and flexural capacity. Recent numerical studies on columns under axial load showed that welding the column's flanges and/or web to the base plate causes significant stresses at the edges of the flange and web elements, which leads to premature failure of the column. In this paper, a finite element model of several cold formed lipped channel cross sections, connected rigidly to the base through the web only, flanges only and web and flanges only, is developed to create different boundary conditions at the bottom of the column. The models are subjected to axial load, and combined axial and moment through an eccentrically applied load. The study is extended to include the effect of the end distance of the welds on the capacity of the column.

Keywords: Cold-formed, Column, Base Connection.

1. INTRODUCTION

The use of cold-formed members as the main frames has made it possible to achieve optimum design and construction of industrial buildings, which are composed entirely of cold-formed sections. The advantages of thin walled sections, such as light weight, easy constructability and durability are the reasons for growth in this field. Portal frames as the premier part of industrial sheds have been investigated by Zaharia and Dubina (2006) and Lim et al. (2016). Dundu and Kemp (2006a,b) has studied a full-scale moment resistant frame of cold-formed lipped channels with connected webs at the joint. The channels at eaves were positioned back-to-back and bolted on the web. Although this study was concerned with the ductility of the connection, it also demonstrated acceptable performance of the back-to-back connection in terms of the control of the torsion and simplicity of the joint. Later Dundu (2012) conducted a set of experimental tests on base connections of single lipped channels. The columns were connected to the base either through flanges, web or both using cold-formed and hot-rolled angle cleats, and it was observed that base connectors fabricated from hot-rolled angle cleats could support columns subjected to axial load and moments, because of their rigidity.

Investigations by Kwon, Chung and Kim (2006) and Zhang, Rasmussen and Zhang (2015) focused on cold-formed portal frames with pitched roofs, and reported the effect of the eaves and apex connections as well as instability due to using slender members. Öztürk and Pul (2015) has performed experimental and numerical studies on the back-to-back connected rafters and showed the effect of stiffener plates on local and flexural buckling of the member. The current study investigates the behaviour of a cold-formed lipped channel bases, as part of a portal frame, which is connected back-to-back at the top (Dundu and Kemp (2006a,b)).

2. STRUCTURAL CONFIGURATION OF THE BASE

A total of 108 numerical model of cold-formed lipped channel columns were performed. In order to investigate the effect of the base connection assembly on the column capacity, three boundary conditions of the column's base were considered (Figure 1). The first category consists of columns that were welded to the base through flanges only (Figure 1(a)), while the other elements of the cross section such as web, lips and corners were free. The length of the weld was set equal to the flat part of the flange and a weld size of 5 mm. The second category consists of lipped channels that were welded to the base through the flat part of the web with the same size of the weld (Figure 1(b)). The last category comprises of cold-formed columns with both flanges and web welded to the base (Figure 1(c)). Preliminary unpublished work revealed that when a cold-formed lipped channel cross-section is partially connected to the base and the connected area is located at the very end of the column, the capacity of the column under axial load will be affected by the excessive stress concentration and deformation of the area near the connection. Based on the results on this work, an end distance of 30mm was used for all models in this paper.

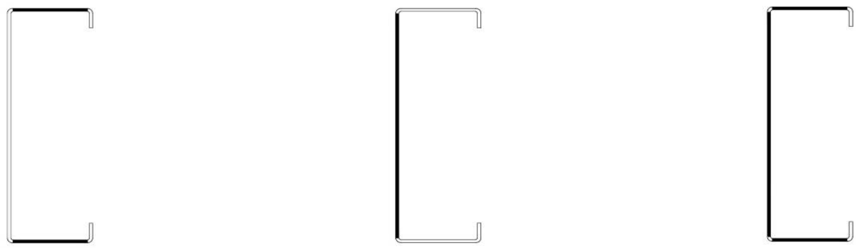

(a) Welded flanges **(b) Welded web** **(c) Welded flanges and web**

Figure 1 Boundary conditions at the column base

To study the effect of free elements of the cross-section on the base-connected part of the column, three different sizes of flanges of 50, 75 and 100mm and lips 15, 20, 25mm were considered. However, in order to apply a constant moment and have a criterion to compare the sections, the depth of the web, radius of corners and section thickness were set to the constant dimensions of 250, 10mm and 3 mm, respectively. The length of all columns was selected to be 1000 mm so that no overall buckling happens in the slenderest column. As proposed in the back-to-back connection of the channels, the load was applied at the web plane Dundu and Kemp (2006a,b). The load was applied at four points, namely; at the centre of the web (point P0), to simulate an axial load, at one-third of the web depth (point P1), at the edge of the section (point P2) and at a distance equivalent to the web depth from point P2 (point P3), as illustrated in Figure 2.

3. NUMERICAL INVESTIGATION

The commercial finite element software ABAQUS was used to simulate the bases, using non-linear analysis, under Dynamic/Explicit step. A linear 4 node shell with reduced integration points (S4R) was used in the analysis. This element has been used in similar works and has shown reliable accuracy and efficiency (Ting and Lau (2016) and Li and Young (2017)). To obtain more accurate results, mesh size on flat parts of the section were set to 5x5 mm, and refined to 3x5 mm on the curved areas. In order to decrease the analysis time without losing significant accuracy, a mass scale of 100 was applied to the model. Reaction forces were retrieved from a set of Reference Points (RP), which were defined at the center of each welded area. In order to simulate the effect of a back-to-back connection well, a square area of the web, with sides equal to the web depth was chosen, at the top of the column, as shown in Figure 2. All elements inside the square are “Tied” to the RP located at the center of the square. This point is restrained against rotating about the X and Z axis, and prevented from translating along the Y axis. Another Reference Point, which is subjected to 5 mm downward displacement along the Z axis, is defined so as to apply a displacement control loading to the column. This Reference Point is restricted from moving in both the X and Y axis, and is connected to the square's Reference Point with a rigid beam using MPC Constraint option of the software. These two RPs simulate boundary conditions of the both ends of the rigid beam.

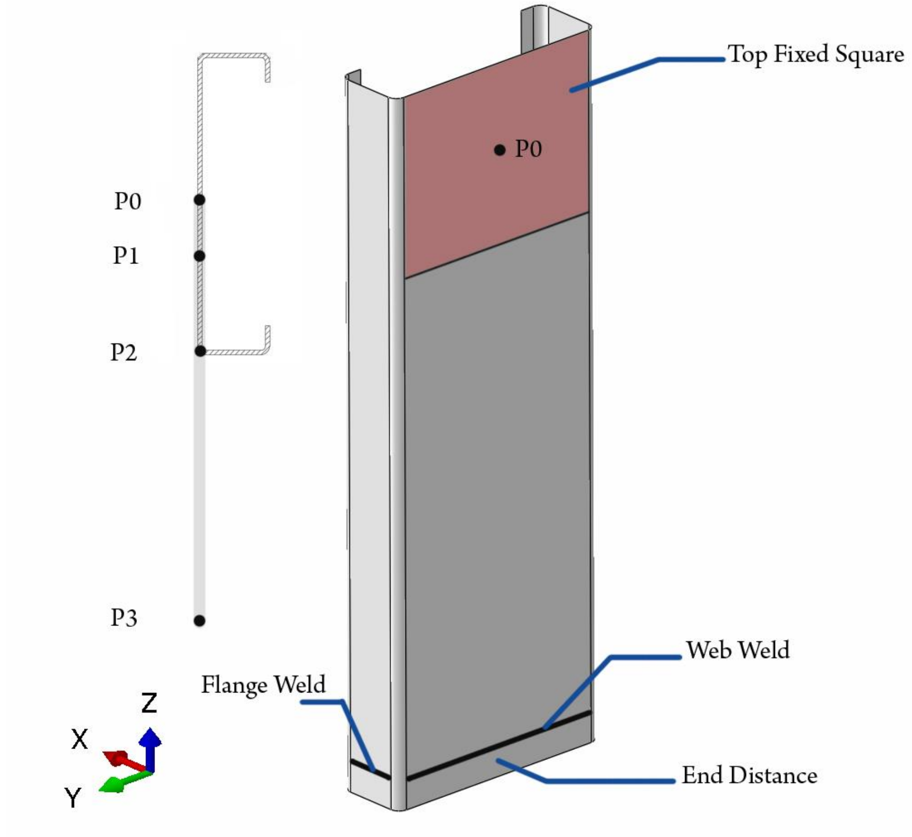

Figure 2 Typical set-up and loading positions

4. MATERIAL MODELLING

The material properties of the numerical model were obtained by tensile coupon tests. The coupons were extracted from the flat and corner areas of the section before performing the test. Flat coupons in the longitudinal direction of the centre of the web represent properties of the virgin material and corner coupons of the section show the effect of cold working on material properties. The coupons and tensile tests were prepared and tested in accordance with ASTM-E8/E8M-09. The measured average material properties of the web and corner areas are shown in Figure 3.

The material definition in ABAQUS for Dynamic/Explicit analysis incorporates density of the material, modulus of elasticity and poison ratio for elastic and also a multi-line graph to represents the non-elastic behaviour of the material. Table 2 contains all data that was used to define two material properties on the software. Material-1 is obtained from the results of the web coupons and assigned to the flat parts of the cross section, viz; web and flanges, and Material-2 represents the material behaviour of the corners.

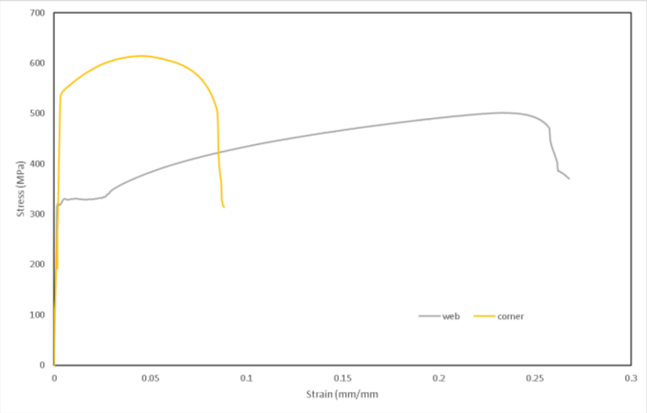

Figure 3 Typical stress-strain graphs

Table 1 - Material properties

	Yield Stress (MPa)	Plastic Strain
Material - 1	330	0
	364	0.012
	426	0.062
	488	0.162
	500	0.212
Material - 2	540	0
	590	0.017
	612	0.032
	614	0.047
	620	0.087
Modulus of Elasticity	200000 MPa	
Poisson's Ratio	0.3	
Density	8.05e-5 N/mm3	

5. RESULTS

The ultimate load capacity of the columns is given in Table 3, and the mode of failure and deformation characteristics of each category is explained below. In this table, a welded column is defined, for example, by C50-15, where C represents the column, 50 represents the width of the flange and 15 represents the width of the lip. Also, loading condition of the column is followed by base connection category is defined under Assembly column.

Table 3 - Ultimate capacity of the columns (kNs)

Assembly	C50-15	C75-15	C100-15	C50-20	C75-20	C100-20	C50-25	C75-25	C100-25
F-P0	190.42	225.94	248.33	199.97	239.97	269.03	209.28	252.55	282.89
F-P1	188.44	221.94	244.49	197.44	235.41	258.60	205.78	243.83	263.32
F-P2	159.10	180.6	193.75	161.21	181.89	190.57	165.13	183.55	192.9
F-P3	82.40	94.51	99.39	85.90	96.68	99.85	87.74	97.13	100.49
W-P0	182.94	209.64	221.34	183.52	211.80	221.93	184.67	211.75	222.60
W-P1	181.86	207.06	220.13	182.70	209.94	220.89	183.42	210.99	221.69
W-P2	167.46	175.92	184.61	169.89	179.81	188.32	171.87	182.08	190.67
W-P3	83.77	93.3	96.72	86.85	95.54	97.56	88.97	96.51	97.97
WF-P0	253.37	271.88	302.39	267.55	295.52	313.0	281.34	308.42	320.47
WF-P1	233.70	262.06	291.45	239.98	272.09	300.92	252.9	284.56	309.64
WF-P2	198.03	209.24	215.95	205.23	217.41	222.6	204.38	221.70	220.88
WF-P3	108.38	118.08	118.67	102.83	117.84	109.28	105.57	120.73	109.63

F – Fixed flanges; W – Fixed web; WF – Fixed web and flanges

5.1. Welded Flanges

The results of the finite element models with the flanges only connected to the base indicate that regardless of loading type, there is a small relationship between columns capacity and the size of the lips. Columns with connected flanges, and under pure axial load experience significant distortional buckling above the base connections, leading to the failure of the column. As shown in Figure 4,

bigger lip provides more stiffening and limit distortional buckling. However, the lip-to-flange ratio defines the behaviour of the column.
In the columns with small flanges, the effect of the lip's size on columns capacity is significant when the moment increases, while on the columns with larger flanges, this effect is insignificant. For example, in the cases C50-15 and C50-25, with assembly conditions of F-P2 and F-P3, an increase in the columns capacity of 6kN is realised, while the difference on the cases with larger flanges such as C100-15 and C100-25, with same assemblies, is not considerable. This behaviour can also be seen in the web cases too.

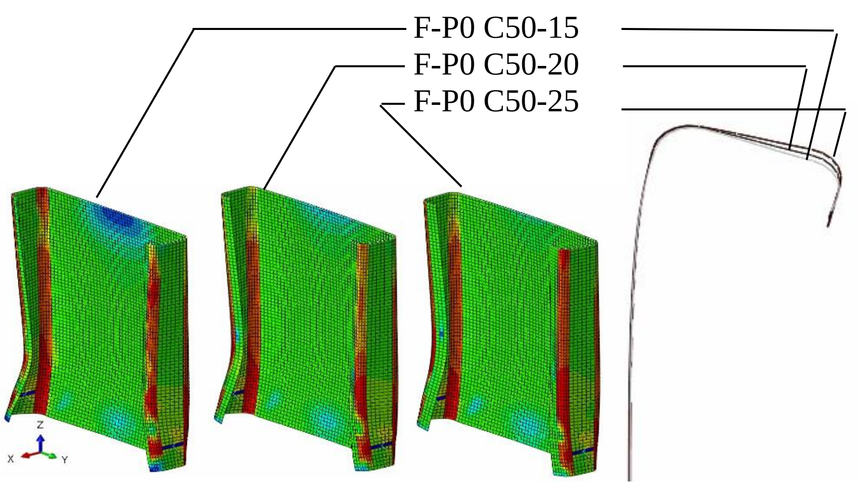

Figure 4 Effect of the lips on the bottom part of the column

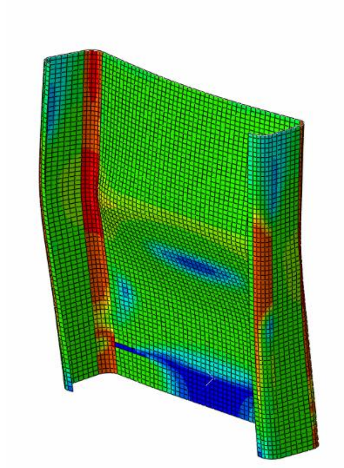

Figure 5 Local buckling of the web in the bottom part of the column

5.2. Welded Web

In cases where the web is welded to the base, the length of the lip has less influence on the column’s ultimate capacity. When the load's eccentricity is less than half of the column's depth, this case shows lower capacity than the cases with welded flanges, especially when it is under pure axial load. As shown in Figure 5, despite fixing a long area which is more than the flanges’ length, local buckling still fails bottom of the column. When the load is applied at point P2, that is, at the edge of the column, local buckling moves to the top of the column, just below the fixed square area. In this condition, columns with welded web show significant improvements in load capacity, compare with the other two cases.

5.3. Welded Flanges and Web

Connecting more cross-section elements at the base, created more stiffening of the column’s cross-section and also provided more contact area at the base to support the applied load. Columns with welded web and flanges show more load capacity than the other cases. The load capacity of the column is clearly larger than the other cases, and this was more significant when the load was applied within the cross-section of the column, that is at points P0 and P1. Failure of the column, under axial load at point P0, is due to local buckling of the web near mid-height. Applying load at point P1, causes a local buckle at the web and flange closer to the loading point. The position of failure is at the upper half of the column. By shifting the loading point from P1 to the edge of the column’s cross-section (P2), the location of failure of the web moved closer to the top of the column. In this situation, there is no significant difference between the maximum load capacity of this column and the one with welded web only. Loading beyond the column’s depth, on point P3, yield the results close to the welded web case.

A thorough scrutiny of the WF-P3 base connection, revealed the results shown in Figure 6. Figure 6 (a) and (b) shows in-plane stresses in the flanges and web separately, where outward and inward arrows represent the tension and compression stresses, respectively. This strip of the cross section is extracted from the bottom, at the top of the welds. As shown in Figure 6 (a) and (b), the flange closer to the loading point and a small portion of the web are in tension while the outer flange and the rest of the web are in compression. Another strip from the mid-height of the column (Figure 6 (c) and (d)) shows that the stresses are as expected, that is, the inner flange and a portion of web are in compression and the rest are in tension. Further studies to find an explanation of these forces is under way.

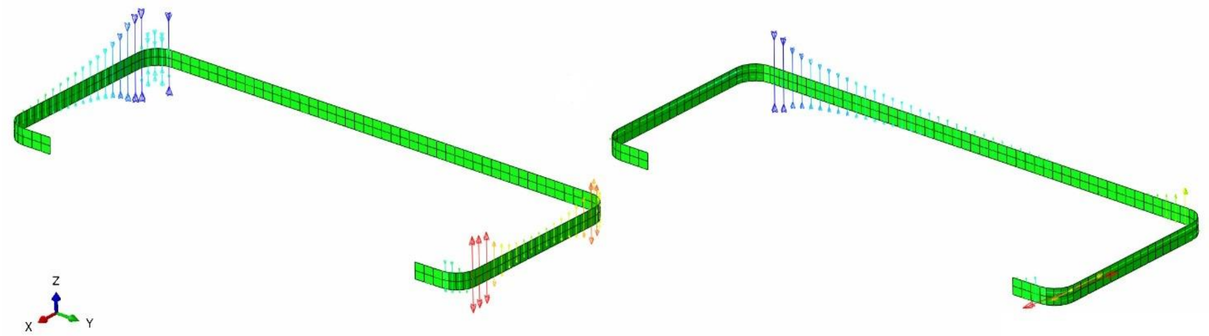

(a) In-plane bottom stresses in the flanges (b) In-plane bottom stresses in the web

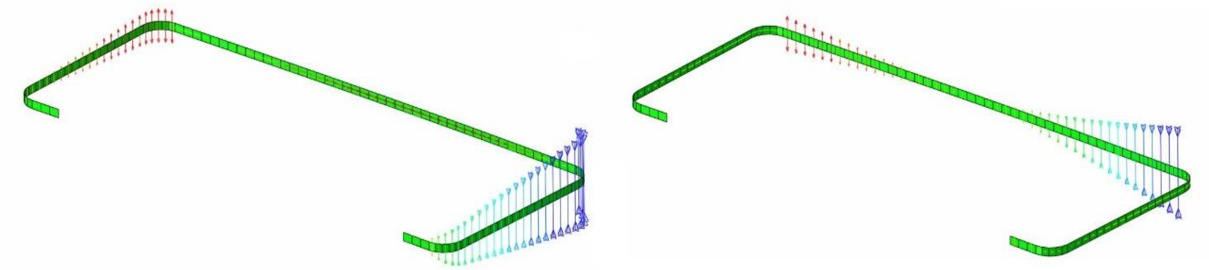

(c) In-plane mid-height stresses in the flanges (d) In-plane mid-height stresses in the web

Figure 6 - Stress at the bottom and mid-height of the column

6. CONCLUSION

In this paper, the capacity of the cold-formed lipped channel sections under both axial and the moment has been investigated, using numerical analysis. The connection at the top of the column was set as an ideal representative of a back-to-back connection to simulate the effect of loading through the web while the other elements of the cross section such as flanges, corners and lips at the top of the column are free. In such a situation, an applied moment on the web can cause distortional deformation at the top of the column, which can propagate down the column. Three different base connections, namely; columns with welded flanges only, columns with welded webs only and columns with both welded flanges and webs were examined. Columns with larger welded flanges showed better performance than similar columns with the welded web when loading was inside the cross section. On the other hand, models with welded web and the load is applied at the edge of the section have shown to be more efficient, in terms of ultimate capacity and connection length. Despite the great expectations of column bases in the last category, where both flanges and web were fixed, numerical models have shown that load is not able to pass through base connections, making the connection inefficient.

7. REFERENCES

Dundu, M. 2012. “Base Connections of Single Cold-Formed Steel Portal Frames.” *Journal of Constructional Steel Research* 78: 38–44.

Dundu, M, and A R Kemp. 2006. “Strength Requirements of Single Cold-Formed Channels Connected.” *Journal of Constructional Steel Research* 62: 250–61.

Kwon, Y.B., H.S. Chung, and G.D. Kim. 2006. “Experiments of Cold-Formed Steel Connections and Portal Frames.” *Journal of Structural Engineering* 132(4): 600–607.

Li, Hai-Ting, and Ben Young. 2017. “Cold-Formed Ferritic Stainless Steel Tubular Structural Members Subjected to Concentrated Bearing Loads.” *Engineering Structures* 145: 392–405.

Lim, James B P et al. 2016. “DSM for Ultimate Strength of Bolted Moment-Connections between Cold-Formed Steel Channel Members.” *Journal of Constructional Steel Research* 117: 196–203.

Öztürk, Ferhan, and Selim Pul. 2015. “Experimental and Numerical Study on a Full Scale Apex Connection of Cold-Formed Steel Portal Frames.” *Thin-Walled Structures* 94: 79–88.

Ting, T C H, and H H Lau. 2016. “Finite Element Analysis Of Axially Loaded Cold- Formed Steel Back-to-Back Channel Built-Up Sections.” In *Eighth International Conference on Steel and Aluminium Structures*,.

Zaharia, Raul, and Dan Dubina. 2006. “Stiffness of Joints in Bolted Connected Cold-Formed Steel Trusses.” *Journal of Constructional Steel Research* 62(3): 240–49.

Zhang, Xi, Kim J R Rasmussen, and Hao Zhang. 2015. “Structural Modeling of Cold-Formed Steel Portal Frames.” *Structures* 4: 58–68.

Proc. 1st International Conference on Structural Engineering Research (iCSER 2017)
20-22 Nov 2017, Sydney, Australia
ISBN: 978-0-6480147-6-8

A Parallel Finite Element tool in Grasshopper

Xiao Lai[1] and Zheng He[2,3]

[1]Ph.D, Dalian University of Technology, Dalian, China
[2]Professor, Dalian University of Technology, Dalian, China
[3]State Key Laboratory of Coastal and Offshore Engineering, Dalian University of Technology, Dalian, China
Corresponding author's E-mail: hezheng1971@126.com

Abstract

Parametric techniques provide a sharing platform for multidisciplinary information. Although some structural analysis tools in parametric platform are widespread, these tools rarely have the capability to estimate seismic responses rapidly and accurately. Considering the severe damage caused by strong earthquakes, a parallel finite element analysis tool is implemented as a plugin in the parametric modelling platform—Grasshopper. With the help of the series of components, engineers could achieve static analysis and nonlinear dynamic analysis to any structure. Some open-source codes are incorporated in the program using C++ programming language, which involve matrix calculation libraries, material constitutive models, etc. Two parallel computing strategies, the parallel state transformation procedures (PSTP) and the parallel factorization of Jacobian (PF), are adopted to make up for the low speed of nonlinear dynamic analysis. In Grasshopper, geometries are converted to structural models through nine new data types, i.e. Material, Section, Line Element, Shell Element, Load, Constraint, Analysis, Damping and Model. A case study on two 14-storey frame-shear wall structures with the same parametric modelling logic has demonstrated the operational convenience of the dynamic analysis tool. Variables include geometric variables, topological variables and structural variables. A top displacement time history is presented to show the different seismic performance of these structural models.

Keywords: Parametric technique, Nonlinear dynamic analysis, Parallel computing, Grasshopper plugin.

1. INTRODUCTION

The Sydney Opera House is the first major architecture project accomplished with the help of computation. In the past 30 years, the rapid developing computer technology has gradually changed its own role in the architectural design. Parametric design is a typical creature using the relationship between elements to manipulate and inform the design of complex geometries. The completion of various nonlinear building, e.g. the Heydar Aliyev Center and the Phoenix International Media Center, demonstrates the powerful modelling capability of parametric design. Parametric technique provides a sharing platform for multidisciplinary information. Despite the parametric design is not new to architecture, it is still not very familiar to engineers. Although some structural plugins, like Karamba (2014), are integrated in Grasshopper (2015), a well-known parametric modelling tool, most of them are just used to help structures stand up or explore new forms. There is still a far way to achieve the intelligent structural design, in which all structural components could be distributed automatically, even create new rational structural systems but without negative influence to architectural functions. So far, a lot of researchers have made efforts to this ultimate goal. Combined with the easy-to-control attribute of NURBS surfaces, Li et al (2011) proposed a NURBS-GM method to optimize the strain energy. Huang et al (2006) improved evolutionary structural optimization (ESO) using a bidirectional algorithm, which means that material could be not only deleted but also added to structures during the optimization process. In order to rich the forms of structures, Mueller and Ochsendorf (2015) developed a web-based program named "Structure Fit" to achieve interactive form-finding in the design space. Flager et al (2009) presented a methodology and optimized their structures while considering structure and energy as objectives. Zhang and Mueller (2017) optimized shear wall layouts by utilizing an improved ground structure method. All the algorithms and tools mentioned above only take into account static loads or wind loads into account but no structural safety under earthquakes. Thus, there is a need to develop a seismic analysis tool in parametric platforms.

2. SEISMIC ANALYSIS IN MULTI-OBJECTIVE OPTIMIZATION

In traditional structural design, engineers mostly care about structural safety, but ignore architectural functions and aesthetics, which deeply intensifies the contradiction between architects and engineers. Optimizing buildings is no longer a pure mechanical problem, but a conundrum including multiple professional requirements, e.g. structural rationality, energy saving, and accessibility. That is the multi-objective optimization in the construction industry. To engineers, structural rationality has two basic meanings: make structures stand up and more efficient mechanically. However, just standing up may be sufficient for a sculpture, but definitely cannot satisfy building requirements. In the life cycle of a building, larger earthquakes are possible to happen, which could cause building collapse and some serious secondary disasters, e.g. spreading fire and rock fall in large area. Thus, seismic analysis should be considered in optimization.

Generally, considering the speed of calculation, engineers prefer using equivalent static loads to estimate seismic responses of structures, especially in conceptual design. However, what should be recognized is that the inaccurate approximation could become the source of a wide range of model adjustments in later stage. The trial-and-error design approach still exists in that way.

The nonlinear dynamic analysis is one of the mainstream methods to improve the calculation accuracy, which calculates building responses at discrete time steps using discretized seismic waves. Due to the consideration of material inelastic properties, the calculated results are reasonably more approximate to those during the design earthquake. Nevertheless, the time history method is a double-edged sword, because discretizing time leads to larger workload simultaneously. And to guarantee the architectural diversity, a lot of parametric structural models should be generated. Then the low calculation speed will become the most insurmountable obstacle for nonlinear dynamic analysis to participate in parametric design.

Compared to the two methods mentioned above, the response spectrum method is a compromise method. On one side, standard response spectrums in design codes are statistical results of series of responses under considerable ground motions. So time integration methods are not necessary in this method, which makes it much faster than time history analysis. On the other side, compared to the equivalent static loads methods, the Duhamel integration method for plotting the response spectrums reflects structural dynamic characteristics originally. Thus, it is more appropriate to apply the response spectrum method in the early process of optimization. And the nonlinear dynamic analysis could be used to check the seismic safety of final optimized structural proposals. Due to the space limitation, only the check part is introduced in this paper.

3. PARALLEL COMPUTING IN SEISMIC ANALYSIS

3.1. Basic procedure

The dynamic equilibrium equation of a nonlinear system can be written as follows:

$$m\ddot{v}(t)+c(t)\dot{v}(t)+k(t)v(t)=p(t) \tag{1}$$

where $\ddot{v}$, $\dot{v}$ and v are the vectors of accelerations, velocities and displacements of a structure, respectively; m, c and k are the matrix of mass, damping and stiffness, respectively. The time history analysis involves a time-step-by-time-step evaluation of building response. Thus, the dynamic equilibrium equation is discretized with the i^{th} analytical time step as follows:

$$m\Delta\ddot{v}_i + c_i\Delta\dot{v}_i + k_i\Delta v_i = \Delta p_i \tag{2}$$

Based on the different assumption to the variation of acceleration in an analytical step, the connection among accelerations, velocities and displacements could be established. So, the equation above could be simplified as follows:

$$F\left(\Delta v_i\right) = 0 \tag{3}$$

With the unbalanced force applied, the Newton-Raphson method is adopted to iteratively approximate the solution at the end of each analytical step, which could be expressed as follows:

$$F'\left(\Delta v_i^k\right) \times s_i^k = -F\left(\Delta v_i^k\right) \tag{4}$$

$$\Delta v_i^{k+1} = \Delta v_i^k + s_i^k \tag{5}$$

where the $F'(\Delta v_i^k)$ is the stiffness matrix, also called the Jacobian, and s_i^k is the increment of displacement vector after the kth iteration in the i^{th} analytical time step.
With a short analytical time step, a complete nonlinear dynamic time history analysis usually requires thousands of iterations, especially to skyscrapers and large span spatial structures. Therefore, it is necessary to speed up nonlinear time history analysis.

3.2. Parallel computing and integration

Parallel computing is a type of computation in which many calculations or the execution of processes are carried out simultaneously. Significant computation workload in material-level state determination is satisfied to achieve the accuracy of nonlinear dynamic analysis. To solve this problem, the state transformation procedures (STP) were proposed by He (2017). In the STP, the sections at integration points are classified into three states, i.e. initial state, elastic state and nonlinear state. It should be noted that when strong earthquake comes, a large portion of sections remains in elasticity, which means their stiffness is still kept as initial value. That is the repeated state determination of sections is not necessary until their nonlinearity occurs. Solving nonlinear equation also takes a lot of time in nonlinear dynamic analysis. Considering the sparseness, symmetry and positive definiteness of stiffness matrix, sparse Cholesky factorization method is appropriate to determine the increment of displacement vector during iteration. The STP and sparse Cholesky factorization are combined with parallel computing technique to achieve higher acceleration.

A new parallel finite element program using C++ program language was developed by Fu et al (2015) to achieve the futures mentioned above. Some open-source codes available are integrated into the program. The main matrix operation library includes Eigen (accessed on 2015), CHOLMOD. OpenMP is integrated to balance thread allocation in parallel computing to avoid meaningless thread wait. Concrete02 (1994) and steel02 (1983) are adopted from OpenSees (2000). In terms of shell element, the famous MCFT (1986) is integrated as 2D concrete material. Fiber beam-column element (1996) and layered shell element (2015) are integrated in the program to reflect structural seismic responses in macroscopic level from material properties in microscopic level.

4. STRCUTRUAL DATA TRANSMISSION

The enormous quantity of model data requires fast information conversion from Grasshopper to the program. The repeated calling to "DllImport" function usually causes severe time waste. Moreover, the existing of global variables in the parallel finite element program heaps up the obstacle to control and monitor variables in multi-process computing. Thus, easy text conversion is adopted in the core component. Nine data types are developed to incorporate all the structural information in the parallel finite element program, i.e. Material, Section, Line Element, Shell Element, Load, Constraint, Analysis, Damping and Model. In material component, users could choose concrete and steel corresponding to Chinese code as well as create material with specific mechanical properties. Geometric information and section information are combined in line element and shell element components. Two kinds of load types are included in the load component, i.e. point load and uniform line load. Constraint component provides various constraints on the degrees of freedom of nodes, e.g. support and diaphragm. So far, three kinds of analysis are included in Analysis component, i.e. the static analysis, the Newmark analysis and the modal analysis. All the structural information above are assembled together, and sent to the core calculation component. For skyscrapers and long span spatial structures, due to the huge number of degrees of freedom, the conversion between geometries and structural elements may increase running hours. Thus, a parallel conversion strategy is adopted in this series of components. The framework of the series of components and some basic modules are presented in Figure 1.

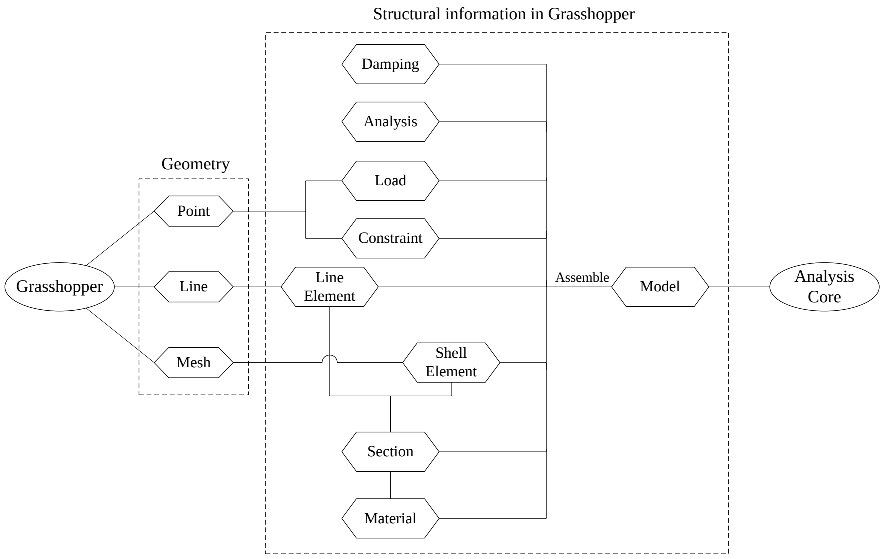

Figure 1. The basic modules of the series of components

5. EXAMPLE

The studied two 14-storey buildings and the modelling logic are illustrated in Figure 2. What should be noticed is that the two models are based on the same parametric modelling logic, which means the change from model 1 to model 2 only requires a few adjustments of sliders. The computational accuracy and efficiency of the analysis core was verified by Fu et al (2015). MCFT and Kent-Park concrete are adopted as material of shell and line elements, respectively. Material properties and geometric information of sections are shown in Table 1. For analytical simplicity, ground motions are applied only in the transverse direction of the structure. In order to make the medium acceleration spectra of the records fit well with the design acceleration spectrum specified in Chinese code (2010), two ground motions are adopted from the ground motions selected by He (2017), i.e. Superstition Hills at Brawley Airport Station, Northridge earthquake at Nordhoff Fire Station and Manjil earthquake at Abbar Station. The peek ground accelerations (PGA) of three waves are amplified to 400gal. Figure 3 illustrates the top displacement time histories.

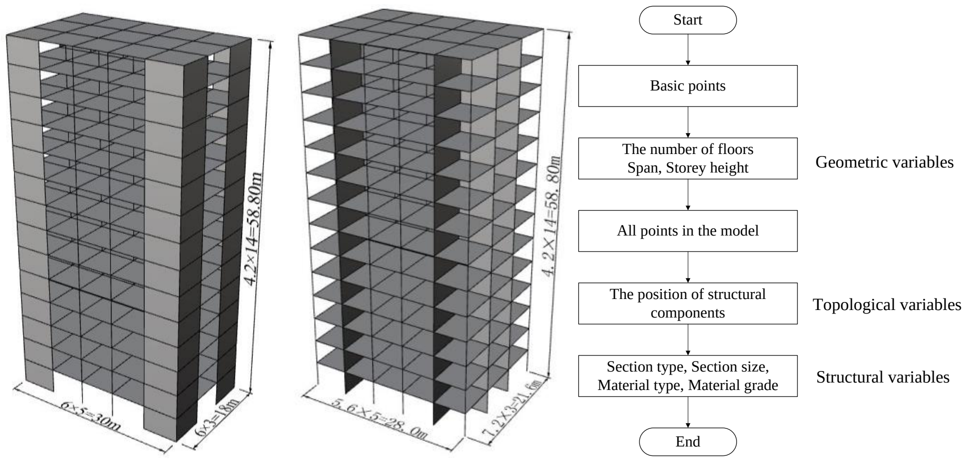

Figure 2. Structural models and modelling logic in Grasshopper

Table 1. Material and geometric information of sections

Parameters	Beam	Column	Shear wall
Section size(m)	0.6×0.3	0.8×0.8	0.2 (thickness)
Concrete maximum strength (N/m^2)	3.25×10^7	3.25×10^7	3.25×10^7
Elastic modulus of concrete (N/m^2)	3.25×10^{10}	3.25×10^{10}	3.25×10^{10}
Steel yield strength (N/m^2)	4.0×10^6	4.0×10^6	4.0×10^6

Note: Floor thickness is 0.15m.

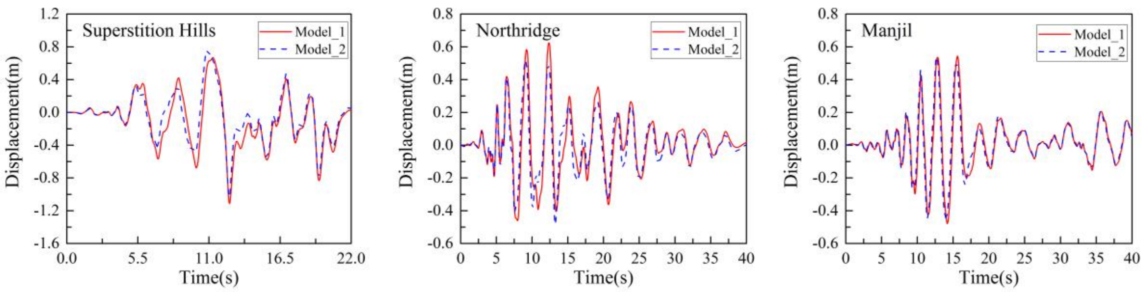

Figure 3. Top displacement time histories of structures

6. CONCLUSION

To consider structural seismic performance in parametric design, a parallel finite element analysis tool is developed as a plugin in Grasshopper. The importance of seismic analysis in multi-objective optimization is emphasized, and the corresponding calculating methods are discussed respectively. Two parallel computing strategies, the parallel state transformation procedures(PSTP) and the parallel factorization of Jacobian(PF), are adopted to accelerate the dynamic analysis. The series of components achieve the data transformation between Grasshopper and the finite element program, which vigorously promotes the speed of structural engineering merging with other architectural fields.

7. ACKNOWLEDGMENTS

This research was financially supported by the National Natural Science Foundation of China (Grant No. 91315301).

REFERENCES

Preisinger C, Heimrath M (2014). Karamba—A Toolkit for Parametric Structural Design, Structural Engineering International, 24(2), 217-221.

Robert McNeel & Associates. (2015). Grasshopper 3D. Retrieved from www.grasshopper3d.com/

Li X, Wu Y, Cui C. (2011). NURBS-GM method for computational morphogenesis of free form structures. China Civil Engineering Journal, 44(10), 60-66.

Huang X, Xie YM, Burry, MC (2006). A new algorithm for bi-directional evolutionary structural optimization, JSME International Journal Series C Mechanical Systems, Machine Elements and Manufacturing, 49(4), 1091-1099.

Mueller CT, Ochsendorf JA (2015). Combining structural performance and designer preferences in evolutionary design space exploration, Automation in Construction, 52, 70-82.

Flager F, Welle B, Bansal P, Soremekun G, Haymaker J (2009). Multidisciplinary process integration and design optimization of a classroom building, Journal of Information Technology in Construction (ITcon), 14(38), 595-612.

Zhang Y, Mueller C (2017). Shear wall layout optimization for conceptual design of tall buildings, Engineering Structures, 140, 225-240.

He Z, Fu S, Ou J (2017). State Transformation Procedures for Fiber Beam-Column Element in Inelastic Dynamic Time History Analysis for Moment-Resisting Frames, Journal of Computing in Civil Engineering, 31(5), 04017036.

Fu S, He Z, Li Z, Tu X, Tao Q (2015). Shared memory parallel computing procedures for nonlinear dynamic analysis of super high rise buildings, In International Conference on Performance-based and Life-cycle Structural Engineering. The University of Queensland. 1629-1637 pp.

Benoit J, Guennebaud G. Accessed via from http://eigen.tuxfamily.org on 7 July 2015.

Yassin M(1994). Nonlinear analysis of prestressed concrete structures under monotonic and cyclic loads. PhD dissertation, University of California, Berkeley, CA, USA.

Filippou FC, Bertero VV, Popov EP (1983). Effects of bond deterioration on hysteretic behavior of reinforced concrete joints, EERC Report, University of California, Berkeley, CA, USA.

McKenna F, Fenves GL, Scott MH (2000). Open system for earthquake engineering simulation, University of California, Berkeley, CA.

Vecchio FJ, Collins MP (1986, March). The modified compression-field theory for reinforced concrete elements subjected to shear, ACI Journal, 83(2), 219-231.

Spacone E, Filippou FC, Taucer FF (1996). Fibre beam-column model for non-linear analysis of R/C frames: Part I. Formulation, Earthquake engineering and structural dynamics, 25(7), 711-726.

Lu X, Xie L, Guan H, Huang Y, Lu X (2015). A shear wall element for nonlinear seismic analysis of super-tall buildings using OpenSees, Finite Elements in Analysis and Design, 98, 14-25.

Proc. 1st International Conference on Structural Engineering Research (iCSER 2017)
20-22 Nov 2017, Sydney, Australia

ISBN: 978-0-6480147-6-8

Numerical Study of the Effects of Container Shape on the Self-Assembly of Granular Particles under Vibration

Reza Amirifar[1], Kejun Dong[1,*] and Qinghua Zeng[2]

[1]Centre for Infrastructure Engineering, Western Sydney University, Sydney, Australia
[2]School of Computing, Engineering and Mathematics, Western Sydney University, Sydney, Australia
*Corresponding author's E-mail: Kejun.Dong@westernsydney.edu.au

Abstract
Granular materials have wide applications in producing structural materials such as concrete and pavement. However, their behaviours are still limited understood. In recent years, characterizing and modelling the structure of granular materials under different conditions has become a hot multidisciplinary research topic attracting both scientists and engineers. In this work, we develop a numerical model based on discrete element method (DEM) to study the structure of granular materials in a container subjected to vibration. In particular, we investigate the influence of shape of the container on the self-assembly of the particles, i.e., the phase change from disordered to ordered structures. Our simulated containers are prisms with different bottom shapes (e.g., circle, equilateral triangle, square and hexagon). For each shape, we conduct simulations under different vibration frequencies and amplitudes. The structure of the vibrated granular material is characterized by packing density (porosity), coordination number, radial distribution function and bond orientation order parameters. Opting for desired vibrational parameters, it is found that the triangular container would produce comparatively more ordered structures. The simulation results manifest the effect of boundary and vibration on the structure of granular materials, which could provide the strategies for controlling the structure of granular materials for optimising the production of structural materials.

Keywords: Granular materials, Self-assembly, Container shape, DEM Method, Vibration.

1 INTRODUCTION

Granular particles, commonly ranging from micrometres to meters, have wide applications in various industries, such as in producing concrete and pavement in infrastructure engineering. However, their behaviours are still limited understood due to insufficient knowledge of their structures. For example, granular materials can act like either fluids or solids under different circumstances (Zhang and Campbell 1992), which often involve the critical changes in their structures. Another paradox is the self-assembly of granular materials, which refers to the transition an assembly of particles from disordered to ordered structure (Lash et al. 2015).

The self-assembly of granular particles was studied for uniform spherical particles both experimentally and numerically (Yu et al. 2006, Jiang et al. 2011, Damasceno et al. 2012). Previous studies focused on generating the packings with maximum level of the geometrical order (Yu et al. 2006). The densest structure in theory would possess the FCC or HCP structures giving the packing density equal to 0.74 (Hales 2005). But it has been acknowledged that a spherical particle packing generally produces a packing density around $\rho = 0.60$ (Yu et al. 2006) in a disordered structure, with minor dependences on material properties and dynamic parameters. To increase the packing density, one may need to induce external agitations to let the particles rearrange. It is found that a vertical one-dimensional (1D) vibration may result in the increase of the packing density to $\rho = 0.64$ (Zhu et al. 2008). But this method cannot further increase the packing density which will need the ordered structure to be generated, i.e., inducing the self-assembly of particles. This can only be achieved by using 3D vibration and batch feeding (Li et al. 2011). These studies, however, were mainly conducted on a rectangular box. Although a few studies demonstrated that a container with specially designed shape can help achieve self-assembly (Nahmad-Molinari and Ruiz-Suárez 2002), no particular studies have been performed to reveal the effect of container shape on the self-assembly of granular particles.

In this work, the effect of geometry of the boundaries and containers on the structure and dynamics of granular particles under vibration is numerically studied. Containers of different shapes are used in the simulations and a 1D vibration is applied to the container. Facilitated by the microscopical information obtained from the simulations, the effects of the container shape as well as vibration conditions on the structural evolutions of the particle system are quantified and characterized.

2 METHOD DESCRIPTION

In this work, granular particle packing under vibration is simulated by discrete element method (DEM) which has wide industrial applications including particle packing, heaping/piling process, hopper flow, mixing and granulation (Zhu et al. 2007, Dong et al. 2009, Kroupa et al. 2012). In this method, discrete particles with translational and rotational motions are modelled based on Newton's second law of motion. It is assumed that a collision process between two particles takes place within a time interval lower than a critical value so that during each time step, the disturbance from any particle cannot propagate beyond its immediate neighbouring particles (Cundall and Strack 1979). The translational and rotational components of the motion of particle i can be written as:

$$m_i \frac{d\mathbf{V}_i}{dt} = \sum \mathbf{F}_i \qquad (1)$$

$$I_i \frac{d\boldsymbol{\omega}_i}{dt} = \sum \mathbf{M}_i \qquad (2)$$

where m_i and I_i are the particles' mass and moment of inertia, respectively; $\mathbf{V}_i$ and $\boldsymbol{\omega}_i$ are the translational and angular velocities of the particle, respectively; and $\mathbf{F}_i$ and $\mathbf{M}_i$ are the total force and torque acting on particle *i* exerted from the neighbouring particles, boundary walls or the vicinal fluid, respectively. As in this work we consider coarse and dry particles, the force term only includes the collision forces between the contacting particles and the boundary walls as well as the gravitational force, considering the overwhelming dominancy of these forces within such media in comparison to other non-contact forces. Once all the forces and torques are known, Equations (1) and (2) can be numerically solved. Thus, the positions, trajectories and velocities of all particles in the particulate system can be traced.

Table 1. List of operational conditions and material properties used in this work

Particle diameter, d (mm)	0.58
Cylindrical container bottom diameter, D (normalised by d)	20
Vibration frequency, f (Hz)	10-100
Vibration amplitude, A (normalised by d)	0.3-1.3
Number of particles, N_p	10000
Particle density, (kg/m^3)	5960
Elasticity modulus, (N/m^2)	1e-7
Poison ratio	0.29
Normal and tangential damping	0.3
Rolling friction coefficient	1e-3
Sliding friction coefficient	0.3

The containers considered in our simulations are prisms with different bottom shapes including circle, equilateral triangle, regular hexagon and square. For each container, the simulation starts at t=0s with particles randomly generated within the container, none of which being in contact with any other and with the container walls. Due to gravity, particles begin to fall down, and reach the bottom or other particle sooner or later. With the energy dissipated during the collisions, they will form a static packed bed at t=0.4s. At t=0.5s, the container begins to vibrate. The 1D vertical vibration continues till t=17.5s, then the simulation goes on for a half seconds to let the packing reach to a final stabilization.

To investigate the effects of the vibrational parameters, a variety of amplitudes and frequencies are used in the simulation. Five amplitudes have been simulated for each container and at each amplitude, six frequencies are used. The inter-particle forces considered are the contact forces modelled by the Hertz-Mindlin and Deresiewicz model with rolling friction (Zhu et al. 2007, Dong et al. 2013). The particles are assumed to be spheres with properties listed in Table 1.

3 RESULTS AND DISCUSSION

3.1 Effects of vibrational parameters

The results are firstly analysed by the macroscopic parameter, packing density ρ, i.e., the volume ratio of particles to the space they occupy. Figure 1 shows the packing density at the end of the simulation (t=18s) for different containers under different vibration conditions. Similar trends can be seen at all diagrams, that is, for each case, packing density experiences an initial growth as the vibration frequency increases and then falls down for larger frequencies, except for two series which have not shown the decreasing of packing density but the trend should be similar if higher f is used. These trends of variations match those of An et al.'s work (An et al. 2009). However, it can be seen that in our simulations, even using 1D vibration, the packing density can increase above 0.64 and reach about 0.7, showing that the packing is partially ordered. The lower frequencies of 10 and 20 Hz have the least impact on the packing density of the resultant particle packing; no matter what amplitude being applied, the packing density will not exceed the random close packing density 0.64. It indicates that in these cases the mechanical energy exerted into the disordered packing via the external vibration is not enough for the particles to reach a more ordered configuration. On the other hand, if A is equal or higher than 1.0d, ρ will also always be lower than 0.64, indicating that a vibration with too high amplitudes will not be favourable to the self-assembly. When A is below 1.0d and f is above 20 Hz, ρ can be found to be greater than 0.64. The optimised vibration frequency at which each series reaches its densest packing would be different depending on the container shape and vibration amplitude.

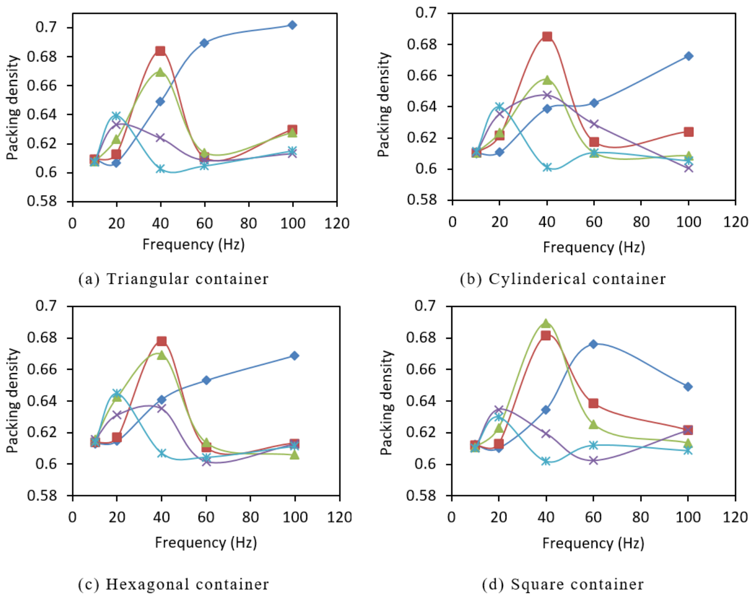

(a) Triangular container (b) Cylinderical container

(c) Hexagonal container (d) Square container

Figure 1. Packing density vs. vibration frequency for different vibration amplitudes and different containers. The legend is same for all: *A=0.3d*, *A=0.55d*, *A=0.8d*, *A=1.0d* and *A=1.3d*.

Comparing different containers, it can be seen that using triangular shape one, packing density can reach the highest value about 0.70. So, the simulations with this container are further analysed. The combined influence of amplitude and frequency on final packing density of the packing in the triangular container is shown in Figure 2. To plot this contour, results of 25 simulations with various A and f are used. It can be clearly seen that the most ordered packing happens for low amplitudes and high frequencies and vice versa. Two regions produce the least dense packing: those where the frequency is very low (no matter how much the amplitude is) and also where the both frequency and amplitude are very high.

3.2 Self-assembly process

The most self-assembled cases based on our simulations occur for the vibration amplitude of 0.3*d* and frequencies of 60 and 100 Hz, as seen in the Figure 3. The packing in the triangular container produces a more and more ordered packing with an increasing particle density as time snaps. The other three containers generate comparable packing densities but generally smaller. It can be seen that during the simulation, the packing density within the triangular container reaches even above 0.7. Corresponding to the high packing density, the self-assembly of the packing in this container also reaches to a relatively high degree.

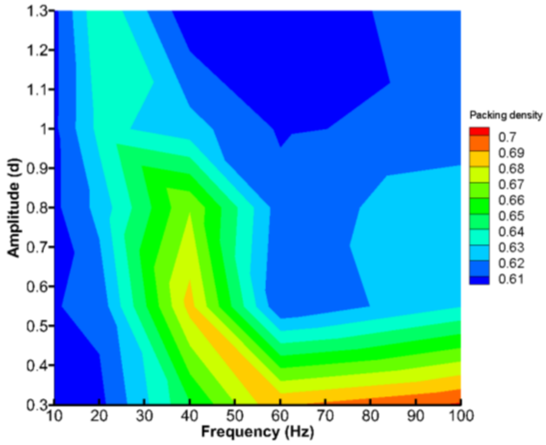

Figure 2. Combined influence of amplitude and frequency on packing density. The data are for the triangular container at the end of the simulation (t=18s)

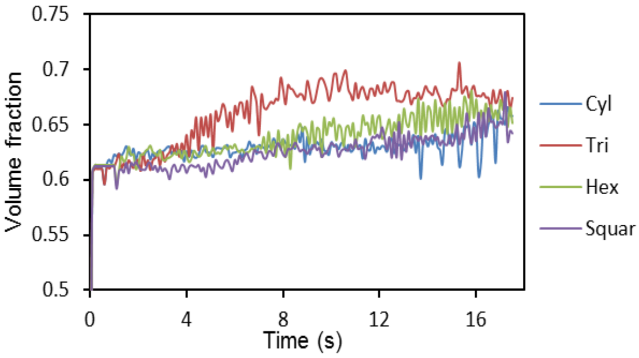

Figure 3. Packing density of different containers for *A*=0.3*d* and *f*=100 Hz

In Figure 4, the most self-assembled configurations of particles at the final stages of the simulations have been displayed from the same view position for different containers at *A*=0.3*d* and *f*=60 Hz. The particles are coloured by the translational velocities. As can be seen, the triangular container forms the best packing in terms of self-assembly; where regions with ordered structures are obvious at the outer parts near the container bottom. It is observed from the velocities of particles that when the particles become more ordered, they get locked to each other and behave as a bulk, i.e. the velocity of the particles at the self-assembled regions would nearly be similar, as if they are acting as a solid phase.

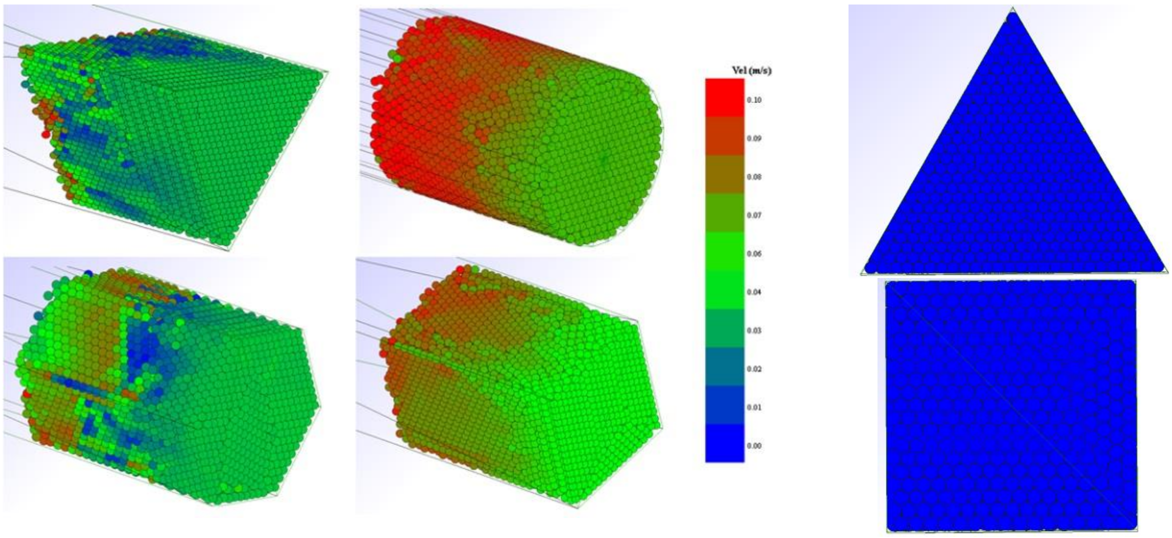

Figure 4. (left) Self-assembled particles for different containers (*A*=0.3*d* and *f*=60 Hz), (right) bottom view of triangular and square containers at the end of the simulation

3.3 Microscopic structure analysis

To better understand the structure evolution in the self-assembly process, the packings are further characterized by several microstructural parameters, the coordination number and orientation order parameters. Coordination number is defined as the number of particles contacting a particle. In Figure 5, the mean coordination number has been shown in relation to the corresponding packing density for different container shapes. It is seen that the mean CN for the vibrated bed in the triangular container can reach 10. This is a sign of presence of partly and locally ordered FCC/HCP structures with CN=12, while the general CN for a disordered packing is 6 (Gervois et al. 1989). Moreover, the mean CN obtained in triangular container is higher than those in other containers, showing a more clear ordered packing and indicating that the effect of container shape on the self-assembly can be more clearly identified by microscopical parameters rather than packing density. On the other hand, it is interesting to see that CN increases from 7 to 10 when ρ increases from 0.6 to 0.68, but does not exceed 10 with further increasing of ρ. This indicates that the further densification of the packing may probably incur the local rearrangement of the neighbour particles rather than the increase of the neighbour particle number. Therefore, we perform the bond orientation order analysis to characterize such possible rearrangements.

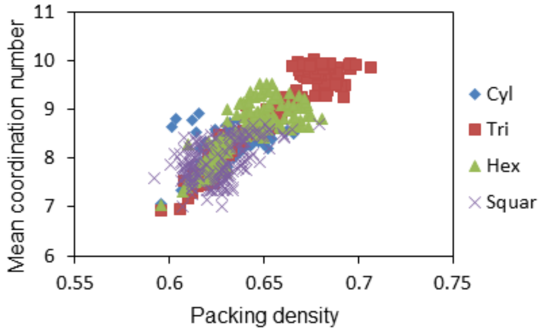

Figure 5. Mean coordination number vs packing density for different containers

Bond orientation order Q_l (l=1,2.,..) is also a commonly used parameter in analysing structure evaluations, especially Q_4 and Q_6 which are effective in identifying the FCC and HCP structures in particle packing (Dong et al. 2009). The bond orientation order Q_l of a particle is calculated based on the spherical harmonics $Y_{lm}(\theta_i, \varphi_i)$ of its bonds to the neighbour particles, where θ_i and φ_i are the polar and azimuthal relative angles of the bonds (Luchnikov et al. 2002). These two parameters are averaged for individual particles. The correlations between the averaged Q_6/Q_4 and the packing density for the vibrated beds in various containers at different times are shown in the Figure 6. When the packing becomes denser, the Q_6 parameter increases rapidly up to 0.52 where ρ reaches about 0.64. When ρ further increases, Q_6 keeps increasing but much slowly, indicating that the bond orientation order

parameters are capable of demonstrating the critical structure change at this point, which is in accordance with the RCP state or MRJ state. If Q_4 and Q_6 of a packing are close to those of ordered structures such as FCC/HCP, the packing structure should be close to these ordered structures. For example, the values of Q4 and Q6 for the FCC structure are 0.190 and 0.575, respectively. The Q6 and Q4 for the packings in the triangular container are closer to these values which means this container is favourable for directing the self-assembly of particles by vibration.
The reason why the triangular container introduces comparatively better self-assembly may be attributed to the effect of the boundary on forming the local ordered structures, like those at the corners of the container (Figure 4), as the crystallization cores for the whole packed bed. This deserves further studies.

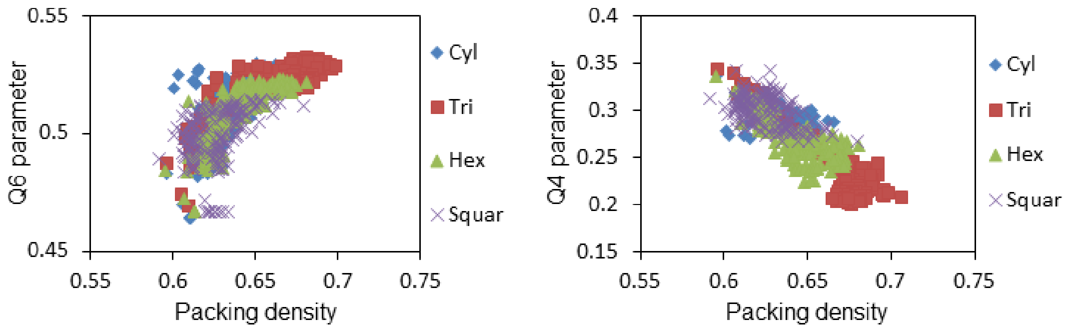

Figure 6. Q4 and Q6 parameters correlated with the their corresponding packing density for different containers (*A*=0.3*d*, *f*=60 Hz)

4 CONCLUSION

In this work, we have employed the DEM method to investigate effects of the container shape on the self-assembly of the granular particles under external vibration. The results of our simulations show that the equilateral-triangular container produces the highest packing densities and also the coordination numbers for the granular particles. For each set of the vibrational parameters, there seems to be an optimum choice on which the packing would have the most values of density and CN parameters. The packing structure has also been characterized by the bond orientation parameters, which shows the corresponding values of Q_4 and Q_6 for the triangular-bottom containers are the least and the most respectively in comparison to those of the packings obtained in other containers. It can be deduced that by employing the most optimized shapes for the particle packing containers, we would have a good chance of generating ordered structures and directing the self-assembly. It is interesting to point out that despite our expectations from the nature that the hexagonal-bottom container would produce the most optimized results, the best outcomes here belonged to the triangular container. The reason seems to be the effects of the triangular container boundaries, in special the corners.

REFERENCES

An, X., Li, C., Yang, R., Zou, R., & Yu, A. (2009). Experimental study of the packing of mono-sized spheres subjected to one-dimensional vibration. Powder Technology, 196(1), 50-55.

Brilliantov, N. V., Albers, N., Spahn, F., & Pöschel, T. (2007). Collision dynamics of granular particles with adhesion. Physical Review E, 76(5), 051302.

Cundall, P. A., & Strack, O. D. (1979). A discrete numerical model for granular assemblies. geotechnique, 29(1), 47-65.

Damasceno, P. F., Engel, M., & Glotzer, S. C. (2012). Predictive self-assembly of polyhedra into complex structures. Science, 337(6093), 453-457.

Dong, K., Wang, B., & Yu, A. (2013). Modeling of particle flow and sieving behavior on a vibrating screen: from discrete particle simulation to process performance prediction. Industrial & Engineering Chemistry Research, 52(33), 11333-11343.

Dong, K., Yang, R., Zou, R., An, X., & Yu, A. (2009). Critical states and phase diagram in the packing of uniform spheres. EPL (Europhysics Letters), 86(4), 46003.

Dong, K., Yu, A., & Brake, I. (2009). DEM simulation of particle flow on a multi-deck banana screen. Minerals Engineering, 22(11), 910-920.

Gervois, A., Lichtenberg, M., Oger, L., & Guyon, E. (1989). Coordination number of disordered packings of identical spheres. Journal of Physics A: Mathematical and General, 22(12), 2119.

Hales, T. C. (2005). A proof of the Kepler conjecture. Annals of mathematics, 162(3), 1065-1185.

Jiang, X., Zeng, Q., Chen, C., & Yu, A. (2011). Self-assembly of particles: some thoughts and comments. Journal of Materials Chemistry, 21(42), 16797-16805.

Kroupa, M., Klejch, M., Vonka, M., & Kosek, J. (2012). Discrete element modeling (DEM) of agglomeration of polymer particles. Procedia Engineering, 42, 58-69.

Lash, M., Fedorchak, M., McCarthy, J., & Little, S. (2015). Scaling up self-assembly: bottom-up approaches to macroscopic particle organization. Soft matter, 11(28), 5597-5609.

Li, C., An, X., Yang, R., Zou, R., & Yu, A. (2011). Experimental study on the packing of uniform spheres under three-dimensional vibration. Powder Technology, 208(3), 617-622.

Luchnikov, V., Gervois, A., Richard, P., Oger, L., & Troadec, J. (2002). Crystallization of dense hard sphere packings: competition of hcp and fcc close order. Journal of molecular liquids, 96, 185-194.

Nahmad-Molinari, Y., & Ruiz-Suárez, J. C. (2002). Epitaxial Growth of Granular Single Crystals. Physical review letters, 89(26), 264302.

Yu, A., An, X., Zou, R., Yang, R., & Kendall, K. (2006). Self-assembly of particles for densest packing by mechanical vibration. Physical review letters, 97(26), 265501.

Zhang, Y., & Campbell, C. S. (1992). The interface between fluid-like and solid-like behaviour in two-dimensional granular flows. Journal of Fluid Mechanics, 237, 541-568.

Zhu, H., Zhou, Z., Yang, R., & Yu, A. (2007). Discrete particle simulation of particulate systems: theoretical developments. Chemical Engineering Science, 62(13), 3378-3396.

Zhu, H., Zhou, Z., Yang, R., & Yu, A. (2008). Discrete particle simulation of particulate systems: a review of major applications and findings. Chemical Engineering Science, 63(23), 5728-5770.

Proc. 1st International Conference on Structural Engineering Research (iCSER 2017)
20-22 Nov 2017, Sydney, Australia
ISBN: 978-0-6480147-6-8

Numerical Analysis of Web Connected Lipped Channels in Compression with Varying End Distances

Saeid Sheikholarefin Bafghi[1] and Morgan Dundu[2]

[1]PhD student, University of Johannesburg, Johannesburg, South Africa
[2]Professor, University of Johannesburg, Johannesburg, South Africa
Corresponding author's E-mail: ssheikholarefin@uj.ac.za

Abstract

This finite element study focuses on the compressive resistance of the cold-formed lipped channels, connected to the base through the web only. The influence of the cross-section geometry, column length and end distance on the ultimate capacity is investigated. The numerical models cover four end distances and three different values for the length of the column, flange width and lip width. A commercial finite element analyses software ABAQUS and a direct strength method (DSM) in were used to determine the nominal capacity of the columns. According to the observations and assumptions, this paper shows that the current DSM distortional equation is not safe for this boundary condition, however, the end distance has positive effect on the column capacity.

Keywords: End distance, Cold-formed, Web.

1. INTRODUCTION

Cold-formed sections (CFSs) are widely used as structural and non-structural members because of their light-weight and ease of fabrication. However, the sections are very sensitive to their boundary conditions and the end-distance of the connected element, if used as structural member. The North American Specification for the Design of Cold-Formed Steel Structural Members(AISI 2012) defines four modes of failure of bolted connection, namely; sheet bearing, sheet tearing, tensile failure in net section and bolt shearing mode of failure. The failure modes were determined from the work of Yu (1982), Zadanfarrokh (1991), Zadanfarrokh and Bryan (1992), LaBoube, Wallace, and Schuster (2002) and Wallace (2009), in which the connected sheets were restrained on both sides by the bolt head and nut, with or without washers. According to SANS 10162-2 (2011), AISI (2012), the minimum end distance of a bolted connection with two or more bolts in the direction of the load, should not be less than 1.5 times the bolt diameter. Kim and Kuwamura (2005) and (2007) has shown that the end/edge distance of bolted thin-walled plates may cause strength erosion if curling of the plates happens before reaching to ultimate strength. However, the strength loss was not significant when the end/edge distance was increased (Kim, Kuwamura, and Cho (2008)).

Recent results of finite element models developed by Sheikholarefin and Dundu (2016) have shown that fixing the edges of the cross-section of cold-formed columns under axial compressive load can cause premature failure due to stress concentrations near the joints of the fixed web, corners and flanges. The material at these areas exceeded the elastic limit and experienced plastic behaviour faster than other areas, resulting in a decrease of the ultimate capacity of the column. The purpose of this paper is to perform a parametric study on columns in order to investigate the effect of the end-distance on the compressive resistance of the cold-formed lipped channel connected through the web only. The end distance, in this case, is the perpendicular length from the edge of the column to the welded connection in the web (Figure 1). Ultimately, the main aim of this study is to find the length of the weld and end distance that produces the largest capacity of the columns.

2. MATERIAL PROPERTIES

The material properties were determined from flat and corner areas of the channels. The flat specimens were taken from the areas of the web with the least effect of cold work. To measure the effect of the cold work on the material properties of the corners, the coupons were prepared from the corners of the web and flange. The outer parts of the corner coupons flattened, while causing the least side effect of deforming in the gauge length, to facilitate gripping of the coupons. Both coupons were cut in the longitudinal direction of the channel. The modulus of elasticity, E, and yield stress, F_y, of 200 GPa and 330 MPa, respectively, were determined from the average true stress-strain curves of the coupons, shown in Figure 1.

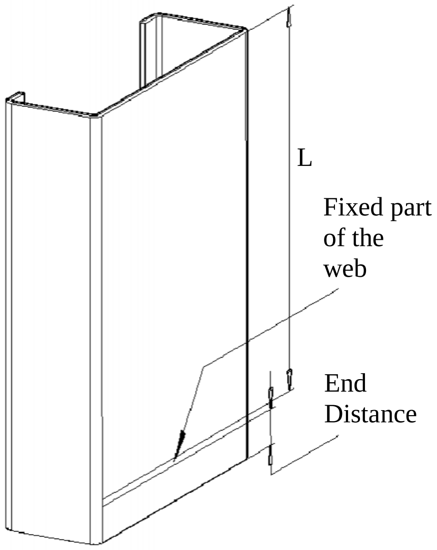

Figure 1 End distance and length of column

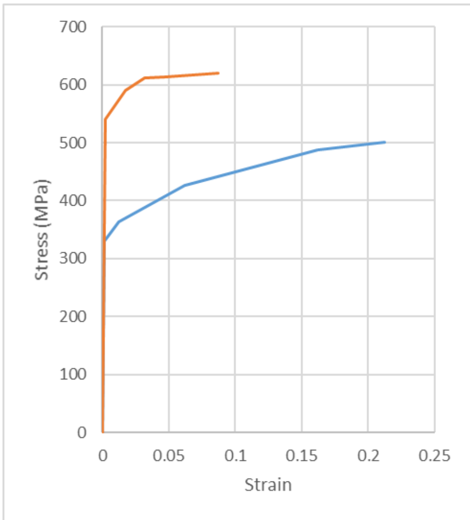

Figure 2 Material properties

3. MODEL SPECIFICATION

To investigate the effect of the end distance on the column capacities, a total of 108 numerical models of cold-formed lipped channel columns, were tested in four main categories. Each category consists of columns with different length and cross-section but same end distance. As shown in Table 1, the first category has no end distance while the other three categories have end distance of 10, 20 and 30mm. The connection of the column to base was attained through a welded strip in the web. The length of the weld was set equal to the flat part of the web and a weld size of 5 mm. Each category was analysed with three column lengths of 500, 1000 and 1500mm. Figure 1 shows the column length, end distance and connected part of the web to the base.

To study the effect of flanges and lips on the axial capacity of the column, three different sizes of flanges of 50, 75 and 100mm and lips of 15, 20, 25mm were considered. The length of the web, radius of corners and section thickness were taken as dimensions of 250, 10mm and 3 mm, respectively. A typical model combination from the details in Table 1 is E10-C500-F50-L20, where E10 represents the end distance (E) of 10 mm, C500 represents the column length (C) of 500mm, F50 represents the flange width (F) of 50 mm and L20 represents the lip width (L) of 20 mm. Commercial finite element software, Abaqus/CAE, was used to model and analyse the columns. A fully fixed boundary condition was defined at the top of the column. Two types of analysis were performed; “Buckling” analysis to obtain the lowest critical elastic buckling load and “Explicit” analysis to achieve the maximum axial capacity of the column, according to the defined materials. In buckling analysis, a shell edge load was applied on the top cross section of column and in Explicit analysis, by moving the fixed support vertically toward the base, a compressive displacement controlled loading was applied to the top of the column. All flat surfaces were meshed to size of 5mm and curves areas refined to 3 by 5 meshes.

Table 1 Details of the numerical models

E	C	F	L
End distance (mm)	Column length (mm)	Flange width (mm)	Lip width (mm)
0 10 20 30	500 1000 1500	50 75 100	15 20 25
Example: E10-L500-C50-20			

4. CAPACITY OF THE COLUMN

4.1. Direct strength method (DSM)

Buckling analysis using Abaqus provides the critical elastic buckling load of the section, according to the load and specimen geometry specifications. However, in the Direct Strength Method (DSM), it is not only the elastic buckling load that should be determined, but also the mode of failure. One major drawback of using the finite element buckling analysis in Abaqus is uncertainty in establishing the failure mode of specimens accurately. A decision was made to estimate the failure mode in Abaqus based on section of the column, which is experiencing the maximum deformation, in both buckling and dynamic analysis. After investigating the deformation of the flanges, corners and lips at the base, it was concluded that distortional buckling can be the dominant buckling mode in all specimens.
The nominal member capacity of a member in compression (P_{nd}) for distortional buckling is calculated from SANS 10162-2 (2011) as given in Equations 1 and 2

For $\lambda_d \le 0.561$ $$P_{nd} = P_y \tag{1}$$

For $\lambda_d > 0.561$ $$P_{nd} = \left(1 - 0.25\left(\frac{P_{crd}}{P_y}\right)^{0.6}\right)\left(\frac{P_{crd}}{P_y}\right)^{0.6} P_y \tag{2}$$

where, P_y is allowable strength, P_{crd} is critical elastic distortional buckling load, P_{nd} is the columns nominal capacity and $\lambda_d = \sqrt{P_y / P_{crd}}$.
The nominal capacity of the columns calculated using the DSM equations is shown in Figure 3. As illustrated in the figure, an increase in the columns capacity was realized when end distance was increased, however it is not significant.

4.2. Effect of the lip and flange

Corners and flanges provide stiffening to the web element. In general, Figure 3 shows that increasing the length of flanges can increase the column's capacity. Although the results from both DSM and ABAQUS agree with this view, ABAQUS models show very close results for the columns with same

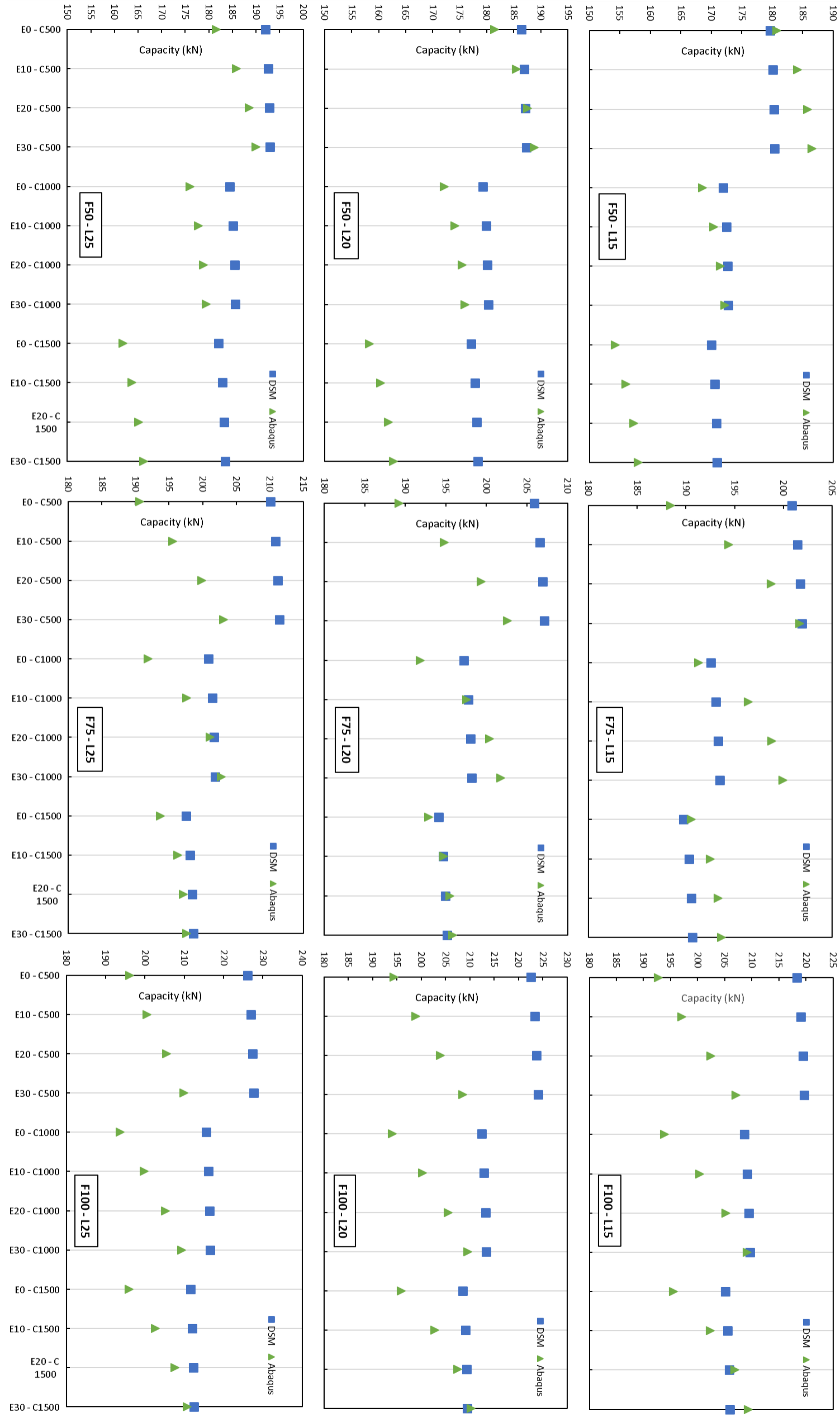

Figure 3 Axial capacity of the columns from the finite element models and DSM

end distance and cross section, but different lengths. Increasing the length of the lip, increases the stiffness of the flange, which indirectly increases the stiffness of the web. The nominal yield capacity (P_{nd}) in Eq.2 is influenced by an increase in area due to an increase in the lip's width. Obviously, this results in a marginal increase in the capacity of the column. This increase in capacity is shown in Figure 3. Abaqus results do not support this. When the width of the flange is increased, the effect of the lip becomes negligible.

4.3. End distance

To investigate the mechanism and effect of the end distance on column capacity, two columns were selected. These columns represent the overall behaviour of the models investigated. Figure 4 show typical stress distributions of a column with no end distance (E0-C500-F75-L20) and that of a column with 30mm end distance (E30-C500-F75-L20) at their maximum axial capacity. The area in a lighter colour indicates the yielded zones of the web. Figure 4(a) illustrates a column without end distance. Considering a cross-section that includes base connection strip, its flanges and lips are connected at top and free at the bottom. Comparing to Figure 4(b), flanges and lips are places in 30mm above the bottom cross-section and are supported by the elements from top and bottom. When a compressive load is applied at the top of the column, free elements of the mentioned cross section of Figure 4(a) have less restrain to resist against opening and deformation than Figure 4(b). Such confinement effect of the end distance let more area of the column to contribute in load bearing before failure. An increase in the end distance in the tested columns with short flange shows a maximum increase of 4 % (about 7 kN) in columns capacity. This increase rises to 8 % (about 15 kN) for the rest of other columns.

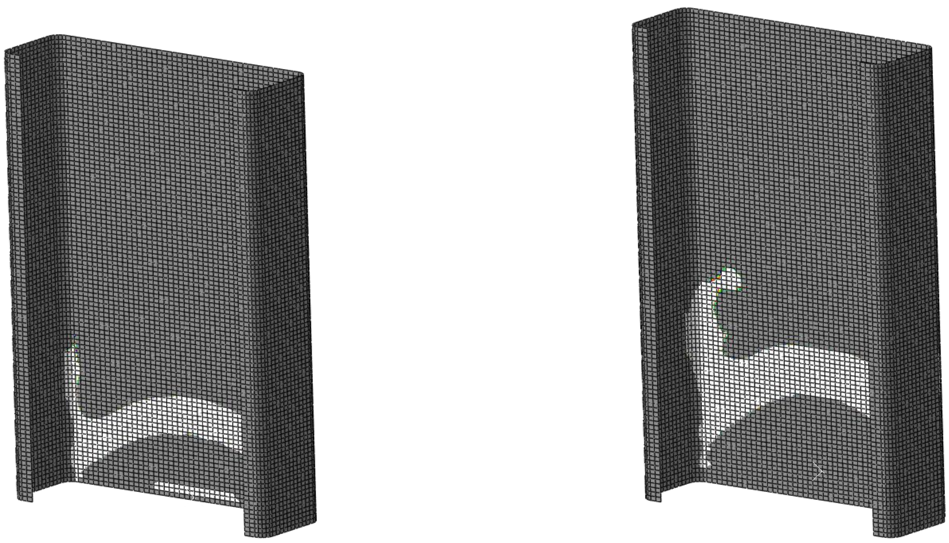

(a) Column with no end distance **(b) Column with 30mm end distance**

Figure 4 Stress distribution of yielded area in bottom port of the column

5. CONCLUSION

This study focused on cold-formed lipped channel columns connected to the base through the web only, under axial compression load. A comparison of the ultimate axial capacity of the columns between finite element numerical models and DSM shows that an increase in the cross-section area due to increase in the length of lip, does not have any remarkable influence on the ultimate capacity of numerical models, but gives higher value using DSM. Although in most cases the predicted nominal capacity of the columns by DSM is higher than the ultimate axial capacity of the same column modelled and analysed using ABAQUS, the difference between the reported capacities are less when the maximum considered end distance is taken into account.

6. REFERENCES

Iron, A. (2012) *Steel Institute, AISI S100-2012. North American Specification for the Design of Cold-formed Steel Structural Members*. Washington DC: American Iron and Steel Institute.

Kim, T. S. and Kuwamura, H. (2005) 'The effect of curling on bolted connection strength of thin steel plates', in *Annual Meeting Architectural Institute of Japan (AIJ)*, pp. 569–570.

Kim, T. S., Kuwamura, H. and Cho, T. J. (2008) 'A parametric study on ultimate strength of single shear bolted connections with curling', *Thin-Walled Structures*, 46(1), pp. 38–53.

LaBoube, R. A., Wallace, J. A. and Schuster, R. M. (2002) 'Calibrations of bolted cold-formed steel connections in bearing (with and without washers)'. University of Missouri--Rolla.

'SANS 10162-2 Structural Use of Steel: Part2: Cold-formed Steel Structures' (2011) in *South African National Standard*.

Sheikholarefin, S. and Dundu, M. (2016) 'A Finite Element Study Of The Influence Of Boundary Conditions On Cold-Formed Column-Channel Bases', in *8th International Conference on Steel and Aluminium Structures*. Hong Kong: The University of Hong Kong, p. 345 (1-8).

Soo Kim, T. and Kuwamura, H. (2007) 'Finite element modeling of bolted connections in thin-walled stainless steel plates under static shear', *Thin-Walled Structures*, 45(4), pp. 407–421.

Wallace, J. A. (2009) 'Research Report', (March).

Yu, W.-W. (1982) 'AISI Design Criteria for Bolted Connections', in *Sixth International Speciality Conference on Cold-Formed Steel Structures*.

Zadanfarrokh, F. (1991) 'Analysis and design of bolted connections in cold formed steel members'. Available at: http://usir.salford.ac.uk/2141/.

Zadanfarrokh, F. and Bryan, E. R. (1992) 'Testing and design of bolted connections in cold formed steel sections'. University of Missouri--Rolla.

Proc. 1st International Conference on Structural Engineering Research (iCSER 2017)
20-22 Nov 2017, Sydney, Australia
ISBN: 978-0-6480147-6-8

`

Application of Thermal Analysis Techniques (TGA, DSC, TMA and Evolved Gases FTIR) in Understanding New Materials

Laurel George[1], Jiunn Jieh Lee[2], Shamila Salek[1], Richard Wuhrer[1]

[1]Advanced Material Characterisation Facility (AMCF), Western Sydney University, Sydney, Australia
[2]NETZSCH Australia Pty Ltd, Kings Park, Australia
Corresponding author's E-mail: L.george@westernsydney.edu.au

Abstract

Thermal analysis of both traditional and new advanced building materials can provide valuable information on their behaviour under different environmental conditions. This type of analysis involves techniques that look at changes in the physical, chemical and mechanical properties of a material as a function of temperature. The Advanced Materials Characterisation Facility (AMCF), located at Western Sydney University's Parramatta campus, is home to a suite of thermal analysis instrumentation that are able to carry out various thermal analysis techniques on small scale samples. These techniques include Thermo-Gravitation Analysis (TGA), Differential Scanning Calorimetry (DSC), Infra-Red (FTIR) analysis of evolved gasses from TGA/DSC and Thermo-Mechanical Analysis (TMA). Properties that can be analysed include mass changes, material phase transitions (e.g. crystalline, amorphous, melting, etc), heat capacity, expansion, tension, young's modulus, sintering, softening points, evolved gases and much more.This paper will provide an overview of each of the thermal analysis instruments housed at the AMCF. Examples of thermal analysis previously undertaken on various materials will also be given in order to show the potential of thermal analysis techniques on future construction materials.

Keywords: Thermal analysis, Thermal properties, Material properties, Instrumentation, New materials

1. INTRODUCTION

With a growing awareness of environmental issues and energy management, there is an increasing need for new advanced building materials with improved properties and more efficient manufacturing processes in the construction industry. In order to better understand and assess these innovative materials, it is important to analyse the structure, durability and damage that may occur.

Thermal analysis of materials can provide valuable information on the behaviour of materials under different environmental conditions, with techniques that look at changes in the physical, chemical and mechanical properties of a material as a function of temperature. A lot of new materials being researched rely heavily on thermal processes and chemical reactions taking place.

Example 1, Phase Changing Materials (PCMs) which are able to store and release thermal energy when necessary as the material changes phase (i.e. melting and solidifying), need to work in a particular temperature range. It is also possible to mix PCMs with flame retardants, and then impregnate them into structural materials (e.g. concrete floors, blocks and plasterboard). It is imperative to know thermal properties such as melting and solidification temperatures, ignition points, absorption/dissipation of thermal energy and how these properties are affected when mixed with other materials (Pielichowska and Pielichowska, 2014).

Example 2, Self-healing polymeric composites are being designed to replace traditionally heavy metal alloys. These new materials possess an intrinsic matrix of capsules or a vascular network which can release a polymer healing agent when damage occurs. In order to be used as structural materials, an understanding of their thermal strength and stability are needed at different temperature conditions, as well as analysis of glass transition temperatures, polymer curing temperatures and their reliability (Hia et al 2016, Guadago et al 2014).

Example 3, Adhesives containing thermally expandable particles, allow for strong adhesion in building materials, but can be easily separated under heat for recycling of parts. For any product using adhesives it is important to look at the product's final structural qualities, particularly the flexibility of the adhesive in both cold and hot temperature environments. Thermal expansion, Young's modulus and glass transition temperatures are important to understand (Banea et al 2014).

Example 4, Geopolymer concretes make use of a mixture of "geopolymer", polymerised chains of inorganic molecules (eg. silica and alumina) that create a hardened binder, industry by-products containing silicate materials such as fly ash, and various aggregates (Noushini and Castel, 2016). This concrete is more resistant to fire, harsh environments and, most importantly, more "green" in terms of production CO_2 emissions. The composition and microstructure has an influence on the thermal properties of the final product. It is important to analyse thermal properties such as curing temperatures, coefficients of thermal expansion (CTE), creep, and phase stability of the final products (Vickers 2015, Kovarik et al 2017, Dey 2014)

Example 5, there is also a need to understand potential hazards associated with new building materials. Recent events such as the Grenfell Tower fire in London (2017) saw the rapid spread of fire due to the use of highly flammable exterior cladding which also reportedly resulted in the production of cyanide gas (Razzall and Moralioglu, 2017). Thermal analysis coupled with evolved gas analysis can be used to identify the gasses produced from heating of modern building materials and at what temperature these gasses occur. This information may also be beneficial in assessing how these materials influence fire dynamics.

2. TECHNIQUES AND EXAMPLES

Thermal analysis includes a number of techniques which monitor and analyse material physical and chemical changes under different temperature conditions. For all types of analysis, samples can be heated or cooled at a consistent rate, multiple times if needed to test durability (dynamic temperature), or held at a particular temperature of interest for testing (isothermal temperature). The temperature can also be programmed to include both dynamic and isothermal sequences.

Samples can be tested at different heating rates, in different atmospheres (e.g. air, nitrogen, argon). A selection of crucibles is available (Figure 1b), and will depend on the temperature range that is to be used, and compatibility with the sample itself. Care also needs to be taken when considering sample size and the reaction of the sample to heat (Figure 1c).

Table 1. A comparison of properties each thermal analysis technique can measure.

<table>
<tr><th>TGA</th><th>DSC</th><th>TMA</th></tr>
<tr><td>Mass change
Decomposition
Moisture content
Thermal stability
Sample composition</td><td rowspan="3">Melting/solidification
Crystallisation
Glass transition
Heat of fusion
Purity analysis
Specific heat
Phase transition
Curing temperature
Sample composition</td><td rowspan="3">Expansion/shrinkage
Compression/tensile strength
Young's Modulus
Load deformation
Penetration
Softening point
Sintering temperature
Hardness/softness
Creep under load
Coefficient of thermal expansion</td></tr>
<tr><th>FTIR</th></tr>
<tr><td>Evolved gas analysis
Sample identification</td></tr>
</table>

Simultaneous Thermal Analysis (STA) is the simultaneous running of two or more thermo-analytical techniques (e.g. TGA, DSC and FTIR) on one sample at the same time. The advantage here is that the results from STA, which is a TGA plot and DSC plot, can be directly compared on the same graph with the knowledge that the sample and test conditions are identical. The following sections are an explanation of the most common thermal analysis techniques. A comparison of properties each thermal analysis technique can measure is shown in Table 1.

2.1. Thermo-Gravimetric Analysis (TGA)

TGA measures a sample's change in mass during heating in a furnace. As a sample undergoes a thermal event (e.g. moisture loss, decomposition, etc.) a mass change will occur and is detected by a microbalance located at the base of the instrument (Figure 1a).

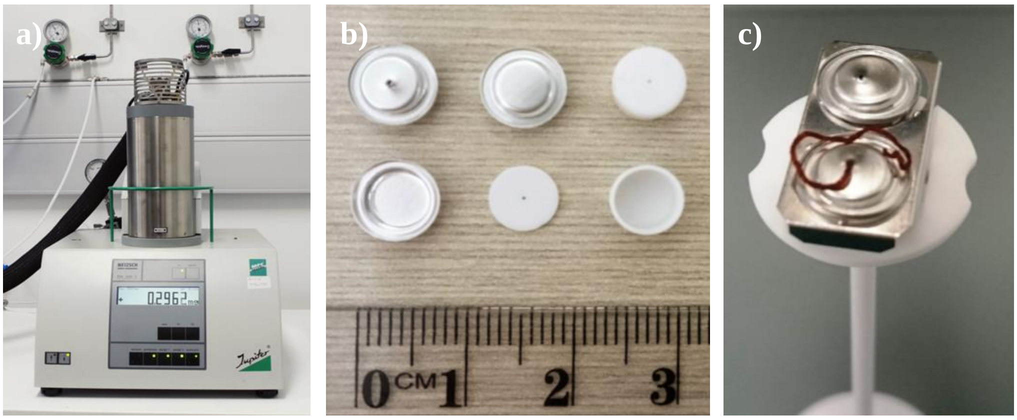

Figure 1. a) TGA setup, b) a selection of crucibles for TGA/DSC analysis (aluminium and alumina), and c) a STA sensor which measures TGA and DSC, with reference crucible (back) and sample crucible (front). Note it is important that sample size is small enough that if it expands, it does not extrude out the top of the crucible as shown above.

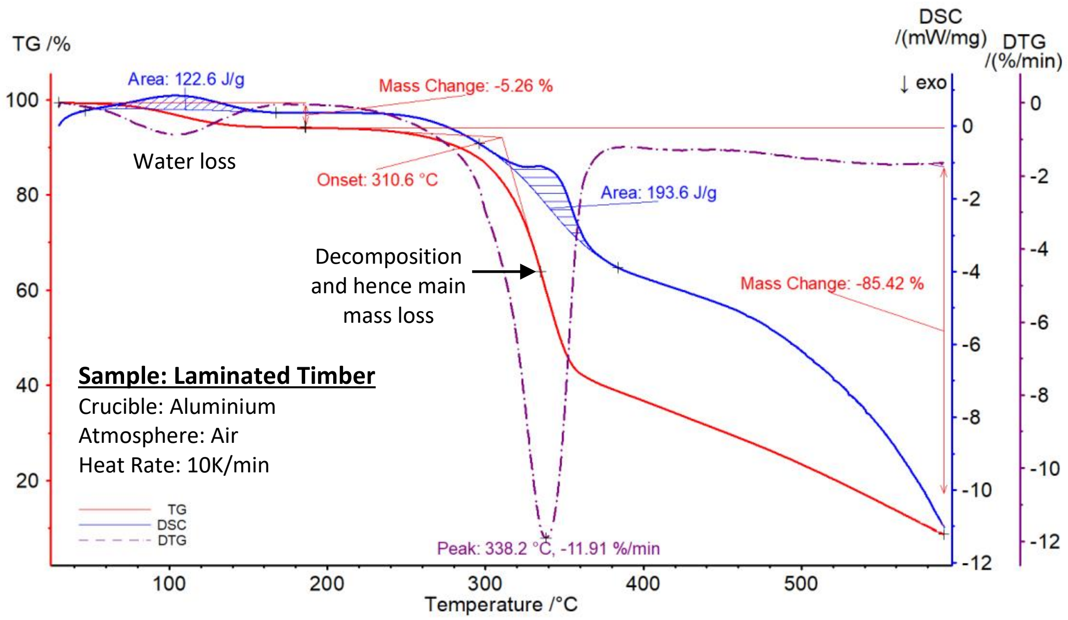

Figure 2. Simultaneous TGA and DSC analysis of a laminated timber sample. The TG curve (red line) shows the loss of mass as the sample was heated. This is compared with the first derivative of the TG curve (dotted line, DTG) which shows the rate of mass loss, and the DSC curve (blue line) which shows the mass loss is associated with an endothermic reaction. The associated heat absorbed can be calculated.

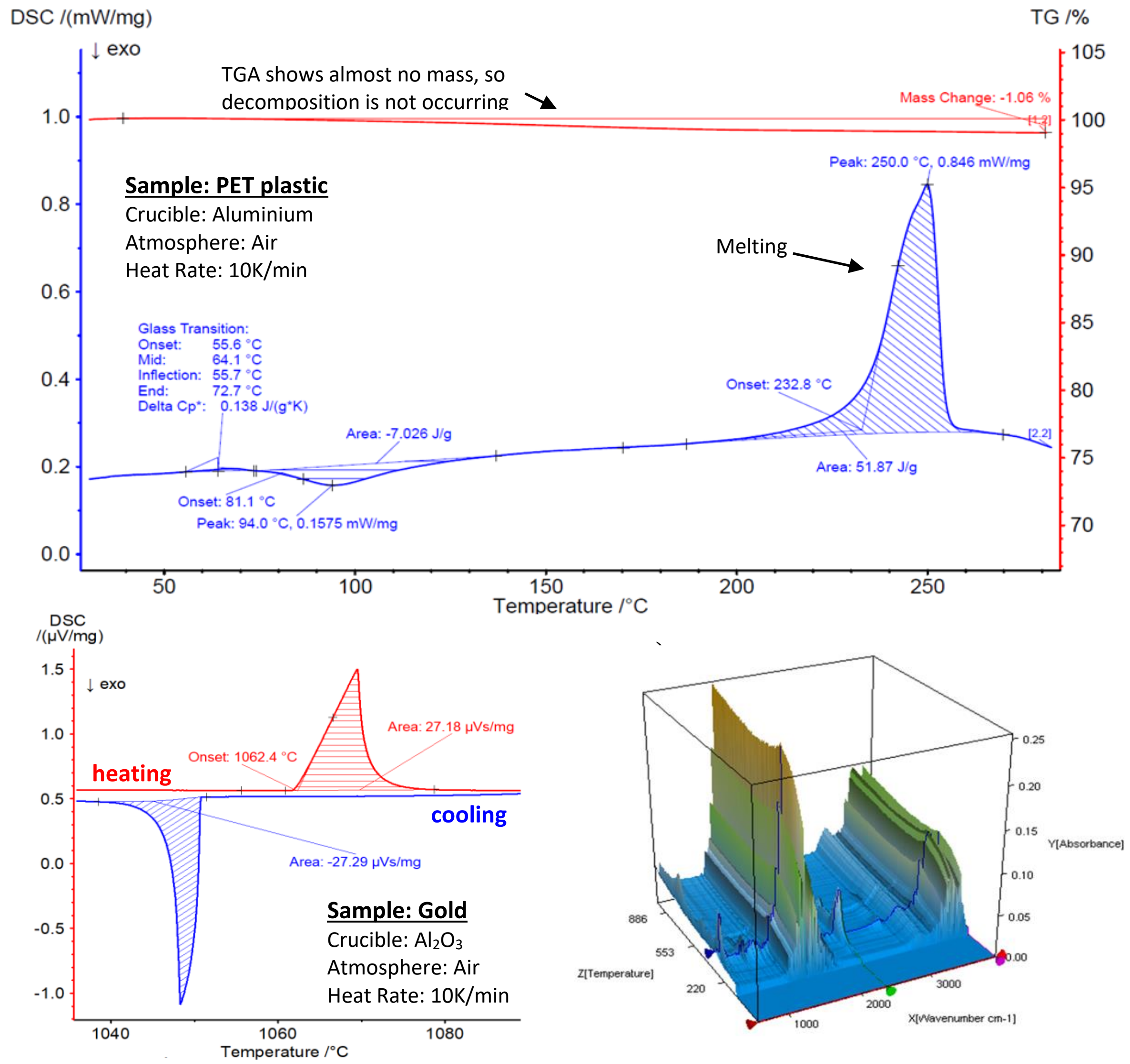

Figure 3. a) STA analysis (TGA and DSC) of a PET plastic sample showing the phase transition, recrystallisation and melting temperatures, b) DSC of a standard gold sample (the heat absorbed/released due to melting/solidification is almost identical, showing the sample is of very high purity), c) an evolved gas FTIR spectrum taken during TGA analysis of an algal material (different gases are coming of at 300ºC).

2.2. Differential Scanning Calorimetry (DSC)

DSC measures the heat into or out of a sample relative to a reference (usually an empty crucible identical to the one holding the sample). A linear heating rate is usually used (e.g. 10°C/min) so the particular temperature at which a thermal event occurs can be found (e.g. melting points, glass transitions, etc.). There are two main types of thermal events; endothermic (where heat is absorbed by the sample, such as melting) and exothermic (where heat is released by the sample, such as crystallisation).

During analysis the sample and reference are maintained at the same temperature, even when the sample undergoes a thermal event. The energy required to maintain a zero temperature difference between the sample and the reference is measured. It is important to note on any graphical results from DSC, which direction represents exothermic or endothermic heat (e.g. in Figures 2 and 3 exothermic heat is down the y-axis).

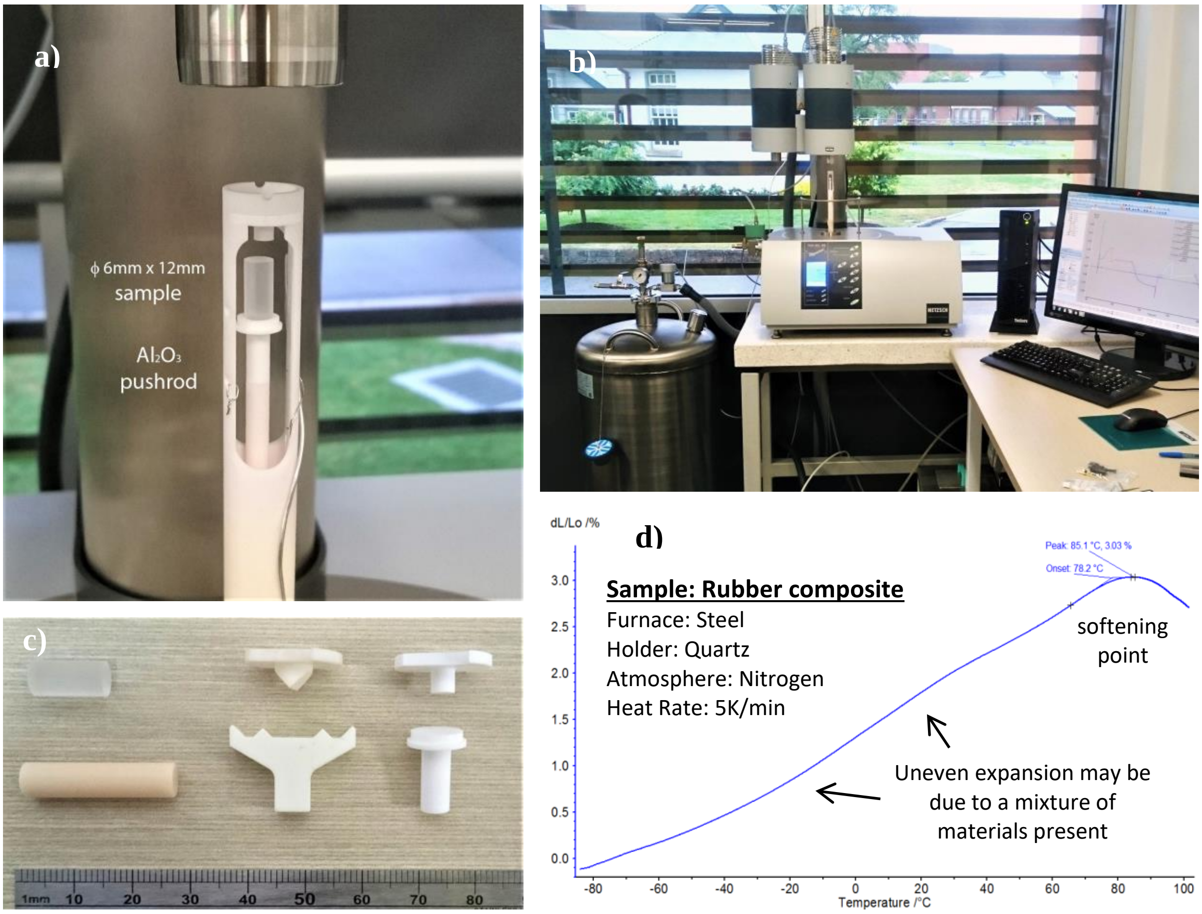

Figure 4. a) TMA setup for high temperature expansion experiments, b) TMA with two furnaces and pressurised liquid nitrogen dewar for negative temperature experiments, c) standard samples (left), and the attachments for high temperature 3-point bending (middle) and expansion (right), and d) results of an expansion experiment (-85 to 100ºC) for a rubber sample showing the material's softening point.

2.3. Fourier Transform Infra-Red (FTIR) Analysis of Evolved Gasses

As a material decomposes under high temperatures, volatile gases may be released. As a TGA or DSC analysis is undertaken, the gases that evolve during the experiment can be collected and sent through a FTIR gas cell for analysis using a special transfer tube. This transfer tube is kept short and at a relatively high temperature (e.g. 200ºC), so gases do not condense on the way to the FTIR detector. The FTIR spectrum can be used to identify gases evolved during the thermal analysis, and at what temperatures they evolved. Figure 3c shows an example of a 3-dimensional representation of the evolved gas FTIR collected from an algae based material.

2.4. Thermo-Mechanical Analysis (TMA)

This versatile instrument determines material dimensional changes under different temperature regimes and different mechanical forces (both static and dynamic). The instrument shown in Figures 4a and 4b, has a choice of two furnaces (Silicon-Carbide and Steel) which can be easily interchanged, two thermocouples types (K and S-type) and two sample holder materials (alumina and quartz). These choices allow for a wide range of materials to be tested under temperatures ranging from -160°C to 1600°C.

The sample holders and push rods also come in different configurations (Figure 4a and 4c), allowing for different testing modes, such as expansion, penetration, compression, tensile and 3-point bending. The vertical design of the TMA's furnace with motorized hoist allows maximum flexibility regarding sample geometries (rods, squares, plates, films, fibres, powders, liquids).

3. CONCLUSIONS

As many new building materials and composites make use the material's inherent thermal properties, thermal analysis techniques such as TGA, DSC, TMA and evolved gas FTIR are essential in order to fully understand their stability and durability when put into use. Simultaneous thermal analysis is preferable, as the sample and conditions are identical. The results from each detector are also complimentary, helping to fully explain any thermal events that occur during analysis, and hence the sample's chemical and physical properties. Care must be taken however, to consider experimental conditions and how they affect results and relate to real-world applications.

4. ACKNOWLEDGMENTS

The authors would like to acknowledge the support of the Advanced Materials Characterisation Facility (AMCF) and Netzsch. We would also like to thank Miss Denise Duff for use of her data on laminated timber.

5. REFERENCES

Banea MD, daSilva LFM, Carbas RJC, Campilho RDSG (2014). Mechanical and thermal characterization of a structural polyurethane adhesive modified with thermally expandable particles, International Journal of Adhesion & Adhesives, 54, 191-199.

Dey T (2014). Thermal properties of a sustainable cement material: effect of cure conditions, Ceramics-Silikáty, 58(4), 275-281.

Guadagno L, Raimondo M, Naddeo C, Longo P, Mariconda A (2014). Self-healing Materials for structural applications, Polymer Engineering and Science, 54(4), 777-784

Hia IL, Vahedi V, Pasbakhsh P, (2016). Self-Healing Polymer Composites: Prospects, Challenges, and Applications, Polymer Reviews, 56(2), 225-261.

Kovárík T, Rieger D, Kadlec J, Krenek T, Kullová L, Pola M, Belsky´ P, France P, Ríha J (2017). Thermomechanical properties of particle-reinforced geopolymer composite with various aggregate gradation of fine ceramic filler, Construction and Building Materials, 143, 599-606.

Noushini A, Castel A (2016). The effect of heat-curing on transport properties of low-calcium

fly ash-based geopolymer concrete, Construction and Building Materials, 112, 464-477.

Pielichowska K, Pielichowska K (2014). Phase change materials for thermal energy storage, Progress in Materials Science, 65, 67-123.

Razzall K, Moralioglu S (2017). Grenfell survivor was diagnosed with cyanide poisoning, Accessed via http://www.bbc.com/news/uk-40568640 on 15 October 2017.

Vickers L, van Riessen A, Rickard WDA (2015). Fire-resistant geopolymers: role of fibres and fillers to enhance thermal properties, Springer Breifs in Materials, 129pp.

ISBN: 978-0-6480147-6-8

Authors Index

ISBN: 978-0-6480147-6-8

Authors Index

ISBN: 978-0-6480147-6-8

THE END